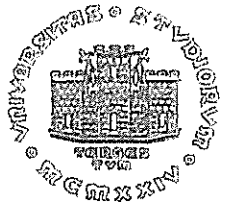

UNIVERSITÁ DEGLI STUDI DI TRIESTE
XXVIII CICLO DEL DOTTORATO DI RICERCA IN FISICA

Numerical simulations of galaxies in cosmological volumes

SETTORE SCIENTIFICO-DISCIPLINARE: FIS/05

Coordinatore:
PROF. PAOLO CAMERINI

Dottorando:
DAVID GOZ

Supervisori:
PROF. PIERLUIGI MONACO
DR. GIUSEPPE MURANTE

Anno Accademico 2014/15

"I'm not a smart man,
but I know what love is."

Forrest Gump

Contents

1

Introduction

In the context of the formation of cosmic structures, galaxy formation is still an open problem. Wide-field surveys and targeted observations across the electromagnetic spectrum reveal that astrophysical processes as star formation, stellar feedback, galaxy outflows, galactic fountains and galaxy interactions are shaping the characteristics of galaxies. Modeling galaxy formation in a cosmological context is considered as one of the biggest challenges in astrophysics today, due to the huge dynamical range, from tens of Megaparsecs, where gravity determines the properties of dark matter haloes hosting galaxies, to the sub-parsec scale where individual stars form. By means of cosmological hydrodynamical simulations, the structure and kinematics of galaxies, as well as their spatial distribution and global properties, can be studied in great detail over cosmic ages, limited by the spatial resolution of the simulation and by the capability to treat the many complex physical processes which are involved.
In this Chapter, the physical properties of local galaxies and the modern numerical techniques in galaxy formation are reviewed, focusing on topics that are related with theoretical studies addressed in this Thesis.

1.1 Physical properties of nearby galaxies

Observations are the fundamental drivers of our understanding of galaxy formation. Many surveys cover a significant fraction of the sky and a wide range of the electromagnetic spectrum, providing photometric and spectroscopic measure-

ments, such as luminosities, colours, sizes and spectra of galaxies. Among the wide-field surveys there are the Galaxy Evolution Explorer Science Surveys in the ultraviolet (GALEX survey; Martin 2005), the Sloan Digital Sky Survey in the optical (SDSS; York & SDSS Collaboration 2000), the Two-Micron All Sky Survey in the near infrared (2MASS; Skrutskie et al. 2006), the *Hershel* Reference Survey in the far infrared (HRS; Boselli et al. 2010) and the Arecibo Legacy Fast ALFA Survey (ALFALFA; Giovanelli et al. 2007) in the radio.

1.1.1 Global properties

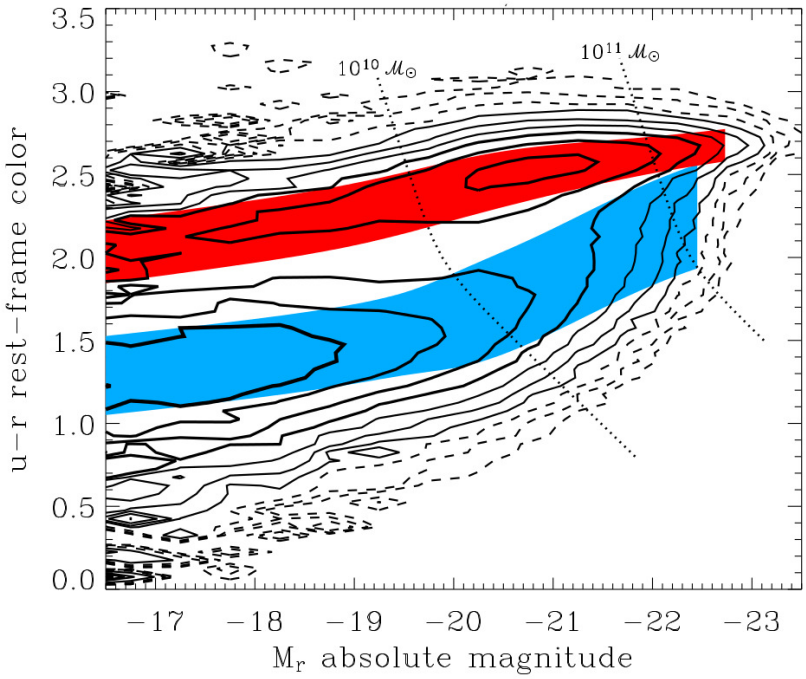

Figure 1.1: Galaxy colour bimodality. The contours are the $u - r$ colour vs M_r luminosity isodensity contours of SDSS galaxies. Red and blue filled regions show the *red* and *blue* sequences. Reproduced from (Baldry et al., 2004).

Surveys have the ability to explore many galaxy properties, and allow us to establish galaxy scaling connections between them. The absolute magnitude, i.e. the intrinsic luminosity of a galaxy, is a fundamental measurable property of galaxies; a colour is the difference in magnitude measured when the galaxy is observed

through two different filters. Figure 1.1 shows the $u - r$ colour against the absolute M_r of galaxies taken from from SDSS sample (Baldry et al., 2004). The distribution is bimodal, namely galaxies can be roughly separated into *blue* cloud and *red* sequences. Blue galaxies have ongoing star formation and their colour is strongly related both to the recent star formation history and dust reddening. Red galaxies have minor recent star formation and mostly are depleted of cold gas. Even though the colour classification is not tightly correlated with morphology (Roberts & Haynes, 1994), blue objects are mainly classifiable as spiral galaxies, while the red sequence contains a mixture of morphological early types.

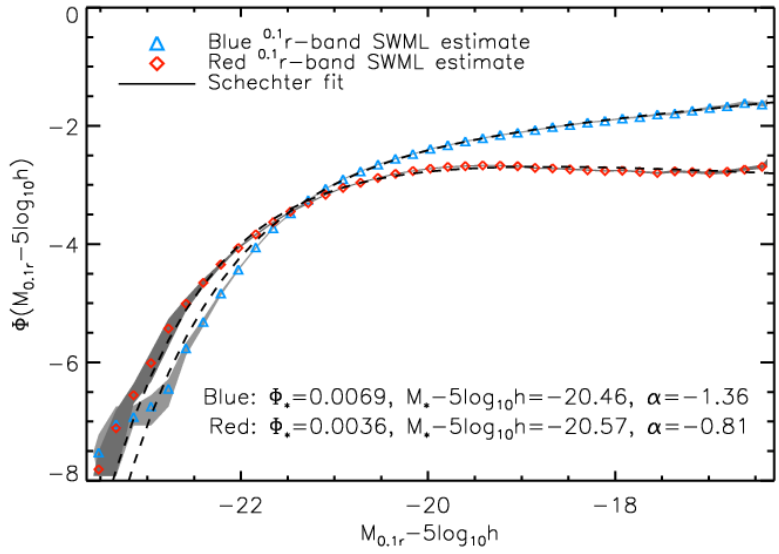

Figure 1.2: The *r*-band SDSS (sixth data release) LF for blue and red galaxies separately. The dashed lines represent the best-fitting Schechter function. Best-fitting values of Schechter parameters for both blue and red galaxies are shown in the figure. Shaded regions represent the 1σ uncertainty. Reproduced from Montero-Dorta & Prada (2009).

The luminosity function (LF) probes the galaxy distribution as a function of luminosity. It is commonly fit, to a good though not perfect accuracy, with an analytic expression provided by the Schechter (Schechter, 1976) function:

$$\Phi(L)dL = \phi^* \left(\frac{L}{L_*}\right)^{\alpha} \exp(-L/L_*) \left(\frac{dL}{L_*}\right) \tag{1.1}$$

where the parameter $\phi*$ is a number per unit volume and L_* is a characteristic galaxy luminosity where the power-law form of the function cuts off. Figure 1.2 shows the optical r-band LF for blue and red galaxies separately from the SDSS (sixth data release) sample (Montero-Dorta & Prada, 2009), as well as their corresponding best-fitting Schechter LFs. The SDSS r-band LF of blue galaxies is well fitted by a Schechter LF with $\alpha = -1.41$. In contrast, the SDSS r-band LF of red galaxies has a negative faint-end slope, corresponding with $\alpha = -0.81$. At the bright end, the blue LF falls below the red LF.

The Sérsic profile (Sersic, 1968) describes how the measured intensity I of a galaxy varies with distance r from its centre. Its mathematical function is defined as:

$$\ln I(R) = \ln I_0 - kR^{1/n}$$

where I_0 is the luminosity at $R = 0$. The parameter n describes the degree of the curvature of the profile and so its light *concentration*. As $n \to 0$, the Sérsic profile approaches a uniform disk, while as n increases the surface luminosity profile is concentrated towards the centre, passing through a Gaussian ($n = 0.5$), an exponential ($n = 1$) and a de Vaucouleurs (de Vaucouleurs, 1959) profile ($n = 4$). Most galaxies are fitted by Sérsic indices in the range $1/2 < n < 10$, and bigger and brighter galaxies tend to be fit with larger n (Caon et al., 1993; Young & Currie, 1994). Although for many galaxies a single Sérsic model does not explain the profile completely, such index is often used as a proxy for morphology (e.g. Shen et al. 2003). Giant elliptical galaxies are well fitted by the de Vaucouleurs profile, while spirals and lenticulars are better fitted by an exponential disk plus a Sérsic central component.

1.1.2 Spiral galaxies

Spiral galaxies consist of disk galaxies with ongoing star formation. Fig. 1.3 shows a sample of optical images of nearby spiral galaxies from the SDSS, sorted by absolute magnitude on the horizontal axis and $g - r$ colour on the vertical axis. The most luminous galaxies likely exhibit nearly regular spiral structure. Many of them host in the centre a prominent reddish and smooth central component, called the *bulge*.

Quantitative morphology focuses on the separation of the bulge from the disk component, by means of packages such as GALFIT (Peng et al., 2002) or BUDDA (de Souza et al., 2004), allowing to recover, for instance, the bulge-over-total ratio (B/T), i.e. the photometric ratio between bulge and bulge plus disk components.

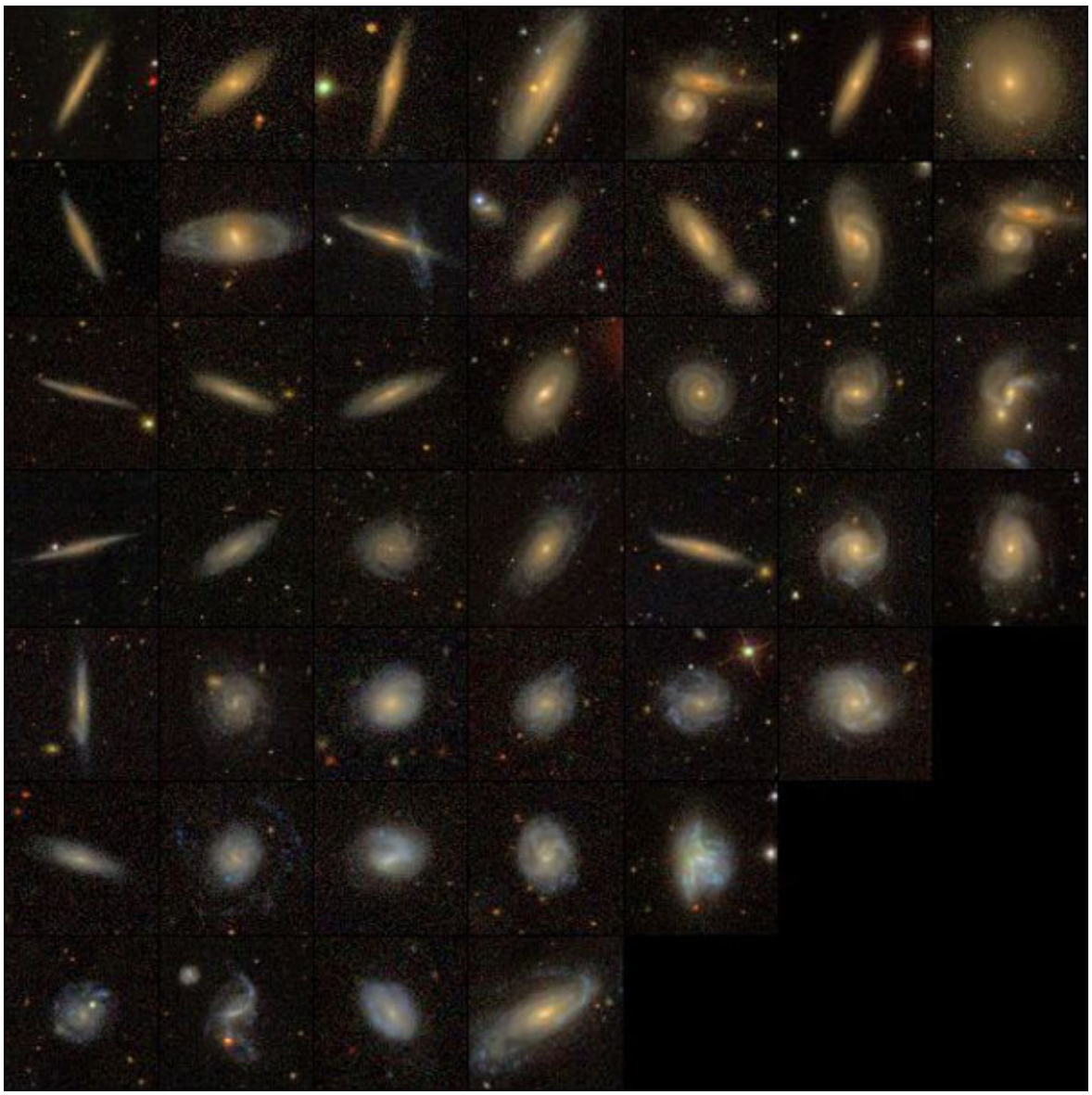

Figure 1.3: SDSS images of spiral galaxies. The images are sorted by absolute M_r magnitude in the horizontal direction from left to right, and $g - r$ colour in the vertical direction. Reproduced from (Blanton & Moustakas, 2009).

Bulges, Pseudobulges and Bars

Classical bulges exhibit high Sérsic index and stars orbit randomly compared to the plane of the galaxy, giving the bulge a distinct spherical form (Kormendy & Kennicutt, 2004). They often contain older stellar populations compared to the stellar disks (Moorthy & Holtzman, 2006).

Pseudobulges are oblate rotators, have exponential profiles, lower surface luminosity (Gadotti, 2008), are not completely gas and dust depleted and are more common in galaxies with lower B/T ratio (Barazza et al., 2008), i.e. late type galaxies.

The common interpretation is that, while classical bulges are built by mergers, pseudobulges are a product of secular processes (Kormendy & Kennicutt, 2004). Internal secular processes are defined to be slow processes, i.e., ones that have timescales much longer than the dynamical time, $t_{\rm dyn} \sim (\mathrm{G}\ \rho\ )^{-1/2}$, where ρ is the mean density and G is the gravitational constant. Therefore, secular processes must operate over long times to be effective, during which the galaxy is free of mergers, and generally involve the interactions of components such as spiral structure and dark matter halos (Kormendy & Kennicutt, 2004).

Bars are elongated stellar structures located in the inner or central regions of disk galaxies (Kormendy & Kennicutt, 2004; Gadotti, 2008). About 60 per cent of nearby disk galaxies are barred when observed in the near-infrared, while this figure lowers when galaxies are imaged in the optical (Eskridge et al., 2000; Barazza et al., 2008). Bars do not strongly influence the global kinematics of their host galaxies, regardless of their strength (Falcón-Barroso et al., 2006; Fathi et al., 2009; Krajnović et al., 2011; Barrera-Ballesteros et al., 2014; Seidel et al., 2015). Bars are typically dominated by evolved stellar populations (Gadotti & de Souza, 2006), although they are also associated with enhanced nuclear and circumnuclear star formation, since non-circular motions of bars cause the migration of gas within the corotation radius towards the galaxy centre, where it can give rise to a starburst or be accreted onto a nuclear black hole.

Molecular and Atomic gas content

Most of the baryons reside in warm and hot gas (this gas is directly detectable in the X-rays) in space between galaxies (Rosati et al., 2002) and the remaining are in the Inter-Stellar Medium (ISM), which includes gas in ionized, atomic and molecular form. Despite cold gas is not completely absent in ellipticals, it is basically located in spiral galaxies. Atomic gas (neutral hydrogen) is traced by HI 21-cm hy-

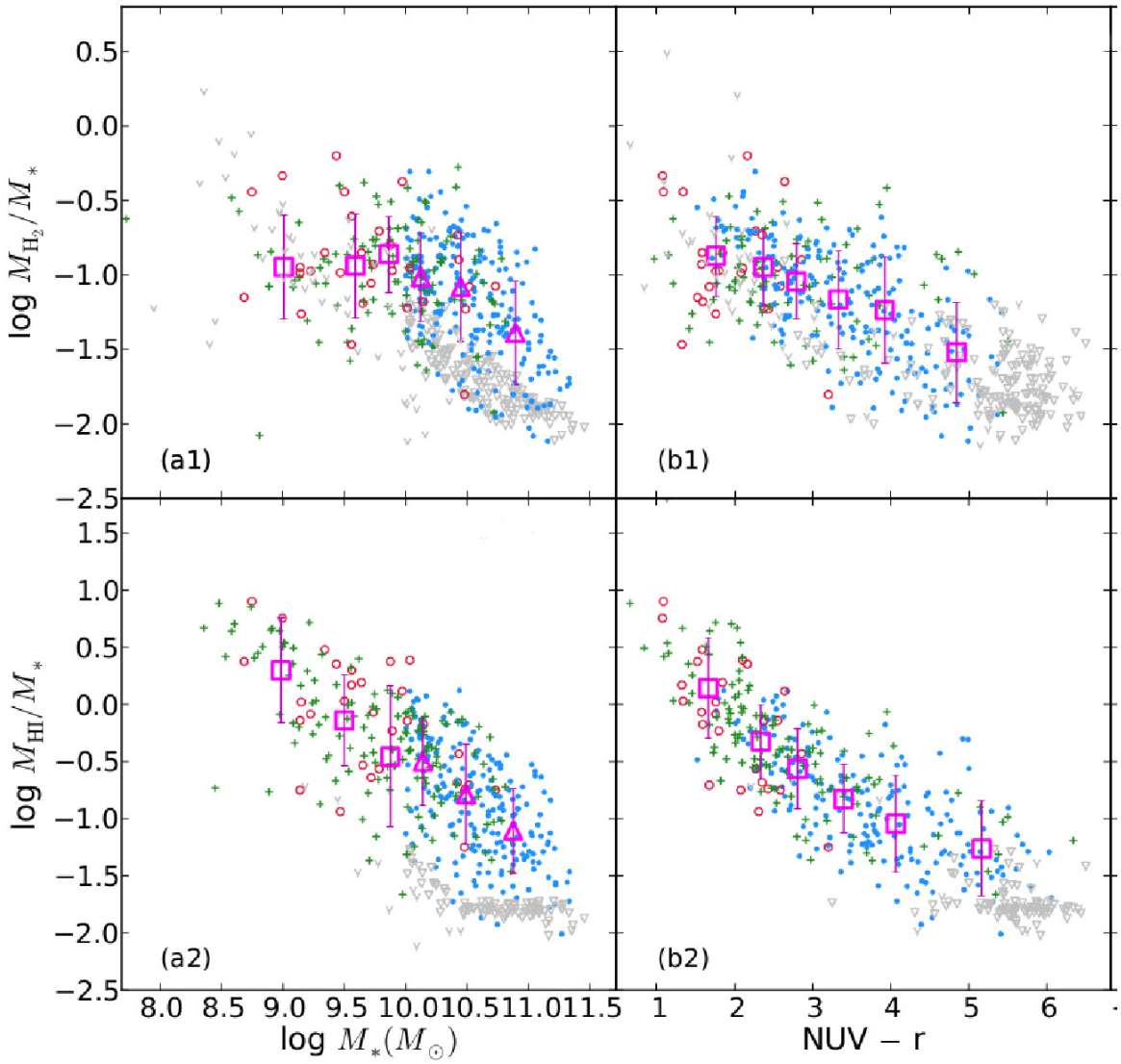

Figure 1.4: Scaling relations of gas-richness (M_{H_2}/M_* and M_{HI}/M_*) as a function of M_* and NUV-r. Red circles, green crosses and blue dots represent SMT, AMIGA-CO and COLD GASS sample, respectively. Dark grey triangles and light grey open arrows show gas fraction upper limits of COLD GASS and AMIGA, respectively. The averaged Log(M_{H_2}/M_*) and Log(M_{HI}/M_*) with their scatters are showed with magenta squares, each bin having same number of galaxies. Reproduced from Jiang et al. (2015).

perfine transition line (Springob et al., 2005; Walter et al., 2008; Haynes et al., 2011) and molecular gas (mainly H_2) mass can be traced by carbon monoxide, typically ^{12}CO(J=1→0) (Young & Scoville, 1991; Saintonge et al., 2011; Lisenfeld et al., 2011) and ^{12}CO(J=2→1) (Leroy et al., 2009).

On the left column of Fig. 1.4 the correlations of the ratio between cold atomic and molecular gas components and the stellar mass (gas-richness) for three samples, namely SMT (Jiang et al., 2015), AMIGA-CO (Lisenfeld et al., 2011) and COLD GASS (Saintonge et al., 2011), are shown as a function of the stellar mass of the host galaxy. The correlation between global properties of galaxies is often called scaling relation. In the massive galaxies, the H_2-richness decreases with increasing M_*, but the mean value seems to be unchanged in low to intermediate M_* galaxies. This means that in the low mass systems, most of their gas is atomic. On the right column of Fig. 1.4 gas-richnesses are correlated with NUV-r colour. High NUV-r values correspond to "red", indicating that the emission is mainly powered by evolved stellar populations, while low values correspond to "blue" star-forming galaxies. The picture is that low mass blue galaxies are more gas rich and especially abundant in HI, but they are inefficient in converting their HI into H_2 molecular clouds and then into stars, while in massive galaxies the star formation efficiency is more consistent and there is less H_2 since it has been consumed in forming stars.

Star formation

Star formation is the main agent of galaxy formation and evolution and it is the process by which dense regions within molecular clouds in the ISM, called star-forming regions, collapse to form stars. Star Formation Rate (SFR) indicators are measures of luminosity, either monochromatic or integrated over some wavelength range, with the aim of targeting emission that is sensitive to young massive stars. The distribution of the initial masses for a population of stars (also called the initial mass function) and a roughly constant star formation over the timescale probed by the indicator are the assumptions required to allow the conversion from the luminosity to a SFR. SFR indicators in the UV/optical/near-infrared (∼0.1-5 μm) probe the light emerging from stars, while SFR indicators in the infrared (∼8-1000 μm) probe the stellar light reprocessed by the dusty ISM (dust reprocessing of light is discussed in more details in Section 1.3). Recent available techniques to measure SFRs of galaxies are based on hybrid SFR indicators which use a weighted combination of UV/optical and infrared luminosities to minimize the systematic effects of dust obscuration.

Schmidt (1959) discussed a fundamental relationship in local normal (i.e. not undergoing a recent burst) spiral galaxies between the gas surface density and the SFR surface density:

$$\Sigma_{\rm SFR} \propto \Sigma_{\rm gas}^{n}$$

with n ∼1-2 (e.g. Kennicutt, 1998), also known as the Schmidt-Kennicutt (SK) law (Kennicutt et al., 2007). Recent observations suggest a tight correlation between SFR and molecular gas (e.g. Blitz & Rosolowsky, 2006; Kennicutt et al., 2007; Bigiel et al., 2008; Leroy et al., 2008); in the outer parts of galaxies, where the molecular fraction is reduced due to low surface density, the SFR per unit gas mass also declines (Bigiel et al., 2010).

Gas-phase metallicity and dust

The gas-phase metallicity is a record of the galaxy's history, encapsulating information about past star formation and metal enrichment accordingly, and infalling/outflowing gas. As shown by Tremonti et al. (2004) gas-metallicity and stellar mass are strongly correlated, with the metallicities approaching an approximately constant value at masses $M_* \gtrsim 10^{10}$ $M_\odot$. This mass-metallicity relationship for spiral galaxies appears to be only a weak function of galaxy environment (e.g Mouhcine et al., 2007; Cooper et al., 2008).

A tiny fraction ∼0.1 per cent of the baryonic mass in spiral galaxies is in form of dust and plays a central role in the astrophysics of the ISM, from the thermodynamics and chemistry of the gas, to the star formation. Dust determines how galaxies look like, shaping their spectral energy distribution: UV/optical radiation is absorbed and scattered and re-emitted in the infrared. Dust is made of amorphous silicates, graphite and polycyclic aromatic hydrocarbons (PAHs) molecules, and currently our understanding of the nature of interstellar dust is based on observations of our own Milky Way (MW) and local galaxies (Draine, 2003; Draine et al., 2007; Jones, 2014). Physical and compositional properties of dust are described in Section 1.3.1.

The dust-to-gas ratio of galaxies appears to be a strong function of the gas-phase metallicity (Draine et al., 2007). Indeed the measured dust-to-gas ratios of many nearby galaxies scale proportionally with their metallicities, at least down to $Z \sim 1/5 Z_\odot$ (Leroy et al., 2011). Recent measurements of the dust-to-gas ratio in nearby, metal-poor (below $1/5$ $Z_\odot$) and low mass galaxies indicate that such galaxies have much less dust than expected based on the linear metallicity scaling (e.g. Vladilo et al., 2011; Rémy-Ruyer et al., 2014; Shi et al., 2014).

Tully-Fisher relation

Galactic disks owe their origins to the same fundamental process as other astrophysical disks: conservation of angular momentum in a system collapsing under gravity eventually leading to arrest of the collapse by rotational support. The gas and (thin-disk) stars in spiral disks are rotation-supported objects, consequently they orbit around the galactic centre. From the peak of the rotation curve it is possible to derive the maximum circular velocity[1] V_c, tracing H_α or HI emission lines (Sofue & Rubin, 2001). The galaxy luminosity L is related to the circular velocity V_c as a power-law, known as the Tully-Fisher (TF) relation (Tully & Fisher, 1977):

$$V_c \propto L^\alpha$$

with a slope $\alpha \sim 0.27$-0.35 (e.g. Pizagno et al., 2007; Courteau et al., 2007), which is a function of bandpass.

1.1.3 Ellipticals, Lenticulars and interacting galaxies

Elliptical galaxies are characterized by their smooth and symmetric morphology and they are dynamically supported by velocity dispersion. Their stellar populations are old and ongoing star formation is absent due to the fact that cold gas content is extremely low. Luminous ellipticals are divided into two classes, those with and without cores. The formers tend to be more luminous, have less rotational support and more signs of triaxiality (Kormendy et al., 2009).

Lenticular galaxies are disk galaxies, but likewise ellipticals they are smooth, concentrated and have low specific star formation rate (Aguerri, 2012). The TF of lenticular galaxies has been less investigated in the literature due to the difficulty in obtaining the circular velocity of these gas-poor galaxies. Nevertheless, several studies indicate that the TF of lenticular galaxies shows a similar slope to that of late-type ones but with a different zero point (Hinz et al., 2003). Bars are found in 29 per cent of lenticular galaxies, suggesting that bars avoid galaxies with large and prominent bulges (Aguerri et al., 2009; Laurikainen et al., 2009; Nair & Abraham, 2010). The most luminous lenticulars with Sérsic index $n > 2$ follow similar relations to elliptical galaxies. On the contrary, less luminous lenticulars with $n < 2$ have structural properties closer to spirals (Aguerri, 2012).

Although not all close encounters between galaxies lead to merger, close enough interactions are likely to eventually result in the merger of the galaxies involved.

[1] Often spiral galaxies have flat rotation curve and the maximum circular velocity or the asymptotic circular velocity are not always well defined.

Galaxy mergers are visible in about 1-2 per cent of all luminous nearby galaxies, but mergers rate strongly changes over cosmic ages as $\propto (1+z)^3$, where z is the redshift. Close pairs of galaxies show a factor of 1.5-2 enhancement in their star formation rate, indicating a relationship between mergers and star formation (Li et al., 2008; Ellison et al., 2008). Besides, "dry-mergers" is a class of red, gas-poor merging galaxies that do not have associated star formation.

1.2 Physical models of cosmological galaxy formation

Numerical simulations have now matured into an essential tool to address the galaxy formation problem in cosmological context. Currently is not possible to simulate observational properties of galaxies, in a cosmological context, from first physical principles. Cosmological simulations are still orders of magnitude away from capturing the spatial scales where stars actually form. Moreover, physical processes such as turbulence, cosmic rays and magnetic fields, that are thought to play a key role on the scales of dense molecular clouds in which stars form (McKee & Ostriker, 1977), are not included yet or captured well in cosmological simulations. Therefore the treatment of the ISM, with multiple gas phases co-existing at very different densities and temperatures, needs to be included in simulations as sub-resolution effective models. Every process that is not explicitly resolved in a simulation, implementing only fundamental laws of physics, is defined to be sub-resolution. Detailed comparisons with observations allow to validate or invalidate such sub-resolution models, but possibly without shedding light on the exact physical nature of the fundamental processes.

1.2.1 The cosmological framework

The current cosmological theory is known as ΛCDM, where CDM is the Cold Dark collisionless Matter which makes up ∼25 per cent of the present cosmic energy-mass density and Λ is the cosmological constant in the form of dark energy comprising ∼70 per cent of mass/energy density, accelerating the expansion of the Universe (Peebles & Ratra, 2003). Baryons, i.e. atoms in stars and ISM, compose the remaining 5 per cent. The ΛCDM model provides a very good account for many properties of the Universe, such as the properties of the cosmic microwave background, the large-scale structure in the distribution of galaxies, the primordial abundances of hydrogen and helium. The parameters required by the ΛCDM are well constrained by observations (e.g. Planck Collaboration & et al., 2015) with

unprecedented accuracy. However, the greatest difficulties in the effort of understanding galaxy formation and evolution arise from the uncertainties on how to model the baryonic physics. Starting from the initial conditions, there are widely tested and applied methods (Section 1.2.2) to compute how the dark matter density field grows and evolves during the expansion of the Universe. The general picture of structure formation is that, when a density peak exceeds a given over-density relative to the background, the region within that peak stops expanding and becomes a gravitationally self-bound structure, commonly referred to as *dark matter halo*. Benckmark simulations such as the Millennium-I (Springel & et al., 2005), Millennium-II (Boylan-Kolchin et al., 2009), or with updated Planck cosmological parameters the MultiDark (Klypin et al., 2014), allow to predict abundance, internal structure, shape, clustering and angular momentum of dark matter halos over cosmic ages.

1.2.2 Numerical tools

Gravity

Gravity solvers, or N-body codes, provide the backbone for every type of simulation. The task is to determine the gravitational force acting on each mass element solving the Poisson equation. In cosmological N-body simulations, equations are solved within a comoving frame, often with periodic boundary conditions. N-body methods are particle-based or mesh-based or a hybrid of them (Springel, 2014). In galaxy formation, the most popular particle-based approaches are the Tree (Barnes & Hut, 1986) and the particle-mesh (PM) (Hockney & Eastwood, 1988) techniques. In the first case the idea is to use the multipole expansion of a distant group of particle to describe its gravity, instead of summing up the forces from all individual particles, as sketched in Figure 1.5. The PM computes the potential on a grid using the Fourier transform of the density field. The accuracy of the PM method depends upon the cell size, while Tree code can track accurately the gravitational force down to the *force softening length*, i.e. the spatial resolution of the simulation. Even if both algorithms scale with particles number N as $O(N \log N)$, the Tree is particularly ideal for strongly clustered particle distributions, while PM is faster when the gravitational potential on large scales is almost homogeneous. For these reasons, to increase the dynamical range, the commonly adopted technique is based on the hybrid Tree-PM approach (e.g. in the GADGET code Springel, 2005).

Nowadays N-body simulations evolve $\sim 10^{12}$ particles and with the advent of the Graphics Processing Units (GPUs) there is the potential for even larger compu-

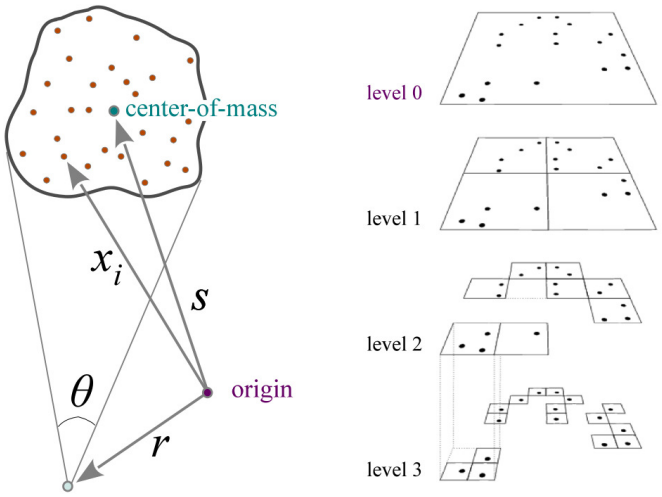

Figure 1.5: On the left: Multipole expansion for a group of particles. Provided the reference point r is sufficiently far away, the particles are seen under a small opening angle θ, and the gravitational field created by the particle group can be approximated by the monopole term at its centre of mass. On the right: Barnes & Hut (1986) Tree algorithm in two dimensions. All particles are enclosed in a square box, which is then hierarchically subdivided until each particle finds itself in a node on its own. Empty cells do not need to be stored. Reproduced from Springel (2014).

tations, even though to exploit such computational power provided by these new hardware is challenging.

Hydrodynamics

Since the mean free paths of atoms, molecules and ions in the ISM tend to be small compared to the size of the structures which they belong to, it is reasonable to approximate the ISM as a smooth fluid. The numerical treatment of the behaviour of the fluid requires to discretize it into separated fluid elements. Typically, assuming a non-relativistic ideal gas equation of state, hydro codes aim to solve the Navier-Stokes equations without viscosity or conduction (called Euler equations), representing mass, momentum and energy conservation.

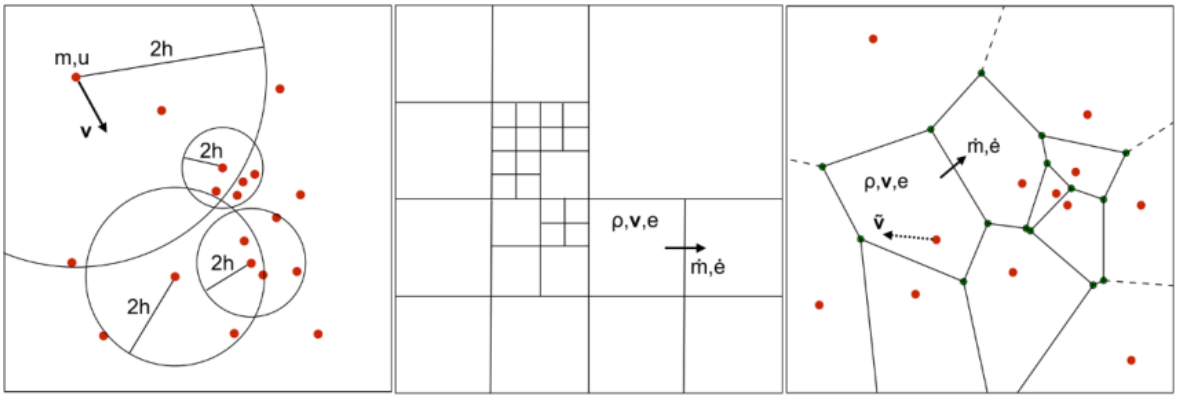

Figure 1.6: The left panel shows how SPH code represents a fluid, with red dots being individual particles carrying a mass m, specific energy u, and velocity $\mathbf{v}$. High concentration of particles samples high density fluid region. The fluid area associated to a particle is defined by the radius $2h$ which encloses (in this case) a constant number of particles (only 4 in this sketch for clarity). The middle panel illustrates an AMR representation of a fluid with three level of refinements. The gas within each cell has density ρ, velocity $\mathbf{v}$ and internal energy e. Cells can exchange mass, momentum and energy. The right panel shows a moving-mesh code. The fluid mass is sampled by particles (red dots) and the fluid volume is partitioned around these by Voronoi tessellation. As usual cells exchange matter, momentum and energy, but the particles move with the fluid flow as in SPH scheme. Reproduced from Dale (2015).

Eulerian method: The Euler equations are numerically integrated in a fixed frame, thus the fluid is divided into *volume elements* which fill the space inside the computational domain. Given the dynamic range involved in modelling galaxy formation, usually the codes adopt the Adaptive Mesh Refinement (AMR) implementation, enabling improved resolution in denser regions and allowing a space adaptivity at the same time. Current AMR hydro codes for galaxy formation are ENZO[2] code (Bryan et al., 2014), RAMSES[3] code (Teyssier, 2010), FLASH[4] code (Fryxell et al., 2000) and ART[5] code (Kravtsov et al., 1997).

Lagrangian method: The most popular Lagrangian method is the Smoothed Particle Hydrodynamics (SPH) (Price, 2012; Springel, 2014). The fluid is discretized into *mass elements* (particles) and the hydrodynamical quantities are obtained via kernel-weighted sum over neighbouring particles within the *smoothing length* (h). The kernel is a spherical function of the distance among particles and the smoothing is done such that most of the mass is concentrated near the particle centre, resulting in an adaptive resolution by construction. In the classical SPH formulation (Monaghan, 1992), the density is evaluated via the kernel-smoothed average over nearby particle masses, then the discretized Euler equations are used to update thermal energy and hydrodynamical acceleration. Adopting a variable h, energy and entropy are not simultaneously conserved in adiabatic flows. If the entropy is the evolved variable, in the so called entropy-conserving SPH (Springel, 2005), this fault is somewhat mitigated, but it creates an artificial pressure as a side-effect, not recognizable in Eulerian code (Agertz et al., 2007). These issues have been tackled with several strategies (e.g. Murante et al., 2011; Read & Hayfield, 2012; Saitoh & Makino, 2013; Hopkins, 2013; Beck et al., 2015), leading to significant improvements. Current SPH hydro codes for galaxy formation are GADGET-2[6] (Springel, 2005), GASOLINE[7] (Wadsley et al., 2004), VINE (Wetzstein et al., 2009), HYDRA[8] (Couchman et al., 2011), CHANGA[9] (Menon et al., 2015), SWIFT[10] (Theuns et al.,

[2]http://enzo-project.org
[3]http://www.ics.uzh.ch/ teyssier/ramses/RAMSES.html
[4]http://flash.uchicago.edu/site/flashcode/
[5]http://www.cs.iit.edu/ zlan/petaart.html
[6]http://wwwmpa.mpa-garching.mpg.de/gadget/
[7]http://imp.mcmaster.ca/software/
[8]http://hydra.sussex.ac.uk/
[9]http://www-hpcc.astro.washington.edu/tools/changa.html
[10]http://icc.dur.ac.uk/swift/

2015) and GIZMO[11] (Hopkins, 2014).

Moving-mesh methods: SPH has excellent conservation properties for energy and momentum, i.e. it is Galilean-invariant. The latter property is not automatically guaranteed in Eulerian codes. Moving mesh codes represent a synthesis between Eulerian and Lagrangian approaches, allowing the mesh itself to move with the flow. Moving mesh codes are Galilean-invariant like SPH ones, but they naturally capture shocks and contact discontinuities as well as grid codes. Recently the moving-mesh technique has been employed in astrophysical fluid codes. AREPO code (Springel, 2010) uses a grid that is both spatially and temporally adaptive, called Voronoi tesselation, subdividing space around particles and following the motion of the fluid at the same time.

Fig. 1.6 illustrates schematically the differences between these approaches.

Sembolini et al. (2015) investigated the performance of 12 modern astrophysical simulation codes, namely CART[12], HYDRA, AREPO and 9 versions of GADGET with different SPH implementations, by carrying out cosmological zoom simulations of a single massive galaxy cluster, aiming to assess the consistency of the different codes in reproducing the spatial and thermodynamical structure of dark matter and non-radiative gas (i.e. cooling and star formation are switched off) in the cluster. They found that codes with classic SPH implementations exhibit continually falling inner entropy profiles, without any evidence of an entropy core, as already pointed out by the Santa Barbara Cluster Comparison Project (Frenk et al., 1999). In contrast grid-based and moving-mesh codes produce extended cores with a large constant entropy core. Modern SPH codes are able to produce entropy cores which are basically indistinguishable from those of the grid-based codes.

1.2.3 Sub-grid physics

The key difference between dark matter and baryons in galaxy formation model is that dark matter has only gravitational potential and kinetic energy, while gas can either dissipate its internal energy (radiative cooling) or absorb energy from the incident radiation field (radiative heating) or other astrophysical sources. Dissipation of energy via radiative cooling plays a central role in many different astrophysical contexts, ranging from the intergalactic medium to molecular clouds. Almost all

[11] http://www.tapir.caltech.edu/phopkins/Site/GIZMO.html
[12] Chicago-ART version (Nagai et al., 2007).

codes for galaxy formation implement the photo-ionization heating and radiative cooling, while radiative transfer calculation (Section 1.3) is a growing field, often developed using massive parallel techniques made available by GPUs.

Cooling, heating and chemical evolution

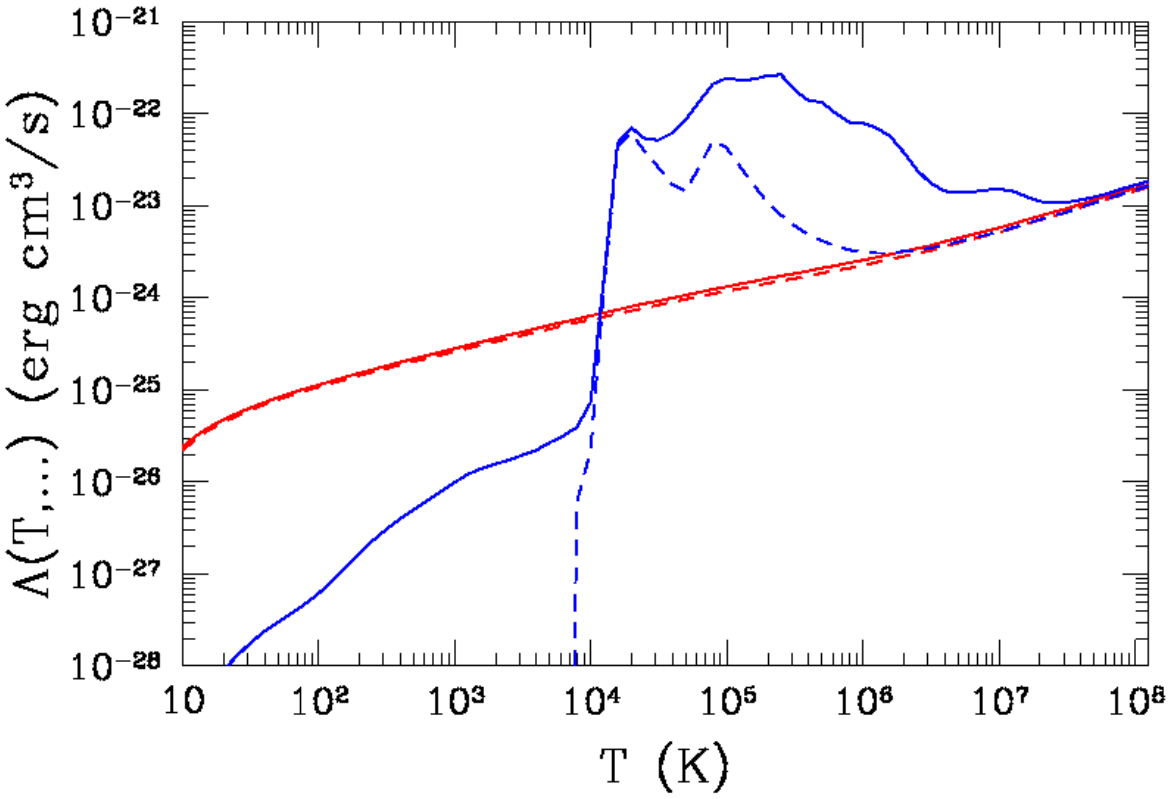

Figure 1.7: Blue dashed and solid lines show the standard cooling function under the assumption of CIE for the metal-free and solar-metallicity gas, respectively. Corresponding red lines show the same cooling functions for the fully ionized gas. Reproduced from Gnedin & Hollon (2012).

The phase structure of a multiphase ISM is determined by the temperature dependence of the cooling rate (McKee & Ostriker, 1977). In the most general case the cooling and heating functions depend on an large set of parameters: gas tem-

perature, baryon number density, the fractional abundance of the different species present in the ISM (atomic and ionic species, various molecules and cosmic dust), the specific intensity of the radiation field as a function of frequency and the heating rate by cosmic rays. Only detailed treatment, for example by means of CLOUDY code (Ferland et al., 2013), with a large set of chemical species using radiative transfer calculations can address such complexity. However, that would make it unfeasible as a method in cosmological numerical simulations. Therefore several simplifications are adopted. Even if a pure optically thin case (excluding cooling and heating due to molecules, dust, cosmic rays) lowers the complexity, the cooling and heating functions depend on hundreds of individual level populations for atomic and ionized species. The next simplification step is to assume that all atoms and ions are in the ionization equilibrium and the level population is in the equilibrium as well. In this limit of ionization equilibrium, the cooling and heating functions only depend on the total abundance of each chemical element. Finally, assuming a solar ratio[13] for heavy elements, then the cooling function becomes only functions of the gas metallicity, temperature and the density. At low densities and faint enough incident radiation field, most of cooling and heating reactions are interactions of an atom/ion with either a photon or an electron, thus the effects of any radiation field can be ignored and the ionization balance of the gas is time-independent. This is commonly called collisional ionization equilibrium (CIE).

Sutherland & Dopita (1993) provided a grid of cooling functions over a wide range of temperature ($10^4 \lesssim T \lesssim 10^8$ K) and metallicity, under the assumption of CIE. However, the incident radiation field can introduce significant modifications to the *standard* cooling function when the CIE assumption breaks down, e.g in the intergalactic medium. Fig 1.7 compares the CIE cooling functions with ones in fully ionized gas, for both metal-free and solar-metallicity gas. In the fully ionization limit, basically only bremsstrahlung takes place and the cooling rate differs from the CIE case by more than two order of magnitude, showing that the radiation field plays a crucial role (Gnedin & Hollon, 2012). The challenge in numerical simulations is to account for the radiation field, achieving both accuracy in modelling cooling/heating functions and feasible computational time. In the real scenario the radiation field varies locally in the ISM, but such treatment requires full radiative transfer calculations (see Section 1.3). In study of galaxy formation it is often sufficient to account for the cosmic background radiation, i.e. a fixed and

[13]Solar metallicity refers to the metallicity of the gas in the solar vicinity, $Z = 0.0134$ (Asplund et al., 2009).

homogeneous redshift-dependent radiation field.

Wiersma et al. (2009), by means of CLOUDY, investigated the effects of heavy elements and ionizing radiation on the radiative cooling of gas with properties characteristic of the ISM and the intergalactic medium, i.e. optically thin gas with densities $n_{\rm H} \lesssim 1$ cm^{-3} and temperatures $T \gtrsim 10^4$K, assuming CIE. They presented a method to incorporate radiative cooling on an element-by-element basis including photo-ionization by an evolving UV/X-ray background (Haardt & Madau, 2001), using precomputed tables, which for heavy elements are functions of density, temperature and redshift.

Since the cooling is metal dependent, to track the enrichment of gas with elements heavier than helium is fundamental. This allows not only to treat properly and self-consistently the metal cooling, but also to model the ISM chemical evolution. Most codes (e.g. Tornatore et al., 2007; Oppenheimer & Davé, 2008; Wiersma et al., 2009) track a suite of individual elements ejected by Type II supernovae (SNe), closely related to the oxygen abundance, by Type Ia SNe that produce the bulk of the iron and by Asymptotic Giant Branch (AGB), whose ejecta dominate the present-day carbon budget.

Star formation and feedback sources

Observations indicate that star formation takes place in dense and cold molecular clouds, with about 1 per cent of the molecular gas, basically H_2, converted into stars per free fall time (Krumholz & Tan, 2007; Bigiel et al., 2008; Leroy et al., 2013). Molecular content depends on its formation rate which predominantly occurs onto dust grain surfaces in metal-enriched ISM (Cazaux & Tielens, 2004), on the balance between its destruction by Lyman-Werner photons from UV radiation field and the amount of self-shielding against interstellar radiation.

The use of the empirical relation, provided by Blitz & Rosolowsky (2006), offers a way to derive the amount of gas into atomic (HI) and molecular (H_2) forms. Analysing local galaxies, they found that the ratio of molecular to atomic gas surface densities is correlated with the disk hydrostatic mid-plane pressure and that the relation between the two is nearly linear. This approach can be used to estimate the molecular fraction in simulations either self-consistently (e.g. Murante et al., 2015) or in post-processing (e.g. Duffy et al., 2012).

In early numerical prescriptions for forming stars within hydrodynamical cosmological simulations (e.g. Katz, 1992; Katz et al., 1996), a SFR, based on Schmidt (1959) law, is assigned to a dense (Jeans-unstable) and converging (negative diver-

gence of the velocity) cold gas particle, namely:

$$\dot{\rho}_* = \frac{\beta \rho_{\rm gas}}{t_{\rm dyn}} \propto \rho_{\rm gas}^{3/2}$$

the ratio between its density and dynamical time, times an efficiency β parameter. The latter is calibrated to match the amplitude of the observed Schmidt-Kennicutt[14] (SK) relation in simulations of disk galaxies. Schaye & Dalla Vecchia (2008) pointed out that, if gas obeys an effective equation of state in a galactic disk, then it obeys a SK relation too. Based on this, they argued that it is straightforward to model star formation without the need of making assumptions about the unresolved ISM.

Early star formation prescriptions were found to produce highly compact disks, meaning that some form of energetic feedback was needed, aiming to obtain extended disks like local grand-design spirals. Since gas circulating inside a dark matter halo falls to the galaxy centre in a few dynamical times, feedback must be efficient enough to eject gas from the halos, but at the same time it must allow a fraction of expelled gas to fall back at low redshift. SNe drive such feedback in two different forms, thermal and kinetic. The thermal energy feedback alone is not efficient, because energy given to a star-forming and high density region is promptly radiated away (e.g. Katz et al., 1996).

Springel & Hernquist (2003) introduced a more refined model to describe the process of star formation (hereafter *effective model*). They treated gas particles eligible to form stars as a multiphase medium, composed by a cold and a hot phase in thermal pressure equilibrium. The *effective model* describes mass and energy flows between the phases with a system of ordinary differential equations (ODEs), with equilibrium solutions that depend on average density and pressure of the gas. The cold gas forms stars at a given efficiency. Kinetic feedback is implemented using a phenomenological prescription, in order to guarantee the onset of galactic winds, i.e. gas particles subject to kinetic feedback which do not interact for some time with the surrounding gas (hydrodynamical decoupling).

When some form of kinetic feedback was employed, numerical simulations succeeded in producing "realistic" disk galaxies, i.e. star formation history, disk age and angular momentum of baryons in the disk are in broad agreement with those observed in present-day massive spirals, but they failed to produce late-type spirals, i.e. low values of B/T, flat rotation curves and low baryon formation efficiency.

[14]SK relation is only observed to hold when the ISM is averaged over $\sim$kpc scale and, if a simulation resolves smaller scales, it becomes dubious the validity of adopting such prescription for the star formation that is calibrated to match this relation.

(e.g. Abadi et al., 2003; Robertson et al., 2004; Governato et al., 2004). Thus much recent effort was spent to incorporate more realistic treatments of the ISM into cosmological simulations (see Section 2.1).

Other studies consider the description of other sources of energy feedback, in addition to SNe. The effect of Active Galactic Nuclei (AGN) feedback was included by some groups (Di Matteo et al., 2003; Springel et al., 2005; Booth & Schaye, 2009; Fabjan et al., 2010; Hirschmann et al., 2014). Besides SNe and AGN, cosmic ray pressure is a known source of feedback that could help in driving massive galaxy winds. Attempts to implement cosmic rays feedback in cosmological simulations were presented, e.g. by Jubelgas et al. (2008), Wadepuhl & Springel (2011) and Uhlig et al. (2012).

Other recent works (Kuhlen et al., 2012; Agertz & Kravtsov, 2015a) have adopted sub-grid recipes to compute the H_2 density and then use that for the SFR. Present-day cosmological zoom-in[15] simulations are starting to be able to resolve the Jeans mass/length of gas (e.g. Hopkins et al., 2013) and, concurrently, ISM simulations including detailed treatments of nonequilibrium chemistry and turbulence (e.g. Mac Low & Glover, 2012) are bridging the gap with cosmological runs.

Fig. 1.8 and Fig. 1.9 show two examples of the current state-of-the-art cosmological hydrodynamical simulations at $\sim$100 pc scale in a volume of $\simeq(100\ \mathrm{Mpc})^3$, namely the Illustris simulation (Vogelsberger et al., 2014) and the Evolution and Assembly of GaLaxies and their Environments (EAGLE) simulation (Schaye et al., 2015). These simulations calibrated the parameters governing star formation and feedback processes in order to reproduce key properties of galaxies at the present epoch, i.e. redshift z=0. Starting with the left column on Figure 1.8, the structure formation in the dark matter component proceeds via the formation of halos in the intersection of filaments which fuel baryons into halos. Indeed there is a strong correspondence between dark matter and baryons (gas) distribution on large scales, comparing the first and second column. The gas surrounding massive halos is hot (third column), due to shock heating and star formation. Metals are spread to large distances by the feedback from stars and AGNs (fourth column).

Figure 1.9 shows the large-scale gas distribution at the present epoch, while the insets zoom in on the stellar light of an individual galaxy after accounting for dust extinction. The figure reveals the morphology of baryonic filaments.

[15] In zooms, a sub-volume within a cosmological chosen region is evolved at much higher resolution, preserving the tidal field from large-scale structure.

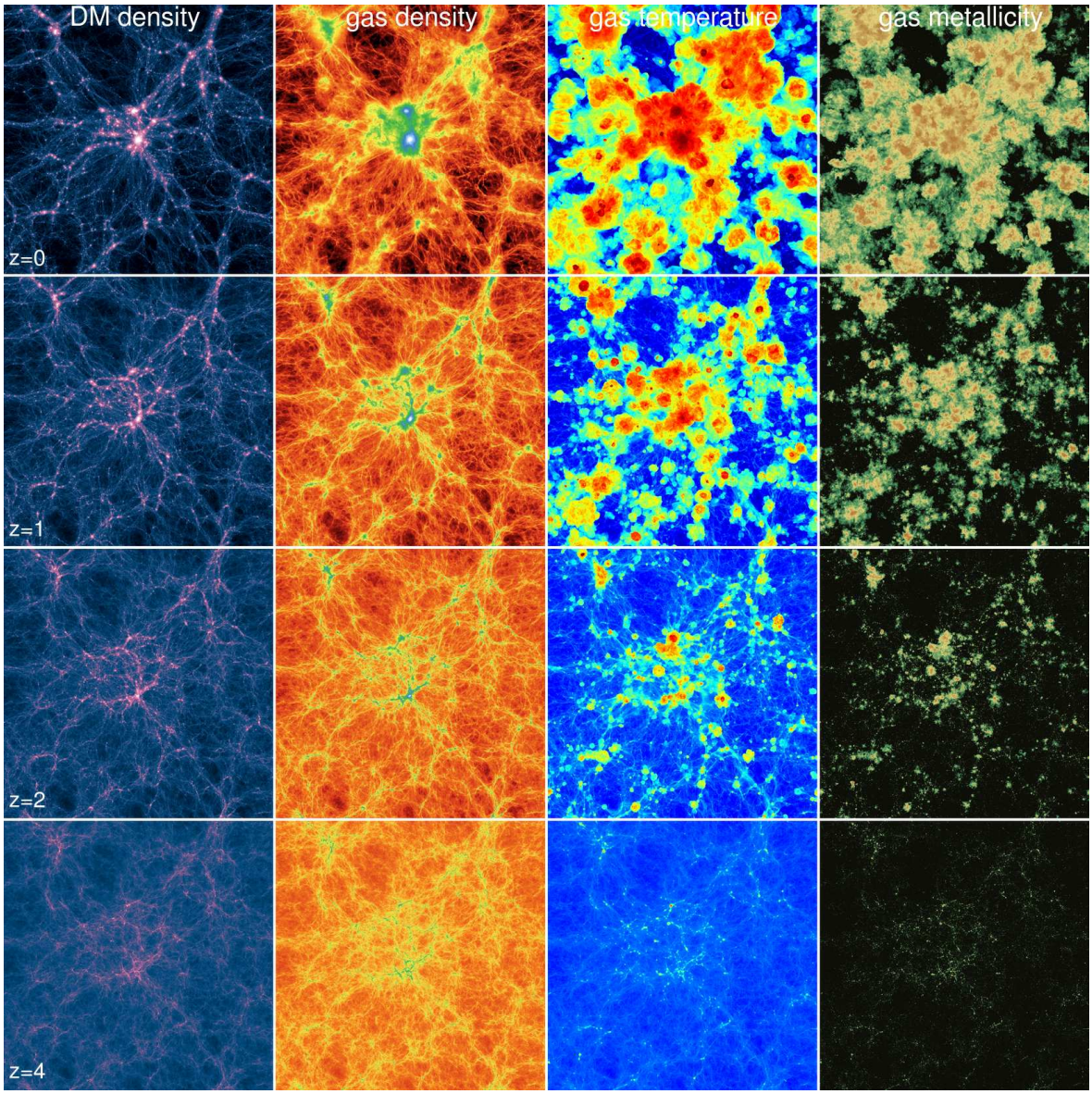

Figure 1.8: Visualization of representative quantities computed by Illustris simulation. From left to right, the dark-matter density, gas density, gas temperature, and gas metallicity are shown at different cosmic ages (from top to bottom: z = 0, z = 1, z = 2, z = 4). The slice is $\simeq$100 Mpc wide. Reproduced from Vogelsberger et al. (2014).

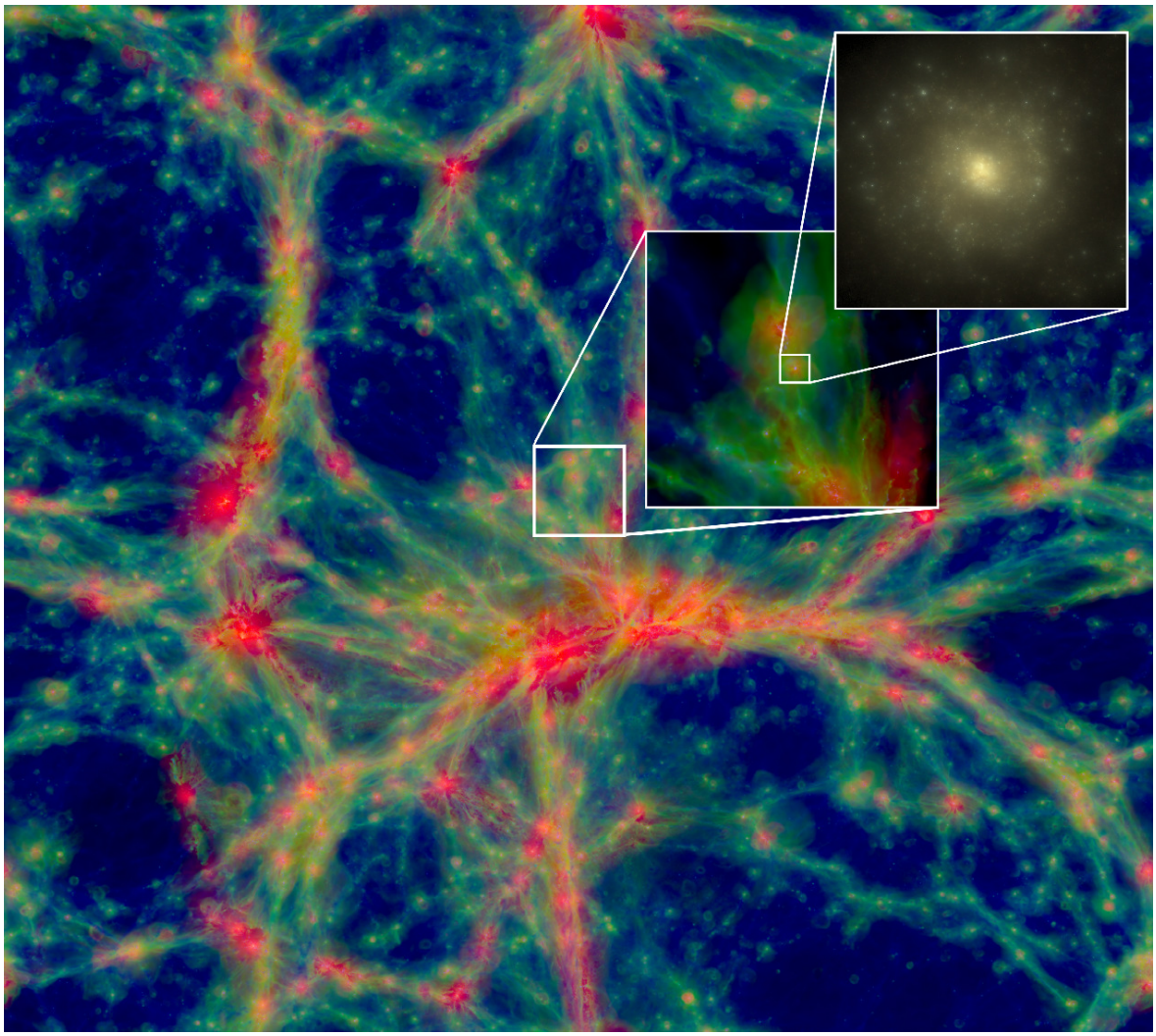

Figure 1.9: The slide shows the whole Eagle simulation box. The map represents the gas density and the colour the gas temperatures (blue through green through red from cooler to hotter). The zoom in to an individual galaxy with stellar mass $3 \cdot 10^{10}$ $M_{\odot}$ shows the optical band stellar light. Reproduced from Schaye et al. (2015).

1.2.4 Realistic disk galaxy simulations

Simulating realistic spiral galaxies in cosmological DM halos has been recognised as a difficult problem to solve, since the first generations of pioneering analyses (Evrard, 1988; Hernquist & Katz, 1989; Barnes & Hernquist, 1991; Hiotelis & Voglis, 1991; Katz & Gunn, 1991; Katz, 1992; Thomas & Couchman, 1992; Cen & Ostriker, 1993; Navarro & White, 1994; Steinmetz & Muller, 1995; Mihos & Hernquist, 1996; Walker et al., 1996; Navarro & Steinmetz, 1997; Carraro et al., 1998; Steinmetz & Navarro, 1999; Sommer-Larsen et al., 1999; Lia & Carraro, 2000). The so-called *cooling catastrophe*, i.e. radiative gas cooling at high redshift that produces a runaway condensation of baryons within forming DM halos, was the basic explanation for the failure in reproducing realistic disk galaxies (Navarro & Benz, 1991; Navarro & White, 1994). As a result, simulated galaxies were too concentrated, compact and rapidly spinning at the present epoch. Moreover, these galaxies exhibited centrally-peaked rotation curves in disagreement with observed flat rotation curves, and did not lie on the observed TF relation.

Many years later, the *Aquila comparison project* (Scannapieco et al., 2012) presented a comparison among 13 different Lagrangian and Eulerian codes, implementing different star formation and feedback (SF&FB) prescriptions. Fig. 1.10 shows face-on and edge-on maps of the projected stellar mass density for the runs. These figures illustrate the morphology of the simulated galaxies; bars, bulges and extended disks are present, but their relative prominence (i.e. B/T value) varies widely from run to run. The galaxy stellar mass also shows large scatter, spanning about a decade from the least (G3-TO) to the most massive (R). The conclusion was that better agreements with observations were obtained with SF&FB models having a more effective feedback.

Different authors (Stinson et al., 2013; Aumer et al., 2013; Vogelsberger et al., 2014; Marinacci et al., 2014; Hopkins et al., 2014; Cen, 2014; Schaye et al., 2015; Agertz & Kravtsov, 2015b; Murante et al., 2015) showed, with improved SF&FB recipes, to be able to produce late-type spiral galaxies with low B/T ratios and low baryon fractions. No consensus has been reached neither on the detailed nature of feedback energy required, nor on the details of its numerical implementation. It is not still clear if SNe alone are sufficient to provide the required energy or if also early stellar feedback, AGN feedback and cosmic ray feedback are needed. Regarding technical points, it is an open question how important the hydro scheme is on which simulations are based and if very high resolution is necessary to obtain realistic disk galaxies. Section 2.1 describes how the ISM is modelled in present-day cosmological simulations of galaxy formation.

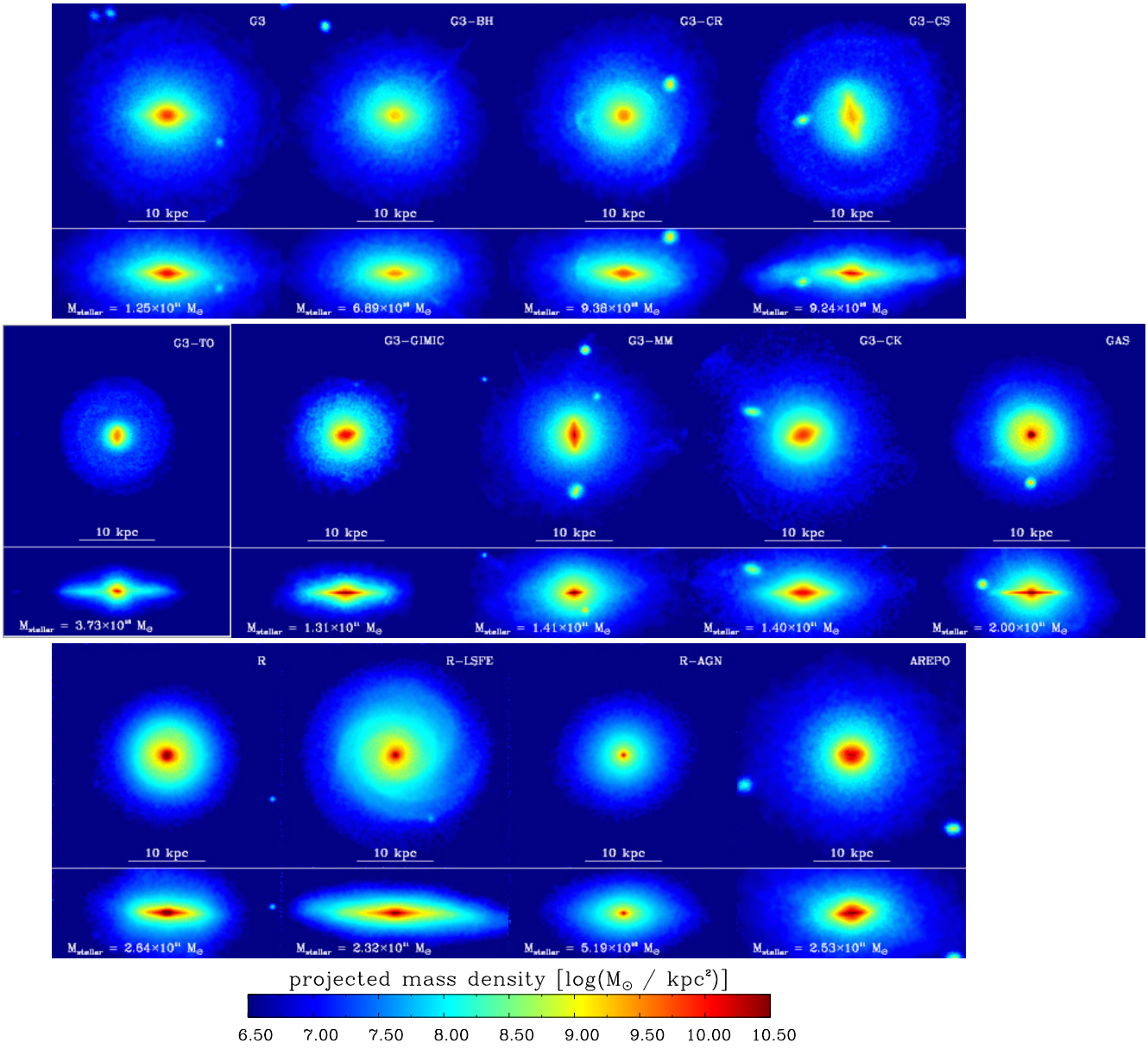

Figure 1.10: *Aquila comparison project*. Face-on and edge-on maps of projected stellar mass density. The face-on projection is along the direction of the angular momentum vector of galaxy stars. The face-on and edge-on maps are 30×30 kpc^2 and 30×12 kpc^2, respectively. The size of each pixel is 58.6 pc on a side and its colour is drawn from a logarithmic colour map of the surface stellar mass density. Reproduced from Scannapieco et al. (2012).

Barred spiral disk

Bars are believed to play a key role in the secular evolution of galaxy disks, particularly in the redistribution of angular momentum of baryonic and dark matter components (Debattista & Sellwood, 1996, 2000). The non-circular motions of bars cause the migration of gas within the corotation radius towards the galaxy centre, where it can give rise to a starburst or be accreted on a nuclear black hole (e.g. Laurikainen et al., 2004; Oh et al., 2012). Also, the formation of a bar is believed to contribute to the formation of a disky or boxy/peanut bulge, often called pseudobulge (Kormendy, 1982; Kormendy & Kennicutt, 2004; Athanassoula, 2005; Debattista et al., 2006).

The emergence of bars in simulated galaxy disks has been addressed in many papers, starting from the pioneering work of Ostriker & Peebles (1973) where stability of a disk-shaped rotating N-body system was obtained only in the presence of an extended spherical halo. The origin of bars was ascribed to secular instabilities of massive disks (e.g. Efstathiou et al., 1982) or to tidal interactions and merging with galaxy satellites, that excite spiral structures or proper bars (e.g. Noguchi, 1996; Dubinski et al., 2008). Sellwood et al. (1998) noticed that disk stability is influenced by the presence of a soft or hard centre (namely a gently or steeply rising inner rotation curve), even when dark matter gives a negligible contribution to the inner part of the rotation curve.

More recent works addressed the effect of halo triaxiality (Curir & Mazzei, 1999) and concentration (Athanassoula & Misiriotis, 2002) on the growth of a bar in a disk hosted by an isolated halo with a Navarro et al. (1996) profile. In these works the initial conditions represent an equilibrium configuration of a disk embedded in a dark matter halo; this setting is suitable to study bar formation in the absence of further external perturbations. Halo triaxiality was reported by Curir & Mazzei (1999) to be a trigger of bar formation, while Athanassoula & Misiriotis (2002) found that the bar strength correlates with halo concentration.

1.2.5 Spheroid-dominated galaxy

Major mergers, i.e. nearly equal mass, can efficiently remove angular momentum from stellar disks, producing velocity dispersion-dominated spheroids (Toomre, 1977; Barnes, 1988, 1992; Mihos & Hernquist, 1996). Minor mergers, i.e. unequal mass down to mass ratios $\sim$1:10, can either assemble the spheroid component of galaxies or thicken disks (Moster et al., 2010). Thus a possible basic explanation is that smooth accretion of gas produces disks, while mergers destroy disks and

build spheroid-dominated objects. Numerical hydrodynamical simulations showed that wet merges (i.e. gas rich) lead to re-formation of disk dominated galaxies, because they do not drive efficient angular momentum loss (e.g. Hopkins et al., 2009). Overall, the emerging picture is that morphological transformations are tightly linked with feedback and quenching processes. Thus, in order to produce a spheroid-dominated population at the present epoch, some feedback process had to remove most of the gas from host galaxies before the merging.

Disk instabilities may contribute *in situ* to the formation of spheroids. If clumps formed in Toomre-unstable disks, expected to fragment into self-bound knots (Toomre, 1964), survive and migrate towards the galactic centre, they may form a classical bulge (e.g. Dekel et al., 2009; Elmegreen et al., 2008; Bournaud et al., 2011). Both isolated and cosmological simulations, adopting different stellar feedback recipes, suggest that clumps modestly contribute in feeding spheroid growth, depending if they survive substantially longer than a disk dynamical time (e.g. Bournaud et al., 2014; Mandelker et al., 2014), or if they are disrupted before reaching the centre (e.g. Genel et al., 2012; Hopkins et al., 2012).

1.2.6 Galaxy morphology distribution

Since most observational studies use visual or photometric (e.g. Sérsic index, B/T ratio) analysis to classify galaxies according to their morphology, detailed quantitative statistical comparisons with the predictions of cosmological simulations are difficult because the structural parameters of disks and bulges determined from kinematics, as is usually done in simulations, have to be compared with those obtained using a photometric decomposition, as done in observations. Scannapieco et al. (2010), producing synthetic observations of the simulation outputs, found that the kinematic B/T ratio estimates are systematically and significantly larger than the photometric ones. Very large hydrodynamical simulations are available, such as Illustris and EAGLE, containing tens of thousands of galaxies whose internal dynamics is at least partially resolved. Snyder et al. (2015) studied the morphology of 10808 galaxies at $z = 0$ from the Illustris project, producing synthetic images, following the technique described in Torrey et al. (2015). They found that optical morphologies correlate with rotational structures and that relative type fractions, as a function of environment, agree roughly with observations.

1.3 3D radiative transfer

The radiative transfer (RT) calculations, using physical quantities tracked by the simulation, provide a way to link both simulations and observations and make broadband Spectral Energy Distributions (SEDs). Predicting the SED of a simulated galaxy is a complex and quite delicate task. The main difficulty and uncertainty of this step is the significant reprocessing of light emitted by stars or, if present, AGN, by means of dusty ISM. Dust grains are efficient at absorbing and scattering ultraviolet (UV) through near-infrared (NIR) photons and then at re-radiating the absorbed energy in the infrared and sub-millimeter (submm) wavelength range (Jones, 2014). Observations across the electromagnetic spectrum (e.g. Hubble, GALEX, ground-based telescopes, ALMA, Herschel, Planck, Spitzer, WISE), have revealed that the SED has a strong dependence on the relative geometry of stars and dust, as well as on the optical properties of dust grains (e.g. Fritz et al., 2012). Therefore, understanding the intrinsic properties of these objects, including the dust itself, requires 3D dust RT calculations.

1.3.1 Physical and compositional properties of dust

Interstellar dust has been the subject of dedicated studies since the early measurements of interstellar reddening by Trumpler (1930). Interstellar reddening occurs because interstellar dust absorbs and scatters blue light waves more than red light waves. To a first approximation, individual dust grains absorb only photons with wavelengths smaller than or similar to the physical size of the grain. Therefore, the fact that the absorption is stronger in the UV, somewhat less in the optical and further less at IR wavelengths, leads to the conclusion that there are many more small dust grains than large ones. Mathis et al. (1977) were able to reproduce the measurements of the ISM extinction curve in the range 0.1-1 μm with a mixture of spherical graphite and silicate grains with a size distribution:

$$N(a)da \propto a^{-3.5}da$$

where a is the grain radius and the distribution extends over a range of radii from 50 nm up to 0.25 μm. The total mass of dust is dominated by the contribution made by large grains, while the total surface area per unit mass is dominated by the contribution made by small grains. Subsequent studies have improved on this simple description (e.g. Draine & Lee, 1984; Weingartner & Draine, 2001a), but it remains a useful guide to the properties of interstellar dust for all the current dust models.

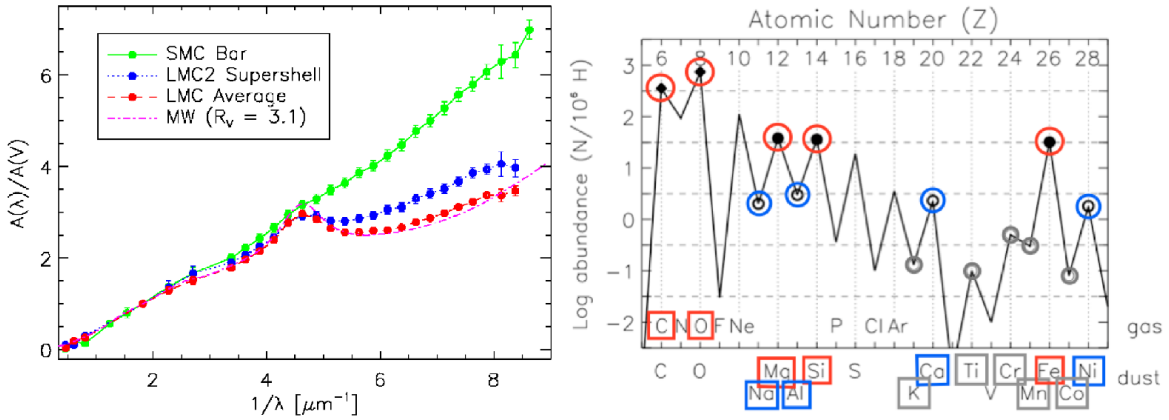

Figure 1.11: Left panel: average extinction curves for the MW, LMC2, LMC, and SMC Bar (Gordon et al., 2003). Right panel: the relative abundances of the elements (with respect to H) as a function of atomic number. The most abundant silicate/oxide and solid (hydro-)carbon dust-forming elements (red), and the minor (blue) and trace (grey) dust-forming elements are highlighted. Reproduced from Jones (2014).

Figure 1.12: Dust of the Andromeda galaxy as revealed in infrared light at 24μm by the Spitzer Space Telescope. Reproduced from Gordon et al. (2006).

Interstellar extinction results in a change in the shape of an observed spectrum. At some wavelength bands the intensity is lowered (absorption features) which can give clues to the chemical composition of the interstellar dust grains. In the extinction versus wavelength plane, known absorption features include the 2175 $\mathring{A}$ bump, the diffuse interstellar bands, the 3.1 μm water ice feature, the 10 and 18 μm silicate features. The general shape of the ultraviolet through near-infrared (0.125-3.5 μm) extinction curve in the MW is characterized by the absolute extinction parameter $R(\lambda, V)$ (Cardelli et al., 1989; Mathis & Cardelli, 1992; Valencic et al., 2004), defined as the ratio $A(\lambda)/A(V)$ between the total extinction at wavelength λ and the V band (540 nm). Left panel of Fig. 1.11 shows the averaged extinction curves for the MW, the Small Magellanic Cloud (SMC) and the Large Magellanic Cloud (LMC) (Gordon et al., 2003). LMC has a weaker 2175 $\mathring{A}$ bump ($\simeq$4.6 μm^{-1}) and stronger far-UV extinction in the region associated with the LMC2 supershell (also known as Tarantula Nebula) compared to the MW. SMC exhibits more extreme far-UV extinction in the star forming Bar and fairly normal ultraviolet extinction with no 2175 $\mathring{A}$ bump.

The right panel of Fig. 1.11 summarises the abundances relative to hydrogen of the most important interstellar dust-forming elements, showing that the dust elemental composition is dominated by C, O, Si, Mg and Fe, resulting in two distinct solid phases: probably the C-rich phase is mostly found in some form of hydrogenated amorphous carbon solid and the O-rich phase most likely consists of amorphous silicates and oxides (Jenkins, 2009, 2014).

Grains radiate as modified black-bodies (MBB) with a strongly wavelength-dependent emissivity $Q_{em} \propto \lambda^{-1}$-$\lambda^{-2}$. Therefore they are inefficient radiators at long wavelengths and have an equilibrium temperature that is hotter than the temperature of a perfect black-body immersed in the same radiation field. Radiative heating of dust grains is expected to be more important than collisions with atoms, electrons, cosmic rays, or other dust grains, because of the large energy density of starlight and the grain's high opacity to starlight. Tiny grains never achieve equilibrium with the radiation field, i.e. they are "stochastically" heated. Large grains will have temperatures of 30-50K and radiate primarily at far-IR wavelengths (50-100 μm). Tiny grains, by contrast, can have instantaneous temperatures of 500-1000K or more, radiating primarily at 1-10 μm. The nature of tiny grains is still poor understood, because grains with 30-50 atoms have about the same size as very large molecules, e.g. Polycyclic Aromatic Hydrocarbon (PAH), and so they are require to be treated by means of quantum mechanics.

NASA's Spitzer Space Telescope has captured infrared emission by dust at 24μm from the Andromeda galaxy (Gordon et al., 2006). In Fig. 1.12, asymmetrical fea-

tures are seen in the prominent ring of star formation. The image reveals a contrast to the traditional view at visible wavelengths, which shows the starlight instead of the dust emission.

1.3.2 The RT problem

The radiative transfer problem is the problem of calculating the propagation of radiation through a medium which can emit, absorb or scatter the radiation. The problem is extremely complex. Galaxies evolve slowly enough that the time dependence can be practically ignored and the equation to solve is the time-independent RT (e.g. Chandrasekhar, 1960):

$$\mathbf{n} \cdot \nabla I(\mathbf{x}, \mathbf{n}, \lambda) = -k(\mathbf{x}, \lambda)\rho(\mathbf{x})I(\mathbf{x}, \mathbf{n}, \lambda) + j(\mathbf{x}, \mathbf{n}, \lambda)$$

where $\mathbf{x}$ is the location in space, $\mathbf{n}$ is a unit vector indicating the direction of the radiation and λ is its wavelength. The left-hand side of this equation represents the change of the intensity I (i.e. the energy carried by the radiation field) over an infinitesimal distance along the path determined by the position $\mathbf{x}$ and the propagation direction $\mathbf{n}$. The first term on the right-hand side represents the extinction when radiation passes through matter; k is the mass extinction coefficient and $\rho(\mathbf{x})$ is the mass density. The second term on the right-hand side represents the source term, i.e. the new luminosity released into the medium at $\mathbf{x}$ in direction $\mathbf{n}$. The complexity of the RT equation depends on the different physical processes which are responsible for extinction, scattering and emission.

Codes for 3D RT are the following: SUNRISE (Jonsson et al., 2010), SKIRT (Camps & Baes, 2015), RADISHE (Chakrabarti & Whitney, 2009), ART^2 (Li et al., 2008), TRADING (Bianchi, 2008) and GRASIL-3D (Domínguez-Tenreiro et al., 2014).

1.4 Contents of the Thesis

The Thesis is organized as follows:

- Chapter 2 is devoted to describe the MUlti Phase Particle Integrator model for feedback and star formation and results of cosmological simulations of disk galaxies carried out with the GADGET-3 code are presented, when this model is used for feedback and star formation;
- in Chapter 3 the emergence and properties of bars in those galaxies are analysed;

- Chapter 4 shows results for a sample of simulated galaxies. Gas mass scaling relations, the SFR and stellar mass relation, and the relation between the gas-phase metallicity and stellar mass are studied and compared with observations of the local Universe. Infrared predicted spectra are obtained post-processing the galaxies with the GRASIL-3D code and compared with observations;
- Chapter 5 presents a preliminary coupling of MUPPI algorithm with a chemical network for self-consistently tracking non-equilibrium abundance and cooling processes of H_2 and H_2-based star formation;
- finally the Chapter 6 gives the conclusions.

2

Simulating realistic disk galaxies with MUPPI

Recent numerical studies of galaxy formation demonstrated that the most crucial ingredient for a successful simulation of a disk-dominated galaxy is proper modeling of star formation and stellar feedback (SF&FB). Since more than one decade, it was recognized that the Inter-Stellar Medium (ISM) plays a key role in determining the efficiency of SN energy which is able to heat the surrounding gas and produce massive galactic outflows. At present, thanks to a careful tuning of models and the introduction of more refined forms of feedback, several independent groups are now succeeding in reproducing disk-dominated galaxies in good agreement with observations. However, no consensus has been reached on the nature of feedback energy required, nor on the details of its numerical implementation. In this Chapter[1], several approaches, developed by different groups, to model the sub-resolution behavior of gas are described. Results of cosmological simulations of disk galaxies carried out with the GADGET-3 TreePM+SPH code (nonpublic evolution of the code GADGET-2, Springel 2005) are presented, where SF&FB are described using MUlti Phase Particle Integrator (MUPPI) model. Starting from two sets of zoomed-in initial conditions of isolated cosmological halos with masses (2-3) $\cdot 10^{12}$ $M_{\odot}$, both available at two resolution levels, in all cases the resulting spiral galaxies have small bulge-over-total stellar mass ratios ($B/T \sim 0.2$), extended stellar and gas disks, flat rotation curves and results are found to be remarkably stable against resolution. Other previous works adopting MUPPI are briefly described.

[1]This Chapter is mainly based on results shown in the paper *Murante G., Monaco P., Borgani S., Tornatore L., Dolag K., Goz D., 2015, MNRAS, 447, 178* (Murante et al., 2015).

2.1 Modeling the ISM

Early star-formation prescriptions produced highly compact disks, failing to obtain extended disks like local grand-design spirals (see Section 1.2.3). Springel & Hernquist (2003) introduced a new, more refined model for describing the process of star formation (hereafter *effective model*), treating gas particles eligible to form stars as a multiphase medium, composed by a cold and a hot phase in thermal pressure equilibrium. The implementation of kinetic feedback by Springel & Hernquist (2003), is usually referred to as *energy-driven* kinetic feedback. In the *momentum-driven winds* implementation, proposed by Oppenheimer & Davé (2006), the outflows are driven by radiation pressure of massive stars.

Stinson et al. (2006) presented the *blast-wave* feedback, employed in the GASOLINE code. After the injection of thermal energy, the cooling of gas particles is switched off for the lifetime of a SN-driven blastwave. This high gas pressure develops naturally a large-scale outflow. Stinson et al. (2013) obtained realistic late-type galaxy, with a moderate mass resolution, adding also *early stellar feedback*, motivated by the expectation that the UV radiation of young stars can quench the star formation rate in cold molecular clouds.

In contrast with Springel & Hernquist (2003), Dalla Vecchia & Schaye (2008) suggested that outflowing gas particles should not be hydrodynamically decoupled and later on in Dalla Vecchia & Schaye (2012) thermal energy is distributed in a selective way, allowing heated particle to expand and produce outflows before energy is radiated away, by imposing a cooling time longer than the soundcrossing time.

Following Marri & White (2003), Scannapieco et al. (2009), revised the SPH scheme to prevent overcooling of a hot phase which is spatially coexisting with cold gas. The multiphase model decouples particles with dissimilar properties, limiting the search of neighbors in a given entropy range. Because of its lower density, SN thermal energy distributed to hot gas is not immediately radiated away. Cold gas particles cumulate SN energy until they can be promoted to become hot particles. Aumer et al. (2013) added a non-decoupled kinetic feedback to the latter scheme, along with feedback from radiation pressure of young massive stars, studied by Hopkins et al. (2011), producing realistic late-type spiral galaxies.

Agertz et al. (2011) shut off cooling for gas receiving SNe energy in RAMSES code. Using a low star formation efficiency and also a low density threshold, they successfully reproduced several observed properties of MW like galaxies.

Ceverino & Klypin (2009), using the ART code, build up a sub-resolution model

for SF&FB starting from ∼50 pc parsec-scale simulations of a portion of a disk galaxy, investigating the role of the SNe feedback on the multiphase ISM. They obtained at high redshift substantial metal-rich outflows with few hundred km/s and occasionally 1000 – 2000 km/s, preventing the overcooling problem. However, the galaxy properties were very sensitive to the sub-resolution model parameters and the model required very high resolution (∼50 pc), consequently they had to stop their cosmological simulation at high redshift, $z = 3$.

Vogelsberger et al. (2014), using AREPO with a modified version of the *effective model*, performed cosmological simulations with various prescriptions of kinetic feedback and in one of them the wind speed depended upon the mass of the host dark matter halo, as in the *momentum-driven winds* implementation proposed by Oppenheimer & Davé (2006). Their simulations included also AGN radiation feedback. They successfully matched the TF relation and the stellar mass-halo mass relation. Marinacci et al. (2013) with the same sub-resolution model produced realistic late-type galaxies, with low B/T ratios and low baryon fractions.

2.2 The MUPPI sub-resolution model

MUlti Phase Particle Integrator (MUPPI) is a model for star-formation and stellar feedback in SPH simulations of galaxy formation developed within the GADGET code and presented in Murante et al. (2010, 2015). The code is loosely based on the model of SF&FB developed by Monaco (2004). The aim of MUPPI model is to provide a description of the multi-phase gas accurate enough to represent in a realistic way the emergent effects of SF&FB on resolved scales, taking into account that, at the typical force resolution (from 100 pc to 1 kpc) and mass resolution (from 10^4 to 10^6 $M_\odot$) of cosmological simulations of galaxy formation, the ISM of a star-forming region has much structure at unresolved scales. Following Monaco (2004), each gas particle is assumed, under a set of conditions, eligible to host star formation and represents a multi-phase ISM that is composed by a hot and tenuous gas phase and a dense cold phase with a low filling factor. These two phases are assumed to be in thermal pressure equilibrium. Then the evolution of a multi-phase particle, within each SPH time-step, is governed by a system of four ordinary differential equations (ODEs) which describes the mass flows among cold, hot and (virtual) stellar components, and the thermal energy flows (cooling, SN feedback and hydro term) of the hot phase. The scheme is the following: cooling deposits hot gas into the cold phase; evaporation brings cold gas back to the hot phase; star formation moves mass from the cold gas to stars; restoration moves

mass from stars to the hot phase. Thermal energy from SNe is injected into the local hot phase, ensuring that it is not quickly radiated away. A kinetic feedback prescription generates the massive outflows needed to avoid the over-production of stars.

2.2.1 The MUPPI algorithm

Within each star forming gas particle of mass $M_{\rm P}$, the masses of the hot, cold and (virtual) stellar components are $M_{\rm h}$, $M_{\rm c}$ and M_*. If $n_{\rm h}$ and $n_{\rm c}$ are the particle number densities of the two gas phases and $T_{\rm h}$ and $T_{\rm c}$ their temperatures accordingly, the condition of pressure equilibrium translates into:

$$n_{\rm h} \cdot T_{\rm h} = n_{\rm c} \cdot T_{\rm c} \tag{2.1}$$

$T_{\rm c}$ should be considered as an effective temperature and is a free parameter of the model. Densities of hot and cold phases are computed starting from their filling factors. Calling $F_{\rm c}$ the fraction of gas mass in the cold phase ($F_{\rm c} + F_{\rm h} = 1$), its filling factors $f_{\rm c}$ and $f_{\rm h}$ are:

$$f_{\rm c} = 1 - f_{\rm h} = \frac{1}{1 + \frac{F_{\rm h}}{F_{\rm c}} \cdot \frac{\mu_{\rm c}}{\mu_{\rm h}} \cdot \frac{T_{\rm h}}{T_{\rm c}}} \tag{2.2}$$

where $\mu_{\rm h}$ and $\mu_{\rm c}$ are the corresponding molecular weights. Then, if ρ is the average gas density, for the cold phase holds (the same for the hot phase):

$$n_{\rm c} = \rho F_{\rm c} / f_{\rm c} \mu_{\rm c} m_{\rm p} \tag{2.3}$$

Blitz & Rosolowsky (2006) found a phenomenological relation between the ratio of surface densities of molecular and atomic gas, and the estimated external pressure exerted on molecular clouds. Thus, MUPPI, employing the hydrodynamic pressure of the particle instead of the external pressure, recovers the molecular fraction $f_{\rm mol}$ as:

$$f_{\rm mol} = \frac{1}{1 + P_0 / P} \tag{2.4}$$

with P_0 a parameter of the model. In Blitz & Rosolowsky (2006), the pressure P_0 at which half of the cold gas is molecular is set to $P_0/k_{\rm B} = 35000$ Kcm^{-3}, with $k_{\rm B}$ being the Boltzmann constant.

A gas particle enters the multi-phase regime every time its temperature drops below 10^5 K and its density is higher than a threshold value $\rho_{\rm thr}$ (free parameter of the model). The multi-phase particle is initialized with all the mass ($M_{\rm P}$) in

the hot component, i.e. $M_{\rm h} = M_{\rm P}$ and the hot temperature is set equal to the gas particle temperature, i.e. $T_{\rm h} = T_{\rm P}$. Then the evolution is described by a system of four ODEs (see below) in which the variables are the masses of the three components, namely $M_{\rm h}$, $M_{\rm c}$ and M_*, and the thermal energy of the hot phase $E_{\rm h}$. At each SPH time-step, the system is integrated with a Runge-Kutta integrator with adaptive timesteps, meaning that each integration time-step of the system is much shorter than the SPH one. To mimic the destruction of molecular clouds due to the activity of massive and dying stars, a multiphase cycle lasts at most a time $t_{\rm clock}$, which is set to be proportional to the dynamical time of the cold phase, i.e. $t_{\rm dyn} = \sqrt{(}3\pi/32G\rho_{\rm c})$. Another way for a particle to exit the multi-phase regime is that its density gets below 1/5 of the entrance density threshold $\rho_{\rm thr}$. If the energy from SNe does not allow to sustain the hot phase ($T_{\rm h} \lesssim 10^5$K), the particle is forced to exit the multi-phase regime.

The ODEs system is the following:

$$\dot{M}_* = \dot{M}_{\rm sf} - \dot{M}_{\rm re} \tag{2.5}$$
$$\dot{M}_{\rm c} = \dot{M}_{\rm cool} - \dot{M}_{\rm sf} - \dot{M}_{\rm ev} \tag{2.6}$$
$$\dot{M}_{\rm h} = -\dot{M}_{\rm cool} + \dot{M}_{\rm re} + \dot{M}_{\rm ev} \tag{2.7}$$
$$\dot{E}_{\rm h} = \dot{E}_{\rm heat,local} - \dot{E}_{\rm cool} + \dot{E}_{\rm hydro} \tag{2.8}$$

The various terms of the system above are computed as follows.
The cooling flow $\dot{M}_{\rm cool}$ is:

$$\dot{M}_{\rm cool} = \frac{M_{\rm h}}{t_{\rm cool}} \tag{2.9}$$

depositing mass onto the cold phase at constant $T_{\rm h}$. The cooling time is computed using hot phase density and temperature. The star formation rate is:

$$\dot{M}_{\rm sf} = f_* \frac{f_{\rm mol} \cdot M_{\rm c}}{t_{\rm dyn}} \tag{2.10}$$

The evaporation is assumed to be proportional to the star formation rate:

$$\dot{M}_{\rm ev} = f_{\rm ev} \cdot \dot{M}_{\rm sf} \tag{2.11}$$

where $f_{\rm ev}$ is a free parameter of the model. In the case of absence of chemical evolution the restoration term is modeled as:

$$\dot{M}_{\rm re} = f_{\rm re} \cdot \dot{M}_{\rm sf} \tag{2.12}$$

adopting the Instantaneous Recycling Approximation (IRA), otherwise it is performed by the chemical evolution code (Tornatore et al., 2007).

The first heating term in Eq. 2.8 reads:

$$\dot{E}_{\rm heat,local} = E_{\rm SN} \cdot f_{\rm fb,local} \cdot \frac{\dot{M}_{\rm sf}}{M_{*,\rm SN}} \tag{2.13}$$

It accounts for the contribution of SN energy from stars formed within the multi-phase particle. $E_{\rm SN}$ and $M_{*,\rm SN}$ are the energy supplied by a single supernova and the stellar mass associated, while $f_{\rm fb,local}$ (free parameter of the model) is the fraction of SN energy that is deposited in the hot phase. The energy radiated away by cooling is:

$$\dot{E}_{\rm cool} = \frac{E_{\rm h}}{t_{\rm cool}} \tag{2.14}$$

The hydro term, $\dot{E}_{\rm hydro}$, takes into account the energy due to interactions with the neighbor particles, computed as the ratio between the energy accumulated during the last SPH-timestep and the timestep itself. This term accounts for the change of the entropy, i.e. an adiabatic expansion or contraction (PdV work), plus the SN energy coming from neighboring particles and the possible effect of artificial viscosity due to the implementation of the hydrodynamic.

Besides the small fraction $f_{\rm fb,local}$ given to the star-forming particle itself, the energy budget from SNe is distributed in the form of both thermal and kinetic energy (the latest described in Section 2.2.3). Thermal energy distributed to neighbors by each star-forming particle can be written as

$$\Delta E_{\rm heat,out} = E_{\rm SN} \cdot f_{\rm fb,out} \cdot \frac{\Delta M_*}{M_{*,\rm SN}} \tag{2.15}$$

Each multi-phase particle distributes its thermal energy along the least resistance path, to mimic the blow-out of SN superbubbles (Monaco, 2004), within its SPH smoothing length and to particles lying within a cone whose axis is aligned along the direction of minus the local density gradient and whose semi-aperture angle is θ (free parameter of the model). Energy contributions are weighted with the SPH kernel, using the distance from the cone axis.

This non-equilibrium dynamics can be summarized as follow:
cooling deposits hot gas into the cold phase at relatively low rate, since it is computed using density and temperature of the hot phase. In this way, the mass of the hot phase decreases, but its temperature is sustained by thermal SNe feedback. The

relation between the pressure, sustained by SNe energy injection, and the molecular fraction (Eq. 2.4) leads to a runaway of star formation, until the molecular fraction reaches the unity. On the other hand, if the particle expands, i.e. lowers its pressure, star-formation is stopped. Therefore, the hydrodynamic interaction with neighboring particles halts the runaway.

At the end of the integration, the new state of the multiphase system is used to recompute the entropy of the gas particle and to include the effect of thermal energy from surrounding SNe.

A new star particle is spawned with the stochastic algorithm described by Springel & Hernquist (2003). In an SPH time-step, MUPPI transforms a mass ΔM_* of gas into stars. If $M_{\rm P} = M_{\rm h} + M_{\rm c} + M_*$ is the total particle mass, then a star particle of mass M_{p*} is spawned by the gas particle with probability:

$$P = \frac{M_{\rm p}}{M_{\rm p*}} \left[1 - \exp\left(-\frac{\Delta M_*}{M_{\rm p}} \right) \right]. \tag{2.16}$$

The mass of the spawned star is set as a fraction 1/N of the initial mass of gas particles, so as to have N generations of stars per gas particle. N = 4 is a reasonable compromise between the needs of providing a continuous description of star formation and of preventing proliferation of low-mass star particles. The mass is taken from the (virtual) stellar mass of the multi-phase particle and, in the case that it is not sufficient, the remaining mass is taken from the cold phase, or from the hot one in the extreme case that is still not enough. Whenever a particle exits the multi-phase regime, its accumulated stellar component, which has not been used to spawn a star, is nulled.

Table 2.1 summarizes the free parameters of the model and their adopted values for all the results shown in Section 2.4 and in Chapter 3.

2.2.2 Chemical evolution and metal cooling

Chemical evolution is treated as in Tornatore et al. (2007). In this code each star particle is treated as a Simple Stellar Population (SSP) whose evolution is followed starting from the time at which it has been spawned from the parent gas particle. Given a stellar Initial Mass Function (IMF), the mass of the SSP is varied in time following the death of stars and accounting for stellar mass losses. The production of several elements is followed through SNII, SNIa and AGB stars. The enriched material is spread among the neighboring gas particles with weights given by the SPH kernel. In the results shown, for each gas particle the code tracks the mass in *H*, *He* and in several other chemical species, namely *C*, *Ca*, *O*, *N*, *Ne*, *Mg*, *S*, *Si*, *Fe*,

T_c	P_0	f_{re}	f_{ev}	$f_\star$	t_{clock}/t_{dyn}	ρ_{thr}	θ	$f_{fb,local}$	$f_{fb,out}$	$f_{fb,kin}$	P_{kin}
300	20000	—	0.1	0.02	1	0.01	60	0.02	0.2	0.6	0.03

Table 2.1: Parameters of MUPPI algorithm and fiducial values. Column 1: Cold phase temperature (K). Column 2: Pressure at which $f_{mol} = 0.5$ (K cm^{-3}). Column 3: restoration fraction computed by the chemical evolution model. Column 4: evaporation fraction. Column 5: star formation efficiency (referred to the *molecular* gas). Column 6: duration of a multi-phase cycle in dynamical times. Column 7: density threshold for multi-phase particles (cm^{-3}). Column 8: Semi-aperture of the cone (degrees). Column 9: SN thermal energy given to local hot gas. Column 10: SN thermal energy given to neighboring hot gas. Column 11: SN kinetic energy given to wind particles. Column 12: Probability for a gas particle to be converted in a wind particle.

plus that in generic other elements. A star particle inherits its metallicity from the parent gas particle.

The results (Section 2.4) assume the IMF proposed by Kroupa et al. (1993), in the range 0.1-100 M$_\odot$, similar to that proposed by Chabrier (2003) in the same mass range, while stellar lifetimes are taken from Padovani & Matteucci (1993). SNII are assumed to be originated by stars more massive than 8 M$_\odot$, while stars more massive than 40 M$_\odot$ are assumed to implode into black holes and so they do not contribute to the chemical enrichment. Metal yields are taken from Woosley & Weaver (1995) for SNII, Thielemann et al. (2003) for SNIa and van den Hoek & Groenewegen (1997) for AGB stars.

The contribution of metals to gas cooling is computed by following the procedure of Wiersma et al. (2009). The gas, exposed to a spatially-uniform time-dependent photoionizing radiation (Haardt & Madau, 2001), is assumed to be dust-free, optically thin and in photoionization equilibrium (more details about gas cooling/heating functions are given in Section 1.2.3).

2.2.3 Kinetic feedback

The kinetic feedback scheme broadly follows the one proposed by Springel & Hernquist (2003). A particle has a probability P_{kin} to become a *wind* particle every time it exits a multi-phase cycle. For some time t_{wind}, with that probability, such particle can receive kinetic energy from neighboring multi-phase particles. Motivated by the fact that outflows are driven by SNII exploding after the destruction of the molecular cloud, this time is set equal to the stellar lifetime of an 8 M$_\odot$ star, t_8,

minus the duration $t_{\rm clock}$ of the past multi-phase cycle:

$$t_{\rm wind} = t_8 - t_{\rm clock} \tag{2.17}$$

For each star-forming particle, the available kinetic energy budget is:

$$E_{\rm kin} = f_{\rm fb,kin} \cdot E_{\rm SN} \tag{2.18}$$

and it is distributed from multi-phase particles to wind particles with the same scheme of thermal energy (see Section 2.2.1). Moreover, in order to avoid hydrodynamical coupling at ∼kpc scale, the wind particle is decoupled from the surrounding gas as long as it receives kinetic energy. However, when the decoupling is not implemented, the resulting galaxy has very similar properties. Table 2.1 specifies the adopted values for $P_{\rm kin}$ and $f_{\rm fb,kin}$, free parameters of the model.

2.3 Simulations

Two sets of cosmological zoomed-in halos are simulated. Their initial conditions describe the evolution of two isolated halos with mass in the range $\sim (1-2) \cdot 10^{12}$ h^{-1} $M_\odot$, both having a quiet merging history since $z \sim 2$. Due to the lack of recent major mergers, these halos are expected to host a disk galaxy at $z = 0$. In both cases initial conditions are available at two resolutions[2]. It is worth to be noted that the evolution of a resimulated object changes when resolution is varied: in fact, power added at small scales modifies the halo's accretion history, e.g. the timing of the mergers and the distribution of the angular momentum. The first set of initial conditions, called GA both in Murante et al. (2015) and in Goz et al. (2015), has been presented by Stoehr et al. (2002). The second set, called AqC in both works, has been presented by Springel et al. (2008) and used, among other papers, in the Aquila comparison project (Scannapieco et al., 2012).

Table 2.2 shows mass and force resolutions[3] used for the simulations, together with the virial mass and radius[4]. Force softening is chosen to be constant in physical coordinates since $z = 6$, while it is comoving with Hubble expansion at higher

[2]In Murante et al. (2015) GA simulation is available at three different resolutions, but in this Chapter results are reported only for two of them, the same shown in Goz et al. (2015).

[3]Lengths are given in units of h^{-1} kpc and masses in units of $M_\odot$ h^{-1}, at variance with the rest of the Chapter where lengths are expressed in kpc and masses in $M_\odot$. This makes more ease the comparison with other works in literature. Softening is expressed in h^{-1}kpc.

[4]Virial quantities are defined as those computed in a sphere centered on the minimum potential particle of the halo and encompassing an overdensity of 200 times the critical cosmic density.

Simulation	M_{DM}	M_{gas}	ϵ_{Pl}	M_{Vir}	R_{Vir}	N_{DM}	N_{gas}	N_{star}
GA1	$1.5 \cdot 10^7$	$2.8 \cdot 10^6$	0.65	$2.30 \cdot 10^{12}$	212.56	133066	68130	178626
GA2	$1.6 \cdot 10^6$	$3.0 \cdot 10^5$	0.325	$2.20 \cdot 10^{12}$	209.89	1214958	534567	1429204
AqC6	$1.3 \cdot 10^7$	$4.8 \cdot 10^6$	0.65	$1.21 \cdot 10^{12}$	169.03	87933	40362	123307
AqC5	$1.6 \cdot 10^6$	$3.0 \cdot 10^5$	0.325	$1.16 \cdot 10^{12}$	166.75	687003	276881	898777

Table 2.2: Basic characteristics of the different runs Column 1: simulation name; Column 2: mass of the DM particles; Column 3: initial mass of the gas particles; Column 4: Plummer-equivalent softening length for gravitational force. Column 5: Virial mass of the DM halo at $z = 0$; Column 6: Virial radius of the DM halo at $z = 0$; Column 7: number of DM particles within the virial radius at $z = 0$; Column 8: number of gas particles within the virial radius at $z = 0$; Column 9: number of star particles within the virial radius at $z = 0$. Masses are expressed in units of $M_\odot/h$ and softening lengths in units of kpc/h.

redshift. The softening of the GA set is scaled with the cubic root of the mass resolution. For the AqC5 and AqC6 simulations the same softenings are used as for GA2 and GA1, respectively.

The GA set adopts a ΛCDM cosmology with $\Omega_m = 0.3$, $\Omega_\Lambda = 0.7$, $\Omega_{baryon} = 0.043$ and $H_0 = 70$ km s^{-1}. Also AqC is run with a ΛCDM cosmology, but with $\Omega_m = 0.25$, $\Omega_\Lambda = 0.75$, $\Omega_{baryon} = 0.04$ and $H_0 = 73$ km s^{-1}.

2.4 Results

In this Section the main results obtained from the highest resolution GA2 and AqC5 halos at $z = 0$ are presented. The ISM properties, the evolution and the effect of resolution of simulated galaxies are described in details in Murante et al. (2015).

In Figure 2.1, face-on and edge-on maps of gas and stellar density for the GA2 simulation are shown. The coordinate system is rotated so that its z-axis is aligned with the vector of angular momentum of star and cold or multi-phase gas particles within 8 kpc from the position of the minimum of the gravitational potential and centered on it. In both papers (Murante et al. 2015 and Goz et al. 2015) all analysis have been performed with this reference system. The presence of an extended disk is evident in both gas and stellar components. The gas disk shows a complex spiral pattern and is warped in the outskirt regions. A spiral pattern is visible also in the outer part of the stellar disk. At the center, a bar is visible both in the gas and in the stellar component. A full analysis of the bar features in the simulated galaxies

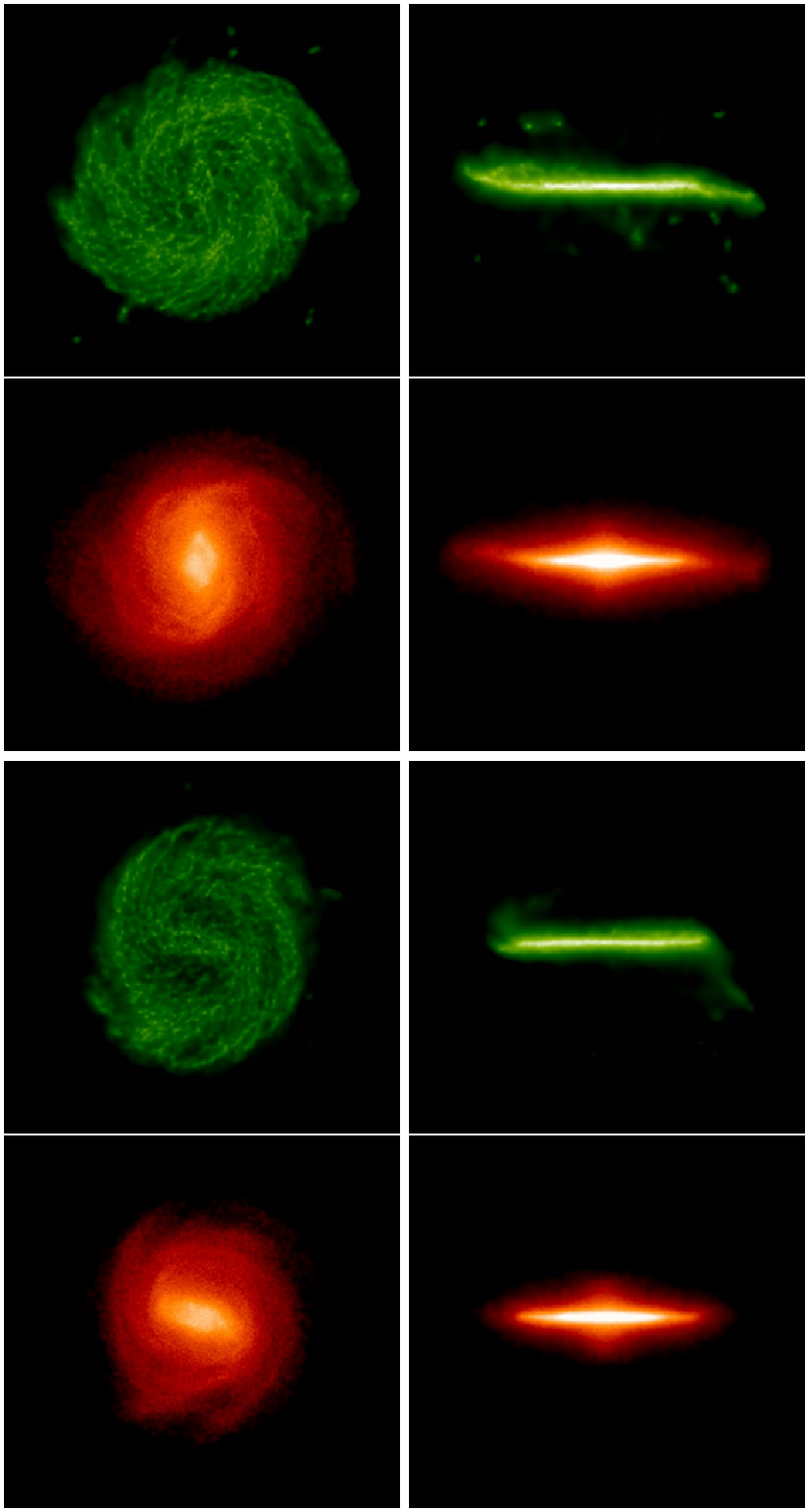

Figure 2.1: First row: gas projected density of GA2 simulation. Second row: stellar projected density of GA2 simulation. Third row: gas projected density of AqC5 simulation. Fourth row: stellar projected density of AqC5 simulation. Left column shows face-on densities, right column shows edge-on densities. Box size is 57 kpc. Reproduced from Murante et al. (2015).

Simulation	R_{gal}	R_d	B/T	$f(\epsilon > 0.8)$	$M_\star$	$M_{*,bulge}$	$M_{*,disk}$	$M_{*,vir}$	M_{cold}	$f_{b,vir}$	f_{gal}	f_J
GA1	30.37	3.93	0.22	0.47 (0.30)	$1.35 \cdot 10^{11}$	$2.91 \cdot 10^{10}$	$1.06 \cdot 10^{11}$	$1.59 \cdot 10^{11}$	$1.95 \cdot 10^{11}$	0.11	0.049	0.56
GA2	29.98	4.45	0.20	0.51 (0.45)	$1.11 \cdot 10^{11}$	$2.26 \cdot 10^{10}$	$8.83 \cdot 10^{10}$	$1.31 \cdot 10^{11}$	$3.49 \cdot 10^{10}$	0.10	0.043	0.54
AQ-C-6	24.15	4.08	0.24	0.51 (0.46)	$8.26 \cdot 10^{10}$	$2.01 \cdot 10^{10}$	$6.25 \cdot 10^{10}$	$0.85 \cdot 10^{11}$	$1.97 \cdot 10^{9}$	0.11	0.057	1.18
AQ-C-5	23.82	3.42	0.23	0.55 (0.54)	$7.32 \cdot 10^{10}$	$1.67 \cdot 10^{10}$	$5.66 \cdot 10^{10}$	$0.77 \cdot 10^{11}$	$2.04 \cdot 10^{10}$	0.10	0.054	0.92

Table 2.3: Basic characteristics of the different runs. Column 1: Simulation name; Column 2: Galaxy radius (kpc), set to 1/10 of the virial radius; Column 3: Disk scale radius R_d (kpc); Column 4: B/T ratio inside the galaxy radius; Column 5: Mass fraction associated to stars having circularity $\epsilon > 0.8$; ϵ is calculated using the method of Scannapieco et al. (2009), while we report in parenthesis the values obtained using the method by Abadi et al. (2003); Column 6: Total galaxy stellar mass, inside R_{gal} ($M_\odot$); Column 7: Stellar mass in the bulge component inside R_{gal} ($M_\odot$); Column 8: Stellar mass in the disk component inside R_{gal} ($M_\odot$); Column 9: Stellar mass within the virial radius ($M_\odot$); Column 10: Cold gas mass ($M_\odot$); Column 11: Baryon fraction within R_{vir}; Column 12: Fraction of total baryon mass in the galaxy; Column 13: Ratio between the specific angular momentum of stars and cold gas within R_{gal} and the specific angular momentum of the dark matter within R_{vir}. R_{vir} is defined as the radius of a sphere centered on the most bound particle of the halo, and encompassing and overdensity $\delta = 200$ with respect to the *critical* density. The bulge mass is defined as twice the mass of counter-rotating stars, those having $j_z/j_{circ} < 0$ in Figure 2.2 and within 5 kpc from the galaxy center.

is presented by Goz et al. (2015) (see Chapter 3).

In Figure 2.1 the same maps for the simulation AqC5 are also shown. The appearance of the galaxy is similar to that of GA2, though here the disk is smaller, the warp in the gas disk is less evident and the distribution of stars shows even clearer spiral pattern and bar.

To quantify the kinematics of a galaxy it is customary to consider the distribution of orbit circularities of the star particles. The circularity ϵ of an orbit is defined as the ratio of the specific angular momentum in the direction perpendicular to the disk, and the specific angular momentum of a reference circular orbit: $\epsilon = J_z/J_{circ}$. Scannapieco et al. (2009) computed the latter quantity as $J_{circ} = r \cdot v_c(r) = r\sqrt{(GM(< r)/r)}$, where r is the distance of each star from the center and $v_c(r)$ the circular velocity at that position. Abadi et al. (2003) instead define $J_{circ} = J(E)$, where $J(E)$ is the maximum specific angular momentum allowed given the specific binding energy E of each star; in this way $\epsilon < 1$.

In the left panel of Figure 2.2, the histograms of circularities of all star particles

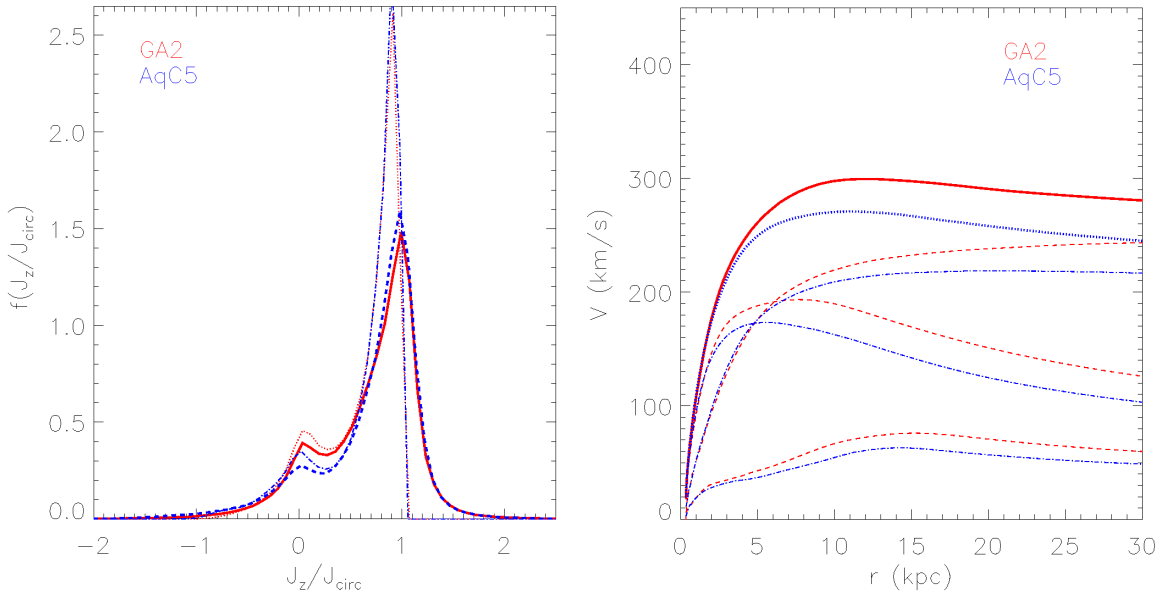

Figure 2.2: Left panel: distribution $f(\epsilon)/d\epsilon$ of the circularity parameter for the GA2 (red continuous and dotted lines) and AqC5 (blue dashed and dash-dotted lines) simulations at $z = 0$, for the stellar component, as a function of the circularity $\epsilon = J_z/J_{\rm circ}$. Thick (continuous and dashed) lines show circularity evaluated as in Scannapieco et al. (2009). Dotted and dash-dotted thin lines, as in Abadi et al. (2003). Distributions are normalized so that $\int f(\epsilon)d\epsilon = 1$. Right panel: rotation curves for the GA2 (red) and AqC5 (blue) simulations. Thick lines show the total curve, thin dashed lines show the contribution of the DM, thin dotted lines that of the gas and thin dotted-dashed lines that of the stellar component. Reproduced from Murante et al. (2015).

within $R_{\rm gal} = R_{\rm vir}/10$ for GA2 and AqC5 simulations are shown, using both methods outlined above. At redshift $z = 0$ both histograms show a prominent peak at $\epsilon \sim 1$, where stars rotating on a disk are expected to lie. The bulge component, corresponding to the peak at $\epsilon \sim 0$, is quite small in both cases, somewhat larger for GA2 than for AqC5. Assuming that counter-rotating star particles ($\epsilon < 0$) constitute half of the spheroidal component, the bulge mass is computed as twice the mass of these counter-rotating stars. B/T is defined to be the ratio of bulge over total stellar mass within $R_{\rm gal}$. This kinematic condition selects both halo and bulge stars. Since the definition is based on the sign of the quantity $J_z/J_{\rm circ}$, it does not depend on the method used to evaluate the circularity distributions. The resulting ratios are $B/T = 0.20$ for GA2 and $B/T = 0.23$ for AqC5.

In the right panel of Figure 2.2, the total rotation curves of GA2 and AqC5 and the singular contribution of DM, gas and stars are shown at redshift $z = 0$. Both galaxies have a remarkably flat rotation curve, reaching their maxima at 11.3 (AqC5) and 11.7 (GA2) kpc, after which they gently decline. The maximum rotation velocities are 270 and 299 km/s respectively, about 20 per cent higher than their circular velocities at the virial radius.

From the previous analysis it is clear that both simulated galaxies are disk-like and with a modest central mass concentration. Compared to the results presented in the *Aquila comparison project*, obtained using an earlier version of MUPPI, these findings clearly demonstrate that the inclusion of metal-dependent gas cooling and, more importantly, the inclusion of kinetic feedback are the reasons for this improvement.

Table 2.3 summarizes the main characteristics of the simulated galaxies at $z = 0$. Here the disk scale radius $R_{\rm d}$ is estimated by fitting an exponential profile to the stellar surface density from 4 to 12 kpc. Stellar masses are reported within $R_{\rm gal}$, cold gas includes multi-phase gas particles and single-phase ones with temperature lower than 10^5 K.
The main characteristics are:

- Both halos host massive disk galaxies. The total stellar mass in the GA2 simulation is $1.02 \cdot 10^{11}$ $M_\odot$, while it is $M_\star = 6.77 \cdot 10^{10}$ $M_\odot$ for AqC5, resulting in more massive galaxies than the MW.

- The cold gas mass, that is assumed to be in the disk, is 28 per cent (GA2) and 26 per cent (AqC5) of the total disk mass, a value which is higher by a factor $2 - 3$ than for the MW.

- The feedback scheme is efficient in expelling baryons from the halo. For

GA2, the baryon fraction within the virial radius is 10 per cent, compared to the cosmic 14.3 per cent, while the baryon mass of the galaxy (stars and cold gas) is 4.3 per cent of the total halo mass. These values are not far from those estimated for disk galaxies like the MW. For AqC5 the baryon fraction within the virial radius is again 10 per cent and the fraction of galaxy mass to total mass is 5.4 per cent.

- The specific angular momentum of galactic baryons (cold gas and stars) in GA2 is 54 per cent of the specific angular momentum of the DM within $R_{\rm vir}$. In the AqC5 simulation, this fraction exceeds 1.

Figure 2.3 shows the stellar TF relation (left panel) and the stellar mass *vs* halo mass relation (right panel) for the two simulations. Galaxy mass is the stellar mass inside $R_{\rm gal}$; velocities are taken from the circular velocity profile, at 2.2 times the disk radius as in Dutton et al. (2011). Symbols represent the position of the simulated galaxies in the plot.

For reference, in the same plot, the positions of AqC5 simulated by Marinacci et al. (2013), Guedes et al. (2011) and Aumer et al. (2013) are shown. The positions of three among AqC5 simulations performed by Scannapieco et al. (2012), namely models G3-TO, G3-CS and R-AGN, are also shown. Both simulated galaxies tend to lie on the high side of the range allowed by observations, as well as other simulated disk galaxies by different groups. This could be ascribed to some remaining limitations shared in all SF&FB models, or related to the way in which simulations are compared to observations. AqC5 galaxy has a stellar mass in good agreement with the finding of Marinacci et al. (2013), but higher than that found by other groups. In Table 2.3, the mass fraction of stars having a circularity larger than $\epsilon = 0.8$ is reported; this quantity can be considered as a rough estimate of the prominence of the *thin* disk.

The right panel of Figure 2.3 shows the relation between stellar mass in the galaxy and virial mass of the DM halo. The green solid line shows the estimate obtained by Guo et al. (2010) using the abundance matching technique. Following Marinacci et al. (2013), the grey area marks an interval of ± 0.2 dex around it. Black dashed line gives the relation obtained by Moster et al. (2010), with dotted lines corresponding to their 1σ error on the normalization. Symbols represent the position of simulated galaxies on this plot, while the lines give the evolution in time of the baryon formation efficiency during the simulations. Again, galaxies tend to lie on the high side of the allowed range of stellar masses. Both the position in the TF relation and that in the stellar *vs* halo mass suggest that simulated galaxies

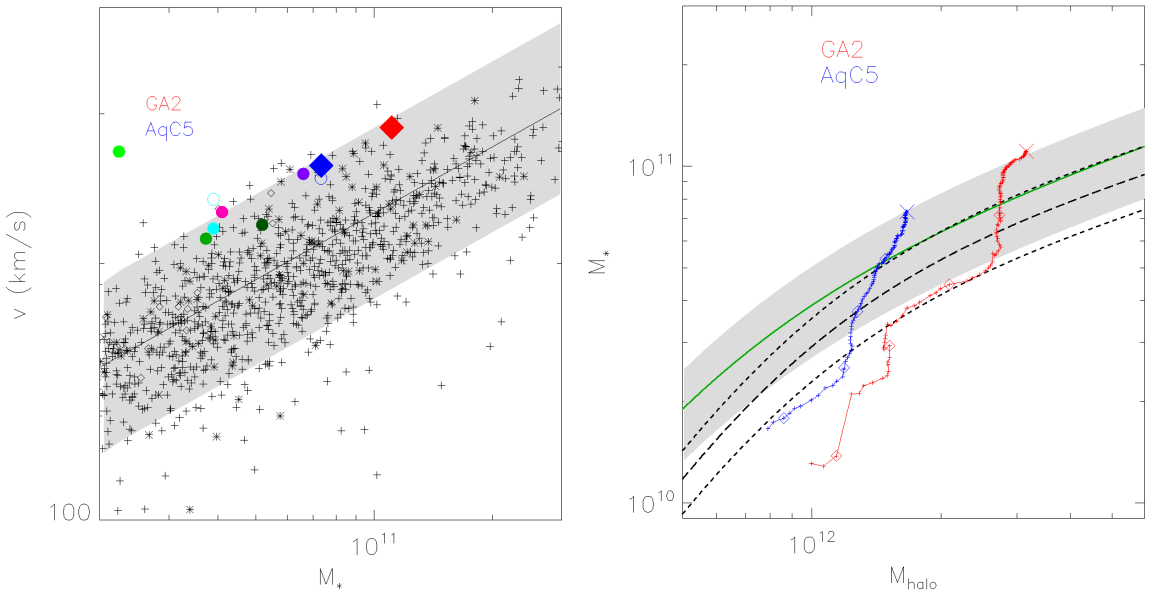

Figure 2.3: Left panel: Tully-Fisher relation for GA2 (red diamond) and AqC5 (blue diamond). Galaxy mass is the stellar mass inside $R_{\rm gal}$; velocities are estimated from the circular velocity profile at $2.2R_{\rm d}$. The line is the fit to observations of disk galaxies done by Dutton et al. (2011). The grey area shows an interval of 0.1 dex around the fit. Plus symbols are data points from Courteau et al. (2007), diamonds from Verheijen (2001) and asterisks from Pizagno et al. (2007). The positions of AqC5 is shown from Marinacci et al. (2013) (purple circle), where V is taken as the circular velocity at 2.2 times their quoted disk radius from their Figure 18. The ERIS simulation (Guedes et al., 2011), using their quoted $V_{\rm peak}$ (open cyan circle) and the circular velocity at 2.2 times their quoted i-band disk scale length, from their Figure 1 (filled cyan circle), is also shown. The magenta circle shows the position of AqC5 simulated by Aumer et al. (2013). Green filled circles show the position in the diagram of AqC5 simulations G3-TO, G3-CS and R-AGN from Scannapieco et al. (2012) (light green: G3-CS; medium green: G3-TO; dark green: R-AGN). For these, circular velocity is evaluated at the radius containing half of the galaxy stellar mass; blue empty circle refer to our AqC5 simulations, when using the same definition of circular velocity. Right panel: evolution of the relation between stellar mass and halo mass ratio of GA2 (red) and AqC5 (blue). Crosses correspond to results at $z = 0$, with the lines (with plus signs) showing the corresponding evolutions. Diamonds show redshifts z = 2,1.5,1.0,0.5. The continuous green line shows the fit to the star formation efficiency of DM halos obtained by Guo et al. (2010) with the abundance matching technique. The grey area is an interval of 0.2 dex around it. The dashed black lines is the same fit, as given by Moster et al. (2010), while the dotted lines show an interval of 1σ on the normalization of the fit. Reproduced from Murante et al. (2015).

are still slightly too massive. The baryon conversion efficiency, defined as $\eta = (M_*/M_{\rm vir})\,(\Omega_{\rm m}/\Omega_{\rm baryon})$ as in Guedes et al. (2011), is $\eta = 0.25$ for GA2 and $\eta = 0.29$ for AqC5.

2.5 Conclusions

Murante et al. (2015) present results of simulations of disk galaxies, carried out with the GADGET-3 code where the sub-resolution model for SF&FB MUPPI (MUlti Phase Particle Integrator) is implemented. The model describes the ISM at unresolved scales, without assumption of self-regulation of the multi-phase system. With respect to the first version of the code described in Murante et al. (2010), the chemical evolution model by Tornatore et al. (2007), metal cooling as in Wiersma et al. (2009) and a prescription for the kinetic feedback are included.

Both simulations, started from zoomed-in cosmological initial conditions of two DM haloes, result in disk galaxies with a bulge-over-total stellar mass kinematic ratio $B/T \approx 0.2$, typical of late-type galaxies. The rotation curves are gently rising for 1-2 disk scale radii and then remain flat. The simulated galaxies lie within the scatter of the observed TF relation. The baryon conversion efficiencies are consistently slightly too large compared to the relation provided by Moster et al. (2010).

The possibility to obtain realistic disk galaxies at moderate resolution and the remarkable numerical convergence of results open the perspective to simulate large volumes of the universe, containing a representative population of galaxies. The natural prosecution of the work is the subject of Barai et al. (2015) paper, in which diffuse gas properties at high redshift of a sample of galaxies are analyzed, and forthcoming papers, such as Goz et al. (prep), in which infrared properties of local simulated galaxies are presented (see Chapter 4).

2.6 Other works adopting MUPPI

Murante et al. (2012) analyzed the gas accretion rate in cosmological numerical simulations of a galaxy-size halo, using GADGET3 code and MUPPI model, as described in Murante et al. (2010), which implemented only thermal feedback. No chemical evolution was included in this version of the code, so the gas was of primordial composition. They distinguished between gas accretion onto the central galaxy (defined as all the matter within $R_{\rm gal}$) and accretion onto the halo (defined

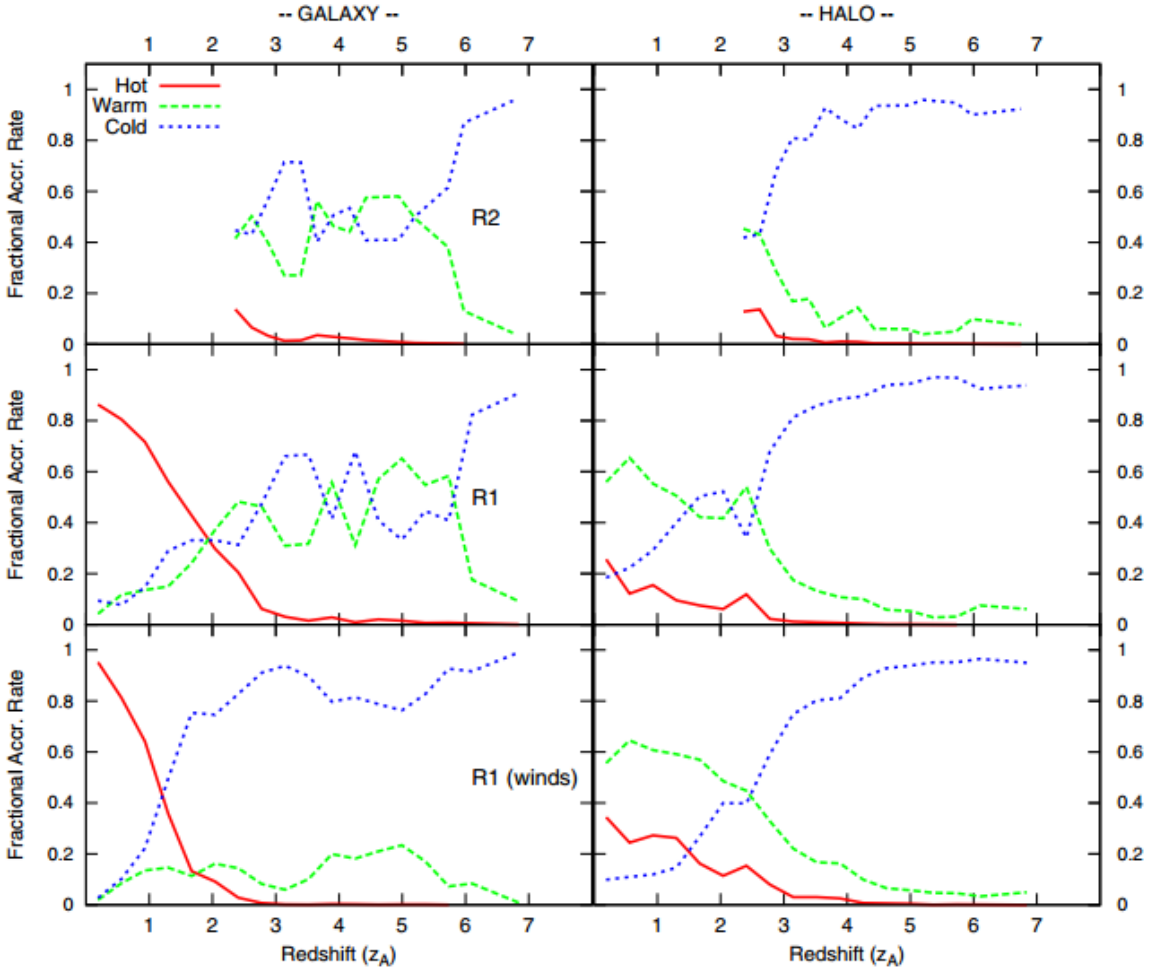

Figure 2.4: Right panels: gas fractional accretion rates onto the halo as a function of the accretion redshift. Left panels: corresponding fractional gas accretion rates onto the galaxy. The hot gas accretion is shown in red, the warm accretion in green and the cold accretion in blue. Reproduced from Murante et al. (2012).

as all the matter included in the redshift-dependent virial radius). They defined three accretion channels: a cold one, including gas particles whose maximum past temperature was lower than 2.5×10^5 K; a hot channel which included gas particles with maximum past temperature larger than 10^6 K; and an intermediate warm channel. Figure 2.4 shows the fractional mass accretion rates in the three channels for the galaxy (left panel) and for the halo (right panel). R1 simulation was equivalent to the GA2 (GA2 basic properties are reported in Table 2.2), while force and mass resolutions of R2 were one order of magnitude better than those of R1 (R2 simulation was run down to $z = 2.5$ only). For comparison, the the R1 (winds) simulation was also run. It adopted the widely used Springel & Hernquist (2003) *effective model* which implemented kinetic feedback. The figure shows that gas was accreted on the halo mainly via the cold channel for all runs considered. At low redshift, $z < 2$, the importance of warm and hot channels increased, in agreement with previous studies (e.g. Kereš et al., 2005). Regarding the accretion onto the galaxy, the cold and the warm channels equally contributed to gas accretion at high redshift in both R1 and R2 simulations. At later times, the hot channel provided the dominant contribution. Results were stable with resolution. The comparison with the *effective model* revealed that simulations with ineffective thermal feedback were unable to heat cold flows into the warm channel, even when they produced significant outflows.

Monaco et al. (2012) studied the SK relation obtained for isolated spiral galaxies in simulations run with the same code as in Murante et al. (2010). Table 2.4 summarizes the properties of the simulations. They showed (Figure 2.5) that MUPPI followed well the standard, molecular and atomic SK relations, with a tight molecular SK that is a straightforward consequence of the model assumptions (pressure-based model of star formation). The molecular SK had a slope of $\sim$1.4, slightly steeper than the 1.2 value found by Bigiel et al. (2008) but in agreement with Liu et al. (2011). The standard SK relation between surface densities of cold atomic+molecular gas and star formation rate of simulated galaxies showed a steepening at low gas surface densities, starting from a knee whose position depended on disc gas fraction, mimicking the predictions of models where the H_2-formation was modulated by metallicity (Krumholz et al. 2009; Gnedin & Kravtsov 2011). Moreover, when the *dynamical* SK relation, i.e. the SK that used gas surface density divided by orbital time, was considered, they found that all simulations stayed on the same non-linear relation, with a scatter that was even lower than that in the molecular SK. They interpreted this result as the balance between energy injection by SNe and dissipation (see the paper for a thorough discussion).

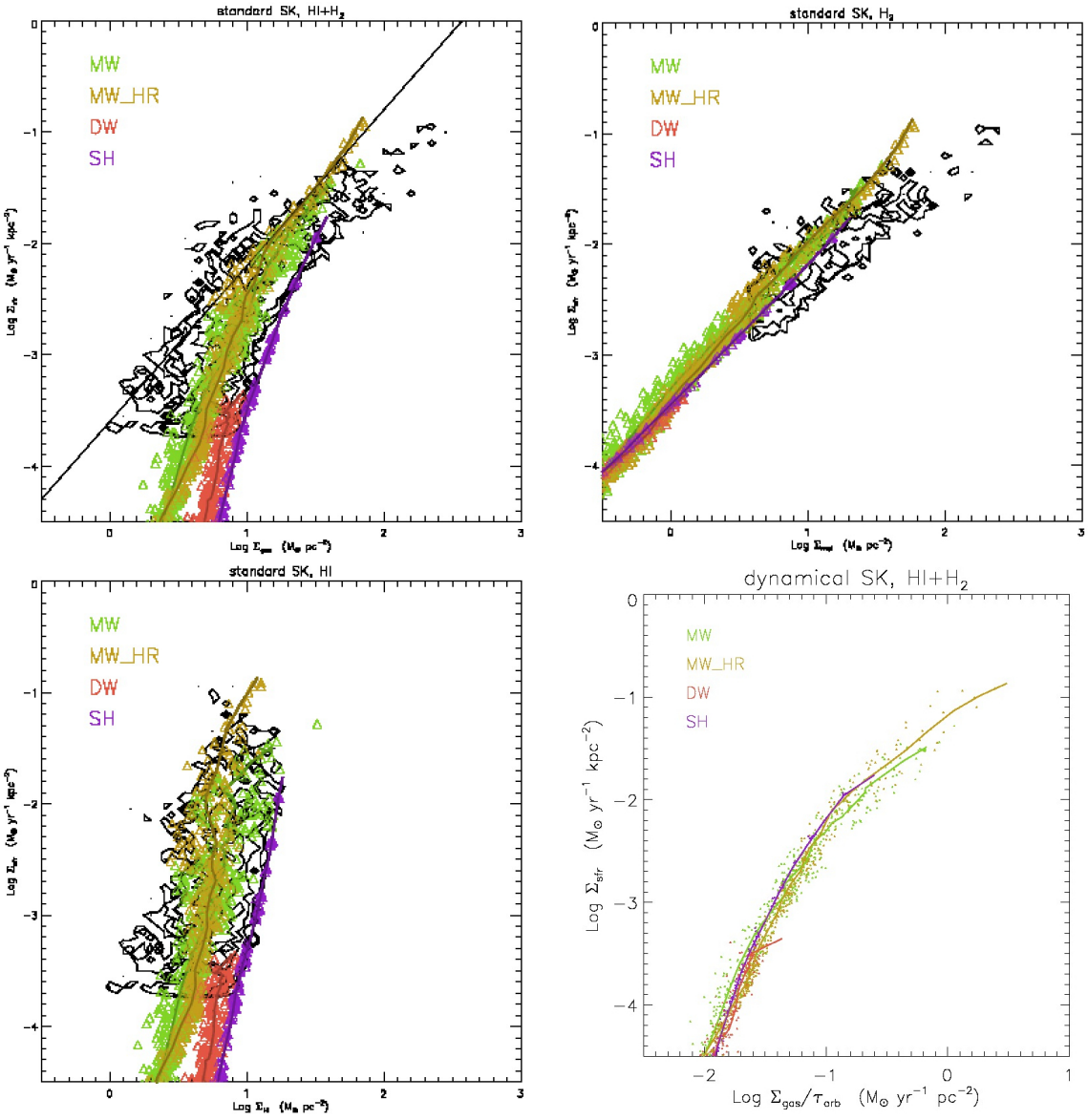

Figure 2.5: SK relations for simulated galaxies. The black contour levels report the data from Bigiel et al. (2008), binned in bins of size 0.5 dex; levels correspond to one, two, five and 10 observational points per bin, gas surface densities include helium. Triangles and thick lines give results for the four simulations in 750 pc bins and in radial profiles in cylindrical coordinates; color coding is given in each panel. The standard SK relation with all gas (HI+H_2) is shown on the top left, standard SK relation with molecular gas (H_2) is shown on the top right and standard SK relation with atomic gas (HI) is shown on the bottom left. Dynamical SK relations for simulated galaxies are shown on the bottom right. Points and thick lines give results for the four simulations in 750 pc bins and in radial profiles in cylindrical coordinates. Reproduced from Monaco et al. (2012).

Name	softening (kpc)	$M_{\rm dm}$ ($M_\odot$)	$m_{\rm dm}$ ($M_\odot$)	$M_\star^{(1)}$ ($M_\odot$)	$m_\star^{(2)}$ ($M_\odot$)	$R_\star$ (kpc)	$M_{\rm cold}$ ($M_\odot$)	$m_{\rm gas}$ ($M_\odot$)	$R_{\rm cold}$ (kpc)	gas fraction
MW	0.69	$9.4 \cdot 10^{11}$	$3.5 \cdot 10^6$	$4.2 \cdot 10^{10}$	$1.3 \cdot 10^6$	4.8	$3.3 \cdot 10^9$	$7.4 \cdot 10^4$	5.6	7.3%
MW_HR	0.41	$9.4 \cdot 10^{11}$	$6.9 \cdot 10^5$	$4.2 \cdot 10^{10}$	$2.6 \cdot 10^5$	4.4	$3.2 \cdot 10^9$	$1.5 \cdot 10^4$	5.4	7.1%
DW	0.42	$1.6 \cdot 10^{11}$	$8.1 \cdot 10^5$	$7.8 \cdot 10^9$	$1.6 \cdot 10^5$	8.5	$1.9 \cdot 10^9$	$3.9 \cdot 10^4$	8.3	20%
SH	0.042	$1.4 \cdot 10^{10}$	$-^{(3)}$	$1.4 \cdot 10^7$	$2.2 \cdot 10^3$	0.77	$1.4 \cdot 10^9$	$8.7 \cdot 10^3$	5.2	99%

Table 2.4: Basic characteristics of simulated galaxies. Column 1: Simulation name. Column 2: Gravitational Plummer-equivalent (P-e) softening for gas particles. Column 3: Mass of DM halo. Column 4: Mass of DM particle. Column 5: Stellar mass. Column 6: Mass of star particle. Column 7: Half-mass radius of stars. Column 8: Cold gas mass. Column 9: Initial mass of gas particle (before spawning stars). Column 10: Half-mass radius of cold gas. Column 11: Gas fraction. Notes (1): for MW, MW_HR and DW stellar masses include both the disc and bulge (only MW and MW_HR) stars present in the initial conditions and the newly formed stars, which are a minority. (2): in the above cases the stellar mass particle of old stars is reported, because new stars (whose particle mass is $m_{\rm gas}/4$) give a negligible contribution to the disc. (3): The DM halo in the SH simulation is static.

Barai et al. (2015) measured and quantified properties of galactic outflows and diffuse gas at $z \geq 1$, in cosmological hydrodynamical simulations with boxsize of 25 and 50 Mpc comoving, using MUPPI model in the updated implementation (thermal and kinetic feedback). Simulations included metal-dependent radiative cooling and heating in the presence of photoionizing background radiation, stellar evolution and chemical enrichment. For comparison with MUPPI, they adopted the *effective model* with variations of kinetic SN feedback, in the energy-driven formalism. Table 2.5 summarizes the properties of different runs. The gas distribution of an example massive galaxy whose halo has a total mass $\mathrm{M_{halo}} = 3.4 \times 10^{12} M_\odot$ (left two columns) and $1.8 \times 10^{12} M_\odot$ (remaining columns) at $z = 2$ is plotted in Figure 2.6 for three runs. Each of the five rows shows a gas/star property projected in the face-on (left) and edge-on (right) planes of a $(100\ \mathrm{kpc})^3$ volume. First row shows the velocity vectors of 7% gas particles, with the outgoing ($v_r > 0$) particles denoted as red and incoming ($v_r < 0$) gas as black. Here the blue circle in the face-on panels and the double blue rectangles in the edge-on panels illustrate the projected bi-cylinder volume used to measure the outflow of each galaxy. Gas density is in the second row, temperature in the third and total metallicity is plotted in the fourth row. *E35nw* and *M25std* presented the formation of a gas disk with extended spiral arms and tidal features. In the no-wind case *E35nw*, the gas disk was bigger in size, more massive, more metal enriched and there was no prominent outflow.

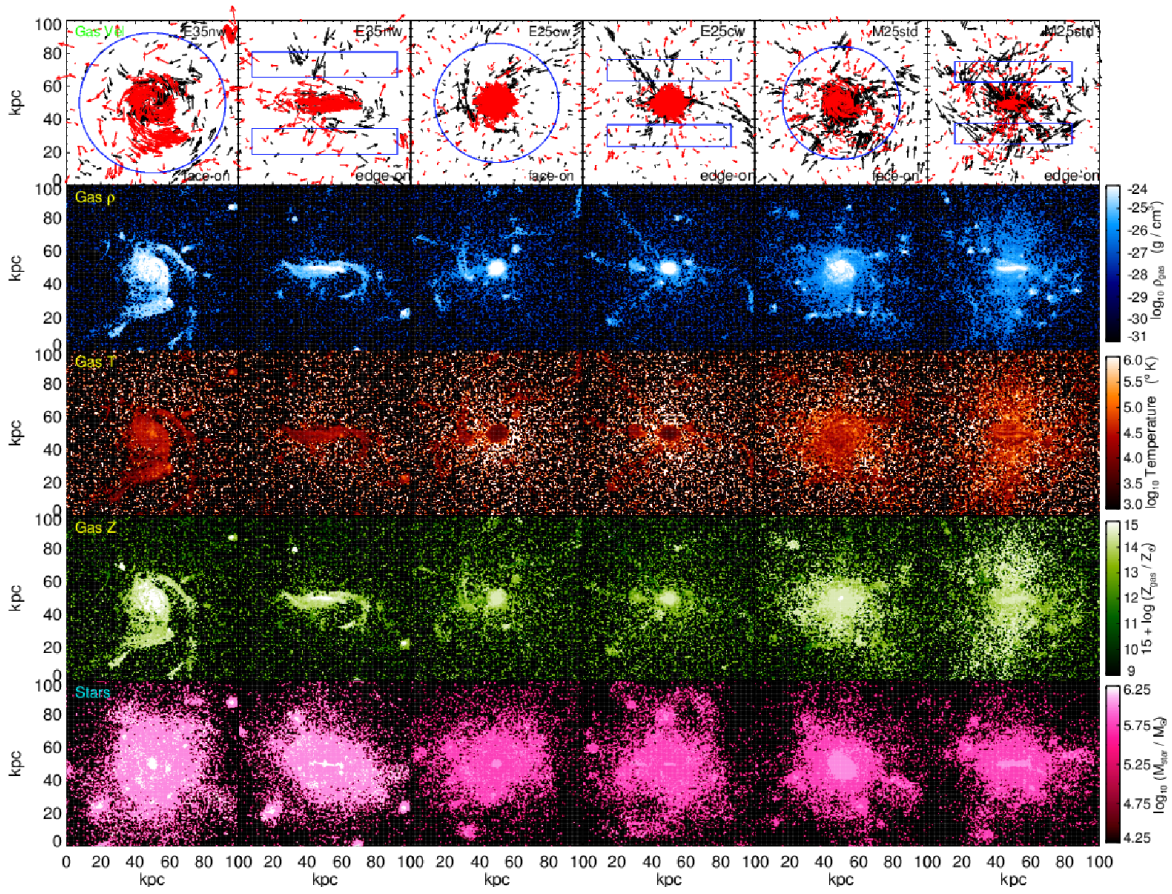

Figure 2.6: Projection of gas kinematics (top four rows) and stars (bottom row) in the face-on (left) and edge-on (right) planes of a (100 kpc)^3 volume centered around a massive galaxy at $z = 2$, in runs: E35nw (left two columns), E25cw (middle two columns), and M25std (right two columns). First row depicts the velocity vectors of 7% of all the gas particles inside the plotted volume, with the outflowing ($v_r > 0$) particles denoted as red and the inflowing ($v_r < 0$) as black. Second row shows gas density, third row is gas temperature and fourth row is gas total metallicity. Bottom row presents the projected stellar mass. In the top row, the blue circle in the face-on panels and the double blue rectangles in the edge-on panels illustrate the projected bi-cylinder volume used to measure outflows. Reproduced from Barai et al. (2015).

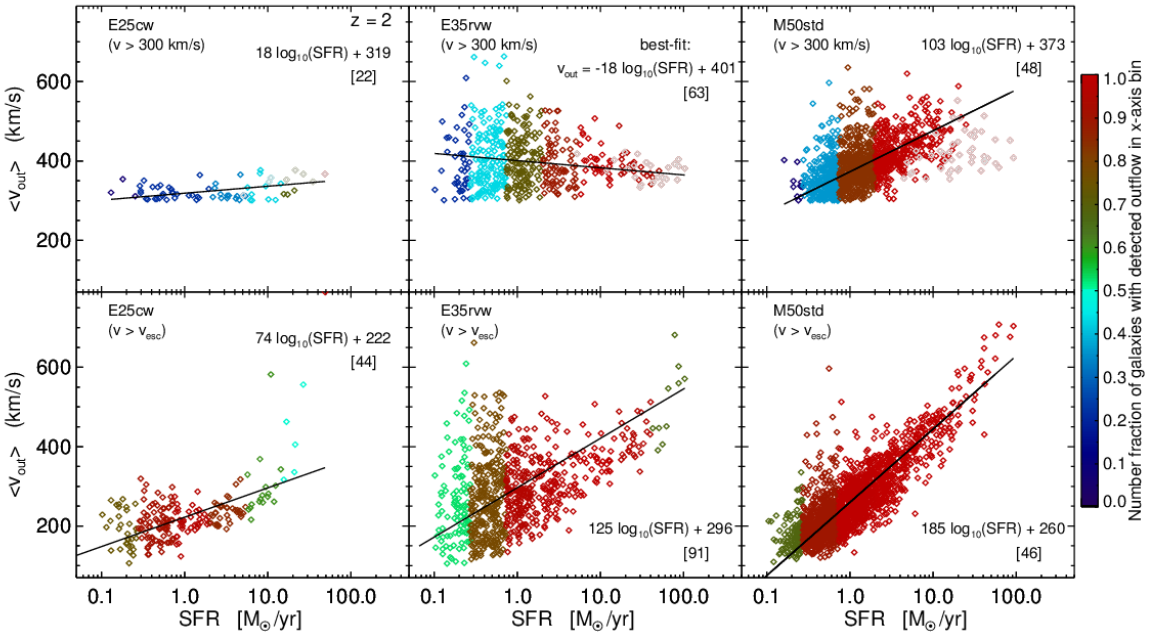

Figure 2.7: Outflow velocity as a function of SFR of galaxies in three runs (details of runs are in Table 2.5): *E25cw* in the left column, *E35rvw* at the middle, and *M50std* in the right. The two rows show different methods of computing outflow, by selecting gas particles above: a constant limiting speed $|v_z| > 300$ km/s at the top, and the escape velocity $|v_z| > v_{\rm esc} \equiv \sqrt{2GM_{\rm halo}/R_{\rm vir}}$ in the bottom. The plotting color depicts the number fraction of galaxies where outflow is detected in bins of galaxy SFR. The grey points in the top row mark galaxies more massive than $M_{\rm halo,lim} = 1.3 \times 10^{12}$ $M_\odot$, where the outflows might not escape the halo potential. The black line is the best-fit relation between $v_{\rm out}$ and log(SFR) obtained by an outlier-resistant two-variable linear regression. The fit coefficients and the "standard deviation" of the fit's residuals (within square brackets) are written inside the panels, using units same as the plotted axes. Reproduced from Barai et al. (2015).

Run Name	$L_{\rm box}$ [Mpc]	$N_{\rm part}$	$m_{\rm gas}$ [$M_\odot$]	$m_\star$ [$M_\odot$]	$L_{\rm soft}$ [kpc]	SF & SN feedback sub-resolution physics				
						Model	v_w	$f_{\rm fb,out}$	$f_{\rm fb,kin}$	$P_{\rm kin}$
E35nw	35.56	2×320^3	8.72×10^6	2.18×10^6	2.77 (comoving)	*Effective*	0			
E35rvw	35.56	2×320^3	8.72×10^6	2.18×10^6	2.77 (comoving)	*Effective*	$v_w(r)$			
E25cw	25	2×256^3	5.36×10^6	1.34×10^6	0.69 (physical)	*Effective*	350			
M25std	25	2×256^3	5.36×10^6	1.34×10^6	0.69 (physical)	MUPPI		0.2	0.6	0.03
M25a	25	2×256^3	5.36×10^6	1.34×10^6	0.69 (physical)	MUPPI		0.4	0.4	0.03
M25b	25	2×256^3	5.36×10^6	1.34×10^6	0.69 (physical)	MUPPI		0.2	0.8	0.03
M25c	25	2×256^3	5.36×10^6	1.34×10^6	0.69 (physical)	MUPPI		0.2	0.6	0.01
M25d	25	2×256^3	5.36×10^6	1.34×10^6	0.69 (physical)	MUPPI		0.2	0.6	0.06
M50std	50	2×512^3	5.36×10^6	1.34×10^6	0.69 (physical)	MUPPI		0.2	0.5	0.03

Table 2.5: Simulation parameters. Column 1: Name of simulation run. Column 2: $L_{\rm box}$ = Comoving side of cubic simulation volume. Column 3: Total number of gas and DM particles in the initial condition. Column 4: Mass of gas particle (which has not undergone any star-formation). Column 5: Mass of star particle. Column 6: Gravitational softening length (of all particle types). Column 7: Model of SF and SN feedback. Column 8: v_w = Wind velocity. Column 9: $f_{\rm fb,out}$ = Thermal feedback energy fraction. Column 10: $f_{\rm fb,kin}$ = Kinetic feedback energy fraction. Column 11: $P_{\rm kin}$ = Probability of kicking gas particles into wind.

In *E25cw* the central gas distribution was spheroidal and most of the outflowing gas lay inside $r < 20$ kpc, because here the wind kick velocity $v_w = 350$ km/s was too small to drive large-scale outflows. The MUPPI run *M25std* produced a well-developed gas outflow propagating perpendicular to the galaxy disk, escaping to $r > 30$ kpc from the galaxy center. Metals were more distributed in runs *E25cw* and *M25std*, since SN winds carried the metals out from the SF regions and enriched the circumgalactic medium. The fourth row also shows that the *M25std* outflow (right two panels) was more metal enriched at 30 kpc from the galaxy, than the *E25cw* case (middle two panels). Stellar mass in the bottom row revealed a central disk-like structure, surrounded by a larger stellar halo. The stellar disk was thinner in the no-wind case *E35nw*, than in the MUPPI run *M25std*.

Moreover, analyzing only central galaxies having a stellar mass higher than $10^9 M_\odot$, they found the following trend at $z = 2$:

- when SN feedback was present, outflowing gas was detected in (30-97)% of the galaxies by number, depending on the model parameters and galaxy mass range. The number fraction of galaxies with outflows correlated with mass and SFR;
- MUPPI model generated a positive correlation of the outflow velocity with galaxy SFR, while the *effective model* showed a constant velocity with a large

scatter. The outflow velocity as a function of SFR of galaxies is plotted in Figure 2.7, illustrating two different methods of computing outflow in the two rows. Outflowing gas particles are selected when their z-velocity component is above: (i) a constant limiting speed or $|v_z| > 300$ km/s in the top panels, and (ii) the escape velocity or $|v_z| > v_{\rm esc} \equiv \sqrt{2GM_{\rm halo}/R_{\rm vir}}$ at the bottom. The plotting color depicts the number fraction of galaxies where outflow is detected in bins of SFR, as indicated by the colorbar on the right;

- MUPPI model presented a stronger and relatively tighter positive correlation of the mass outflow with galaxy SFR. The *effective model* run with kinetic SN feedback exhibited a weak positive correlation of the mass outflow with SFR, with a slope flatter than the MUPPI models.

Hence the MUPPI model, using fully local properties of gas as input to the sub-resolution recipe, was able to produce galactic outflows whose velocity and mass outflow rate correlate with global properties of the galaxy (halo mass, SFR).

3

Properties of barred spiral disks

In this Chapter[1] a quantification of the properties of bars in two N-body+SPH cosmological simulations of spiral galaxies, named GA and AqC, is presented. The Initial Conditions (ICs) were obtained using the zoom-in technique and represent two dark matter (DM) halos of $2 - 3 \times 10^{12}$ $M_{\odot}$, available at two different resolutions. The properties of the resulting galaxies are presented in Chapter 2. The GA galaxy has been found to host a bar of length 8.8 kpc, present at the two resolution levels even though with a slightly different strength. Classical bar signatures (e.g. pattern of streaming motions, high $m = 2$ Fourier mode with roughly constant phase) are consistently found at both resolutions. Even if a close encounter with a merging satellite at $z \sim 0.6$ (mass ratio 1 : 50) causes a strong, transient spiral pattern and some heating of the disk, the onset of bar instability is found to take place when the disk is Toomre-unstable. The AqC galaxy has a slightly different history: it suffers a similar tidal disturbance due to a merging satellite at $z \sim 0.5$ but with a mass ratio of 1 : 32, that triggers a bar in the high-resolution simulation, while at low resolution the merging is found to take place at a later time, so that both secular evolution and merging are plausible triggers for bar instability.

[1]This Chapter is mainly based on the paper *Goz D., Monaco P., Murante G., Curir A., 2015, MNRAS, 447, 1774* (Goz et al., 2015).

3.1 Bars in cosmological halos

The study of bar formation in cosmological halos has been faced in two ways. Curir et al. (2006) built zoomed ICs of DM halos in cosmological volumes, let them evolve with an N-body code and substituted a selected DM halo with a model disk+halo system, where the disk was set in gravitational equilibrium with the cosmological halo. That paper considered purely stellar disks, while stellar plus gas disks were presented in Curir et al. (2007) and the effect of star formation was considered in Curir et al. (2008). In these works it was shown that halo triaxiality, at the level commonly found in simulated DM halos, triggers the formation of bars. The presence of gas leads to the destruction of the bar after a few dynamical times if the disk gas fraction is higher than $\sim$ 20 per cent, but the switching on of star formation inhibits this destruction. Different conclusions were reached by Berentzen et al. (2006), who noticed that the formation of a bar was weaker in halos with higher triaxiality. Athanassoula et al. (2013) showed the complex influence of halo triaxiality on the bar strength: at earlier times it triggers an instability while, at later times when secular evolution takes place, it has a stabilizing effect.

The second way of studying bar formation consists in addressing the emergence of bars in fully cosmological simulations of the formation of spiral galaxies (Scannapieco & Athanassoula, 2012; Kraljic et al., 2012; Okamoto, 2013; Guedes et al., 2013; Okamoto et al., 2015; Goz et al., 2015). The obvious advantage of this approach, of a much more realistic representation of gravitational forces within a non idealized DM halo, is balanced by the difficulty in obtaining a realistic disk galaxy in this context. This is where the sub-resolution modeling of stellar feedback becomes crucial (see Section 2.1).

Scannapieco & Athanassoula (2012), using the version of GADGET (Springel, 2005) described in Scannapieco et al. (2006), found long and strong bars in two simulated galaxies; in particular the strengths, lengths and projected density profiles of the bars were found within the range of values given in the observations of Gadotti (2011). Kraljic et al. (2012), using the Eulerian code RAMSES, studied the evolution of galactic bars in a sample of 33 zoomed-in cosmological halos. They found that after $z \approx 1$ almost 80 per cent of spirals galaxies host bars and they suggested that the epoch of bar formation starts from the late *secular* phase and contributes to the growth of pseudobulges, even if the bulge mass budget remains dominated by the contribution of mergers. Furthermore, most of the bars formed at $z \lesssim 1$ persists up to $z = 0$, while early bars at $z > 1$ often disappear and reform several times. Okamoto (2013) analyzed two simulations of disk galaxies with disky

pseudobulges (Sersic index $n < 2$), one of which presents a strong bar and a *boxy-bulge*. They concluded that, at variance with the standard picture, the main channel of pseudobulge formation is high-redshift starbursts and not the secular evolution of the disk, although this contributes to it in a non-negligible way. Guedes et al. (2013) used their Eris simulation to investigate the interplay between a stellar bar and the formation and evolution of a pseudobulge. They found, again at variance with the standard picture, that the bulk of mass in their pseudobulge forms early ($z \sim 4$), fast (~ 2 Gyr) and in situ, starting from a bar instability triggered by tidal interactions with a passing satellite. The bar is destroyed ($z \sim 3$) by several minor mergers, then reforms later ($z \sim 2$), again triggered by tidal interactions, but the redistribution of angular momentum within stars and gas, driven to the center by the bar itself at $z \sim 1$, leads to the gradual breakup of the bar structure. Recently Okamoto et al. (2015) studied the evolution of two bars formed in cosmological Milky Way-sized halos. As commonly found in idealized simulations, the rotation speed of the stronger bar was found to decrease with time by transferring its angular momentum to the dark matter halo, while other behaviours, such as oscillations of pattern speed, were more peculiar to the cosmological case. The weaker bar was found to slow down, while its amplitude was staying constant. The authors pointed out that the main difference between idealized and cosmological simulations is the inclusion of energy and mass released from stellar populations, which leads to a different central density structure.

3.2 Simulations

The main properties of simulations are reported in this Section, while all details are discussed in Section 2.3.

The two sets of ICs are resimulations of DM halos of mass $\sim 3 \times 10^{12}$ $M_\odot$ (GA) and $\sim 2 \times 10^{12}$ $M_\odot$ (AqC), with quiet merger history since $z \sim 2$ so as to avoid the risk of late-time major mergers that can severely damage or destroy the disks. As a matter of fact, both galaxies happen to suffer a minor merger of mass ratio of order 1 : 50 (GA) and 1 : 30 (AqC) at $z \sim 0.5$. For both sets of ICs two resolution levels are used with initial gas particle masses of $\sim 2 \times 10^6$ $M_\odot$ (GA1 and AqC6) and $\sim 3 \times 10^5$ $M_\odot$ (GA2 and AqC5). Plummer-equivalent softening at $z < 6$ is set, for the two resolutions, to 0.65 and 0.325 kpc/h in physical coordinates, at higher redshift it is kept fixed in comoving coordinates.

Table 3.1 reports the main properties of the four sets of ICs, together with the main properties of their central galaxies at $z = 0$. Simulations were post-processed

Simulation	$\epsilon_{\rm Pl}$ (kpc/h)	M_{gas} ($M_\odot$/h)	M_{star} ($M_\odot$/h)	N_{star}	$R_{\rm gal}$ (kpc)	M_{bulge} ($M_\odot$)	M_{disk} ($M_\odot$)	B/T
GA2	0.325	$3.0 \cdot 10^5$	$7.5 \cdot 10^4$	1154243	29.98	$1.4 \cdot 10^{10}$	$8.8 \cdot 10^{10}$	0.20
GA1	0.65	$2.8 \cdot 10^6$	$7.0 \cdot 10^5$	146196	30.37	$2.0 \cdot 10^{10}$	$1.1 \cdot 10^{11}$	0.22
AqC5	0.325	$3.0 \cdot 10^5$	$7.5 \cdot 10^4$	803889	23.82	$1.1 \cdot 10^{10}$	$5.7 \cdot 10^{10}$	0.23
AqC6	0.65	$2.4 \cdot 10^6$	$6.0 \cdot 10^5$	111989	24.15	$1.4 \cdot 10^{10}$	$6.3 \cdot 10^{10}$	0.24

Table 3.1: Basic characteristics of the different simulations. Column 1: simulation name; column 2: Plummer-equivalent softening length for gravitational forces, fixed in physical coordinates below $z = 6$ and in comoving coordinates at higher redshift; column 3: mass of the gas particles; column 4: mass of the star particles; column 5: number of star particles within $R_{\rm gal} = R_{\rm vir}/10$; column 6: virial radius $R_{\rm vir}/10$; column 7: stellar bulge mass at $z = 0$; column 8: stellar disk mass at $z = 0$; column 9: bulge-over-total stellar mass ratio at $z = 0$.

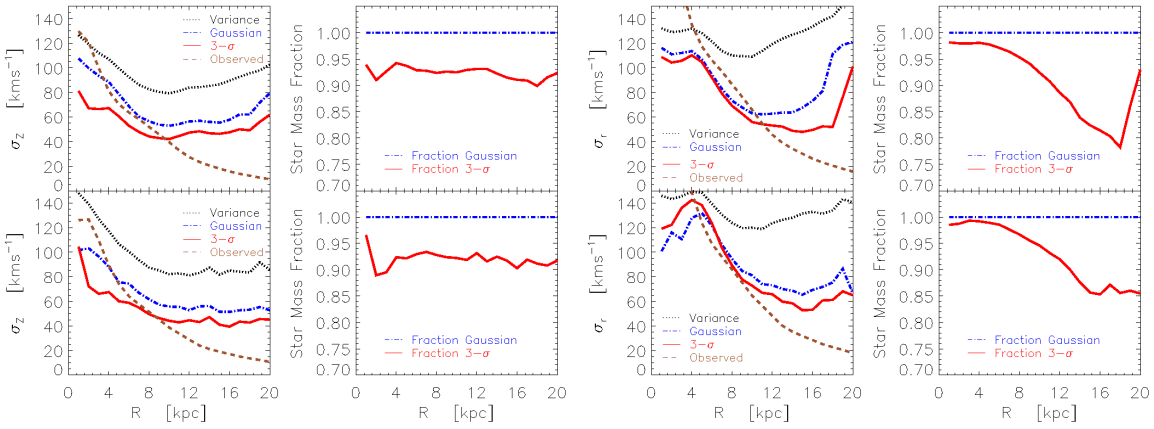

Figure 3.1: Vertical velocity dispersion σ_Z and σ_r, and fractions of mass used to compute the relative dispersion; the variance and Gaussian fit methods use all particles, so for these the latter quantity is unity, while the $3-\sigma$ rejection method excludes particles with large velocities and in this case the latter quantity gives the fraction of mass that has not been excluded. The upper figures give results for GA2, the lower figures for GA1. The left pair of panels gives results for σ_Z, the right pair for σ_r. Dotted black, dot-dashed blue, continuous red and dashed brown lines give respectively the r.m.s, Gaussian, $3-\sigma$ rejection and observation-oriented estimates of velocity dispersion.

with a standard Friends-of-Friends (FoF) algorithm to select the main halo of the high-resolution region and with the substructure-finding code SubFind (Springel et al., 2001) to select satellites. The galaxy is assumed to be constituted by stars and cold ($T < 10^5$ K) or multi-phase gas particles, hereafter called "galaxy particles". The galaxy was first identified as the object laying within 1/10 of the virial radius $R_{\rm vir}$, centred on the centre of mass of the FoF halo, then the galaxy position was refined by computing the centre of mass of galaxy particles lying within 8 kpc (a distance at which it is unlikely to find satellite galaxies) and by iterating the computation with the new centre until convergence within 1 pc was reached. This position is very similar to the centre of the main substructure of the FoF halo, computed by SubFind using the position of the most bound particle. The reference frame was then aligned with the inertia tensor of galaxy particles, with the Z-axis[2] along the eigenvector corresponding to the largest eigenvalue and in the direction so as to have a positive scalar product with the angular momentum; the other two axes were aligned with the other eigenvectors so as to preserve the property $\hat{X} \times \hat{Y} = \hat{Z}$. Whenever a significant disk is present, the angular momentum of the galaxy particles within $R_{\rm gal} = R_{\rm vir}/10$ is always very well aligned, within less than one degree, with the Z-axis.

3.3 The GA1 and GA2 galaxies

In this Section, the GA galaxies obtained at the two resolution levels are studied, GA1 (lower resolution) and GA2 (higher resolution). Both simulations are shown to address the stability of result with respect to resolution.

3.3.1 The vertical structure of the disk

The relatively high values of the force softening used in these simulations do not let to resolve the vertical structure of the stellar thin disk. Nevertheless the kinematic state of the disk is relevant in the study of disk instabilities, as it is well known that kinematically a hot disk is more stable than a cold one (see, e.g., the analysis based on the Toomre parameter presented below). From this point of view, it is a better choice to address the distribution of stellar velocities in place of stellar positions. Indeed, the force exerted by a planar distribution of mass depends mostly on its mass surface density, a quantity that is independent of disk scale height, so

[2] In this Chapter the small letter z is used to denote redshift and the capital letter Z to denote the spatial vertical axis.

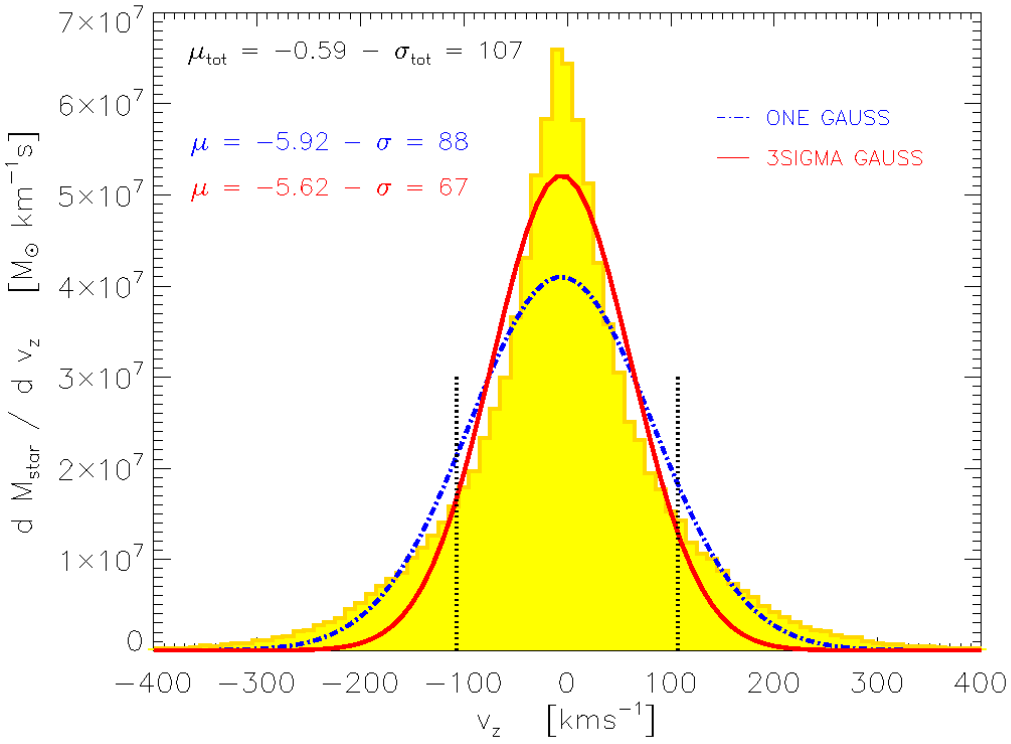

Figure 3.2: Mass-weighted histogram of stellar velocities for GA2 in the radial bin from 3 to 4 kpc for the GA2 galaxy at $z = 0$. Measured average and r.m.s are $\mu_{tot} = -0.59$ km/s and $\sigma_{tot} = 107$ km/s, the r.m.s. is denoted by two dotted black vertical lines. The resulting fits (top left of the panel) for averages and dispersion with the Gaussian fit (dot-dashed blue line) and 3-σ rejection (continuous red line) methods are reported in the figure with the same colour as the corresponding line, in km/s.

the velocity dispersion of stars is expected to be more convergent with resolution than the scale height itself. Below, the velocity dispersion is computed both in the vertical, Z-direction and in the radial, r-direction. The latter enters in the Toomre stability criterion.

To compute stellar velocity dispersion, all stars within $R_{\rm gal}$ from the centre are used, so at each polar radius there is a mix of stars from the disk and from the stellar halo[3]. Assuming that the thin disk is the most massive component and that its vertical or radial velocities are roughly Gaussian distributed, the (mass-weighted) variance of disk stars will be severely affected by the minor component with a higher velocity dispersion. Figure 3.1 shows, for both GA2 (upper panels) and GA1 (lower panels), the mass-weighted root mean square (r.m.s.) of vertical (left panels) and radial (right panels) velocity dispersion of all stars as black lines. Figure 3.2 reports, for the radial bin from 3 to 4 kpc, the mass-weighted histogram of vertical velocities in which black vertical lines mark the r.m.s. of the distribution, that is clearly not representative of the width of the main component.

To improve this measure two options are tested: a Gaussian fit of the distribution of velocities in each bin of polar radius (blue lines in the two Figures) and a Gaussian fit with recursive rejection of $> 3-\sigma$ interlopers, performed until convergence is reached (red lines in the two Figures). Since the $3-\sigma$ rejection method implies that some mass is discarded, Figure 3.1 reports on the right of velocity profiles the fraction of mass that is used to compute them, as a function of radial distance. The Gaussian fit method uses all the mass, so it is reported as a line at unity. It can be noticed that, for both velocity components, the Gaussian fit method gives significantly lower velocity dispersion, while a further suppression is obtained with the $3-\sigma$ rejection method. The predicted distributions are shown in Figure 3.2, again as blue and red lines. From this figure, it is clear that the $3-\sigma$ rejection method gives the most faithful representation of the width of the main mass component, at the modest cost of excluding less than 10 per cent of mass in the case of vertical velocity dispersion σ_Z and an amount ranging from 1-2 per cent at small radii to $\sim$20 per cent at large distances in the case of the radial velocity dispersion σ_r. Also the velocity distributions is fitted with two Gaussians, but the results were unstable and for this reason this method is dropped.

Figure 3.1 compares these estimates of σ_Z and σ_r with observational estimates. Leroy et al. (2008) computed the Toomre Q parameter for the THINGS sample of local galaxies. Since direct measurements of stellar velocity dispersion are *"ex-*

[3]Some contribution may come from a thick disk component, whose study is however hampered by the relatively poor softening used and is anyway beyond the interests of the present work.

tremely scarce", in their Appendix B they assumed that the stellar scale height $h_\star$ is constant throughout the disk, that this same quantity is related to the disk scale radius $r_\star$ through the observed relation $h_\star = r_\star/7.3$ and that stars are isothermal in the Z-direction. As a result:

$$\sigma_Z = \sqrt{\Sigma_\star \frac{2\pi G r_\star}{7.3}}, \tag{3.1}$$

where $\Sigma_\star$ is the disk stellar surface density. For the radial velocity dispersion, the same authors assumed that $0.6\sigma_r = \sigma_Z$. For the GA1 and GA2 disks disk scale length $r_* = 3.93$ and 4.45 kpc are used as estimated in Murante et al. (2015) by fitting the radial profile of stellar mass surface density. These estimates are shown in the Figure 3.1 as brown lines. As a result, at $r < 10$ kpc both the Gaussian and the $3-\sigma$ rejection methods yield velocity dispersions that are broadly compatible with those that would be expected in an observed galaxy. In more detail, GA1 shows a marginally hotter disk, especially as far as radial motions are concerned, but these are influenced by the radial streaming motions due to the bar itself, that will be quantified below. The outer parts of the disk are significantly hotter than this estimate, at large distances, disk scale lengths start to increase, so this discrepancy could be not very significant.

This analysis demonstrates that, despite the relatively large softenings used, the kinematic state of disks is compatible with the observations, at least in the inner regions that are subject to bar instability. However, these velocity dispersions are severely affected by numerics and the marginally hotter GA1 disk clearly supports this warning. Murante et al. (2015) presented results of simulations of the GA1 obtained with different softenings and showed that, while lower values of the softening result in higher stellar velocity dispersion (simply measured there as r.m.s.), convergence was not yet fully achieved for the value of softening used here. Therefore these velocity dispersions are very likely influenced by 2-body scattering of star particles, but this influence does not lead to unrealistic thickening of the disk.

3.3.2 Morphology and circularities

Density maps of the two galaxies are given in Figure 2.1. Figure 3.3 shows maps of stellar mass surface density for the central part of the two simulated galaxies at redshift 0. Each map spans $\pm$12.5 kpc in each dimension. The figure shows, on the upper panels, the maps of the GA2 simulation in the XY-, XZ- and YZ-plane, while the lower panels show the same maps for the GA1 simulation. The colour coding represents the Log surface density and values are given in the colour bar. The

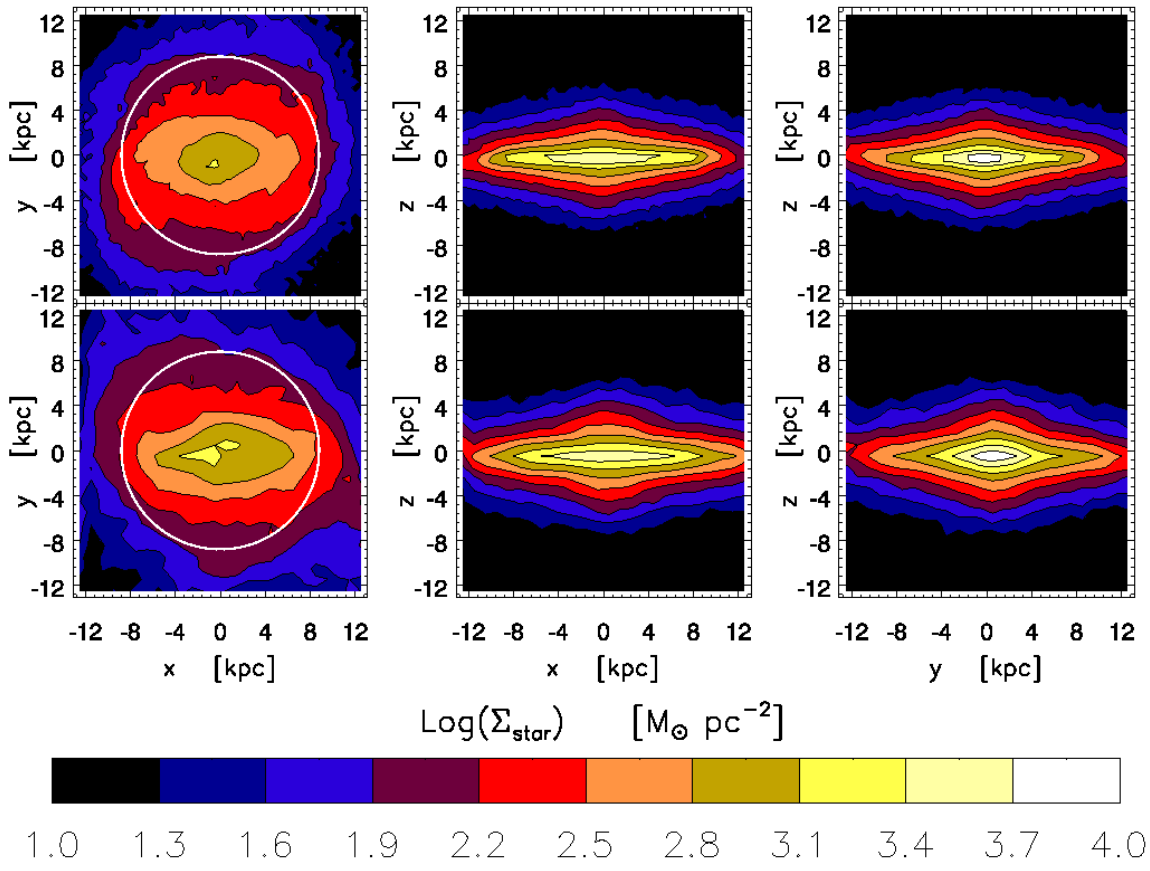

Figure 3.3: Projected stellar maps of the GA2 (upper panels) and GA1 (lower panels) galaxies at $z = 0$ in boxes centred on the galaxy that extend 25 kpc across. Colour coding follows the Log of stellar mass surface density as indicated by the colour bar. The three columns show projections in the face-on XY-plane (left), edge-on XZ-plane (middle) and edge-on YZ-plane (right). The white circle marks the bar length $L_{\rm bar}$.

maps were obtained by projecting all star particles within $R_{\rm gal}$ and smoothing the resulting surface densities on a grid, whose pixel size is set equal to the softening length in both cases. In both simulations the isodensity contours in the face-on map are not round but present a flattened structure; the bar is aligned along the X-axis. The edge-on maps sample the bar along its long (XZ projection) and short (YZ projection) axes and, as expected, the isodensity contours are flatter when the disk particle distribution is seen along the major bar axis.

The circularity of a star particle is here defined following the method proposed by Scannapieco et al. (2009) (details in Section 2.4), so that:

$$\epsilon = j_Z / j_{\rm circ} \tag{3.2}$$

Figure 3.4 shows 2D histograms of circularities as a function of polar radius r along the galaxy disks, for both galaxies at six different times. A disk is expected to be visible as a narrow distribution around $\epsilon \sim 1$, while a component scattering around $\epsilon \sim 0$ will be identified as a bulge or a spherical halo, depending on r. The 2D histograms are shown as a map of mass per unit bin size (kpc and circularity in the two dimensions), with isodensity contours showing the preferential locus of star particles. For each row, the upper and lower panels give the histogram for GA2 and GA1 respectively. Starting from the upper left panels, the two rows show results for $z = 1.5$, 1, 0.7, 0.5, 0.2, 0. These times are chosen to follow the main phases of the formation of the bar, as it will be explained below. This figure allows to monitor the formation of the disk in the two simulations. The first point that is worth noting is that the circularity histograms are notably independent of resolution, thus GA1 and GA2 will be described together. At $z = 1.5$ the galaxy is mostly a spheroid, while a disk has started to form at $r < 6$ kpc. A clear and thin disk structure is visible at $z = 1$. The structure is broader at $z < 0.6$, where tidal interactions with a satellite of mass $M_\star = 1.2 \times 10^9$ $M_\odot$, that culminate with a minor merger at $z = 0.35$, are heating the disk. Beyond $z = 0.2$, the region at intermediate circularities, $\epsilon \sim 0.5$ and at $1 < r < 5$ kpc, starts to be populated, especially for the GA1 galaxy. Because stars in the bar have large systematic radial motions, this is a sign of the emergence of a bar structure.

The fraction of stellar mass as a function of circularity, i.e the projection in radius of the circularity histograms of Figure 3.4, is shown on the left panel of Figure 2.2 for $z = 0$. B/T values at $z = 0$ are reported in Table 3.1.

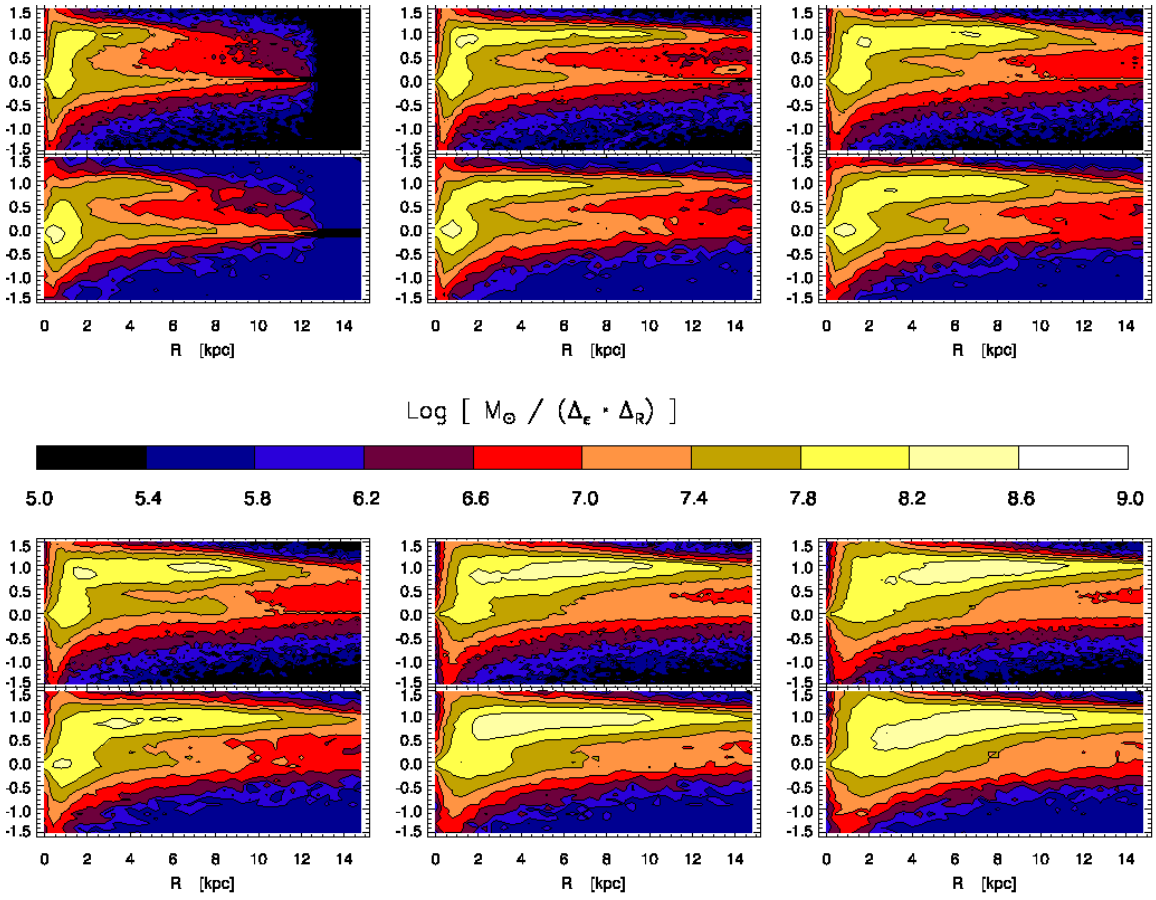

Figure 3.4: 2D histograms of circularity (Eq. 3.2) and polar radius, at six different times. In each panel, colour coding refers to the Log of stellar mass per unit bin area as indicated by the colour bar, the black lines are the corresponding isodensity contours. Each pair of panels gives results for the GA2 (upper panels) and GA1 (lower panels) galaxies. From the upper left panels, redshifts are $z = 1.5$, 1, 0.7, 0.5, 0.2, 0.

3.3.3 Kinematics of the central region

Here the kinematics of the central region of the galaxy, that hosts both bar and bulge, is quantified. It will be demonstrated in Section 3.3.5 that in GA1 as well as in GA2 a bar appears only towards the end of the simulation, starting from $z = 0.2$, so here only the galaxy at $z = 0$ is analysed.

As suggested by Okamoto (2013), the expected kinematic signature of a bar is a higher value of line-of-sight velocities with respect to vertical ones. Following that paper, Figure 3.5 shows the velocity dispersion σ_{los} of stars along the *line of sight* (the Y axis in the density maps; red lines in the figure) and along the vertical direction σ_Z (Z axis; blue lines in the figure). Velocity dispersions were computed with the 3-σ rejection method explained in Section 3.3.1.

While vertical velocity dispersion reaches values of $\sim 50 - 60$ km/s with a very flat dependence on distance from the centre, radial velocity dispersion takes higher values. In the GA2 case, radial velocities peak at $\sim$ 100 km/s, twice the vertical ones, while in the GA1 case an even higher peak (130 km/s) is present. In both cases, a small dip at the galaxy centre is present.

A pronounced, radial streaming pattern is expected in non-axisymmetric potentials like that of a stellar bar (e.g. Bosma, 1978). Figure 3.5 shows 2D maps, in the face-on XY plane, of average radial velocities computed on the same size and grid as in Figure 3.3. To minimize contamination from halo motions, median velocities are computed only for stars lying within 1 kpc from the midplane. As shown in the colour bar below, blue/black colours denote negative velocities, while yellow/while colours denote positive velocities. A symmetric and squared pattern of streaming motions is evident in both cases, with higher velocities for the GA1 galaxy. At larger distances from the centre, the velocity pattern connected to the spiral arms is very visible for GA2. The conclusion is that the kinematics of stars in the inner regions of these galaxies is dominated by streaming motions as expected.

3.3.4 Quantification of bar strength and length

Following the analysis of Scannapieco & Athanassoula (2012) and Kraljic et al. (2012) the strength of the bar is quantified. This is based on the Fourier transform of the surface density of the disk:

$$\Sigma(r,\theta) = \frac{a_0(r)}{2} + \sum_{n=1}^{\infty} [a_n(r)\cos(n\theta) + b_n(r)\sin(n\theta)] \tag{3.3}$$

where r is the polar radius and θ the azimuthal position on the disk plane. To

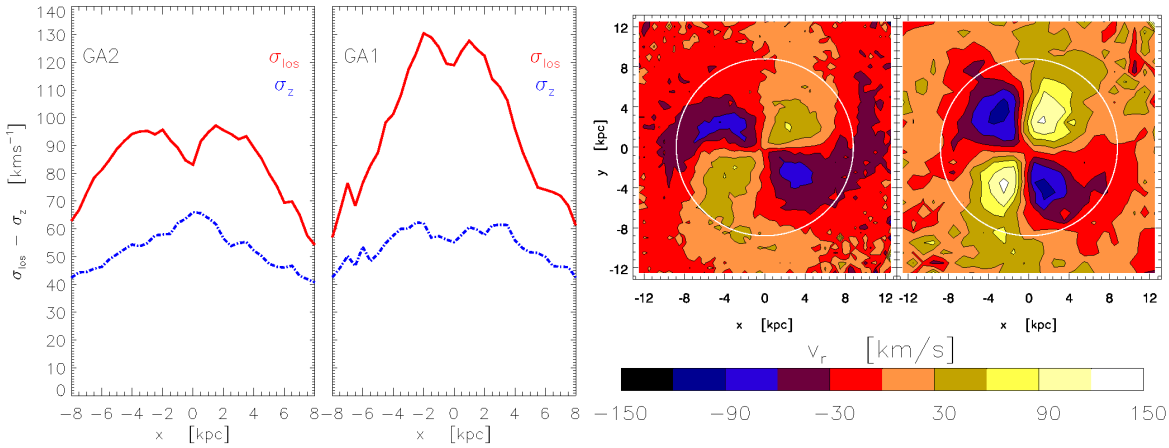

Figure 3.5: Left panel: profiles of line-of-sight velocity dispersion σ_{los} (continuous red lines) and vertical velocity dispersion σ_Z (dot-dashed blue lines) of stars at $z = 0$, when the galaxy (GA2 on the left and GA1 on the right) is observed edge-on in the direction perpendicular to the bar main axis. Right panel: radial velocity maps on face-on views (XY projection) of the two simulated GA2 (on the left) and GA1 (on the right) galaxies. The boxes are 25 kpc across. Colour coding follows the median radial velocity of stars within 1 kpc from the midplane, as indicated by the colour bar. The white circle marks the bar length $L_{\rm bar}$.

perform the transform, particles are radially binned and the following coefficients are computed for each bin:

$$a_n(r) = \frac{1}{\pi}\int_0^{2\pi} \Sigma(r)\cos(n\theta)d\theta\,, (n \geq 0) \tag{3.4}$$

$$b_n(r) = \frac{1}{\pi}\int_0^{2\pi} \Sigma(r)\sin(n\theta)d\theta\,, (n > 0) \tag{3.5}$$

where Σ is the surface density of the stellar disk. The Fourier amplitude of each mode is defined as:

$$C_n(r) = \sqrt{a_n^2(r) + b_n^2(r)}\,, \quad C_0(r) = a_0(r)/2 \tag{3.6}$$

The presence of a bar is revealed by a significant value of the C_2 component, that is higher than even components of further order.

Figure 3.6 shows the amplitudes of the first four even components, normalized to the $n = 0$ one, C_n/C_0. In both cases the C_2 component is significantly higher than the other components; for the GA2 it peaks at a value of 0.4 at 6 kpc, with a broad plateau starting from 2 kpc. GA1 shows a narrower plateau between 5 and 7 kpc, reaching a higher value of 0.7. This confirms that, consistently with the higher radial velocities, the bar in the GA1 simulation is stronger than in GA2. Higher order moments show smaller and smaller values in both cases; they peak at different scales and this is a sign that the bar is not perfectly symmetric. Odd modes have small values and this is again consistent with what is expected from a bar-like pattern.

These results are broadly consistent with observations that show a variety of radial Fourier profiles of bars, ranging from simple symmetric profiles, that can be represented by two overlapping Gaussian components, to more complex curves. Since C_n/C_0 value spans between 0.4 and 0.8 (Elmegreen & Elmegreen, 1985; Ohta et al., 1990; Ohta, 1996; Aguerri et al., 1998, 2003; Buta et al., 2006), both GA galaxies would be classified as barred. Moreover, the amplitudes of GA2 show relatively high values also at large radii, where the signature of streaming motions (Figure 3.5) is already lost but prominent spiral arms are present. This shows a limit of the analysis based simply on Fourier amplitudes, where spiral arms give weak signatures that can be confused with those of bars.

To evaluate the length of the bar, among many published methods (e.g. Combes & Elmegreen, 1993; Debattista & Sellwood, 2000; Michel-Dansac & Wozniak, 2006), the one proposed by Athanassoula & Misiriotis (2002) is used. This is based on

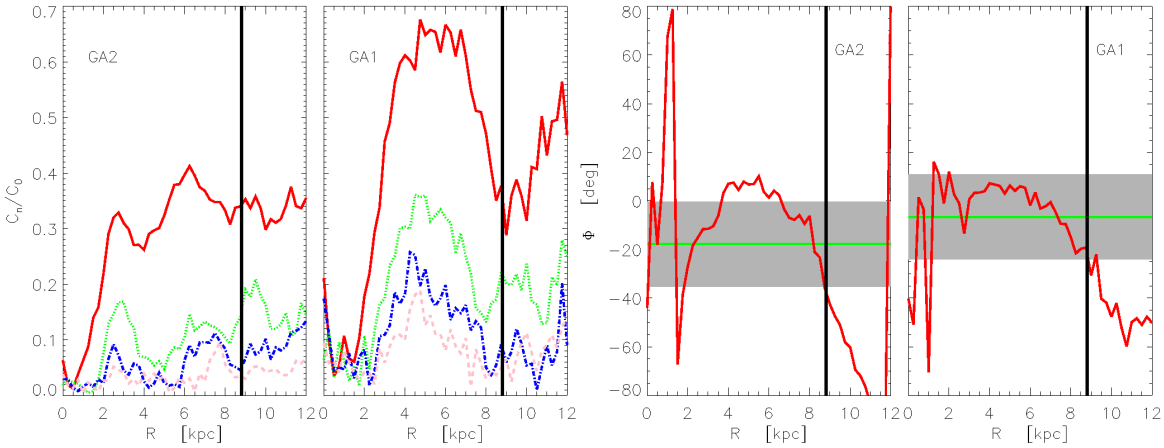

Figure 3.6: Left panel: Fourier amplitudes C_n/C_0 for even components $n = 2$ (continuous red line), $n = 4$ (dotted green line), $n = 6$ (dot-dashed blue line), $n = 8$ (dashed pink line) for stars of GA2 (on the left) and GA1 (on the right). The black lines mark the bar length $L_{\rm bar}$ kpc. Right panel: phase of stellar distribution for GA2 (on the left) and GA1 (on the right). Red lines report the phase Φ of the $n = 2$ mode as a function of radius, the green horizontal line marks the overall phase $\Phi_{\rm disk}$ of the disk within 12.5 kpc. The shaded area gives the allowed range of $\Phi_{\rm disk} \pm \arcsin(0.3)$. The black lines correspond to the bar length $L_{\rm bar}$.

the fact that, for an ideal bar, the phase of the $m = 2$ mode should be constant as long as the probed scale is within the bar, while beyond it the phase is expected to fluctuate due to spiral arms. This method is implemented by calculating, for each radial bin, the phase Φ of the $m = 2$ mode as:

$$\Phi(r) = \arctan\left(b_2(r)/a_2(r)\right) \tag{3.7}$$

The average phase is computed applying Equations 3.4 and 3.5 to all star particles with $r < 12.5$ kpc, then computing Φ_{disk} as in Equation 3.7. The result is reported on the right panel of Figure 3.6 as a red line, while the green one corresponds to the average phase. The bar length is defined as the largest radius where these two last quantities differ less than a certain value. As discussed in Athanassoula & Misiriotis (2002), the choice of the constant is somehow arbitrary. In that paper the authors suggested a range of $\pm\arcsin(0.3)$, while tighter ranges were used by other authors (e.g. Kraljic et al. (2012) used $\pm\arcsin(0.1)$). The GA2 bar is caught in an early development phase (see Section 3.3.5) and it is still weak, so the more permissive criterion of $\pm\arcsin(0.3)$ is adopted. For both GA2 (left panel) and GA1 (right panel) the phase fluctuates in the inner 1-2 kpc, then is relatively stable for several kpc and goes out of the shaded region at 8.8 kpc in both cases. It must be noticed that the phase of GA2 gets marginally above the shaded region from 4 to 6 kpc, but given the arbitrariness of the used value this minor issue is neglected. $L_{\text{bar}} = 8.8$ kpc is taken as a measure of bar length (see the vertical black line in the Figure) and notice that it is remarkably independent of resolution.

Another possible method proposed by Athanassoula & Misiriotis (2002) to evaluate the length of the bar is based on the scale at which the Fourier coefficient C_2/C_0 goes to zero. Indeed, for an ideal bar on an axisymmetric disk, this coefficient should show a plateau and then drop quickly beyond the bar. In a more realistic context one should define a threshold with respect to the maximum and define the bar length as the radius at which the amplitude of the Fourier mode gets below it. In Figure 3.6 the vertical black lines denote the bar length as estimated by the phase method. In the GA1 case, using a drop of the coefficient by a factor of two, it would give almost the same bar length, while, as noticed above, in the GA2 case the spiral pattern gives a signal comparable to that of the bar. L_{bar} is reported as a circle also in Figures 3.3 and 3.5 and in both cases the estimated bar length separates the inner region, dominated by flattened isodensity contours and streaming motions, from the outer region dominated by spiral arms. This lets to conclude that the phase method gives a fair estimate of L_{bar}.

Compared with ~ 300 observed galaxies presented in Gadotti (2011), L_{bar} value

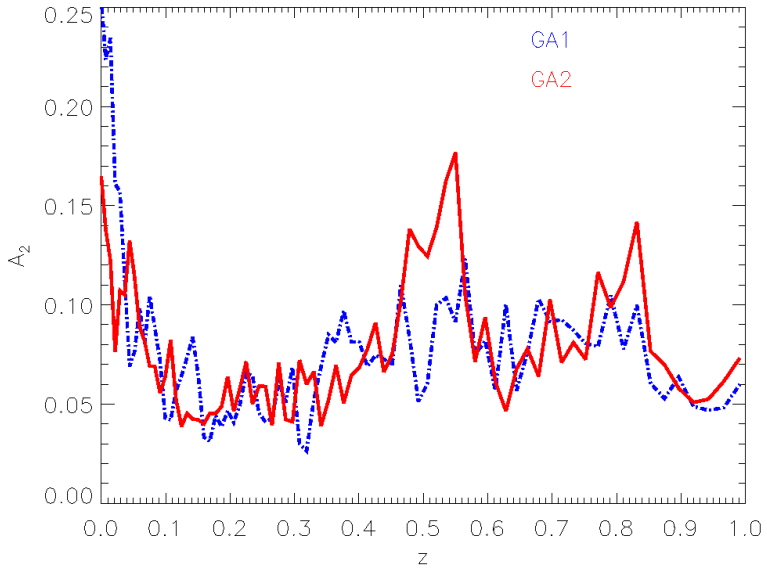

Figure 3.7: Relative mode strength A_2 as a function of redshift for the GA1 (dot-dashed blue) and GA2 (continuous red) galaxies, starting from $z = 1$.

is at the high end of the distribution given in this observational work, but well compatible with it.

3.3.5 The origin of bar instability

To estimate the time at which the bar is triggered, the growth of the bar strength is quantified by computing the so-called relative mode strength A_2. This is the ratio of the integrals, weighted by area, of the coefficients C_2 and C_0 over the bar length $L_{\rm bar}$, taking into account its value estimated by the previous method in Section 3.3.4.

$$A_2 = \frac{\int_0^{L_{\rm bar}} C_2(R) R dR}{\int_0^{L_{\rm bar}} C_0(R) R dR} \tag{3.8}$$

This calculation is performed for all simulation outputs since $z = 1$, when the disk is still young and both GA1 and GA2 show no sign of a bar. Figure 3.7 shows the evolution of A_2 with redshift for GA2 (red line) and GA1 (blue line). At $z < 0.7$, two different episodes of growth of A_2 are visible at z from 0.6 to 0.45 (at

least for GA2) and at $z < 0.2$. The episode at $z \sim 0.5$ is due to a minor merger already mentioned above. A satellite of stellar mass 1.25×10^9 $M_\odot$ in GA2 and 1.35×10^9 $M_\odot$ in GA1 performs close orbits around the main galaxy. For GA2, the closest encounter is found at $z = 0.57$, where the distance of the satellite from the galaxy centre is 12 kpc. The stellar mass ratio is 1 : 50 at the beginning of the interaction, slowly decreasing because of the continuous growth of the stellar mass of the central galaxy. Two more close encounters are found before the satellite is tidally disrupted into the halo of the main galaxy ($z = 0.35$). These interactions trigger non-axisymmetric perturbations, so that GA2 acquires A_2 values equivalent to those at $z = 0$. During this period the disk is noticeably disturbed and a bar-like morphology is visible only in one output (the time interval between outputs being ~ 100 Myr). In the left panel of Figure 3.8 a face-on density map of GA2 at $z = 0.55$ (just after the nearest encounter) is shown, analogous to Figure 3.3, and in the right panels the C_2/C_0 and phase diagrams, analogous to Figures 3.6. While disk morphology is clearly disturbed, the C_2 coefficient takes on significant values especially at large radii, while the phase analysis reveals that the structure does not behave as a bar. So the high value of A_2 is determined by the outer spiral arms more than by a central bar. This transient lasts from the first near passage of the satellite to its destruction, ~ 700 Myr in total, corresponding to $\sim 3 - 4$ revolutions of the disk. Then the A_2 coefficient quickly returns to ~ 0.1 and keeps decreasing slowly with time.

The history of GA1 is similar. In this case the satellite is never found at distances smaller than 20 kpc so, while the mass ratio is very similar, the tidal disturbance is smaller and the jump in A_2 is much less evident.

The A_2 coefficients start to grow for both galaxies after $z = 0.2$, ~ 2 Gyr after the minor merger has ended (i.e. after ~ 10 disk revolutions). In this period the instability grows at an accelerating pace. The growth has a markedly different time evolution with respect to the instability episode triggered by the minor merger. This suggests that the bar formation is due to the secular evolution of the disk. Moreover, the nice coincidence of the timing of bar growth at the two resolutions and the similar length of the resulting bar suggest that this instability is physical and not purely numerical, while the difference in bar strength is explained by the quick raise of the bar instability, so the GA1 at $z = 0$ happens to be caught at a higher A_2 value.

To investigate the physical cause of this bar instability, there are two criteria commonly adopted in literature to assess when a disk is unstable to bar formation. The first one, proposed by Efstathiou et al. (1982) and based on N-body simulations, predicts that the regulator of bar instability is the contribution of the disk to the

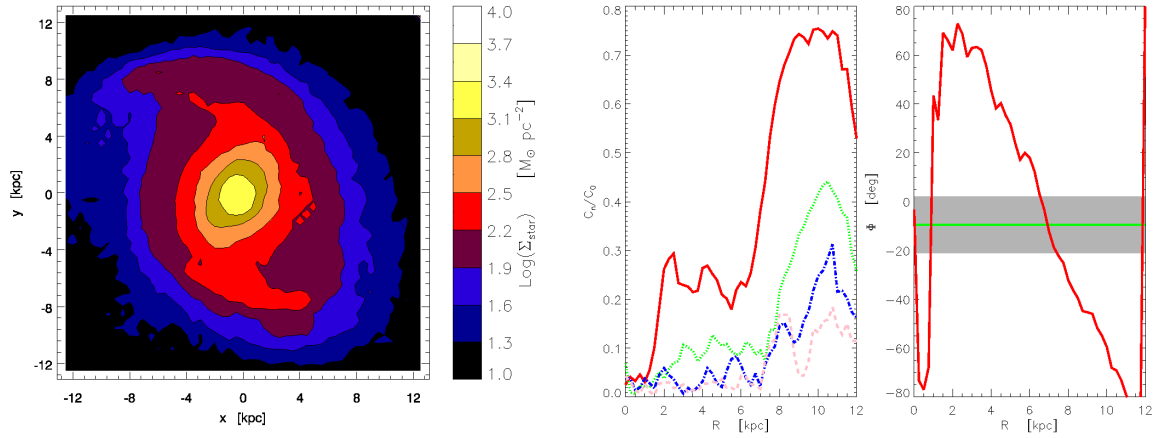

Figure 3.8: Stellar mass surface density maps (left panels), Fourier amplitudes (middle panel) and phase (right panel) for the GA2 galaxy at $z = 0.55$. Symbols and colours are like in Figures 3.3, 3.6.

rotation curve:

$$\Upsilon_{\rm disk} = \frac{V_{\rm disk}}{\sqrt{GM_{\rm disk}/R_{\rm disk}}}, \tag{3.9}$$

where, $M_{\rm disk}$, $R_{\rm disk}$ and $V_{\rm disk}$ are disk mass, radius and velocity respectively. Bar instability takes place whenever $\Upsilon_{\rm disk} \leq \epsilon_{\rm lim} \simeq 1$. To calculate this quantity, for $M_{\rm disk}$ is used the mass of galaxy particles within 10 kpc and with circularities $0.7 < \epsilon < 1.3$, for $R_{\rm disk}$ the half-mass radius of the same particles, and for $V_{\rm disk}$ the maximum of the galaxy rotation curve within 10 kpc ($V_{\rm disk}$ depends upon the total mass, i.e. baryons+DM). Results do not change if a different aperture is employed to define disk mass and radius. Left panel of Figure 3.9 shows the quantity $\Upsilon_{\rm disk}$ as a function of redshift, in both cases computed either using only star particles (blue lines) or all galaxy particles (red line). As usual, the left panel gives results for GA2, the right panel for GA1. The shaded regions denote values lower than a threshold $\epsilon_{\rm lim} = 1.1$ (Efstathiou et al., 1982) applying to a pure stellar disk, while a lower threshold of 0.9 has been suggested to apply to gas disks. As a result, although Y decreases with time, it takes on values in any case above the suggested threshold.

The local stability of a self-gravitating disk to radial perturbations is usually evaluated using the Toomre (1964) stability criterion. Though Toomre-unstable disks are expected to fragment into self-bound knots, a mildly unstable disk may

develop a bar (Julian & Toomre, 1966). Furthermore Athanassoula & Sellwood (1986) proposed that $Q > 2$ might be a general criterion against bar formation, since for these high Q values collective density waves become very weak and growth rates of all instabilities are reduced.

To compute the Toomre parameter of a two component disk (with stars and gas), as in Monaco et al. (2012), the simplified approach of Wang & Silk (1994), that with high velocity dispersion approximates well the more accurate expression recently proposed by Romeo & Wiegert (2011), is used. Starting from the separated component Q values:

$$Q_*(r) = \frac{\kappa\sigma_r}{3.36G\Sigma_*} \tag{3.10}$$

$$Q_g(r) = \frac{\kappa\sigma_r}{3.36G\Sigma_g} \tag{3.11}$$

where, for each component, $\Sigma(r)$ is its surface density, $\sigma_r(r)$ its radial velocity dispersion and $\kappa(r) = V(r)\sqrt{2 + 2d\ln V/d\ln r}/r$ the epicyclic frequency of the disk. The effective $Q_{\rm tot}(r)$ parameter of the disk is computed as:

$$Q_{\rm tot}(r) \simeq \left(\frac{1}{Q_g} + \frac{1}{Q_*}\right)^{-1} \tag{3.12}$$

Radial velocity dispersion is computed with the $3-\sigma$ rejection method described in Section 3.3.1, using as stellar surface density the one obtained rejecting $> 3-\sigma$ interlopers[4]. In all cases, the gas has a minor impact on $Q_{\rm tot}$. In fact, using Q_* alone would lead to the same conclusions.

Right panel of Figure 3.9 shows $Q_{\rm tot}$ as a function of polar radius at redshift 0, 0.2, 0.6 and 1.0. Left panel of Figure 3.10 shows $\langle Q\rangle$, the average value of $Q_{\rm tot}$ in the scale range from 3 to 8 kpc, computed for all available outputs of the two simulations at $z \leq 1$. In these plots the grey region denotes the $Q < 1$ values of the Toomre parameter where the disk is expected to be unstable. These galaxies are found to be formally stable at $z > 0.3$, but the Toomre parameter steadily decreases with time. From Figure 3.9 it is seen that, at $z = 0.6$, the disk of GA2 gets weakly unstable both at the centre and at ~ 6 kpc. As $z = 0.2$ this second instability region has got wider, while $\langle Q\rangle$ has got below the value of unity since $z \sim 0.3$. The GA1

[4]With respect to the Gaussian fit, the $3-\sigma$ rejection method yields at the same time lower σ_r and lower $\Sigma_\star$ (Figure 3.1) and these corrections compensate in the value of $Q_\star$, that is then very insensitive to the method used.

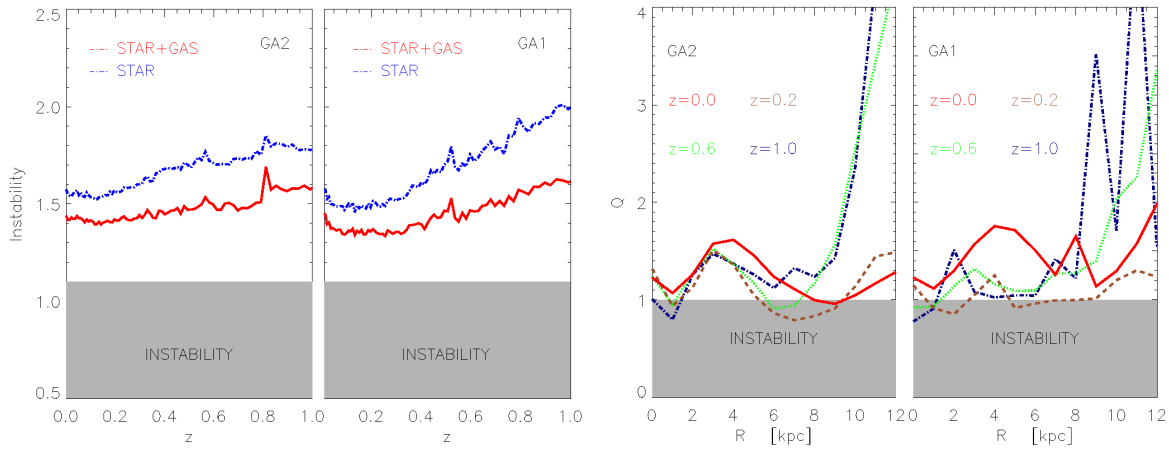

Figure 3.9: Left panel: Y_{disk} as a function of redshift for star particles (dot-dashed blue line) and for all galaxy particles (continuous red line); the shaded area marks the instability region corresponding to $\epsilon_{\text{lim}} = 1.1$. Right panel: Toomre parameter $Q_{tot}(r)$ at $z = 0, 0.2, 0.6, 1.0$ (continuous red, dashed brown, dotted green and dot-dashed blue lines respectively). The shaded areas show the region where disk are formally unstable.

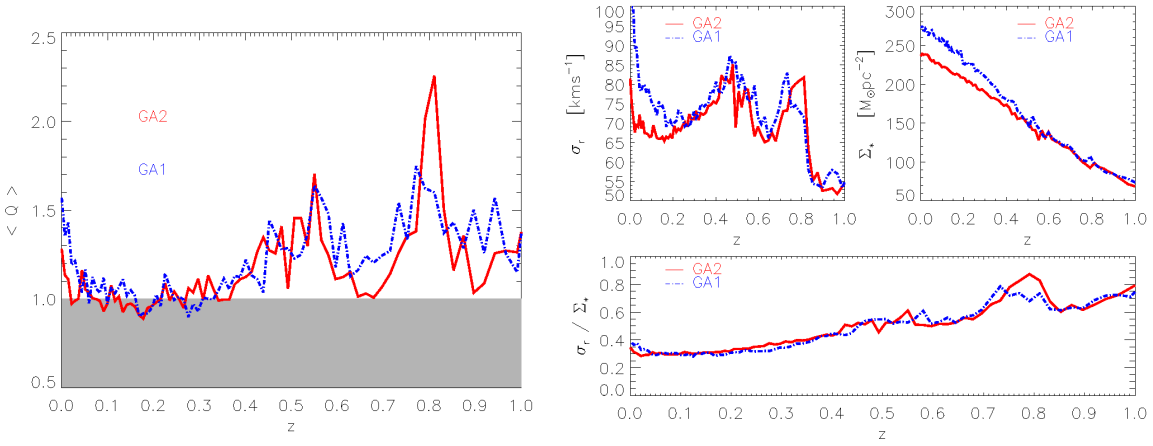

Figure 3.10: Left panel: average value of the Toomre parameter from 3 to 8 kpc, as a function of redshift, for GA1 (dot-dashed blue line) and GA2 (continuous red line). The shaded areas show the region where disks are formally unstable. Right panel: disk radial velocity dispersion (top left panel), stellar disk surface density (top right panel) and their ratio as a function of redshift (bottom panel). All these quantities are averaged from 3 to 8 kpc. Continuous red line for GA2 and dot-dashed blue line for GA1.

galaxy becomes unstable at $r \sim 2$ and 6 kpc only at $z = 0.2$, but the evolution of $\langle Q \rangle$ is very similar to that of GA2. For both galaxies, the rise of the Toomre parameter at later time is due to the raise of σ_r, that is driven by the development of the radial streaming pattern.

Although the detailed behaviour of these galaxies is far from simple, the beginning of the instability roughly coincides with the time when $\langle Q \rangle$ gets lower than the canonical threshold value of 1. Hence the behaviour of bar instability in these galaxies is consistent with the simple hypothesis that a bar is triggered by a secular instability. Assuming the validity of the criterion $\langle Q \rangle < 1$, the tidal disturbance at $z = 0.55$ takes place when the disk is still stable, while disk heating due to tidal interaction leads to an increase in velocity dispersion and therefore in $Q_{\rm tot}$ value. This may explain why the bar-like feature of GA2 is transient.

The reason for the late-time secular decrease of $Q_{\rm tot}$ towards the instability region is mostly due to the accumulation of the disk mass rather than to a variation of disk velocity dispersion. Right panel of Figure 3.10 shows the average disk radial velocity dispersion, stellar surface density and the ratio of the two. All quantities

are evaluated in the range $3 \leq r \leq 8$ kpc and as a function of redshift. The radial velocity dispersion (Figure 3.10) is boosted by the tidal interaction with the satellite and then it decreases before growing at $z \simeq 0.1$ in both GA1 and GA2, while stellar surface densities (also in Figure 3.10) increase always with time. Accordingly, their ratio decreases with time (on the right bottom of Figure 3.10). This demonstrates that the decrease of $Q_{\rm tot}$, that is the most likely cause of the bar, is the accumulation of the disk mass at low redshift, due to the continuous infall of gas into the DM halo.

3.3.6 The role of halo triaxiality

As mentioned in the Section 1.2.4, halo triaxiality is a potential trigger of bar instability. In Curir & Mazzei (1999) and Athanassoula & Misiriotis (2002), model disks were placed into DM halos at a given redshift. As a matter of fact, this implies that the gravitational influence that the formation of the disk has had on the structure of the halo itself is neglected. The impact of the formation of a gaseous disk on the shape of a dark matter halo and its transformation from prolate to oblate in the inner part was already studied in isolated systems by Dubinski (1994), Debattista et al. (2008), in cosmological environment by Kazantzidis et al. (2004), Tissera et al. (2010), Abadi et al. (2010) and more recently by Zemp et al. (2012), Bryan et al. (2013). DeBuhr et al. (2012) inserted live stellar disks inside Milky Way-like dark matter halos from the Aquarius simulations, finding a strong effect on the shapes of the inner halos which evolve to become oblate.

In Murante et al. (2015) it has been shown that, consistently with many other papers (e.g. Governato et al., 2012), the inner slope of the dark matter halo of the GA2 simulation is flatter than the typical $\rho \propto r^{-1}$ slope obtained when particles are collisionless. This is due to the combined action of the adiabatic contraction caused by the formation of the galaxy and the violent expansion due to episodic massive outflows. The same process induces changes in the DM distribution in the region occupied by the galaxy.

To address the influence that the formation of the galaxy has on the inner regions of the DM halo, a simulation of the GA2 has been performed switching off hydrodynamics, cooling and star formation, thus treating both DM and gas particles as collisionless particles; in the following this simulation is called GA2-cless. For the GA2 and GA2-cless simulations the inertia tensor of all DM particles within $R_{\rm gal}$ (30.64 kpc for GA2-cless, 29.98 kpc for GA2) is computed and the ratios among the eigenvalues I_i (with $i = 1, 2, 3$), ranked in decreasing order, are quantified. In GA2-cless is found that $I_1/I_2 = 1.07$, $I_1/I_3 = 1.39$ and $I_2/I_3 = 1.30$, indicating

a roughly prolate shape with significant triaxiality. In GA2, where the DM halo has hosted a forming spiral galaxy, the ratios of eigenvalues are $I_1/I_2 = 1.13$, $I_1/I_3 = 1.14$ and $I_2/I_3 = 1.01$, indicating an oblate and nearly axisymmetric shape. Moreover, the eigenvector corresponding to the largest eigenvalue of the inertia tensor, i.e. to the direction where the halo is flattened, is found to be aligned with the galaxy angular momentum within 4.37°. This alignment lets to infer that the oblate shape is due to the formation of the disk itself.

In conclusion the influence of the triaxiality on disk dynamics should not be addressed without considering, at the same time, the influence that astrophysical processes bringing to disk formation have on the triaxiality of the inner part of the DM halo.

3.4 The Aq5 and Aq6 galaxies

The two AqC simulations show a different behaviour with respect to the GA ones. Figure 3.11 shows the surface density maps and Figure 3.12 shows face-on map of radial velocities, the Fourier coefficients and phases and the evolution of A_2 and $\langle Q \rangle$, the latter being averaged again on $3 < r < 8$ kpc. The higher resolution AqC5 galaxy at $z = 0$ has a bar with properties similar to the one of GA2 (Figure 3.11), visible as an elongation of the isodensity contours, but with a slightly smaller size with respect to the GA galaxies (Figure 3.11). The signature of streaming motions very clearly confirms the visual impression (Figure 3.12). The Fourier analysis (Figure 3.12) confirms the presence of a bar with maximal amplitude of $C_2/C_0 \sim 0.5$ at ~ 4 kpc and a bar length of $L_{\rm bar} = 6.3$ kpc. Spiral arms here give a much smaller contribution to the amplitude of the $m = 2$ mode.

The origin of this bar is however different: in the bottom left panel of Figure 3.12 the A_2 coefficient starts to increase at $z \sim 0.6$, while the disk is stable according to $\langle Q \rangle$. As mentioned in Section 2.3, this galaxy happens to suffer a minor merger at roughly the same time as the GA galaxy. In particular, at $z = 0.52$, the galaxy suffers a near passage at ~ 20 kpc of a 1.6×10^9 $M_\odot$ satellite, with a mass ratio of $1:32$ with respect to the main galaxy. Further near passages are at $z = 0.43$ and $z = 0.35$, when the satellite gets tidally destroyed. These times are reported in Figure 3.12 as vertical black lines. This coincides with the time interval where the A_2 coefficient increases from ~ 0.05 to ~ 0.17 and it supports the idea that this bar is triggered by a tidal interaction. The main difference with respect to the GA galaxy lies in the higher mass ratio, though the merger is still considered minor.

The AqC6 galaxy behaves differently. Analogously to the GA simulations, the

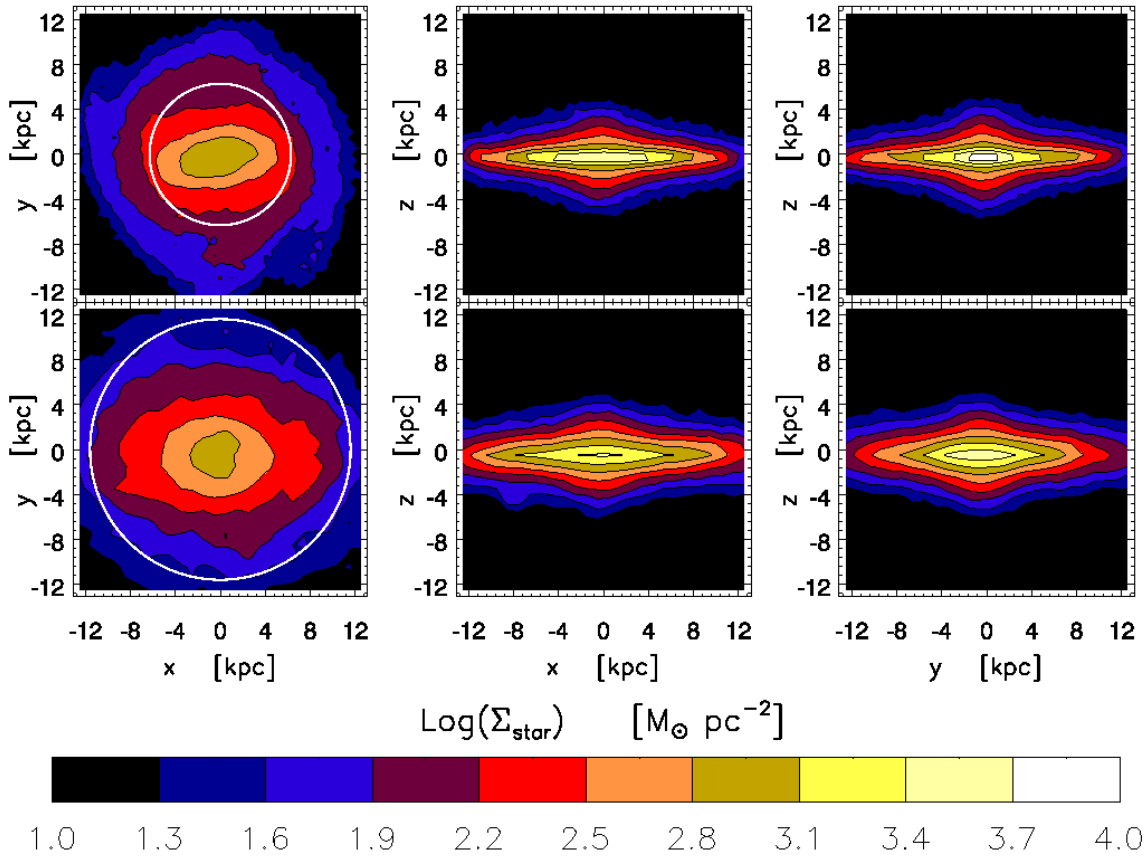

Figure 3.11: As in Figure 3.3: projected stellar maps of the AqC5 (top panels) and AqC6 (bottom panels) galaxies at $z = 0$. The white circle marks the bar length $L_{\rm bar}$.

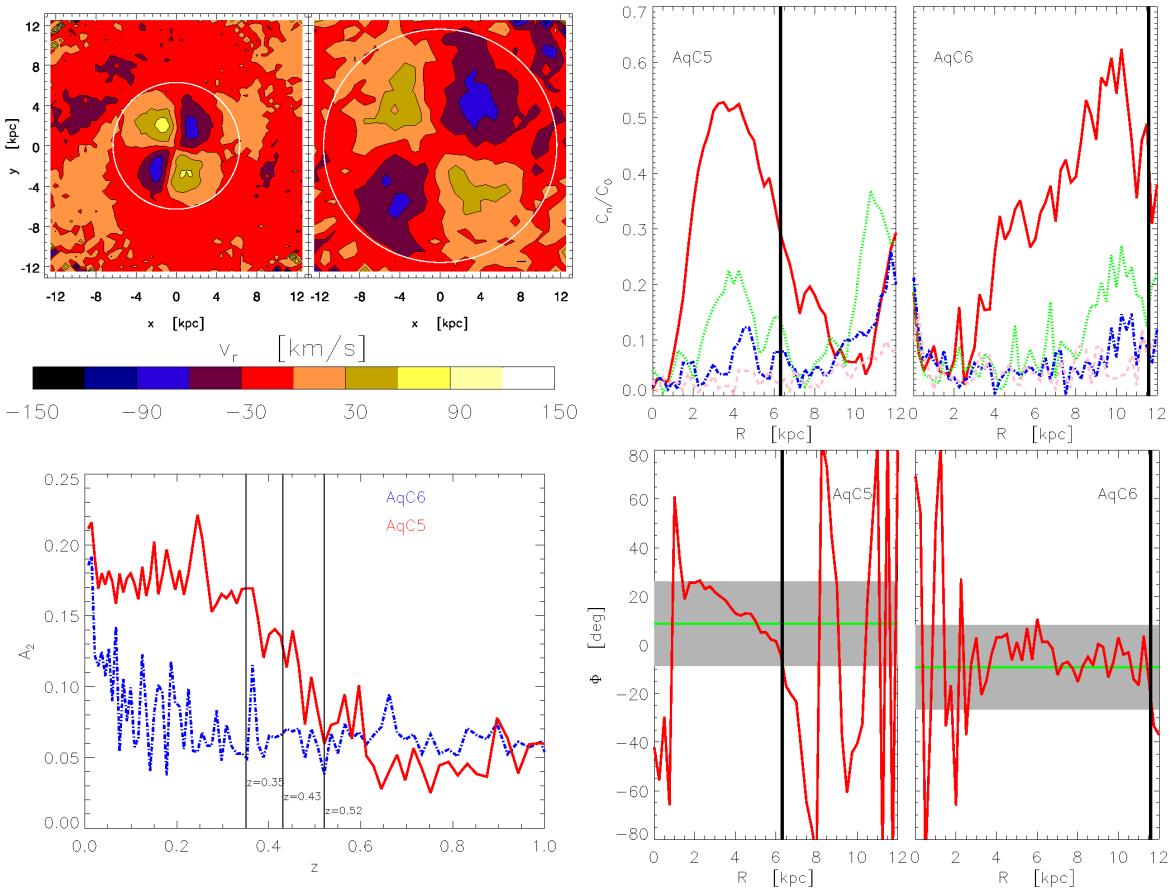

Figure 3.12: Top left panel: as in Figure 3.5, radial velocity maps on edge-on views of the two simulated AqC5 (left panel) and AqC6 (right panel) galaxies. The white circle marks the bar length $L_{\rm bar}$. Top right panel: as in Figure 3.6, Fourier coefficients of the AqC5 (left panels) and AqC6 (right panels) galaxies. Upper panels show the amplitude of even Fourier coefficients, the lower panels the phase of C_2. The black lines mark the bar length $L_{\rm bar}$. Bottom left panel: as in Figures 3.7 and 3.9, evolution with redshift of A_2 (upper panel) and $\langle Q \rangle$ (lower panel) for the AqC5 (continuous red lines) and AqC6 (dot-dashed blue lines). Vertical lines give the times of near passages and final merger of the satellite. Bottom right panel: as in Figure 3.6, Fourier phase of C_2. The black lines mark the bar length $L_{\rm bar}$.

perturbation from the satellite does not trigger a bar. Indeed, the dynamics of the merger is different in this case: the satellite suffers a much slower orbital decay, so that the apocenter of the orbit is still ~ 30 kpc at $z = 0.45$. The closest encounter, at 19 kpc, is found only at $z = 0.24$, while the tidal disruption takes place at $z = 0.14$. At such late times the $Q_{\rm tot}$ parameter is close to 1 and the A_2 coefficient starts to raise again as in the GA case. While the cause in this case seems to be the disk secular evolution (driven by the progressive accumulation of the disk mass, as in Figure 3.10), it cannot be excluded that the bar is tidally triggered.

Figures 3.11 and 3.12 show that in this case the bar-like signatures in streaming motions and Fourier analysis are relatively strong, but the bar is very long, with an estimated length of $L_{\rm bar} = 11$ kpc and the isodensity contours are not very flattened. The galaxy appears to be caught during the early development of a very strong and long bar.

3.5 Conclusions

Chapter 2 shows results of simulations of disk galaxies in $\sim 2 - 3 \times 10^{12}$ $M_\odot$ halos, using two sets of ICs (GA, Stoehr et al. (2002) and AqC, Springel et al. (2008), Scannapieco et al. (2009)) at two resolutions. In all cases, extended disks were obtained with low B/T ratios and general properties (disk size, mass surface density, rotation velocity, gas fraction) that are consistent with observations of the local universe. These galaxies develop a bar at low redshift. In this Chapter, based on the paper Goz et al. (2015), the properties of these bars are quantified, starting from morphology and kinematics of the inner region of the galaxies, then performing a Fourier analysis of the mass surface density map to assess the strength and length of the bars. The physical conditions that cause bar instability are investigated and it is found that a combination of low values of Toomre parameters and minor mergers can explain the emergence of bars in simulations.

Main conclusions are the following:

(i) The close similarity of bar properties at $z = 0$ and of the development of the instability at $z \leq 0.3$ for GA2 and GA1, that differ in mass resolution by a factor of 9.3, disfavours the hypothesis that these bars are a result of a numerical instability due to poor resolution.

(ii) Despite the softening does not let to spatially resolve the vertical structure of the disk, simulated disks have vertical and radial velocity dispersion compatible with observations, at least for $r < 10$ kpc.

(iii) In the GA simulations the morphology and kinematics of the inner $\sim$ 10 kpc are fully consistent with the presence of a bar. In both cases the typical kinematic signatures of increased line-of-sight velocity dispersion and radial streaming motions are present. The Fourier analysis shows that C_2/C_0 peaks to values of 0.4 and 0.7 in the GA2 and GA1 cases, that the bar length is $L_{\rm bar} \simeq 8.8$ kpc in both cases.

(iv) The time evolution of A_2 shows that this instability starts at $z = 0.2$ and quickly rises at $z = 0$ for both GA2 and GA1, so the difference in bar strength is likely due to a small time offset in the growth of the structure.

(v) Before the onset of bar instability, disks result to be stable according to the criterion proposed by Efstathiou et al. (1982) and they are very close to the threshold of Toomre instability, with $Q_{\rm tot} \simeq 1$.

(vi) In the GA series, a minor merger taking place from $z = 0.57$ to $z = 0.35$, with a stellar mass ratio of $1 : 50$, results, especially in GA2, in a transient tidal disturbance with high values of the A_2 coefficient which disappears as quickly as it has appeared. A Fourier analysis reveals that the perturbation is due to a strong spiral pattern rather than to a bar.

(vii) The AqC simulations follow a different path. At a higher resolution (AqC5), a minor merger taking place from $z = 0.52$ to $z = 0.35$ induces a true bar that lasts until the end of the simulation. The $\langle Q \rangle$ parameter is greater than 1 before the first close encounter with the satellite, but the mass ratio is higher in this case ($1 : 32$) and this likely justifies the different behaviour of AqC5 with respect to GA2. The final bar has a length of $L_{\rm bar} = 6.5$ kpc.

(viii) There is a minor merger also in AqC6 but it takes place at later times. In this case the disk gets barred in a way similar to the GA galaxy. However, in this case the role of the merger in the triggering of the bar cannot be excluded. The resulting bar is very long ($L_{\rm bar} = 11$ kpc) and it is caught in a relatively early phase of development.

(ix) The formation of the disk influences the triaxiality of the inner regions of the DM halo. In the GA2-cless simulation, performed treating both DM and gas particles as collisionless particles, the DM halo is triaxial, while in GA2, where the halo has hosted the formation of a spiral galaxy, the inertia tensor of the DM halo is roughly oblate and its eigenvector corresponding to the largest eigenvalue is found to be well aligned with the galaxy angular momentum.

> Thus, special care is needed in addressing the role of triaxiality on bar instability when disks are embedded in DM halos extracted from collisionless simulations.

Overall, simulations are consistent with a relatively simple picture of bar instability being triggered either by secular processes in Toomre-unstable disks ($Q_{\rm tot} \lesssim 1$) or by minor mergers, when the stellar mass ratio is at least of order $1:30$. With mass ratios as small as $1:50$, the merger can stimulate transient features that may look like bars but do not pass a test based on Fourier phases. Of course, these simulations do not give sufficient statistics to provide this picture with the proper justification. Several versions of the code, modelling different processes and varying the parameters, are tested on these sets of ICs and bars may or may not come out, depending on the detailed state of the galaxy. For instance, the AqC5 galaxy in the Scannapieco et al. (2012) paper, run with a previous version of the code with pure thermal feedback, primordial cooling and no chemical evolution, showed a very strong bar (the whole disk had collapsed into a cigar-like structure). A similar thing happens to GA2 when simulated with the same version of the code. In this two cases the bar is found to be triggered by the two minor mergers discussed above, while the disks are Toomre-stable before the merger. The difference in this case is that, due to the fact that feedback is less effective in limiting star formation in small halos, mass ratios are much larger.

As a concluding remark, results are found to be stable with resolution at least in the GA case, hence the origin of the bar is considered physical rather than purely numerical. However, the presence of a bar depends on the fine details of the disk structure and its environment that are not yet numerically under full control, as the different timing of the satellite merging in AqC5 and AqC6 testifies. So these results are not a premise to a robust prediction of the presence of bars in simulated disks, but they will let to better investigate the emergence of this complex phenomenon that, although it has been observed since the beginning of extragalactic astronomy, is still not completely understood.

4

Infrared properties of simulated galaxies

In this Chapter[1] results of galaxies at $z = 0$ in cosmological hydrodynamical simulation, performed using the GADGET-3 code and MUPPI for feedback and star formation, are presented.

Global properties of the simulated sample, such as the distributions of the stellar, atomic and molecular, dust masses and B/T ratio, are shown. The scaling relations of the atomic and molecular gas, the SFR and stellar mass relation (*main sequence*), and the relation between the gas-phase metallicity and the stellar mass, are presented and compared with observations (such relations are introduced in Section 1.1.2).

Infrared (IR) predicted spectra are obtained by means of GRASIL-3D, a code devoted to calculate the emerging Spectral Energy Distribution (SED) of a simulated galaxy (the radiative transfer problem is introduced in Section 1.3). IR SEDs are binned by stellar mass, gas metallicity, SFR and morphology and compared with a set of IR templates calibrated with observations on nearby galaxies taken from the Herschel Reference Survey (HRS).

The Chapter is organized as follows. Section 4.2 is devoted to describing the code used to post-process the simulation, GRASIL-3D, including the modification introduced to interface it with MUPPI. The simulation and the selection of the objects are described in Section 4.3, while tests on GRASIL-3D are discussed in Section 4.4. In Section 4.5 the main properties of the observational samples to compare with

[1]This Chapter is mainly based on the paper Goz, Monaco, Granato, Murante, Domínguez-Tenreiro, Obreja, Annunziatella & Tescari (prep).

are presented. The global properties and the scaling relations of the simulated sample are presented and discussed in Section 4.6. In Section 4.7 the calibration of GRASIL-3D parameters is addressed. Section 4.8 is devoted to present and discuss the comparison with HRS sample. The results are summarized in Section 4.9.

4.1 Introduction

Simulations are well suited to investigate the relation among gas mass, SFR, stellar mass and other galaxy properties because the gas dynamics is followed self-consistently and no relations between the local and global properties of the gas are necessarily imposed. The strength and implementation of feedback mechanisms in sub-grid models are crucial factors for shaping the distributions of gas components and metals in and around galaxies (Section 1.2.3). Thus, a comparison with observations is mandatory to test whether the simulations reproduce the scaling relations of baryonic components of galaxies, shedding light on the physical drivers of the observed relations.

Barai et al. (2015), studying the properties of galactic outflows and diffuse gas at $z \geq 1$ in galaxies (Section 2.6), showed that MUPPI distributes metals more adequately than the *effective* model (Section 1.2.3). In this Chapter the mass-metallicity relation (introduced in Section 1.1.2), being extensively studied in local galaxies in the past decade (e.g. Tremonti et al., 2004), is explored, using the simulation presented by Barai et al. (2015). Observed scaling relations of atomic and molecular cold gas components of nearby gas-rich star-forming galaxies are provided by Jiang et al. (2015); the galaxies are selected from the Submillimiter Telescope (SMT) sample, the Analysis of the interstellar Medium of Isolated GAlaxies and CO Legacy Database for GASS (AMIGA-CO) samples. Since this study (introduced in Section 1.1.2) focuses on nearby galaxies of intermediate-stellar mass, it can provide a good benchmark for comparison with a sample of simulated galaxies in which star-formation and feedback are modelled by MUPPI.

Gas and dust are tightly connected in galaxies (Section 1.1.2), as shown by the measured dust-to-gas ratios of many nearby galaxies that scale proportionally with their metallicities (at least for non metal-poor and low-mass galaxies). Dust in the interstellar medium reprocesses the light emitted by stars, shaping the SEDs of the galaxy (Section 1.3). Dust emission has been studied in local galaxies (e.g. Ciesla et al., 2014), versus parameters such as the stellar mass, the metallicity, the SFR, the morphology, etc. Simulated galaxies are post-processed with GRASIL-3D code (Domínguez-Tenreiro et al., 2014), in order to obtain the infrared SEDs and compare

them with observations. The code takes into account differential spectra of stellar populations, the effect of attenuation of photons originating inside the molecular clouds and the global distribution of star and dust; it solves the radiative transfer equation (Section 1.3.2) under the assumption of thermal equilibrium for dust grains bigger than a given size (usually 250$\mathring{A}$), with a size dependent temperature, and a proper treatment of small grains and of polycyclic aromatic hydrocarbons (PAHs) features dominating the mid-infrared part of the SED.

4.2 SED model: GRASIL-3D

The kernel of GRASIL-3D (Domínguez-Tenreiro et al., 2014) is based on the formalism of the widely employed GRASIL (GRAphite and SILicate) model (Silva et al., 1998; Silva, 1999; Granato et al., 2000) and it is designed to be applied to objects characterized by an arbitrary geometry, such as simulated galaxies (Obreja et al., 2014) and galaxy clusters (Granato et al., 2015).

4.2.1 Inputs to GRASIL-3D from the simulation

The aim of GRASIL-3D is to calculate multiwavelength SEDs and images of galaxies identified in simulations.

The quantities required for the SED evaluation are:

(i) stellar and gas matter distribution $\rho_{*,g}(\mathbf{r}, t)$ (where $*$ and g mark star and gas respectively);

(ii) stellar and gaseous metallicity $Z_{*,g}(\mathbf{r}, t)$;

(iii) star ages and gas densities.

To smooth out the functions above, GRASIL-3D uses a Cartesian grid whose cell size is set by the smoothing length used in the simulation code.

4.2.2 Treatment of the molecular clouds

It is well known that the molecular clouds (MCs) are the sites in which star formation takes place. As a consequence the stars spend part of their life within or close to MCs, thus the dust reprocessing of the starlight must be taken into account. The gas is sub-divided in a dense phase associated with young stars (star-forming MCs) and in a diffuse phase (*cirrus*) where more evolved (*free*) stars and MCs are placed.

The young stars leave the parent clouds in a time-scale $t_{\rm esc}$. The MCs are represented as spherical clouds with optical depth $\tau \propto \delta\Sigma_{\rm mc}$ (δ is the dust-to-gas mass ratio and $\Sigma_{\rm mc} = m_{\rm mc}/r_{\rm mc}^2$ is the mass surface density of the MC), with a central source whose radiative transfer through the MCs is computed.

The original code presented by Domínguez-Tenreiro et al. (2014) adopts a log-normal probability distribution function for the gas density in order to derive the amount of gas in the form of MCs for each gas particle provided by the simulation. Since MUPPI algorithm already evaluates the fraction of hydrogen in molecular form, by means of the Blitz & Rosolowsky (2006) relation, the code was modified to manage directly this molecular content, while the rest of the gas particle mass is assigned to the *cirrus*.

The total mass in active MCs, $M_{\rm mc}$, can be obtained through the following steps:

(i) for each cold gas particle i, the molecular fraction, $f_{{\rm mc},i}$, is provided by MUPPI;

(ii) the mass of the i-th cold gas particle m_i is split into $m_i^{\rm NDG} = m_i\ f_{{\rm mc},i}$ for its non-diffuse gas content and $m_i^{\rm DG} = m_i\ (1 - f_{{\rm mc},i})$ for its diffuse gas content;

(iii) $M_{\rm mc}$ is the sum of the non-diffuse gas content of gas particles:

$$M_{\rm mc} \equiv \sum_i m_i^{\rm NDG} \tag{4.1}$$

The MC grid-density and dust content

$M_{\rm mc}$ is distributed in such a way that it is proportional to the density of young stars in order to ascribe all the MCs to recent star formation. This because in MUPPI algorithm a new star particle is spawned stochastically, as described in Section 2.2.1.

The steps are the following:

(i) the mass of the i-th *young* star particle (described in the next Section) is m_i;

(ii) the global MC to young star mass fraction is evaluated as

$$\alpha = \frac{M_{\rm mc}}{M_{\rm y}^*} \tag{4.2}$$

where $M_{\rm y}^* \equiv \sum_i m_i$;

(iii) the positions and masses of star particles are loaded in order to obtain the density $\rho_{y,k}^*$ at the k-th grid cell, where "y" stands for *young stellar population*;

(iv) the MC density at the k-th grid cell is:

$$\rho_{\rm mc,k} = \alpha \times \rho^*_{y,k} \tag{4.3}$$

(v) therefore the MC mass at the k-th grid cell is:

$$M_{\rm mc,k} = V_k \times \rho_{\rm mc,k} \tag{4.4}$$

where V_k is the k-th cell volume.

At each grid cell, a number of MCs is placed as follows:

$$N_{\rm mc,k} = \frac{M_{\rm mc,k}}{m_{\rm mc}} \tag{4.5}$$

where $m_{\rm mc}$ is the mass of a single molecular cloud and is a free parameter of the model.

Since the simulation provides the metallicity of each gas particle, the dust content of the k-th cell is evaluated assuming that the dust-to-gas mass ratio δ is proportional to the (local) metallicity:

$$\delta(Z_k) = \frac{Z_{{\rm gas},k}}{110 \times Z_\odot} \tag{4.6}$$

where $Z_{{\rm gas},k}$ is the average metallicity of gas particles at the k-th grid cell.

Young stellar populations

The stars are assumed to spend part of their life within or close to optically thick MCs and then gradually escape from them as they get older on a time-scale $t_{\rm esc}$. This modelling allows an age-selective extinction, with the most UV-luminous and young stars suffering larger dust extinction than older ones.

The parametrization of the fraction $f(t)$ of the stellar populations energy radiated inside MCs, as a function of their age, is the following:

$$f(t) = \begin{cases} 1 & t \leq t_{\rm esc} \\ 2 - t/t_{\rm esc} & t_{\rm esc} \leq t \leq 2t_{\rm esc} \\ 0 & t > 2t_{\rm esc} \end{cases} \tag{4.7}$$

where $t_{\rm esc}$ is a free parameter setting the fraction of light which can escape the star forming region and it mimics the MC destruction by young and luminous stars.

The SED, $L_\nu^{y,*}(t_i, \mathbf{Z}_i, \mathbf{r}_i)$, for each young star particle ($i = 1, ..., N_{y,*}$) placed at $\mathbf{r}_i$, with mass m_i, age t_i and metallicity $\mathbf{Z}_i$, is calculated assuming the Chabrier (2003) IMF and the stellar emission modelled following Bruzual & Charlot (2003).

4.2.3 Cirrus component

The *cirrus* component of the i-th gas particle is given by

$$m_i^{\mathrm{DG}} = m_i(1 - f_{\mathrm{mc},i}) \tag{4.8}$$

where $f_{\mathrm{mc},i}$ is provided by MUPPI (see Section 4.2.2). Therefore the diffuse gas density is

$$\rho_c(\mathbf{r}_i) = (1 - f_{\mathrm{mc},i}) \times \rho_{\mathrm{gas}}(\mathbf{r}_i) \tag{4.9}$$

and the diffuse dust density at the k-th grid cell is, accordingly:

$$\rho_{\mathrm{dust},k} = \delta(Z_k) \times \rho_{c,k} \tag{4.10}$$

where $\delta(Z_k)$ is as in equation 4.6.

4.2.4 Dust model

The dust is assumed to consist of a mixture of carbonaceous and silicate spherical grains and PAHs. The dust composition used for the diffuse *cirrus* is the one proposed by Weingartner & Draine (2001a) and it consists of a mixture of neutral and ionized particles, the ionization fraction depending on the gas temperature, the electron density and the ultraviolet field. Domínguez-Tenreiro et al. (2014) retain the same dust mixtures for the MCs as originally used by the GRASIL code. Both dust distributions are calibrated on the same observables, i.e. the *cirrus* emission and the average extinction curve in the MW (described in Section 1.3.1).

4.2.5 SED determination

The aim of GRASIL-3D is to calculate the rest frame emergent luminosity at given direction (θ,ϕ) and wavelength λ from the simulated galaxy. The radiant flux reads:

$$F_\lambda(\theta,\phi) = 4\pi \sum_k V_k j_{\lambda,k} \exp[-\tau_{eff,\lambda}(k;\theta,\phi)] \tag{4.11}$$

where the sum is over the different volumes V_k of the grid and

$$j_{\lambda,k} = j_{\lambda,k}^{\mathrm{mc}} + j_{\lambda,k}^{*} + j_{\lambda,k}^{\mathrm{c}} \tag{4.12}$$

is the volume emissivity of the k-th volume element at wavelength λ, coming from MCs, *free* stars and *cirrus* component, respectively, and $\tau_{eff,\lambda}(k;\theta,\phi)$ is the effective optical thickness for *cirrus* absorption from the k-th volume element to the outskirts of the galaxy along the (θ,ϕ) direction.

RT in MCs

The RT in the MCs is solved using the Granato & Danese (1994) code, by means of the λ-iteration method, i.e. at each successive iteration the local temperature of the dust grains is calculated from the radiation field of the previous iteration.

The emerging SED from MCs depends on the optical depth $\tau_{\rm mc}$:

$$\tau_{\rm mc} \propto \delta\Sigma_{\rm mc} = \delta\frac{m_{\rm mc}}{r_{\rm mc}^2} \tag{4.13}$$

Although the surface density, $\Sigma_{\rm mc}$, is the same for all the MCs, the value of $\tau_{\rm mc}$ must be calculated separately for each MC, because δ is set by the local metallicity, i.e. within the k-th cell.

RT through the *cirrus*

The RT through the *cirrus* is evaluated with the following assumptions:

(i) the effect of the self-absorption is ignored;

(ii) the effect of UV-optical scattering is approximated by means of an effective optical depth (Rybicki & Lightman, 1979):

$$\tau_{eff,\lambda}^2 = \tau_{abs,\lambda}(\tau_{abs,\lambda} + \tau_{sca,\lambda}) \tag{4.14}$$

Thus the local radiation field within the i-th grid cell, $J_{\lambda,i}$, due to the extinguished emissions of the MCs and *free* stars from all the other cells, can be calculated as:

$$J_{\lambda,i} = \sum_k V_k(j_{\lambda,k}^{\rm mc} + j_{\lambda,k}^{*}) \times \exp[-\tau_{eff,\lambda}(i,k)]/r^2(i,k) \tag{4.15}$$

where $r(i,k)$ is the distance from the i-th to the k-th grid cells. Within the same cell, i.e. where $r(i,k)$ goes to zero, the cell is split into N_P random points, P_n, each of them representing a small volume $V(P_n) = V_i/N_p$.

4.3 Simulation

The box-size of the simulation is $L_{\rm box}$ = 25 Mpc comoving, using $N_{\rm part} = 2 \times 256^3$ DM and gas particles in the initial condition, and the gas particle mass is $m_{\rm gas} = 5.36 \times 10^6$ $M_\odot$. The Plummer-equivalent softening length for gravitational forces is set

to $L_{\rm soft}$ = 2.08 kpc comoving for the evolution up to z = 2, then it is held fixed at $L_{\rm soft}$ = 0.69 kpc in physical unit from z = 2 up to z = 0. The adopted MUPPI parameters of the run analysed in the present work are: $f_{b,out}$ = 0.2, $f_{b,kin}$ = 0.5, P_{kin} = 0.02, slightly different to the ones used by Barai et al. (2015) in the simulation called *M25std*, due to small changes in the chemical sector. Table 2.5 summarizes the properties of simulations presented by Barai et al. (2015). An in-depth description of MUPPI parameters is given in Section 2.2.1. Through the Chapter the simulation is called MUPPIBOX simulation.

4.3.1 Identifying galaxies and orientation

To select galaxies from the MUPPIBOX simulation the procedure is the following. The simulation is post-processed with a standard Friends-of-Friends (FoF) algorithm to select the main haloes of the high-resolution regions and with the substructure-finding code SubFind (Springel et al., 2001). The particles which constitute the galaxy are assumed to be stars and cold ($T < 10^5$ K) or multi-phase gas particles. To quantify the morphology of the galaxies in the sample the B/T ratio (described in Section 2.4) is adopted, taking into account all star particles within $R_{\rm gal} = R_{\rm vir}/10$ and aligning the reference frame with the inertia tensor of galaxy particles.

To make the analysis robust, all MUPPIBOX galaxies contain at least a stellar mass of $2 \cdot 10^9$ $M_\odot$ within $R_{\rm gal}$. This ensures that each object is resolved with at least $\simeq 2 \cdot 10^3$ star particles.

The luminosity of a galaxy depends on the aperture size. In massive galaxies ($M_* \sim 10^{11}$ $M_\odot$) the total luminosity and colour can be affected by not negligible light in the extended halo and by the inclusion or exclusion of small blue satellites below the significance of those identified by SubFind. Through the analysis the aperture size is fixed to $R_{\rm gal}$. The effects on the SED taking other apertures are discussed in Section 4.4.2.

The line of sight for the SED evaluation is chosen consistently to lie along an axis of the simulated box coordinates, yielding an essentially randomised orientation for each galaxy.

4.4 Tests on GRASIL-3D

This Section is devoted to study more in detail the effects on the SED (i) of the grid size adopted by GRASIL-3D to perform the radiative transfer calculation, (ii) of the

Galaxy	$R_{(gal)}$	$R_{(P)}$	$B/T_{(R_{gal})}$	$B/T_{(R_P)}$	$M_{*(R_{gal})}$	$M_{*(R_P)}$	$M_{gas(R_{gal})}$	$M_{gas(R_P)}$	$M_{dust(R_{gal})}$	$M_{dust(R_P)}$
GA1	30.37	12.41	0.22	0.23	$1.35 \cdot 10^{11}$	$1.15 \cdot 10^{11}$	$2.44 \cdot 10^{11}$	$1.84 \cdot 10^{10}$	$2.69 \cdot 10^{8}$	$1.89 \cdot 10^{8}$
ID12318	9.39	6.52	0.49	0.53	$4.31 \cdot 10^{9}$	$3.76 \cdot 10^{9}$	$1.65 \cdot 10^{9}$	$1.14 \cdot 10^{9}$	$1.48 \cdot 10^{7}$	$1.03 \cdot 10^{7}$
ID3	17	4.43	0.34	0.59	$5.1 \cdot 10^{9}$	$1.85 \cdot 10^{9}$	$2.45 \cdot 10^{9}$	$7.12 \cdot 10^{8}$	$2.01 \cdot 10^{7}$	$4.95 \cdot 10^{6}$

Table 4.1: Basic characteristics of selected galaxies. Column 1: Simulation name; Column 2: Galaxy radius (kpc), set to 1/10 of the virial radius; Column 3: Petrosian radius (kpc), defined in Eq. 4.4.2; Column 4: B/T ratio inside the galaxy radius; Column 5: B/T ratio inside the Petrosian radius; Column 6: Total galaxy stellar mass ($M_\odot$), inside the galaxy radius; Column 7: Total galaxy stellar mass ($M_\odot$), inside the Petrosian radius; Column 8: Total galaxy gas mass ($M_\odot$), inside the galaxy radius; Column 9: Total galaxy gas mass ($M_\odot$), inside the Petrosian radius; Column 10: Total galaxy dust mass ($M_\odot$), evaluated by GRASIL-3D, inside the galaxy radius; Column 11: Total galaxy dust mass ($M_\odot$), evaluated by GRASIL-3D, inside the Petrosian radius.

aperture size to identify galaxies and (iii) the impact of the dust emissivity index on the FIR emission.

These tests are performed on three galaxies, namely GA1, ID12318 and ID3. The mass resolution and force softening of GA1 simulation, extracted from a zoom-in simulation and described in Chapter 2 and 3, are comparable to those of the simulated cosmological box analysed in the present Chapter. ID12318 and ID3 belong to the simulated cosmological box and their stellar masses are close to the median value of the MUPPIBOX sample. ID3 galaxy is found to be a merger. Table 4.1 summarizes the main characteristics of the selected galaxies. All the quantities marked by (R_{gal}) are evaluated within the galaxy radius, while by (R_P) within the Petrosian radius (Section 4.4.2); gas mass includes multi-phase gas particles and single-phase ones with temperature lower than 10^5 K.

4.4.1 Resolution effects

The force softening sets the space resolution of the simulation. GRASIL-3D uses a Cartesian grid to smooth out the star and gas distributions of the simulation and its size is set by the force softening.

The effects on the SED, setting the grid size twice and four times the force softening, are tested. The variation, $\Delta\delta$, of the SED is defined as:

$$\Delta\delta \equiv \left(\frac{L(\lambda) - L_{\rm ref}(\lambda)}{L_{\rm ref}(\lambda)} \cdot 100 \right) \% \tag{4.16}$$

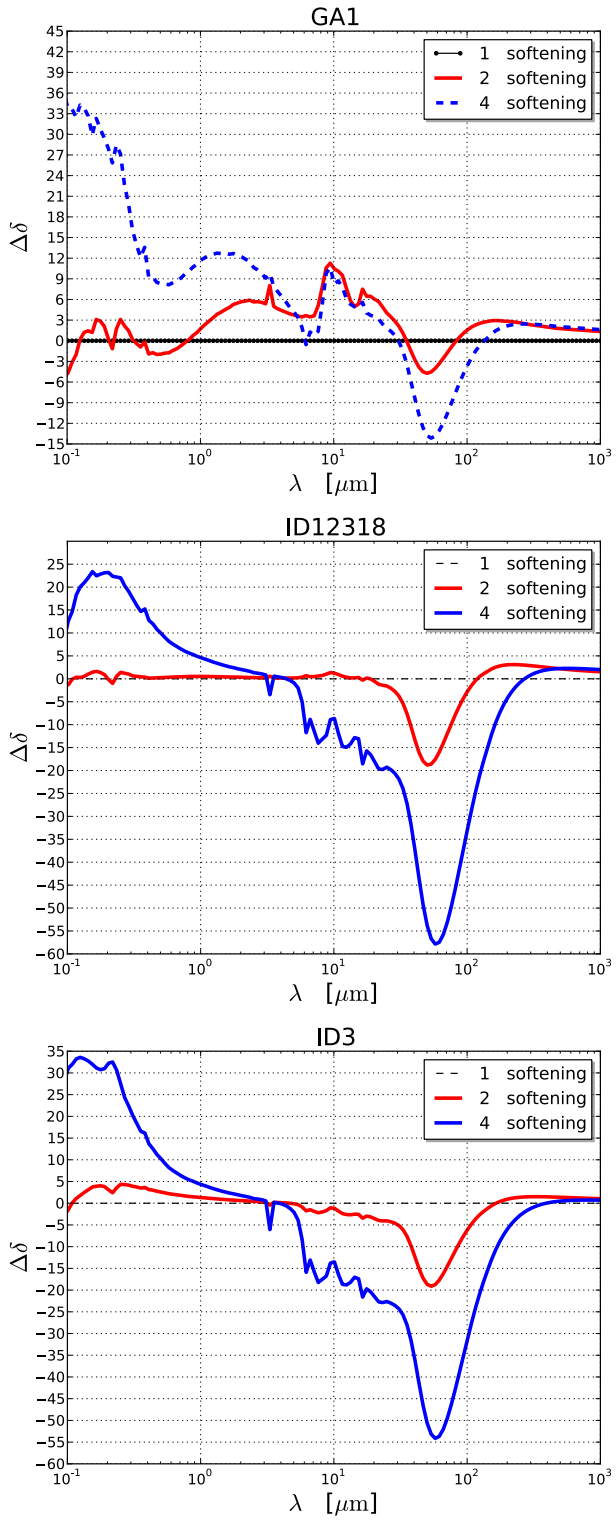

Figure 4.1: From top to bottom the variations on the SED, defined as in Equation 4.16, in function of the wavelength for the GA1, ID12318 and ID3 galaxies. The grid size is set twice (red line) and four times (blue line) the force softening of the simulation.

where $L_{ref}(\lambda)$ is the reference SED calculated with the grid size set by the force softening. Figure 4.1 shows how $\Delta\delta$ varies as a function of the wavelength. In the GA1, setting the grid size twice the force softening, the SED shows a variation less than 3% in the FUV-NIR ($\leq$ 10 μm) and FIR ($\geq$ 100 μm) parts of the spectrum, while in the PAH region ($\simeq$ 10 μm) the variation increases at most up to $\simeq$ 10%. Setting the grid size four times the force softening, the FUV part of the spectrum presents a variation at most up to 30%, the optical-midIR $\sim$ 10%, while the FIR shows a variation less than 3%.

On ID12318 and ID3 galaxies, setting the grid size twice the force softening, the SED is unaffected, except for a variation at most up to 20% in the PAH region. On the contrary, if the grid size is four times the force softening, then the variation on the SED reaches up to $\simeq$ 30% in the FUV, $\simeq$ 55% in the PAH region and the peak at $\simeq$ 100 μm is affected at $\simeq$ 35%.

Moreover the median broadband SED of the entire MUPPIBOX sample is found to be convergent by varying the grid size by a factor 2. Therefore the time-consuming calibration of GRASIL-3D parameters, discussed in Section 4.7, is addressed setting the grid size twice the force softening, while the results are presented setting the grid size equal to the force softening of the simulation.

4.4.2 Choice of aperture

Observations cannot measure the radial profile of a galaxy out to arbitrarily large radii because, at some point, the light from the galaxy disappears into the noise of the background sky. One common quantity used to quantify galaxy sizes is the measure of the distance-independent Petrosian radius (Petrosian, 1976), defined as the radius at which the averaged intensity of light equals a fraction of the radial light profile at that radius. The computation of the Petrosian radius is implemented as:

$$\Sigma(R_P) = \eta \left(\frac{\int_0^{R_P} \Sigma(r) 2\pi r dr}{\pi R_P^2} \right) \tag{4.17}$$

where $\Sigma(r)$ is the stellar surface density, R_P the Petrosian radius and η a constant. Observations use the surface brightness, but an equivalent definition can be given using the stellar mass surface density. Shimasaku et al. (2001) chose $\eta = 0.2$ investigating the photometric properties of bright galaxies taken from the Sloan Digital Sky Survey. The Petrosian radius of simulated galaxies is calculated using the stellar mass instead of the luminosity. Table 4.1 reports the basic characteristics

of selected galaxies within R_{gal} and R_P with $\eta = 0.2$.

In all tests the Petrosian aperture translates in a lower emission from UV up to FIR compared to the case in which R_{gal} is adopted. More massive galaxies, such as GA1, tend to have extended light distributions and, observationally, the luminosity assigned to them depends on how such light is taken into account, yielding significative differences in the luminosity and stellar mass functions in the high tail (Bernardi et al., 2013). Similarly, analysis show that the luminosities of MUPPIBOX galaxies with $M_* \gtrsim 10^{11}$ $M_\odot$ are mildly sensitive to the adopted choice of aperture size. However, this is not the case for the low mass galaxies, such as ID12318, for which the fraction of light in the extended halo is considerably lower. On ID3 object the Petrosian aperture leads to the exclusion of the merger and the resulting object is below the stellar mass threshold of $M_* = 2 \cdot 10^9$ $M_\odot$ adopted in this work.

Since there are only 10 galaxies in the sample more massive than $M_* \sim 10^{11}$ $M_\odot$, the results, presented in this Chapter, are not affected by the choice of the aperture and robustly yield same conclusions. For these reasons, through all the analysis the aperture size is held fixed to R_{gal}.

4.4.3 Modified black-body emission

The dust emission at FIR to sub-mm wavelengths, dominated by big dust grains in thermal equilibrium with the local radiation field, is often modelled as a modified black-body emission of the form:

$$I_\lambda \propto B_\lambda(T_{dust})\lambda^{-\beta} \tag{4.18}$$

where $B_\lambda(T_{dust})$ is the dust black-body emission at temperature T_{dust} and β is the dust emissivity index. The robustness of this approach is based upon laboratory experiments which show temperature-dependent spectral slope variations, with $1.5 < \beta < 2.5$ (Boudet et al., 2005; Jones, 2014). However the most recent measurements on silicates to date, besides confirming tight β-T correlation, also show how the emissivity slope varies with wavelengths and exihibit more complex power-law behaviour (Coupeaud et al., 2011). GRASIL-3D employs the *canonical* approach by Draine & Lee (1984), which yields a power-law decline $\beta = 2$, despite recent observations of dust in the diffuse ISM with the Planck mission (e.g. Planck Collaboration et al., 2014) indicate a dust emissivity index $\beta = 1.62 \pm 0.10$.

Figure 4.2 shows the infrared SEDs of the GA1 galaxy obtained with $\beta = 2.0$ and $\beta = 1.6$. Adopting the lowest value $\beta = 1.6$, the SED is basically unaffected below

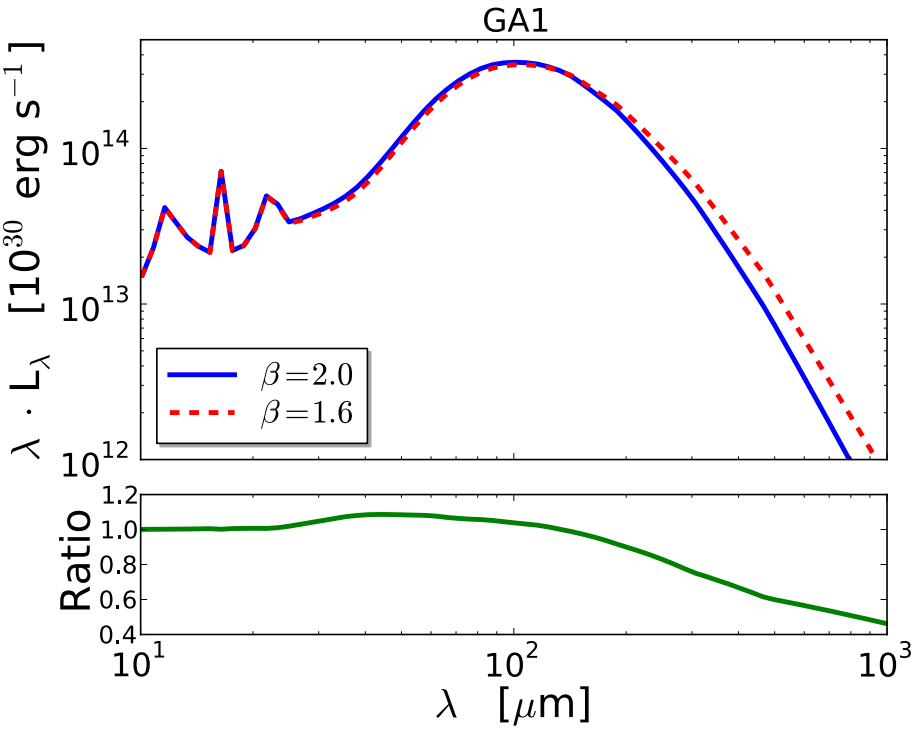

Figure 4.2: IR SEDs of the GA1 galaxy obtained with the dust emissivity index set to $\beta = 2.0$ (continuous blue line) and $\beta = 1.6$ (dashed red line) and their ratio.

the peak that occurs at $\simeq$ 100 μm, while above the luminosity shows a variation of $\simeq$60% at $\simeq$ 500 μm. The SEDs of ID12318 and ID3 galaxies are unaffected in all bands.

The median broadband SED of the entire MUPPIBOX sample is found to be convergent by varying the dust emissivity, which is held fixed to $\beta = 2$ during the presentation of the results.

4.5 Observational data

The GRASIL-3D parameters, namely the time for newly born stars to escape from the parent molecular cloud and the optical depth of molecular cloud, require to be calibrated. This is addressed comparing the predicted near-UV to far-IR SEDs of the MUPPIBOX sample with the broadband SEDs of two samples, namely Local Volume Legacy (LVL) (Cook et al., 2014a,b) and PACS Evolutionary Probe (PEP) (Gruppioni et al., 2013).

Since HRS (Boselli et al., 2010) is a benchmark study of dust in the nearby Universe, MUPPIBOX sample is compared with the HRS infrared SED templates available to the community via the HEDAM[2] website.

To be consistent with the adopted MUPPIBOX mass threshold, data are selected with stellar mass Log(M_*) $\geq$ 9.3 $M_\odot$ in all the analysis presented.

The following sections briefly describe the main properties of the observational samples.

4.5.1 LVL sample

LVL sample (Cook et al., 2014b,a) consists of 258 local galaxies ($D \leq$ 11 Mpc). Although the galaxies span a wide range in galaxy type, the sample is dominated by dwarf galaxies due to its volume-limited nature. For each object the SED cover the range *FUV-MIPS160* ($\simeq$ 0.1-160 μm) and the stellar mass and SFR are provided.

4.5.2 PEP sample

The PEP sample (Gruppioni et al., 2013) includes the most popular and widely studied extragalactic blank fields: COSMOS, Lockman Hole, EGS and ECDFS, GOODS-N and GOODS-S. One detailed description of PEP fields and survey properties is presented by Lutz et al. (2011), Berta et al. (2010). Only object with redshift

[2] http://hedam.lam.fr/HRS/

$z < 0.1$ are taken into account. The SEDs sample covers the range *U-SPIRE500* ($\simeq$ 0.4-500 μm), but the stellar mass and the SFR are not available in the PEP catalogue.

To obtain such quantities, the SED fitting technique using MAGPHYS (da Cunha et al., 2008) is applied. For each galaxy in the sample, MAGPHYS uses a Bayesian approach to find the template at a given redshift that best reproduces the observed galaxy fluxes. Since spectroscopic redshifts are available for all galaxies, it is held fixed instead of leaving it as a free parameter. The templates are obtained from libraries of stellar population synthesis models Bruzual & Charlot (2003) with a Chabrier (2003) IMF and a metallicity value which can be in the range 0.02-2 $Z_{\odot}$. In order to be consistent with the simulated SEDs, the Chabrier (2003) library is used. The outputs of the code are the parameters of the model that reproduce the galaxy fluxes and their probability distribution function (PDF) best. The median value of the PDF is chosen as the stellar mass of the galaxies, while the 1σ uncertainty is given by the difference between the 16% and 84% percentiles.

4.5.3 HRS sample

The HRS is a volume limited sample complete at $z = 0.085$ above stellar mass of $\approx 10^{10.4}$ $M_{\odot}$. HRS contains 322 galaxies, among which are 62 early-types and 260 late-types. The IR SEDs of the HRS galaxies covers the range from 8 to 500 μm, using the photometry on Spitzer/IRAC and WISE images and using measurements available in the literature from Spitzer/MIPS, Herschel/PACS, Herschel/SPIRE, and IRAS. Ciesla et al. (2014) used the HRS survey to compute the mean spectral energy distribution of the whole sample of late-type galaxies to derive the typical SED of nearby *normal* galaxy. Moreover they binned the best-fit models of the sample by stellar mass, dust mass, SFR, metallicity and morphological type.

4.6 Global properties of the MUPPIBOX sample

The distributions of the stellar, atomic and molecular, dust masses and B/T ratio of the simulated sample are analysed at $z = 0$. The scaling relations of the atomic and molecular *gas-richness* with stellar mass, the SFR-M_* relation (*main sequence*) and the relation between the gas-phase metallicity and the stellar mass, are presented and compared with observations.

The histograms on Figure 4.3 show that $\simeq$ 80% of the sample is made up of galaxies with total stellar mass lower than 10^{10} $M_{\odot}$, and $\simeq$ 90% of the atomic and molecular hydrogen is locked in those galaxies. Approximately half of the entire

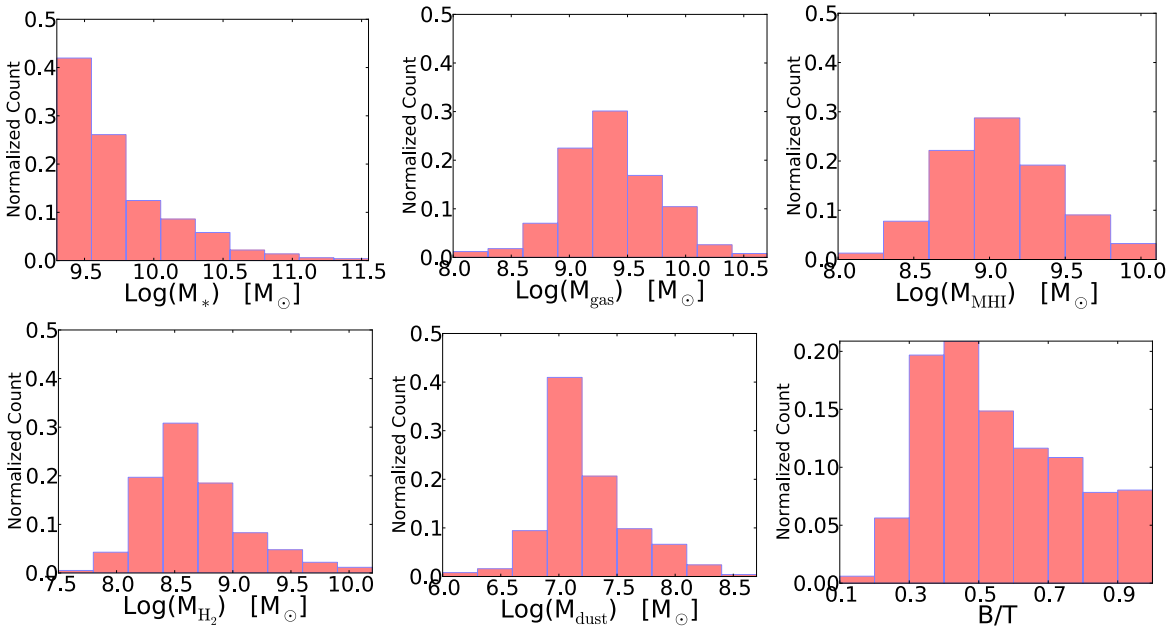

Figure 4.3: Distributions of the MUPPIBOX sample. Upper panels: from left to right, the distribution of stellar mass, the distribution of total (atomic and molecular) gas mass, and the distribution of the atomic gas mass. Bottom panels: from left to right, the distribution of molecular mass, the distribution of dust mass and the distribution of the circularity. The dust mass of each galaxy is evaluated by GRASIL-3D.

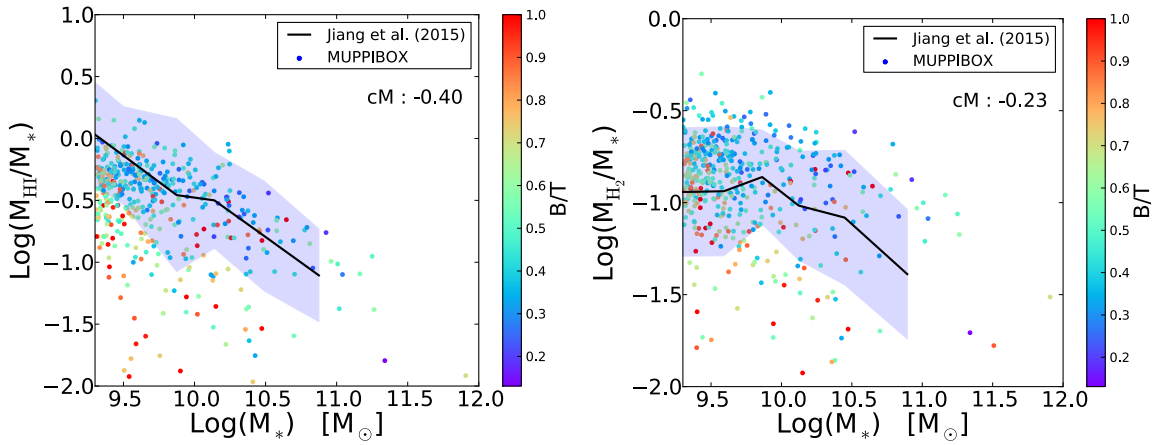

Figure 4.4: Left panel: scaling relation for atomic *gas-richness* with stellar mass. Right panel: scaling relation for molecular *gas-richness* with stellar mass. Solid black lines show the averaged values and filled regions the corresponding 1σ scatters of Jiang et al. (2015). Spearman's rank correlation coefficient values (cM) for the MUPPIBOX galaxies are reported in the plots. In all the plots colorbar shows the ratio B/T.

sample has $\mathrm{Log}(\mathrm{M_{dust}}) \simeq 7\ \mathrm{M_\odot}$ and $B/T < 0.5$, and massive objects with $\mathrm{Log}(\mathrm{M_*}) > 10.5\ \mathrm{M_\odot}$ and with high value of bulge-over-total are rare.

4.6.1 The HI and H_2 scaling relations

The scaling relations of the *gas-richness* $\mathrm{M_{H_2}/M_*}$ and $\mathrm{M_{HI}/M_*}$ with stellar mass of the MUPPIBOX sample are studied, comparing them with averaged values with their scatters of Jiang et al. (2015). They combined the STM sample with the AMIGA-CO samples. As shown by Figure 4.4, $\mathrm{M_{H_2}/M_*}$ of MUPPIBOX galaxies is always lower than unity, while, only in the low mass star end, $\mathrm{M_{HI}/M_*}$ can reach values higher than unity. $\mathrm{M_{H_2}/M_*}$ is roughly constant in the range $\mathrm{M_*} < 10^{10}\ \mathrm{M_\odot}$, and then shows a mild anticorrelation with $\mathrm{M_*}$, while $\mathrm{M_{HI}/M_*}$ decreases with increasing stellar mass. $\mathrm{M_{HI}/M_*}$ anti-correlates much better with the stellar mass than $\mathrm{M_{H_2}/M_*}$ does as the Spearman coefficients indicate, and in agreement with Jiang et al. (2015). However MUPPIBOX galaxies are HI-poorer than observed by Jiang et al. (2015) low stellar mass end.

Figure 4.4 shows that the *gas-richness* depends primarily on the total mass and increases along the Hubble sequence, as shown by the B/T on the colour-bar,

Mass bin (Log(M_*))	n_M	n_P	n_L	Log(SFR)$_{(M)}$	Log(SFR)$_{(P)}$	Log(SFR)$_{(L)}$
9.3 - 9.5	175	12	17	-0.68	-0.39	-0.83
9.5 - 10	219	34	17	-0.42	-0.45	-0.59
10 - 10.5	76	24	8	0.11	-0.37	-0.18
10.5 - 11	18	12	16	0.54	-0.16	0.06

Table 4.2: Column 1: Stellar mass bin ($M_\odot$); Column 2: number of MUPPIBOX galaxies within the mass bin; Column 3: number of PEP galaxies within the mass bin; Column 4: number of LVL galaxies within the mass bin; Column 5: median SFR in the MUPPIBOX sample ($M_\odot$ yr^{-1}) within the mass bin; Column 6: median SFR in the PEP sample ($M_\odot$ yr^{-1}) within the mass bin; Column 7: median SFR in the LVL sample ($M_\odot$ yr^{-1}) within the mass bin.

in agreement with observations (Roberts & Haynes, 1994). Scaling relations are present also at fixed morphological type, implying that part of the scatter in the *gas-richness* as a function of morphology is due to the large scatter in the stellar mass within a given range of B/T.

4.6.2 The main sequence

Several studies measured the $SFR - M_*$ relation (e.g. Elbaz et al., 2007, 2011; Noeske et al., 2007; Peng et al., 2010), called the *main sequence*. There are many techniques for measuring the rate at which stars are being formed, the aim is to detect the emission that probes recent star formation, avoiding as much as possible contamination from evolved stellar populations.

Since usually in observations "recent" refers to timescales $\approx$ 50-100 Myr (e.g. Kennicutt, 1998; Calzetti et al., 2005; Calzetti, 2013), the star formation rate is averaged over 100 Myrs in the MUPPIBOX sample. In the simulated galaxies, apart a decrease of the scatter in the *main sequence*, there is not a substantial discrepancy between the instantaneous SFR provided by the gas particles and the SFR averaged over a bin of time of the order of hundred Myrs.

HRS sample provides a $SFR - M_*$ relation for the local Universe. Left panel of Figure 4.5 shows a comparison between MUPPIBOX sample and the best HRS linear fit, obtained taking into account late-type star-forming galaxies. Overall there is a good agreement with the HRS *main sequence* at $z = 0$, even if simulated low-mass systems tend to have lower SFR. Moreover in the left panel of Figure 4.5 MUPPIBOX objects are compared with LVL and PEP samples. MUPPIBOX galaxies exhibit a

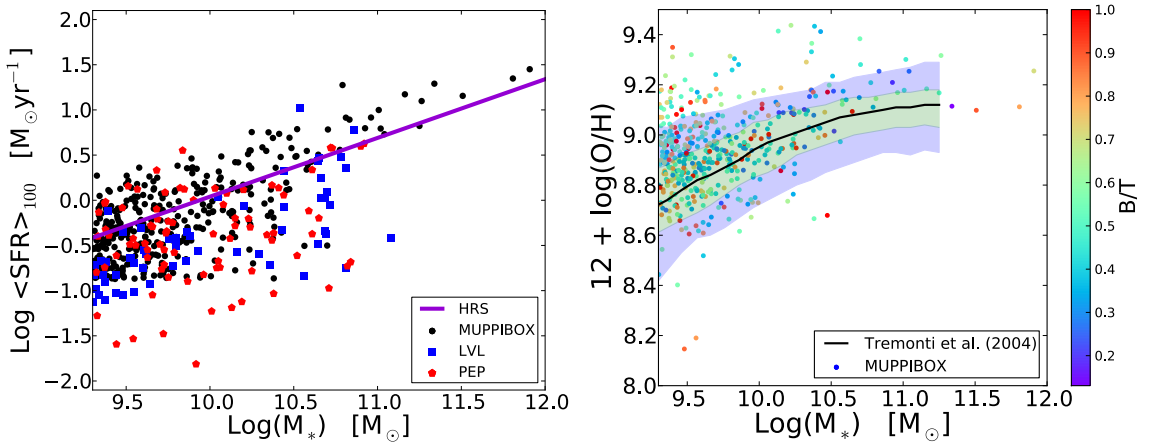

Figure 4.5: Left panel: the galaxy star formation main sequence. Black points show MUPPIBOX galaxies, blue squares and red pentagons show LVL and PEP samples respectively, while the solid violet line marks the HRS relation. Right panel: relation between stellar mass and gas-phase oxygen abundance, solid black line shows the median value of Tremonti et al. (2004) and filled regions contain 68% and 95% of the data. In the plot colorbar shows the ratio B/T.

scatter comparable to that of PEP sample and on average a higher SFR than LVL sample. Table 4.2 summarizes the number counts and the median SFR of the data sets in different mass bins.

4.6.3 The gas-phase metallicity

Tremonti et al. (2004) utilized SDSS data at $z \sim 0.1$ to study the relation between gas-phase metallicity and stellar mass. They found a correlation between gas-phase oxygen abundance and stellar mass with scatter of $\pm$ 0.1 dex which extends over more than 2 orders of magnitude in stellar mass and a factor of 10 in oxygen abundance.

The ratio O/H is the abundance by number of oxygen relative to hydrogen. So for each gas particle the value $O_{\rm P} \equiv 12 + \log(M_{\rm O}/(16 * M_{\rm H}))$ is calculated, where $M_{\rm O}$ and $M_{\rm H}$ are the masses of oxygen and hydrogen. The oxygen abundance of the galaxy is taken as the particle-mass weighted median value of $O_{\rm P}$. The right panel in Figure 4.5 shows a relatively good agreement with the observed distribution (black line), in which most of the galaxies falls within 1σ spread of the data (blue transparent filled region). Nevertheless, the plot shows also that low-mass galaxies

tend to be metal-richer compared to the average value provided by observations.

4.7 Calibrating GRASIL-3D parameters

The total stellar and gas mass (both atomic and molecular) of a simulated galaxy, as well as its total bolometric luminosity in the absence of dust, are predicted by the simulation. Therefore, the sum of MC and *cirrus* total masses is fixed to the total gas mass (M_{H_2}+M_{HI}) and the sum of the young and *free* stars is also fixed to the galaxy total stellar mass.

The parameters introduced by GRASIL-3D in the RT calculation are (i) the time for newly born stars to escape from parent MC, t_{esc}, and (ii) the MC surface density, $\Sigma_{mc} = m_{mc}/r_{mc}^2$, which, with the local dust-to-gas ratio δ, determines the optical depth of the MC, i.e. $\tau \propto \delta\Sigma_{mc}$.

In order to calibrate the GRASIL-3D parameters, the radius of the MC is held fixed at r_{mc} = 15 pc, leaving only m_{mc} free to set Σ_{mc}; the latter value for r_{mc} matches observed SEDs of local galaxies (Silva et al., 1998; Granato et al., 2000) and does not prevent us from exploring the parameter space introduced by GRASIL-3D computation.

In the following Section the calibration procedure is presented, discussing in detail the variations on the median SEDs of the MUPPIBOX sample changing the values of the parameters t_{esc} and m_{mc}.

4.7.1 Calibration procedure

The GRASIL-3D parameter calibration is performed comparing the predicted near-UV to far-IR SEDs of the MUPPIBOX sample with the broadband SEDs of LVL and PEP samples. LVL, PEP and MUPPIBOX galaxies are selected with $\mathrm{Log}(M_*) > 9.3$ $M_\odot$ and are divided in different stellar mass bins and for each of them simulated galaxies are post-processed using GRASIL-3D, at fixed m_{mc}, employing different values for t_{esc}. In Figure 4.6 the columns refer to different stellar mass bins, while the rows refer to different values of m_{mc}. In those plots, masses are in $M_\odot$, t_{esc} in Myrs and the resulting SEDs are normalized to the IRAC1 band (3.6 μm). In every plot orange and violet dashed lines represent the median value for PEP and LVL samples respectively, while the corresponding filled regions show the 1σ uncertainty given by the difference between the 16% and 84% percentiles and, finally, the continuous colour lines show the median values of MUPPIBOX galaxies for different employed escape times of young stars from the parent MCs.

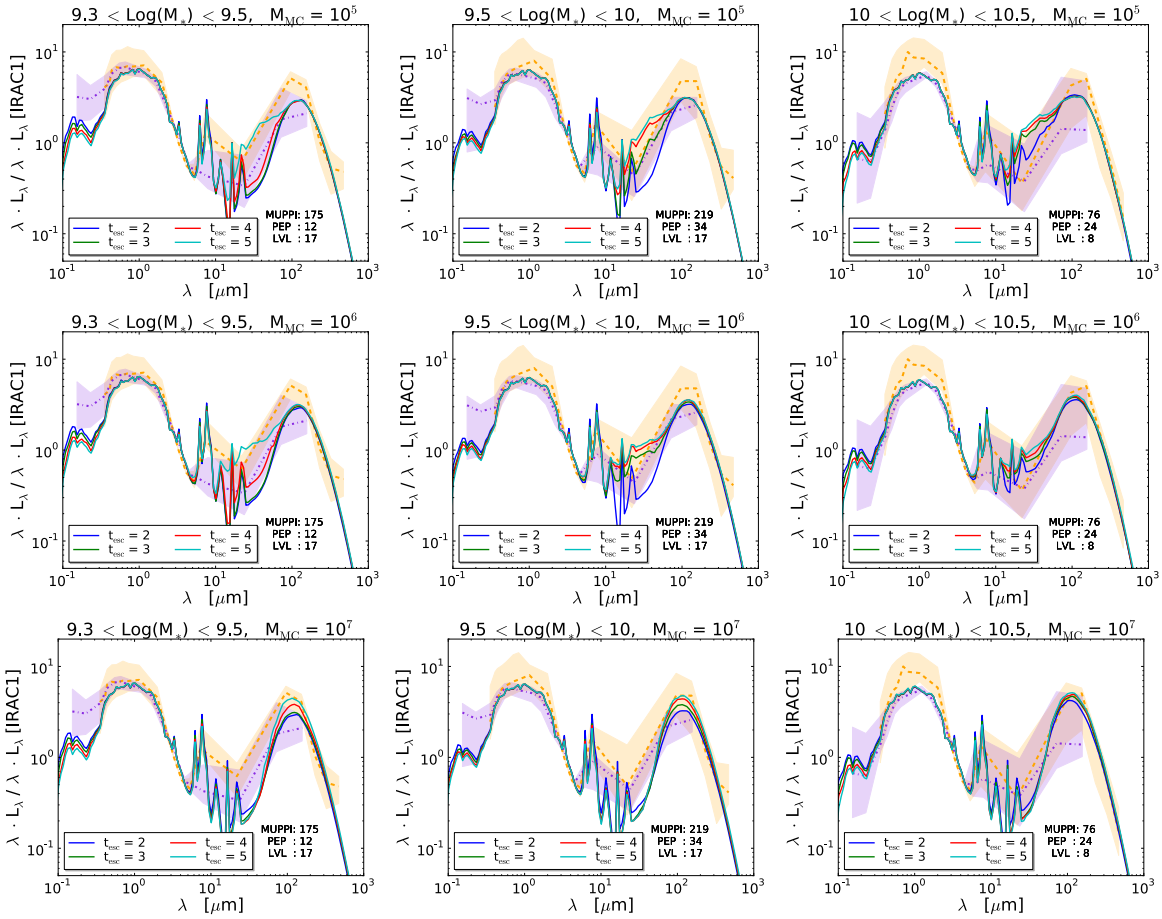

Figure 4.6: Calibration of GRASIL-3D parameters. In the column on the left the galaxies are selected in the mass range 9.3 < Log(M_*) < 9.5 $M_\odot$, on the middle in the mass range 9.5 < Log(M_*) < 10 $M_\odot$ and on the right in the mass range 10 < Log(M_*) < 10.5 $M_\odot$, for m_{mc} = 10^5 $M_\odot$ (top row), m_{mc} = 10^6 $M_\odot$ (middle row) and m_{mc} = 10^7 $M_\odot$ (bottom row). In each plot all the SEDs are normalized to the IRAC1 band (3.6 μm), continuous colour lines show the median values for different t_{esc}, while orange and violet dashed lines represent the median value for PEP and LVL samples respectively, and finally the corresponding filled regions gives the 1σ uncertainty. Every plot reports the number of galaxies in the MUPPIBOX sample, PEP sample and LVL sample (MUPPI, PEP and LVL respectively).

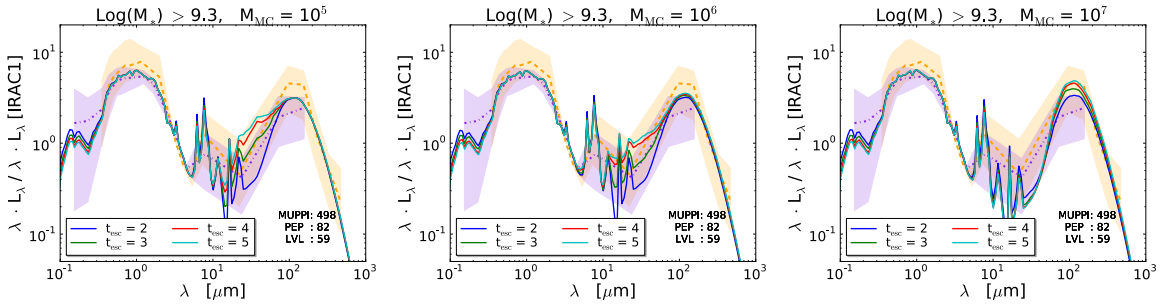

Figure 4.7: Calibration of GRASIL-3D parameters. In all plots only galaxies with Log(M_*) $>$ 9.3 $M_\odot$ and m_{mc} = 10^5 $M_\odot$ (left), m_{mc} = 10^6 $M_\odot$ (middle), m_{mc} = 10^7 $M_\odot$ (right) are taken into account. In each plot all the SEDs are normalized to the IRAC1 band (3.6 μm), continuous colour lines show the median values for different t_{esc}, while orange and violet dashed lines represent the median value for PEP and LVL samples respectively, and finally the corresponding filled regions gives the 1σ uncertainty. Every plot reports the number of galaxies in the MUPPIBOX sample, PEP sample and LVL sample (MUPPI, PEP and LVL respectively).

Reasonable values for t_{esc} (2,3,4,5 Myrs) and m_{mc} (10^5-10^6-10^7 $M_\odot$) are explored, as adopted in previous works (e.g. Silva et al., 1998; Granato et al., 2000; Domínguez-Tenreiro et al., 2014; Obreja et al., 2014; Granato et al., 2015). As expected, with t_{esc} increasing from 2 to 5 Myrs at fixed m_{mc}, the UV emission decreases, but the MC emission increases and the *cirrus* emission in the PAH region decreases. Hence, the net result is that the emission increases from the PAH region up to $\sim$ 100 μm, leaving the peak unaffected. On the other hand, as m_{mc} increases from 10^5 up to 10^7 $M_\odot$ at fixed t_{esc}, the *cirrus* emission is unaffected, but the bulk of the MC emission moves to longer wavelengths (lower dust temperature) due to the increased optical depth. The net result is a decreased emission in the PAH region but a higher IR-peak.

In what follows the results are discussed for every mass bin, represented by the columns in Figure 4.6. Table 4.2 summarizes the main properties, such as SFR and number count, of the samples in the selected mass bins.

- Left column - 9.3 $<$ Log(M_*) $<$ 9.5 $M_\odot$:

  From *FUV* up to mid-IR ($\sim$ 10 μm) there is not substantial variation among different values of m_{mc} which, on the contrary, mostly affects the IR-peak. The PAH emission is considerably enhanced by the highest value t_{esc} = 5 Myrs, even if for m_{mc} = 10^7 $M_\odot$ the bulk of the MC emission is considerably

shifted at lower frequency due to the increased optical depth, depleting for all the available t_{esc} the PAH emission.

- Middle column - $9.5 < \mathrm{Log}(M_*) < 10\ M_\odot$:

  The global trend reflects what has been already discussed for the previous mass bin. The SEDs with values t_{esc} = 3-4 Myrs are quite well in agreement with PEP and LVL samples in the PAH region, except for the the highest value $m_{mc} = 10^7\ M_\odot$.

- Right column - $10 < \mathrm{Log}(M_*) < 10.5\ M_\odot$:

  The SEDs with lower values t_{esc} = 2-3 Myrs are better in agreement with PEP and LVL samples in the PAH region.

In all the explored mass bins the highest $m_{mc} = 10^7\ M_\odot$ appears to overestimate the optical depth enhancing the IR-emission and at the same time to decrease the PAH-emission. $m_{mc} = 10^6\ M_\odot$ fits better in all the mass bins the PEP and LVL's median values. Furthermore the best values for the escape time are low-intermediate ones, i.e. t_{esc} = 2-3 Myrs.

Results for all the galaxies ($\mathrm{LogM}_* > 9.3\ M_\odot$) are shown in Figure 4.7. t_{esc} = 3 Myrs fits better the median PEP and LVL's values in the PAH region. There is no substantial difference between 10^5 and $10^6\ M_\odot$ for the m_{mc}.

The values $m_{mc} = 10^6\ M_\odot$ and t_{esc} = 3 Myrs are set for all the analysis presented in the Chapter. Figure 4.8 shows the best fit with these parameters. It is worth to be noted that Granato et al. (2000), combining a semianalytic galaxy formation model with GRASIL, found a good overall agreement with observations for a sample of *normal* (i.e. not selected galaxies undergoing a recent burst) spirals ($B/T < 0.5$), employing the same set of parameters.

4.8 Comparisons with HRS

After the calibration of GRASIL-3D parameters, the aim is to compare the absolute IR luminosity (8-1000 μm) of MUPPIBOX sample with the HRS one, this time checking SED normalizations and not only their shapes. The stellar mass limit of HRS is $\sim 10^9\ M_\odot$, a factor of ~ 2 lower than the resolution limit of the simulation, so the comparison with SEDs binned in stellar mass will be limited to $M_* > 2 \cdot 10^9\ M_\odot$.

In Figure 4.9 and Figure 4.10 the samples are divided according to the stellar mass content and SFR respectively. In every plot continuous red line shows the

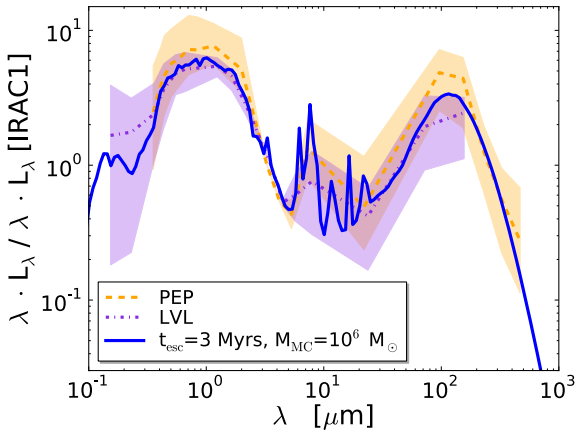

Figure 4.8: Best fit of GRASIL-3D parameters calibration. Galaxies are selected with Log(M_*) $>$ 9.3 $M_\odot$ in MUPPIBOX, LVL and PEP samples. All the SEDs are normalized to the IRAC1 band (3.6 μm). Continuous blue line shows the median value of MUPPIBOX sample with t_{esc}=3 Myrs, and m_{mc}=10^6 $M_\odot$, while orange dashed and violet dot-dashed lines represent the median value of PEP and LVL samples respectively, and the corresponding filled regions give the 1σ uncertainty.

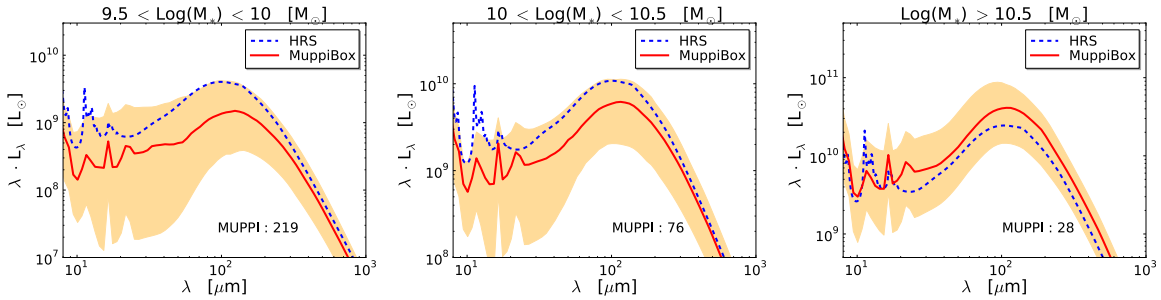

Figure 4.9: Comparison with HRS. Selection in stellar mass bin. From the left to the right the galaxies are selected with 9.5 $<$ Log(M_*) $<$ 10 $M_\odot$, 10 $<$ Log(M_*) $<$ 10.5 $M_\odot$ and Log(M_*) $>$ 10.5 $M_\odot$. In every plot the blue dashed line shows the median value in the relative mass bin of the HRS sample, the continuous red line and the orange filled region show the median value and the 1σ uncertainty of the MUPPIBOX sample. MUPPI reports the number of MUPPIBOX galaxies in the selected bin.

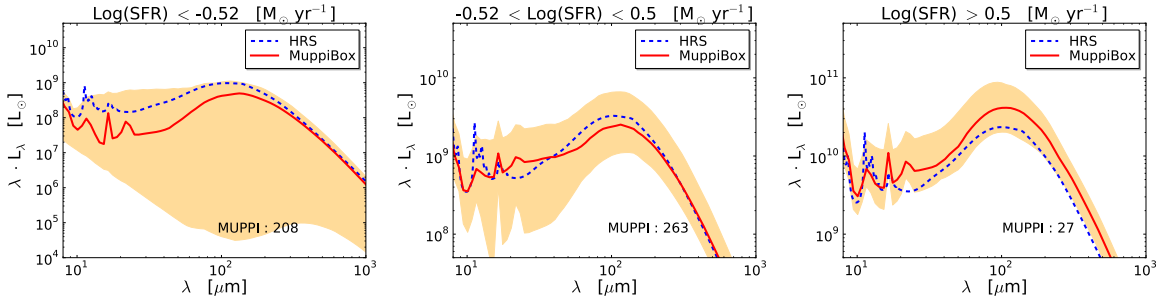

Figure 4.10: Comparison with HRS. Selection in SFR bin. From the left to the right the galaxies are selected with Log(SFR) $<$ -0.52 $M_\odot$ yr^{-1}, -0.52 $<$ Log(SFR) $<$ 0.5 $M_\odot$ yr^{-1} and Log(SFR) $>$ 0.5 $M_\odot$ yr^{-1}. In every plot the blue dashed line shows the median value in the relative SFR bin of the HRS sample, the continuous red line and the orange filled region show the median value and the 1σ uncertainty of the MUPPIBOX sample. MUPPI reports the number of MUPPIBOX galaxies in the selected bin.

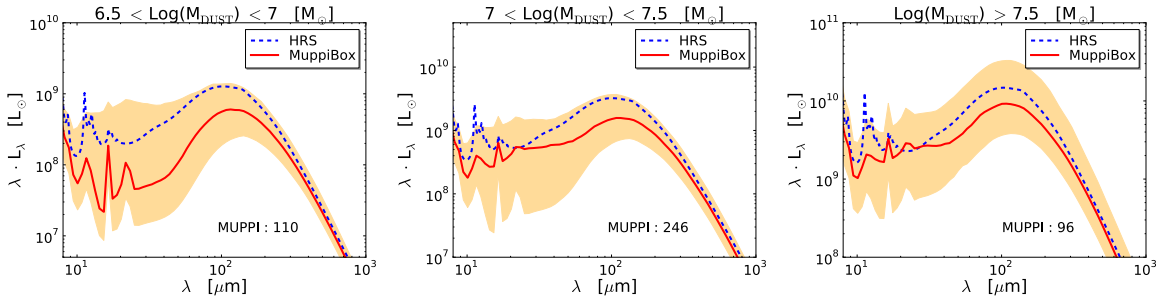

Figure 4.11: Comparison with HRS. Selection in dust mass bin. From the left to the right galaxies are selected with 6.5 $<$ Log(M_{DUST}) $<$ 7, 7 $<$ Log(M_{DUST}) $<$ 7.5 and Log(M_{DUST}) $>$ 7.5. In every plot the blue dashed line shows the median value in the relative mass bin of the HRS sample, the continuous red line and the orange filled region show the median value and the 1σ uncertainty of the MUPPIBOX sample. MUPPI reports the number of MUPPIBOX galaxies in the selected bin.

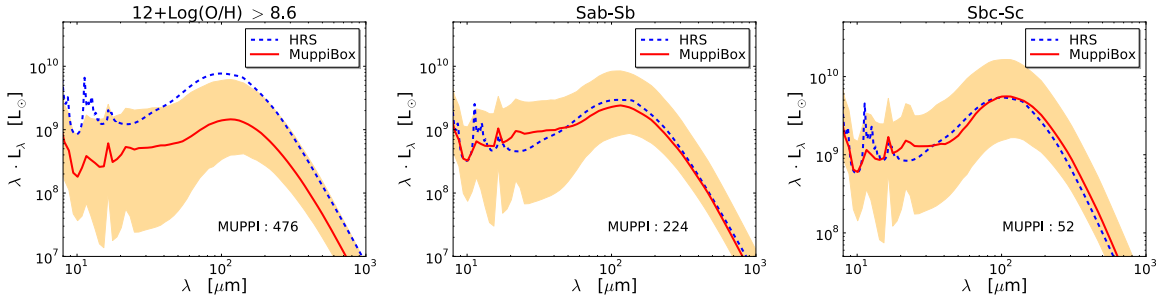

Figure 4.12: Comparison with HRS. Selection in gas metallicity bin and morphology. On the left galaxies are selected with 12+Log(O/H) $>$ 8.6, on the middle Sab-Sb morphological type corresponds to B/T in the range [0.1, 0.5] and on the right Sbc-Sc corresponds to B/T in the range [0.05, 0.33]. In every plot the blue dashed line shows the median value in the relative bin of the HRS sample, the continuous red line and the orange filled region show the median value and the 1σ uncertainty of the MUPPIBOX sample. MUPPI reports the number of MUPPIBOX galaxies.

median MUPPIBOX infrared SED, while the blue dashed line shows the HRS one; orange filled region shows the 1σ uncertainty, given by the difference between the 16% and 84% percentiles, on the median of the MUPPIBOX sample; Ciesla et al. (2014) do not give scatter for their SEDs. The plots reflect the trend of the *main sequence* in which, on average, MUPPIBOX galaxies with Log(M_*) $\gtrsim$ 10.5 $M_\odot$, corresponding to Log(SFR) $\gtrsim$ 0.5 $M_\odot$ yr^{-1}, have SFRs greater than HRS ones and higher IR bolometric luminosity accordingly. SED shapes are very similar to the observed ones, peak positions are closely reproduced with the exception of the smallest galaxies where dust is colder.

In Figure 4.11 the sample is divided in relation to the dust mass content; in the dust mass bins 6.5 $<$ Log(M_{DUST}) $<$ 7, 7 $<$ Log(M_{DUST}) $<$ 7.5 and Log(M_{DUST}) $>$ 7.5 $M_\odot$, the median MUPPIBOX stellar masses are Log(M_*) = 9.40, Log(M_*) = 9.61 and Log(M_*) = 10.25 $M_\odot$ respectively.

In Figure 4.12 the sample is binned according to the gas-phase metallicity and morphology. The median stellar mass of simulated galaxies on the left panel of Figure 4.12 is Log(M_*) = 9.62 $M_\odot$, so with a large number (almost the entire sample) of low-mass and low-luminous galaxies. This leads to a worse agreement with HRS mean value which, at $\simeq$ 100 μm, is above the MUPPIBOX scatter.

To compare with HRS templates binned by morphological type, the B/T esti-

mates proposed by Oohama et al. (2009) are adopted. They made a bulge-disk decomposition on 737 spiral and lenticular galaxies taken from the SDSS galaxy sample for which morphological types are estimated. They studied B/T as a function of morphological types of disk galaxies and they found for Sab-Sb type galaxies the value B/T = 0.29 $\pm$ 0.2, and for Sbc-Sc type galaxies the value B/T = 0.19 $\pm$ 0.14. Figure 4.12 shows the median MUPPIBOX and HRS IR SEDs for Sab-Sb (middle panel) and Sbc-Sc (right panel) galaxies. Even if the kinetic B/T decomposition overestimates what would be photometrically measured, as already mentioned in Section 1.2.6, with the adopted morphological classification a very good agreement with HRS is found.

4.9 Conclusions

In this Chapter the properties of a sample of simulated galaxies have been quantified, starting from the gas mass scaling, the main sequence and the the gas-phase metallicity, then performing the RT calculation by means of GRASIL-3D to assess the IR dust emission and make direct photometric comparisons with data coming from observations.

The main conclusions are the following:

(i) In the context of ΛCDM cosmology, MUPPIBOX galaxies show properties in agreement with those observed in the local Universe, dominated by late-type galaxies. The majority of simulated galaxies lies within the scatter of the observed gas-richness scaling relations (Jiang et al., 2015), shows on average a good agreement with the HRS main sequence and falls within 1σ of the observed Tremonti et al. (2004) relation. However, at the low-mass end, simulated galaxies are gas-poorer, too passive and metal-richer than the observed ones.

(ii) The RT calculation performed by GRASIL-3D requires the calibration of two physically motivated parameters, i.e. the time for newly born stars to escape from their parent molecular clouds and their optical depth. The calibration is performed comparing the shapes of the normalized SEDs of the MUPPIBOX sample with those of LVL and PEP samples. Exploring reasonable ranges for the parameters, predicted near-UV to far-IR SEDs are well in agreement with the shapes of the median SEDs of PEP and LVL samples.

(iii) Absolute median IR luminosity (8-1000 μm) of MUPPIBOX sample is compared with HRS one. In agreement with the main sequence, the HRS median IR luminosity is well within 1σ of the simulated result, with a difference less than 0.5 dex, meaning that simulated sample fairly reproduces both the shape and the normalization of the infrared observed luminosity in the local Universe. Moreover MUPPIBOX galaxies have been binned by stellar and dust mass, star formation rate, metallicity and morphological type and compared with the IR best-fit models of the HRS sample. In all the selected bins the difference between the median simulated and observed HRS values reaches at most 0.5 dex, with a mean value of $\simeq 0.25$ dex.

The agreement of results presented in this paper with observations is promising, showing that MUPPI, using fully local properties of gas as input to the sub-resolution recipe, meets the aim of simulating large cosmological volumes, representatives of the local Universe. The simulations do not require any post-processing tool in order to derive the atomic and molecular fractions in each gas particles, but they are evaluated on the fly by MUPPI algorithm, adopting the phenomenological prescription provided by Blitz & Rosolowsky (2006). A more effective feedback mechanism for the low-mass end galaxies, able to better regulate their star formation, is necessary. It is worth pointing out that AGN feedback, resulting from gas accretion onto super-massive black holes, is another missing ingredient and it should regulate the star formation in the high-mass end.

5

Molecular hydrogen and molecular cooling

An accurate treatment of the multiphase ISM in simulations of galaxy formation requires to follow the evolution of the thermal state of the gas as well as the evolution of its chemical state, including its molecular chemistry. Maio et al. (2007) presented one implementation of H_2-chemistry in GADGET, which is suitable to deal with both primordial and metal-enriched gas; the model does not take into account H_2 formation onto dust grains and its UV-photodissociation.

In this Chapter[1] a *preliminary* chemical network is presented; it is able to solve the thermal and chemical evolution of the cold phase of a MUPPI particle, modelling the molecular cooling which dominates the cooling rate at $T < 10^4$ K. The main goal, motivated by the tight observed connection between molecular hydrogen and star formation (e.g. Bigiel et al., 2008), is to track self-consistently the non-equilibrium abundance and cooling processes of H_2 and H_2-based star formation in simulations, instead of employing the phenomenological relation by Blitz & Rosolowsky (2006) as the current version of MUPPI does. The model presented by Maio et al. (2007) has been extended to take into account the effect of H_2 formation onto dust grains and its UV-photodissociation and it has been coupled (in preliminary form) with the MUPPI algorithm.

The Chapter is organized as follows. Section 5.1 is devoted to describe the chemical network presented by Maio et al. (2007). Section 5.2 presents the chemistry of

[1]Some of the results presented in this Chapter are related with contents shown in the Master Thesis *Di Cerbo, P. - "Modelli di formazione e distruzione di idrogeno molecolare in simulazioni di formazione di galassie", 2015* (Di Cerbo, 2015). I participated to the supervision of this Thesis.

molecular hydrogen, while models for molecular hydrogen formation suited for applications in galaxy formation simulations are described in Section 5.3. Section 5.4 describes how the chemical network presented by Maio et al. (2007) has been extended. Section 5.5 presents the preliminary coupling of the chemical network with the MUPPI algorithm. Section 5.6 investigates the ability of the chemical network coupled with MUPPI to recover the phenomenological nearly linear relation between the ratio of molecular to atomic gas and its pressure provided by Blitz & Rosolowsky (2006) (BR). Section 5.7 shows the tests of the effect of using the H_2 calculated by the modified chemical network (instead of the BR prescription) on star formation, on a simulated disk galaxy. Concluding remarks are given in Section 5.8.

5.1 The Maio et al. (2007) chemical network

Maio et al. (2007) extended an existing implementation in GADGET of H_2 chemistry (Yoshida et al., 2003), in order to include HD, HeH^+ and metal cooling below 10^4 K, since gas with primordial and metal-enriched composition is expected to be relevant for the formation and evolution of cold objects.

The process that allows the gas to cool down to $\sim$10 K is the conversion of kinetic energy into radiation that eventually escapes from the system (in the optically thin regime). This occurs via inelastic collisions which lead electrons to upper states, followed by de-excitations and subsequent emission of radiation. Cooling processes depend on the type of elements considered and of transitions involved. Below 10^4 K and for a primordial composition, Hydrogen, helium, some H_2-based molecules and HD are expected to be the main coolants, but, if the ISM is polluted by metals, such heavier elements dominate the cooling rate, thanks to a larger number of possible atomic transitions with different energy gaps.

More in detail, the chemical network presented by Maio et al. (2007) is able to follow the evolution of e^-, H, H^+, He, He^+, He^{++}, H_2, H_2^+, H^-, D, D^+, HD and HeH^+, dealing with the contribution from fine structure transitions of oxygen, carbon, silicon and iron at $T < 10^4$K, in which the populations of the levels, for each species, have been computed using the detailed balancing principle.

HD cooling has some influence on the high-redshift gas-clumping properties, while metal cooling has a significant impact at low-temperature. The left panel of Figure 5.1 highlights that only H_2 and HD can be useful to cool the gas down to some 10^2 K in primordial gas, while right panel of the same figure shows that the heavy elements become the most-efficient coolants in metal-enriched ISM.

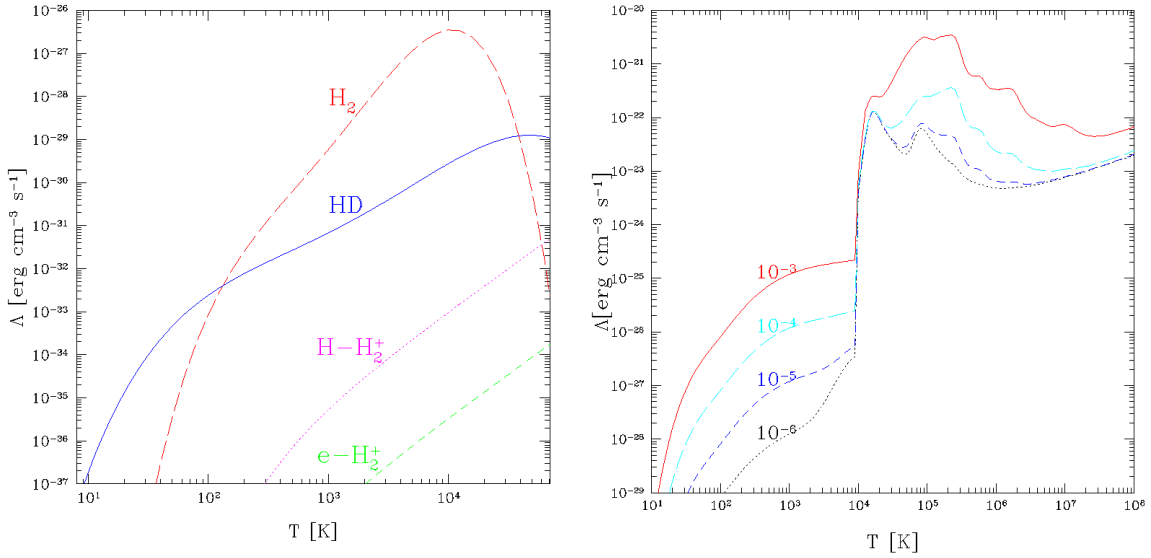

Figure 5.1: Left panel: cooling functions for a primordial gas with hydrogen number density $n_{\rm H} = 1{\rm cm}^{-3}$ and the following fractions for the different species: $x_{\rm HD} = 10^{-8}$, $x_{\rm H_2} = 10^{-5}$, $x_{\rm H_2^+} = 10^{-13}$ and $x_{\rm e^-} = 10^{-4}$. The H_2 cooling function (long-dashed line) is plotted with the HD (solid line), H-impact H_2^+ (dotted line) and e-impact H_2^+ (short-dashed line) cooling functions. Right panel: Total cooling due to hydrogen, helium, metals, H_2 and HD molecules as a function of the temperature, for gas having $n_{\rm H} = 1{\rm cm}^{-3}$, $x_{\rm H_2} = 10^{-5}$ and $x_{\rm HD} = 10^{-8}$. Labels refer to different amount of metals, with metal fraction of 10^{-3} (solid line), 10^{-4} (long-dashed line), 10^{-5} (short-dashed line) and 10^{-6} (dotted line). Reproduced from Maio et al. (2007).

5.1.1 Numerical method

Non-equilibrium atomic and molecular reactions are characterized by creation and destruction rates which can differ by many orders of mag among the different species and reactions. As a result, explicit schemes for integration can be unstable unless unreasonably small time steps, smaller than the shortest dynamical time in the reaction, are taken. For this reason computation with many reactions involved is inefficient in modelling the ISM in cosmological simulation of galaxy formation. Usually stiff sets of equations are integrated by means of implicit methods which generally involve iterative procedures to achieve convergence. Some algorithms are able to identify the disparity in time scales among the species and to switch between stiff and non-stiff solvers.

The code uses to solve the kinetic rate equations with multi-species chemistry in non-equilibrium, and self-consistently employed by Maio et al. (2007) and before by Yoshida et al. (2003), is based on the method developed by Anninos et al. (1997). The method is based on a Backward Differencing Formula (BDF) for the required stability when solving stiff sets of equations and it is designed, in particular, for both accuracy and speed. Backward differentiation methods are stable when applied to problem of the kind $\dot{y} - f(y,t)$ (Oran & Boris, 1987). Other methods, such as Adams-Bashforth and Runge-Kutta algorithms, are unstable, less accurate or more expensive computationally (Anninos et al., 1997) (but see Section 5.8).

Solving the kinetic equations

Two-body chemical reaction involves the interaction of two reactants p and q to yield two products l and m. Schematically:

$$p + q \xrightarrow{\text{k}} l + m \tag{5.1}$$

where k is the reaction rate.

Given a mixture of chemical elements, for each species i, the variation in time of its number density n_i is:

$$\frac{dn_i}{dt} = \sum_p \sum_q k_{pq,i} n_p n_q - \sum_l k_{li} n_l n_i \tag{5.2}$$

where $k_{pq,i}$ is the creation rate from species p and q and k_{li} is the destruction rate from interactions of the species i with the species l. Both creation and destruction

rates are temperature-dependent. A complete list of the reactions in the code presented by Maio et al. (2007) is given in Table 5.1 while the temperature evolution of the reaction rates for H_2 chemistry is shown in Figure 5.2; continuous lines refer to reactions in which H_2 forms, while dashed lines refer to reactions in which H_2 is destroyed.

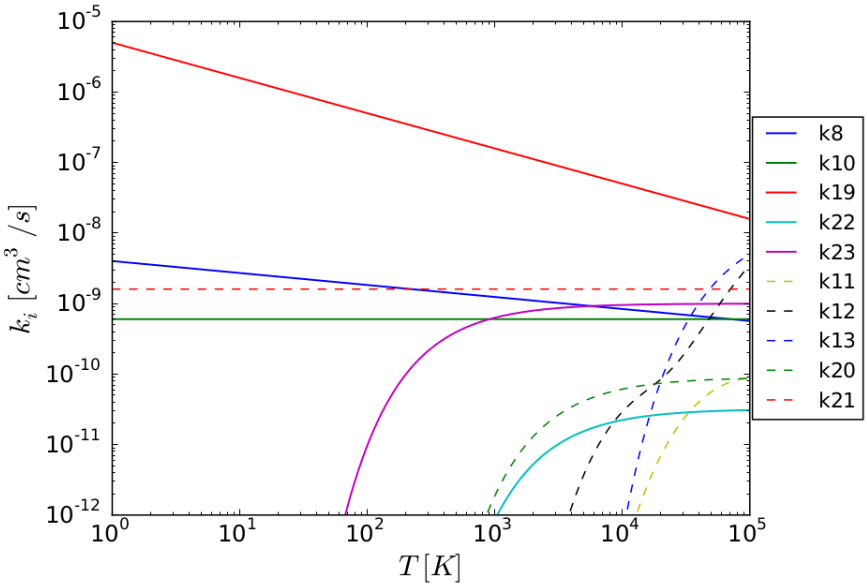

Figure 5.2: Temperature evolution of the reaction rates for H_2 chemistry. Continuous lines refer to reactions in which H_2 forms, while dashed lines refer to reactions in which H_2 is destroyed. Labels refer to the number of reactions in Table 5.1. Reproduced from Di Cerbo (2015).

Equations 5.1.1 can be written as:

$$\frac{dn_i}{dt} = C_i(T, n_p, n_q) - D_i(T, n_l)n_i \tag{5.3}$$

where the creation coefficient for the species i is introduced, in ($cm^{-3}s^{-1}$) as:

$$C_i = \sum_p \sum_q k_{pq,i} n_p n_q \tag{5.4}$$

and the destruction coefficient, in (s^{-1}), as:

$$D_i = \sum_l k_{li} n_l \tag{5.5}$$

ID	Reactions	References for the rate coefficients
1	$H + e^- \rightarrow H^+ + 2e^-$	A97 / Y06
2	$H^+ + e^- \rightarrow H + \gamma$	A97 / Y06
3	$He + e^- \rightarrow He^+ + 2e^-$	A97 / Y06
4	$He^+ + e^- \rightarrow He + \gamma$	A97 / Y06
5	$He^+ + e^- \rightarrow He^{++} + 2e^-$	A97 / Y06
6	$He^{++} + e^- \rightarrow He^+ + \gamma$	A97 / Y06
7	$H + e^- \rightarrow H^- + \gamma$	A97 / Y06
8	$H^- + H \rightarrow H_2 + e^-$	A97 / Y06
9	$H + H^+ \rightarrow {H_2}^+ + \gamma$	A97 / Y06
10	${H_2}^+ + H \rightarrow H_2 + H^+$	A97 / Y06
11	$H_2 + H \rightarrow 3H$	A97
12	$H_2 + H^+ \rightarrow {H_2}^+ + H$	S04 / Y06
13	$H_2 + e^- \rightarrow 2H + e^-$	ST99 / GB03 / Y06
14	$H^- + e^- \rightarrow H + 2e^-$	A97 / Y06
15	$H^- + H \rightarrow 2H + e^-$	A97 / Y06
16	$H^- + H^+ \rightarrow 2H$	P71 / GP98 / Y06
17	$H^- + H^+ \rightarrow {H_2}^+ + e^-$	SK87 / Y06
18	${H_2}^+ + e^- \rightarrow 2H$	GP98 / Y06
19	${H_2}^+ + H^- \rightarrow H + H_2$	A97 / Y06
20	$D + H_2 \rightarrow HD + H$	WS02
21	$D^+ + H_2 \rightarrow HD + H^+$	WS02
22	$HD + H \rightarrow D + H_2$	SLP98
23	$HD + H^+ \rightarrow D^+ + H_2$	SLP98
24	$H^+ + D \rightarrow H + D^+$	S02
25	$H + D^+ \rightarrow H^+ + D$	S02
26	$He + H^+ \rightarrow HeH^+ + \gamma$	RD82, GP98
27	$HeH^+ + H \rightarrow He + H_2^+$	KAH79, GP98
28	$HeH^+ + \gamma \rightarrow He + H^+$	RD82, GP98

Table 5.1: Set of reactions in the code. P71 = Peterson et al. (1971); KAH79 = Karpas (1979); RD82 = Roberge & Dalgarno (1982); SK87 = Shapiro & Kang (1987); A97 = Abel et al. (1997); GP98 = Galli & Palla (1998); SLP98 = Stancil et al. (1998); ST99 = Stibbe & Tennyson (1999); WS02 = Wang & Stancil (2002); S02 = Savin (2002); GB03 = Glover & Brand (2003); S04 = Savin et al. (2004); Y06 = Yoshida et al. (2007). Reproduced from Maio et al. (2007).

Equation 5.3 is solved with a BDF, in which all source terms are evaluated at the advanced time step. The discretization of Equation 5.3 yields:

$$n_i^{t+\Delta t} = \frac{C_i^{t+\Delta t}\Delta t + n_i^t}{1 + D_i^{t+\Delta t}\Delta t} \tag{5.6}$$

The solver has been optimized further due to the fact that H^- and H_2^+ in the molecular hydrogen production process have always low concentrations and large rate coefficients, meaning that they do not strongly affect the concentrations of hydrogen, helium and electrons. This translates into a separation of the nine species into fast and slow reactants. The former, i.e. H^- and H_2^+, are decoupled from the slow reactants and treated independently because their kinetic time scales are much shorter than the ones of the other species, so they can be considered in equilibrium at all times. The equilibrium abundance of H^- can be written independently of H_2^+ as:

$$n_{H^-} = \frac{k_7 n_H n_e}{(k_8 + k_{15})n_H + k_{14} n_e + (k_{16} + k_{17})n_{H^+}} \tag{5.7}$$

neglecting the reaction 19 in Table 5.1 due to low concentration of both H^- and H_2^+. Then given the abundance of H^-, $n_{H_2^+}$ can be evaluated at the equilibrium as:

$$n_{H_2^+} = \frac{k_9 n_H n_{H^+} + k_{12} n_{H_2} n_{H^+} + K_{17} n_{H^-} n_{H^+}}{k_{10} n_H + k_{18} n_e + k_{19} n_{H^-}} \tag{5.8}$$

Due to the intrinsic nonlinearity of Equation 5.3, not all source terms can be evaluated at the advanced time levels. The first improvement of Yoshida et al. (2003) is made by updating sequentially each species, rather than updating all species simultaneously from the values at the previous time step. The second one is done by subcycling within a single time step in such a way that the maximum fractional change in the electron concentration is limited to a given quantity per time step:

$$\Delta t = \epsilon \frac{n_e}{\dot{n}_e} \tag{5.9}$$

where ϵ is a free parameter, usually set $\epsilon = 0.1$ (this value has been held fixed for all results presented in this Chapter).

Solving for the energy

The system is a mixture of different species characterized by a single temperature. Hence, the energy changes are computed from radiative cooling and heating from

microphysical processes, as:

$$\frac{du}{dt} = -\dot{E}_{\rm cool} + \Gamma \tag{5.10}$$

where u is the specific internal energy, in the right-hand side the terms are the cooling and heating processes, respectively.

More in detail, the cooling term is evaluated as:

$$\dot{E}_{\rm cool} = \dot{E}_{\rm Comp} + \sum_j \sum_l \dot{\lambda}_{jl}(T)\rho_j\rho_l \tag{5.11}$$

where $\dot{E}_{\rm Comp}$ is the Compton cooling/heating due to interactions of free electrons with the cosmic microwave background radiation and λ_{jl}(T) are the cooling rates related to the interactions between the species j and l.

The heating term reads:

$$\Gamma = \sum_j J_j(\nu)\rho_j \tag{5.12}$$

where $J_j(\nu)$ are integrals due to photoionizing and photodissociating heating, i.e.:

$$J_j(\nu) = \int_{\nu_{0,j}}^{\infty} 4\pi\sigma_j(\nu)I(\nu)\frac{h\nu - h\nu_{0,j}}{h\nu}d\nu \tag{5.13}$$

where $\sigma_j(\nu)$ are the cross section for a given process and $\nu_{0,j}$ a threshold frequency for the species i.

The code treats cooling and heating mechanisms in the case of optical thin gas. The original code (Yoshida et al., 2003) models Compton cooling/heating and Bremsstrahlung (Black, 1981), hydrogen and helium cooling from collisional ionization, excitation and recombination (Hui & Gnedin, 1997), photoionization and photodissociation heating (details in Anninos et al., 1997; Abel et al., 1997). Maio et al. (2007) included HD-cooling functions from Lipovka et al. (2005) and metal-dependent cooling ($T < 10^4$K). The treatment of metal cooling has been included by computing the populations of the levels, for each species, using the detailed balancing principle, assuming that the UV radiation ionizes carbon, silicon and iron, while oxygen remains neutral since its first ionization potential is higher than 13.6 eV.

The subcycling procedure to set up the subcycle time steps (Equation 5.9), described in the previous paragraph, is used also to update the energy, at fixed density for the mixture of species, in the cooling/heating step.

5.2 Molecular gas in the ISM

Formation of molecular hydrogen involves two physically distinct channels: in numerous two-body reactions in the gaseous phase, from rare ions such as H^- and H_2^+, and on the surface of dust grains, which serve as catalysts (a complete reference for these processes is Richings et al., 2014). Since H^- and H_2^+ are rare, the reactions are slow; this channel of H_2 dominates in gas with primordial composition because it does not require any metal and it is connected with the formation of Pop III stars at high redshift. The fraction of molecular hydrogen forming in the gas phase saturates at 10^{-3} - 10^{-2} and it increases only in high density environment, $\sim 10^{12}$ cm^{-3}, when 3-body reactions become efficient. Based on reaction time arguments, it is well established that the formation of H_2 must proceed predominantly by grain surface reactions (Hollenbach & Salpeter, 1971). It is usually assumed that atomic hydrogen accumulates on the surface of dust grains where the interaction rate of two H atoms is larger. Hence, the formation rate, R_D, is usually modelled as:

$$\frac{dn_{H_2}}{dt}|_{dust} = R_D = R_0 D_{MW} n_{HI} n_{HI} \tag{5.14}$$

where R_0 is the reaction rate and D_{MW} measures the abundance of dust relative to the solar neighbourhood: i.e. $D_{MW} = 1$ implies the same abundance of dust per unit mass of gas as in the MW ISM in the solar vicinity. $R_0 \sim 3.5 \times 10^{-17}$cm^{3}s^{-1} has been measured by Wolfire et al. (2008) and this rate is known to depend on the dust temperature.

However, the equilibrium abundance of H_2 in diffuse gas depends also on the intensity of the InterStellar Radiation Field (ISRF) in which it resides. Photons in the Lyman and Werner bands (LW), at energies between 11.3 and 13.6 eV, photodissociate H_2 and H_2-based species. Moreover, molecular hydrogen is destroyed by collisions with atoms and other molecules when gas temperature raises above $\sim$5000 K. ISRF is modelled based on the observations of various line ratios in the ISM (e.g. Draine, 1978; Mathis et al., 1983). In the MW the radiation field decreases with the distance from the galactic centre and in the solar vicinity its value is $J_0 \approx 10^6$phot/cm^2/s/eV/rad.
Hence, defining:

$$U_{MW} \equiv \frac{J_{LW}}{J_0} \tag{5.15}$$

where J_{LW} is the average radiation field in the LW bands; in the solar neighbourhood U_{MW} = 1 by definition. Chen et al. (2009) found that, in high redshift $z \sim 2$

galaxies, the radiation field can raise up to values $U_{\rm MW} = 30 - 300$.

As discussed in Section 1.3, dust absorbs radiation over a very large range of wavelengths and, as a first approximation, the dust opacity, being a smooth function of wavelengths, can be considered constant over the narrow LW bands. Dust opacity has been well studied in local galaxies, i.e. MW and two Magellanic clouds, and it is roughly proportional to the dust-to-gas ratio (Weingartner & Draine, 2001b):

$$\sigma_{\rm LW} = D_{\rm MW}\sigma_0 \tag{5.16}$$

with $\sigma_0 = 1.7 \times 10^{-21}{\rm cm}^2$ and $D_{\rm MW} = 1$ in the MW.

Therefore the presence of dust translates into a *shielding* effect against the dissociation of molecular hydrogen due to the ISFR. Accounting for continuum shielding over a narrow band is relatively easy and so the molecular hydrogen photo-dissociation rate Γ is:

$$\Gamma \approx e^{-\bar{\tau}_{\rm d}}\Gamma_{\rm LW} \tag{5.17}$$

where $\bar{\tau}_{\rm d} \equiv \bar{\sigma}_{\rm d} N_{\rm H}$ is the average dust opacity in the LW bands, $N_{\rm H}$ is the total hydrogen column density and $\Gamma_{\rm LW}$ is the photo-destruction rate in the absence of any shielding. Commonly the photo-destruction rate is written as $\Gamma = S_{\rm D}\Gamma_{\rm LW}$, through the shielding factor $S_{\rm D}$ defined as:

$$S_{\rm D}(D_{\rm MW}, N_{\rm H}) = e^{-D_{\rm MW}\sigma_0 N_{\rm H}} \tag{5.18}$$

Also the molecular self-shielding (*optically thick* regime) plays a role, but the modelling of such effect is complex because the probability of dissociation varies significantly for different lines within the LW bands. Thus, the shielded photo-destruction rate is represented as a sum over individual, optically thin or thick lines as a function of that probability and it gives rise to a self-shielding factor which falls at a rate lower than the exponential decline for an individual line. Draine & Bertoldi (1996) provided an approximation for the self-shielding factor:

$$S_{\rm H_2} = \frac{1-\omega_{\rm H_2}}{(1+x)^2} + \frac{\omega_{\rm H_2}}{(1+x)^{1/2}} e^{-0.00085(1+x)^{1/2}} \tag{5.19}$$

where $x \equiv N_{\rm H_2}/(5 \cdot 10^{14}){\rm cm}^{-2}$ and $\omega_{\rm H_2}$ is treated as an adjustable parameter. Top panel on Figure 5.3 shows the molecular self-shielding factor as a function of H_2 column density. $S_{\rm H_2}$ is reported as a red line; a gradual decline of the self-shielding factor, $S_{\rm H_2} \propto N_{\rm H_2}^{-0.75}$ (red dotted line), is apparent for almost 8 orders of magnitude, but at very high density, $N_{\rm H_2} \gtrsim 10^{22}{\rm cm}^{-2}$, the fall-off becomes steeper, when,

basically, the molecular cloud behaves as a continuum optically thick medium. For comparison, exponentially falling off shielding factor (dust shielding with MW dust and fully molecular gas) is shown as a blue line.

Gnedin et al. (2009) proposed a model for the distribution of column density inside each molecular cloud. They used a Sobolev-like approximation:

$$N_{H_2} \approx n_{H_2} L_{Sob} \tag{5.20}$$

where

$$L_{Sob} \equiv \frac{\rho}{2|\nabla\rho|} \tag{5.21}$$

which provides an essentially unbiased estimate for the true column density obtained by the integration along random lines of sight (Figure 1 in Gnedin et al. 2009).

Models accounting for non-equilibrium molecular chemistry, for the creation of H_2 onto the surface of dust grains, for photo-destruction by LW photons and relative shielding from ISFR, are able to match the observed surface densities of atomic and molecular gas on scales which are comparable to the typical resolution of simulations ($\gtrsim$ 500 pc), where they are actually measured (bottom panel of Figure 5.3). Models like the one shown by Gnedin & Kravtsov (2011) capture the observed saturation of the atomic surface density at $\sim 10 M_\odot pc^{-2}$.

5.3 Modelling molecular hydrogen in cosmological simulation

This Section is devoted to the description of models for molecular hydrogen formation suited for applications in galaxy formation simulations which include non-equilibrium formation of H_2.

Gnedin et al. (2009) implemented a model within the ART code (Section 1.2.2) that includes non-equilibrium formation of H_2 on dust and treatment of both its self-shielding and shielding by dust from the dissociating UV radiation, obtained using the Optically Thin Variable Eddington Tensor (OTVET) method (Gnedin & Abel, 2001). More in detail, starting from a chemical network for H_2 suitable to work in metal-free (without metals and dust) and optically thin (no shielding) regime, they incorporated into the network:

- the H_2 formation on dust, modelling the dust formation rate as (somewhat

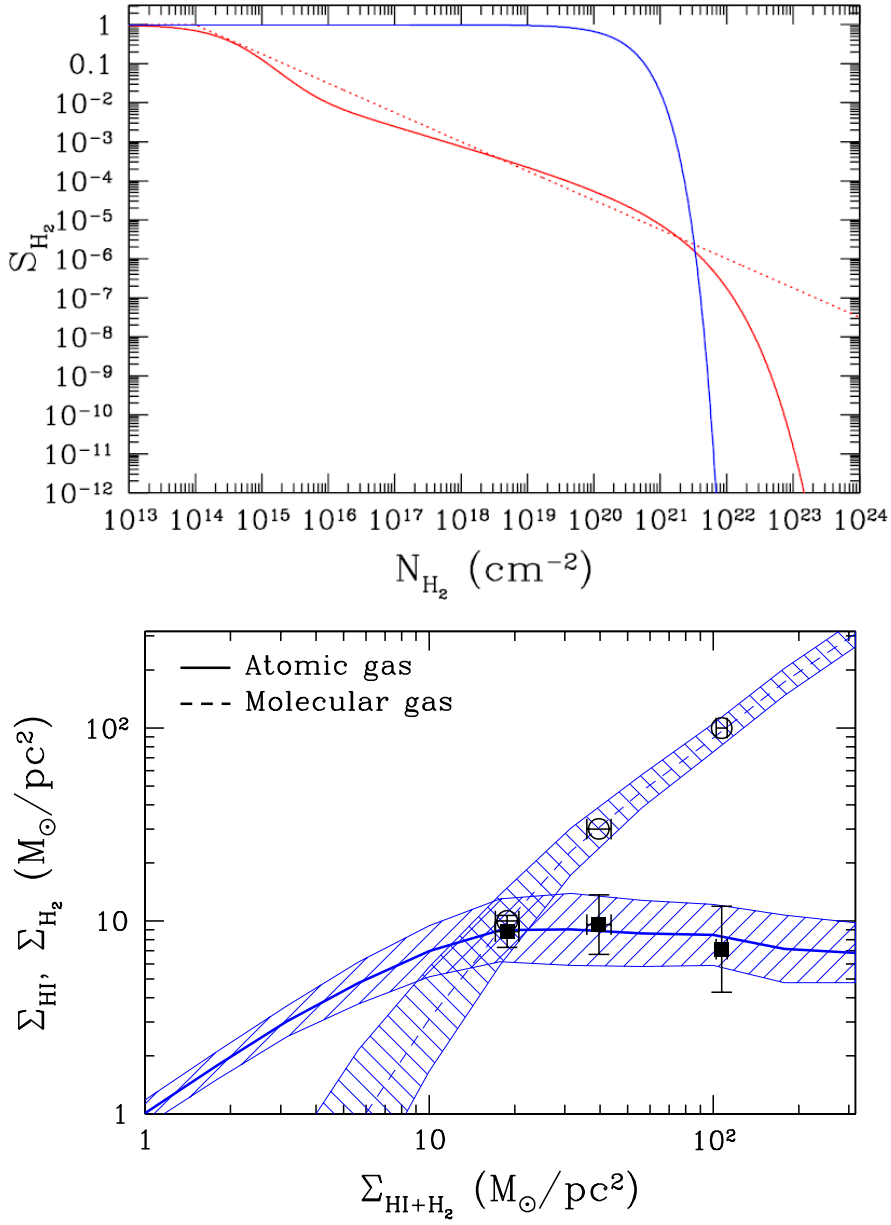

Figure 5.3: Top panel: solid red line shows the molecular self-shielding factor as a function of H_2 column density. For comparison, exponentially falling off shielding factor (dust shielding with MW dust and fully molecular gas) is shown as a blue line. Red dotted line is a power-law approximation for the self-shielding factor $S_{H_2} \propto N_{H_2}^{-0.75}$. Reproduced from Draine & Bertoldi (1996). Bottom panel: average atomic and molecular gas surface densities as functions of the total (neutral) hydrogen gas surface density averaged over 500 pc scale for the (DMW = 1,UMW = 1) simulation case (blue lines/bands for mean/rms). Filled squares and open circles with relative error bars mark the observed average and rms atomic and molecular hydrogen surface densities from Wong & Blitz (2002). Reproduced from Gnedin & Kravtsov (2011).

similar to Equation 5.14):

$$\frac{dX_{H_2}}{dt}|_{\rm dust} = R_{\rm d} n_{\rm b} X_{\rm HI}(X_{\rm HI} + 2X_{H_2}) \tag{5.22}$$

where X_i denotes the number fraction of the species i, $n_{\rm b}$ is the total number density of baryons and for $R_{\rm d}$ they adopted the observationally determined value from Wolfire et al. (2008), also assuming that the dust-to-gas ratio scales linearly with gas metallicity Z (in solar unit) and that the gas is clustered on scales unresolved in the simulations, so that the effective H_2 formation rate is higher in proportion to the gas clumping factor $C_\rho \equiv \langle\rho^2\rangle / \langle\rho\rangle^2$, yielding:

$$R_{\rm d} = 3.5 \times 10^{-17} Z C_\rho \ [{\rm cm^3 s^{-1}}] \tag{5.23}$$

C_ρ is a free parameter of the model. However, by means of numerical simulations of turbulent molecular clouds, it is possible to infer plausible range of values, $C_\rho \sim 3 - 10$ (e.g. McKee & Ostriker, 2007);

- shielding by dust grains modelled as:

$$S_{\rm d} = e^{-\sigma_{\rm d,eff}(N_{\rm HI} + 2N_{H_2})} \tag{5.24}$$

following Draine & Bertoldi (1996) (see also Equation 5.18);

- the H_2 self-shielding modelled as in Equation 5.19.

With this model they showed that the transition from atomic to fully molecular phase depends primarily on the metallicity and clumpiness of the ISM. They implemented a star formation recipe based on the local density of molecular hydrogen, showing that, since dust-channel formation strongly affects the H_2 fraction, metallicity (and hence dust) acts as a natural "feedback" mechanism because it reduces star formation in the low-mass, low-metallicity progenitors of galaxies, but also speeds up star formation once conditions for the conversion of large fraction of atomic to molecular gas are realized. Moreover they showed that, beyond certain flux level, the effect of UV radiation on the ability of ISM to form molecular clouds saturates and that the global Schmidt-Kennicutt (described in Section 1.1.2) relation between star formation and gas surface densities is also affected by processes controlling conversion from atomic to molecular gas.

Christensen et al. (2012) implemented in the GASOLINE code a method for tracking the local, non-equilibrium abundance of H_2 in simulations based on the local

formation and destruction rates. The implementation of molecular hydrogen, its formation on dust grains, dust shielding and H_2 self-shielding are derived from Gnedin et al. (2009) described above. Regarding the H_2 photodissociation by LW radiation, they assumed that the UV radiation from extragalactic sources takes the form of a cosmological background varying with redshift, using Haardt & Madau (1996). The cosmological background had been found to have a negligible impact on the star formation, as also observed in Gnedin & Kravtsov (2011). For the sake of computational speed, but also for an easier numerical implementation, they made the approximation that the amount of stellar LW flux experienced by gas particles is based on the average flux from nearby stars, calculated using the tree built for the gravity calculation (gravity solvers are briefly described in Section 1.2.2). Within each cell of the tree, they assumed that the amount of LW flux coincident on a given gas particle is a function of the amount of LW radiation emitted by star particles within the same cell. They found that their results are consistent with the observed Tully-Fisher (described in Section 1.1.2) and Schmidt-Kennicutt one (described in Section 1.1.2).

5.4 The modified version of the chemical network

The chemical network developed by Maio et al. (2007) and discussed in Section 5.1, has been devised to investigate the formation and evolution of primordial structures at high redshift. As discussed in Section 5.3, a model for molecular hydrogen formation suited for applications in galaxy formation should include treatments of both H_2-formation onto dust grains and its dissociation by LW photons. This Section describes how the chemical network has been extended to take into account such processes.

5.4.1 H_2 formation on dust

The modelling of the H_2 formation onto dust grains follows the approach proposed by Gnedin et al. (2009), i.e.:

$$\frac{dn_{\mathrm{H_2}}}{dt}|_{\mathrm{dust}} = C_{\mathrm{dust}} n_{\mathrm{HI}}^2 = 3.5 \times 10^{-17} Z/Z_{\odot} C_{\rho} n_{\mathrm{HI}}^2 \tag{5.25}$$

where Z is the particle metallicity and C_{ρ} is the clumping factor as defined in Equation 5.23. Thus, the equation for the evolution of the molecular hydrogen

becomes:

$$\frac{dn_{\mathrm{H_2}}}{dt} = C_{\mathrm{H_2}}(T, n_p, n_q) + C_{\mathrm{dust}} n_{\mathrm{HI}}^2 - D_{\mathrm{H_2}}(T, n_l) n_{\mathrm{H_2}} \tag{5.26}$$

For consistency the equation for the atomic hydrogen becomes:

$$\frac{dn_{\mathrm{HI}}}{dt} = C_{\mathrm{HI}}(T, n_p, n_q) - D_{\mathrm{HI}}(T, n_l) n_{\mathrm{HI}} - C_{\mathrm{dust}} n_{\mathrm{HI}} \tag{5.27}$$

5.4.2 H_2 destruction by LW photons

Radiation above 13.6 eV is quickly absorbed by the dense neutral hydrogen. However, assuming that the ISM is optically thin to radiation below the HI ionization limit, the resulting soft-UV background of radiation has sufficient energy to photodissociate H_2 by means of the Solomon process,

$$H_2 + \gamma \longrightarrow H_2^* \longrightarrow HI + HI \tag{5.28}$$

thus inhibiting H_2 formation (and consequently star formation).

The very simple model proposed by Machacek et al. (2001) is followed in order to investigate the negative feedback effects of this soft-UV radiation on H_2. The radiation field is assumed to be constant with mean photon energy of 12.87 eV. In terms of the constant mean flux $j(\nu_{\mathrm{LW}})$, the H_2-photodissociation rate coefficient for the Solomon process denoted in Equation 5.28 is:

$$k_{\mathrm{LW}} = 1.1 \cdot 10^8 \frac{j(\nu_{\mathrm{LW}})}{\mathrm{erg\ Hz^{-1} s^{-1} cm^{-2}}}\ \mathrm{s^{-1}} \tag{5.29}$$

where $j(\nu_{\mathrm{LW}})$ (erg $\mathrm{Hz^{-1} s^{-1} cm^{-2}}$) is treated as a fixed free parameter.
Hence, the Equation 5.26 is modified as follows:

$$\frac{dn_{\mathrm{H_2}}}{dt} = C_{\mathrm{H_2}}(T, n_p, n_q) + C_{\mathrm{dust}} n_{\mathrm{HI}}^2 - D_{\mathrm{H_2}}(T, n_l) n_{\mathrm{H_2}} - k_{\mathrm{LW}} n_{\mathrm{H_2}} \tag{5.30}$$

and Equation 5.27 accordingly:

$$\frac{dn_{\mathrm{HI}}}{dt} = C_{\mathrm{HI}}(T, n_p, n_q) + k_{\mathrm{LW}}(n_{\mathrm{H_2}}) - D_{\mathrm{HI}}(T, n_l) n_{\mathrm{HI}} - C_{\mathrm{dust}} n_{\mathrm{HI}} \tag{5.31}$$

Mathis et al. (1983) computed the variation of the intensity of the ISRF with the galactocentric distance, finding that at $\sim$5 kpc from the centre of the galaxy the mean flux in LW band is $j(\lambda \simeq 0.1\mu m) \simeq 7.93 \cdot 10^{-23}$ erg $\mathrm{Hz^{-1}\ s^{-1}\ cm^{-2}}$.

5.5 Coupling MUPPI with the chemical network

This Section describes the preliminary implementation of the (modified) chemical network coupled with the MUPPI algorithm within GADGET-3.

In the MUPPI algorithm, described in detail in Section 2.2.1, a star-forming particle is composed by a dense, cold phase and a hot, tenuous gas phase. These two gas phases are assumed to be in thermal pressure equilibrium and the temperature of the cold phase, T_c, is fixed. The evolution of a multi-phase particle is described by a system of ODEs in which the variables are the masses of the components, namely the cold mass (M_c), the hot mass (M_h) and the (virtual) stellar mass (M_*), and the thermal energy of the hot phase. At each SPH timestep, the system is integrated with a Runge-Kutta (RK) integrator with adaptive timesteps. A mixture of species, i.e. atoms and molecules, are supposed to be locked in the cold phase. The chemical network should track the evolution of the abundances of species and the temperature of the cold phase.

In the first implementation, the (modified) chemical network is used as an independent physics module while, during the simulation, MUPPI performs star formation and feedback as usual. This means that the chemical network does not play any role on the evolution of the cold phase of gas particles, thus the outputs of the chemical network do not affect the results of the simulation (*"mute"* chemical network). Here the implementation of the *mute* chemical network is discussed.

5.5.1 Mute chemical network

MUPPI gives an estimate of the properties of the ISM, as sampled by each multi-phase gas particle; in particular, the physical quantities related to the cold gas phase as e.g. mass and density. The cold gas phase is precisely that in which H_2 can form and accumulate. The RK integrator divides each hydrodynamical timestep in a given number of subcycle timesteps, Δt_{RK}. Then, the method is the following:

- M_c, M_* and the density of the cold phase, ρ_c, are stored before (M_c^b, M_*^b, ρ_c^b) each Δt_{RK}. Cold and stellar masses are also stored after (M_c^a, M_*^a) each Δt_{RK} (where "*b*" and "*a*" stand for *before* and *after*). Within each Δt_{RK} the MUPPI algorithm, integrating the set of ODEs, evolves the mass of the cold phase from M_c^b to M_c^a and the stellar one from M_*^b to M_*^a. If star formation takes place within Δt_{RK}, i.e. $\Delta M_* \equiv M_*^a - M_*^b > 0$, then M_c^b is decreased by an amount of mass proportional to the molecular fraction within the cold phase

(Equations 2.4, 2.6 and 2.10), meaning that the molecular mass is converted into stars.

- After each $\Delta t_{\rm RK}$ the chemical network routine is called. The network evolves the abundances and the temperature of the mixture within $\Delta t_{\rm RK}$; it requires as inputs the initial temperature and the density of the mixture of species, and their initial abundances; the abundance of the i-species is defined to be the fraction in number density, $f_{n,i} = n_i \mu m_p / \rho$, where n_i is the number density of the i-species, m_p is the proton mass, μ and ρ are the mean molecular weight and the density of the mixture of species, respectively;

  if the gas particle has just entered the multi-phase regime and $\Delta t_{\rm RK}$ is its first RK timestep, it has been initialised by MUPPI with all the mass in the "hot" component, so $\rho_{\rm c}^b = 0$. Thus, the initial density of the mixture is the density of the gas particle (i.e. the density of the hot phase) and the initial temperature of the mixture is $T_{\rm c}$. The chemistry is initialized with abundances HI = $0.99 \mu f_{\rm H}$, HeI = $\mu f_{\rm He}/4$, HII = $0.01 f_{\rm H}$, $\rm H^-$ = 10^{-15}, $\rm H_2^+$ = 10^{-21}, where $f_{\rm H}$, $f_{\rm He}$ are the hydrogen and helium mass fractions of the gas particle, respectively, while the other species abundances are set to zero; the initial abundances must be initialised such that $\sum_i f_{n,i} = 1$ (in the calculation of μ also metals in the particle are taken into account);

  otherwise, the computation re-starts with the abundances calculated by the chemical network at the previous RK timestep after some corrections (discussed at the next point) required for consistency with the evolution of the particle within the given $\Delta t_{\rm RK}$. The initial density is $\rho_{\rm c}^b$ and the initial temperature is the one calculated by the chemical network at the previous RK timestep.

  In both cases, the final temperature calculated by the chemical network is a *mute* variable, i.e. it is not used by MUPPI because the temperature of the cold phase, $T_{\rm c}$, is fixed. The abundances of species are *mute* too in this first implementation. However, such a final temperature is utilized in the next $\Delta t_{\rm RK}$ of the molecular evolution. When the particle exits its multi-phase stage, it loses memory of the computed chemical abundances and of the *mute* network temperature. When the particle next enters multi-phase stage, the initialization starts from the beginning as described above.

- The mass of the mixture of species during the computations of the chemical network is fixed, so the abundances evolve at fixed total mass equal to the

one of the cold phase before the RK timestep, M_c^b. To mimic the process of star formation also on molecules tracked by the chemical network, whenever MUPPI provides a positive star formation rate within Δt_{RK}, ΔM_* is subtracted from the H_2 mass calculated by the chemical network; if the amount of H_2 mass is not enough (it is possible since the star formation does not depend on the integration of the chemical network), the H_2 mass is nulled and the remaining mass is subtracted from the abundances of the other species. The same is done when the mass of cold phase decreases, for instance due to evaporation. When instead the mass is increased by cooling of the hot phase, such a new cold gas is added to the neutral hydrogen abundance.

This numerical experiment aims to investigate the ability of the (modified) chemical network coupled with MUPPI to recover the phenomenological nearly linear relation between the ratio of molecular to atomic gas and its pressure provided by Blitz & Rosolowsky (2006).

5.6 Reproducing the Blitz & Rosolowsky relation with the modified chemical network

Blitz & Rosolowsky (2006) showed that the ratio of the surface densities of molecular and atomic gas in a sample of galaxies, probing a large range in mass and metallicity, correlates with the external disk pressure and that the relation (hereafter BR) between the two is nearly linear, over 3 orders of magnitude in pressure. They estimated the external disk pressure for disk galaxies from the midplane pressure in an infinite, two-fluid disk with locally isothermal stellar and gas layers.

They fitted a linear relation between $\log(P_{ext}/k)$ and $\log(R_{mol})$, where $R_{mol} \equiv \Sigma_{H_2} / \Sigma_{HI}$, to estimate the parameters for a power-law relationship between the two variables:

$$R_{mol} = \left(\frac{P_{ext}}{P_0} \right)^{\alpha} \tag{5.32}$$

The derived value for the power-law index was $\alpha = 0.92 \pm 0.07$.

As discussed in Section 2.2.1, MUPPI implements a slight simplified version of the BR relation, using hydrodynamic pressure in place of external pressure, aimed to estimate the molecular fraction within the cold phase of a multi-phase particle, defined as:

$$f_{mol} = \frac{1}{1 + P_0/P} \tag{5.33}$$

Simulation	Ω_M	Ω_Λ	Ω_{baryon}	H_0	M_{DM}	M_{gas}	ϵ_{Pl}	C_ρ
GA0	0.3	0.7	0.043	70	$1.4 \cdot 10^8$	$2.6 \cdot 10^7$	1.4	10

Table 5.2: Basic characteristics of the GA0 simulation. Column 1: simulation name; Column 2: mass density parameter including DM and baryons; Column 3: mass density of the dark matter; Column 4: mass density of baryons; Column 5: Hubble constant; Column 6: mass of the DM particles; Column 7: initial mass of the gas particles; Column 8: Plummer-equivalent softening length for gravitational force; Column 9: clumping factor. Masses are expressed in units of $M_\odot/h$, H_0 in km s^{-1} and softening length in units of kpc/h.

where $P_0 = 20000$ Kcm^{-3} and P the hydrodynamic pressure of the gas particle.

To test the ability of the *mute* chemical network to recover the BR relation (Equation 5.33), a cosmological zoomed-in halo, which belongs to the GA set and described in Section 2.3, is simulated at low resolution. Table 5.2 shows the parameters of the adopted ΛCDM cosmology, force and mass resolutions used for the simulation and the value of the clumpy factor, C_ρ, used in the chemical network. The values of MUPPI parameters are reported in Table 2.1. Several runs of the GA0 simulation were performed using different values of the parameter $j_{\nu_{LW}} = 0, 10^{-22}, 3 \cdot 10^{-22}, 10^{-21}, 3 \cdot 10^{-21}, 5 \cdot 10^{-21}$ erg Hz^{-1}s^{-1}cm^{-2} (Equation 5.29); these values have been suggested by Haiman et al. (2000), which studied the effect of $j_{\nu_{LW}}$ in the suppression of H_2 abundance. As discussed in Section 5.4.2, the LW flux is not evaluated self-consistently within the star forming particle, but it has been held fixed through the simulations for all the particles.

The H_2-mass fraction within the cold phase of multi-phase particles is defined as $f_{H_2} \equiv M_{H_2}/(M_{H_2} + M_{HI})$, where M_{H_2} and M_{HI} are the molecular and atomic hydrogen masses calculated by the chemical network. Figure 5.4 shows the comparison at redshift $z = 0$ between the BR relation and the 2D histograms of f_{H_2} as a function of pressure for different values of $j_{\nu_{LW}}$. The gas particles belong to the entire simulated volume. In each panel of Figure 5.4, colour coding refers to the Log of cold mass per unit bin area of multi-phase gas particles as indicated by the colour bar and the continuous violet line shows the BR relation (Equation 5.33). In Figure 5.4 $j_{\nu_{LW}}$ increases from left to right and from top to bottom. In each panel particles sample the BR relation and in most runs there is good agreement; it must be noticed that MUPPI particles follow exactly the violet continuous line during the simulation. The increasing radiation field has multiple effects. First, a given fraction of H_2 requires enhanced pressure to be produced. Second, isodensity contours

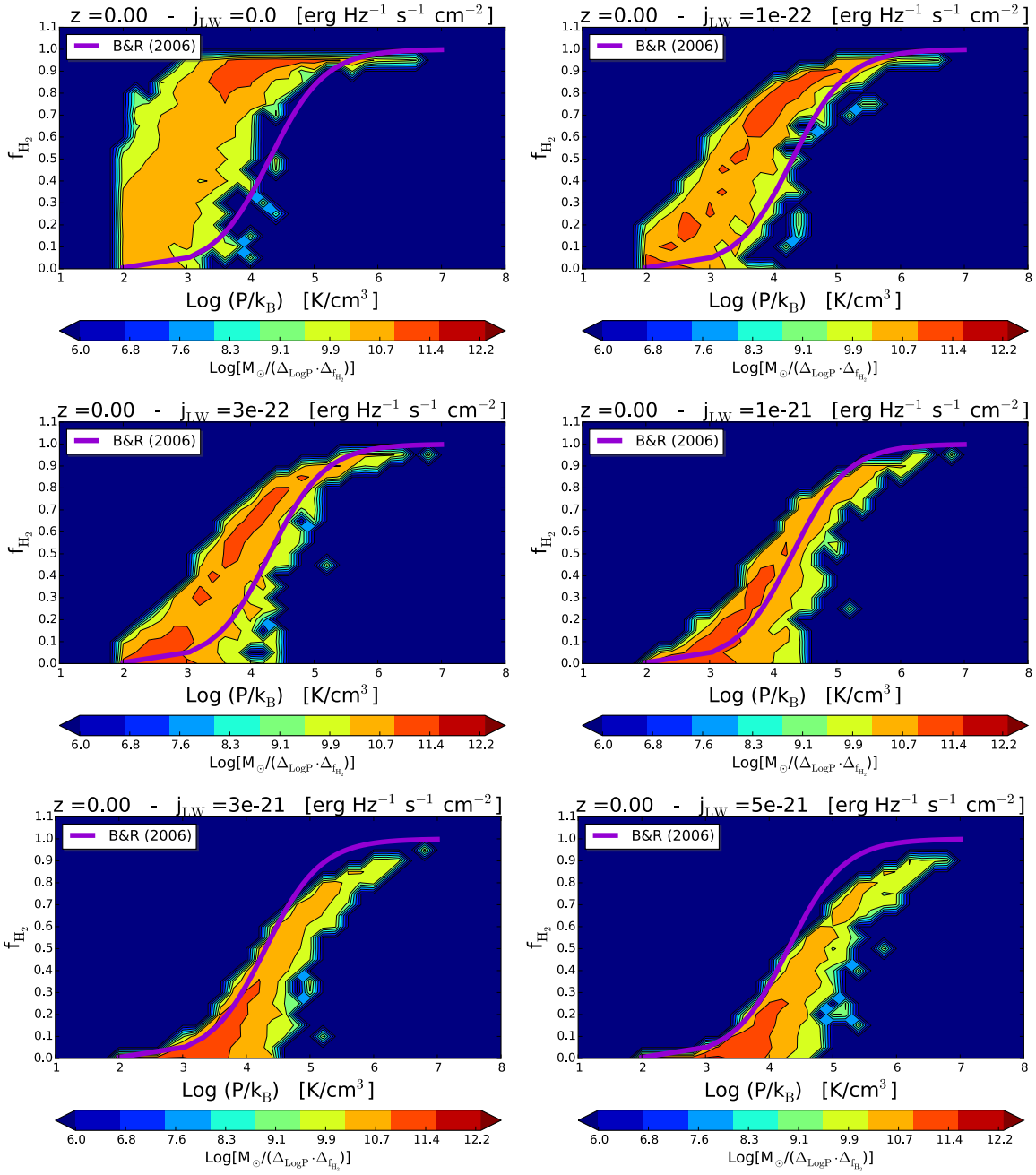

Figure 5.4: 2D histograms of H_2-mass fraction and pressure at redshift $z = 0$, at six different values for $j_{\nu_{LW}}$ (erg $Hz^{-1}s^{-1}cm^{-2}$). H_2-mass fraction is calculated by the chemical network. In each panel, colour coding refers to the Log of cold mass per unit bin area as indicated by the colour bar, the black lines are the corresponding isodensity contours and the continuous violet line shows the BR relation (Equation 5.33).

Simulation	$j_{\nu_{LW}}$ ($\times 10^{-22}$ erg Hz^{-1}s^{-1}cm^{-2})	R_{gal} (kpc)	M_{bulge} ($M_\odot$)	M_{disk} ($M_\odot$)	M_{tot} ($M_\odot$)	B/T
AqC6		23.87	$1.75 \cdot 10^{10}$	$5.84 \cdot 10^{10}$	$7.59 \cdot 10^{10}$	0.23
AqC6$_{j1}$	1	23.88	$2.08 \cdot 10^{10}$	$5.75 \cdot 10^{10}$	$7.83 \cdot 10^{10}$	0.27
AqC6$_{j3}$	3	24.56	$1.83 \cdot 10^{10}$	$6.94 \cdot 10^{10}$	$8.77 \cdot 10^{10}$	0.21
AqC6$_{j10}$	10	24.75	$3.97 \cdot 10^{10}$	$5.27 \cdot 10^{10}$	$9.24 \cdot 10^{10}$	0.43

Table 5.3: Basic characteristics of the different AqC6 simulations. Column 1: simulation name; column 2: value for H_2-photodissociation rate $j_{\nu_{LW}}$ in unit of 10^{-22} erg Hz^{-1}s^{-1}cm^{-2}; column 3: galaxy radius $R_{gal} = R_{vir}/10$; column 4: stellar bulge mass at $z = 0$ within R_{gal}; column 5: stellar disk mass at $z = 0$ within R_{gal}; column 6: total stellar mass at $z = 0$ within R_{gal}; column 7: bulge-over-total stellar mass ratio at $z = 0$.

reveal that the preferential *locus* of particles shifts towards lower values of f_{H_2} for increasing $j_{\nu_{LW}}$. Third, particles lie on the BR relation with decreasing scatter as $j_{\nu_{LW}}$ increases.

The BR relation is observed to hold in galaxies of the local Universe but the validity of this assumption at high redshift is questionable. Figure 5.5 shows the redshift evolution of the f_{H_2} as a function of pressure at fixed $j_{\nu_{LW}} = 10^{-21}$ erg Hz^{-1}s^{-1}cm^{-2}. The isodensity contours reveal some redshift evolution of the BR relation, however these preliminary findings do not clarify if such a dependence is realistic, or is due to the over-simplified assumption that the LW flux within each multi-phase particle is constant at all redshifts. This point is one of the most important to be addressed in future development of the present research.

5.7 Star formation from molecules

In the numerical experiments presented above, the abundances of the species calculated by the chemical network are not used during the simulation, but they are only used in the post-processing analysis as discussed in the previous Section. The star formation rate of a multi-phase particle is proportional to the molecular fraction within its cold phase (Equation 2.10). Since the chemical network is found to give molecular fractions that are broadly consistent with the BR relation even with the adopted simplified implementation, the next numerical experiment is to study the properties of a disk galaxy when in Equation 2.10 the molecular fraction is given by the chemical network, i.e. $f_{mol} = f_{H_2} = M_{H_2}/(M_{H_2} + M_{HI})$, where M_{H_2} and M_{HI} are the molecular and atomic hydrogen masses calculated by the chemical network.

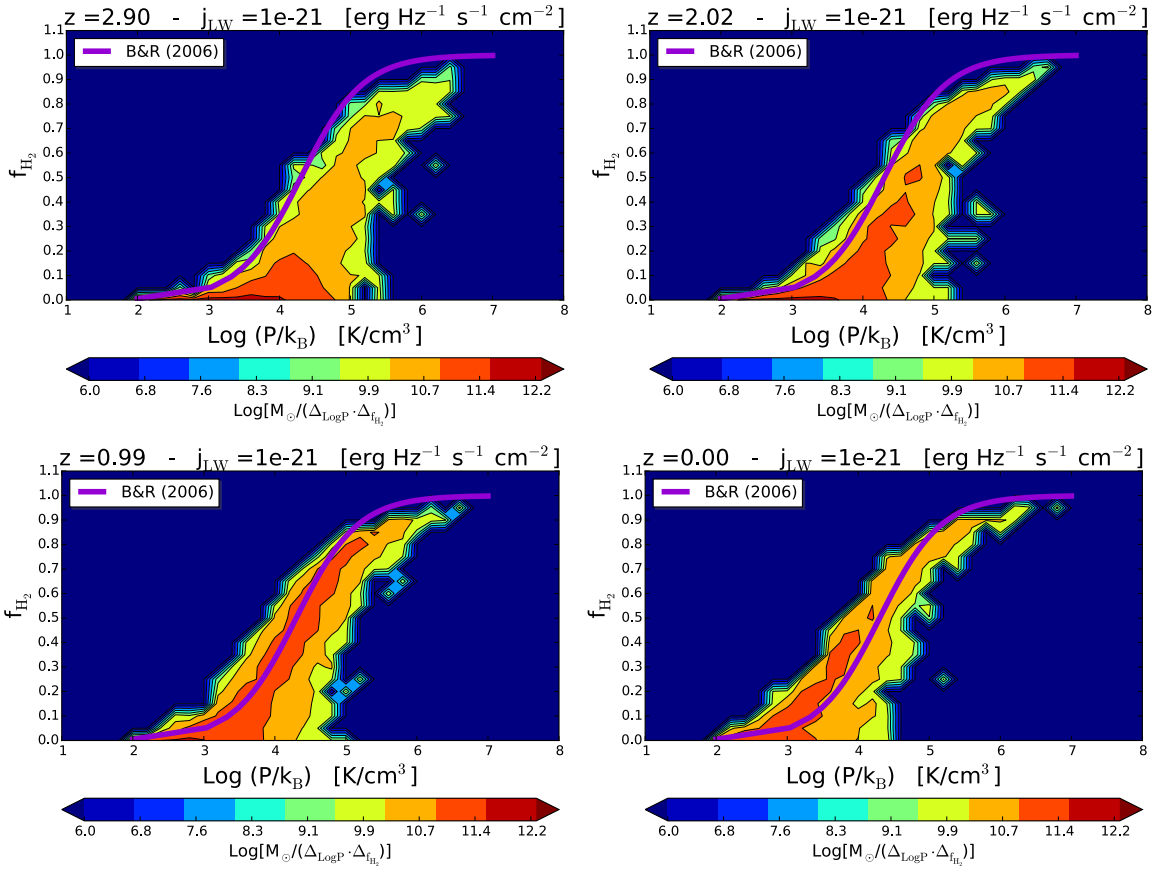

Figure 5.5: 2D histograms of H_2-mass fraction and pressure at four different redshift and at fixed $j_{\nu_{\rm LW}} = 10^{-21}$ erg Hz^{-1}s^{-1}cm^{-2}. H_2-mass fraction is calculated by the chemical network. In each panel, colour coding refers to the Log of cold mass per unit bin area as indicated by the colour bar, the black lines are the corresponding isodensity contours and the continuous violet line shows the BR relation (Equation 5.33). From the upper left panel, redshift are $z = 3, 2, 1, 0$.

The coupling of MUPPI with the chemical network remains the same as discussed in Section 5.5.1, but now the chemical network is no longer *mute*. Note however that the evolution of the molecular fraction and of the ISM are still separated. In each RK step, $f_{\rm mol}$ is set by $f_{\rm H_2}$ calculated by the chemical network at the end of the previous RK step.

AqC6 simulation, that belongs to the AqC set and described in Section 2.3, is run with this new implementation and compared to the "standard" AqC6, i.e. the AqC6 simulation run without the chemical network. AqC6 simulation is described in great detail in Chapter 2 and Chapter 3, but the adopted MUPPI parameters of the runs analysed in the present Section are $f_{b,out} = 0.2$, $f_{b,kin} = 0.5$, $P_{kin} = 0.02$, slight different to the ones used in the previous Chapters. Three runs of the AqC6 simulation are performed with different values of the parameter $j_{\nu_{\rm LW}}$ in unit of 10^{-22} erg Hz^{-1}s^{-1}cm^{-2}, namely AqC6$_{j1}$ with $j_{\nu_{\rm LW}} = 1$, AqC6$_{j3}$ with $j_{\nu_{\rm LW}} = 3$ and AqC6$_{j10}$ with $j_{\nu_{\rm LW}} = 10$. The galaxies are selected with the same method discussed in Section 3.2. Table 5.3 reports the main properties of the four simulations, together with the main properties of their central galaxies at $z = 0$.

Figure 5.6 shows maps of stellar mass surface density for the central part of the simulated galaxies at redshift 0, obtained as in Figure 3.3. From top to bottom, the AqC6, the AqC6$_{j1}$, the AqC6$_{j3}$ and the AqC6$_{j10}$ are shown. When galaxies are seen face-on (first row), the roundness of the isodensity contours increases from top to bottom, corresponding to a higher value of the radiation field. When the galaxies are seen edge-on (second and third columns), the flatness of the isodensity contours decreases from top to bottom. Disks are more extended and bulges are more compact decreasing $j_{\nu_{\rm LW}}$.

To quantify the kinematics of galaxies the distribution of orbit circularities of the star particles is taken into account, following the method proposed by Scannapieco et al. (2009), described in Section 2.4. Top panel of Figure 5.7 shows the histograms of circularities of all star particles within $R_{\rm gal}$; black line for AqC6, red line for AqC6$_{j1}$, green line for AqC6$_{j3}$ and blue line for AqC6$_{j10}$. The visual impression of Figure 5.6 is confirmed by these distributions, where the growing radiation field leads to a prominent bulge component $\epsilon \sim 0$, to a low number of stars with $\epsilon \sim 1$, where stars rotating on a disk are expected to lie, and to a high number of stars with intermediate circularity $0.3 \lesssim \epsilon \lesssim 0.7$. The resulting ratios of bulge over stellar mass[2] within $R_{\rm gal}$ are B/T = 0.23 for AqC6, B/T = 0.27 for AqC6$_{j1}$, B/T = 0.21 for AqC6$_{j3}$ and B/T = 0.43 for AqC6$_{j10}$.

Bottom panel of Figure 5.7 shows the total rotation curves of galaxies, defined

[2]Here the simple kinematic estimate of B/T described in Section 2.4 is used.

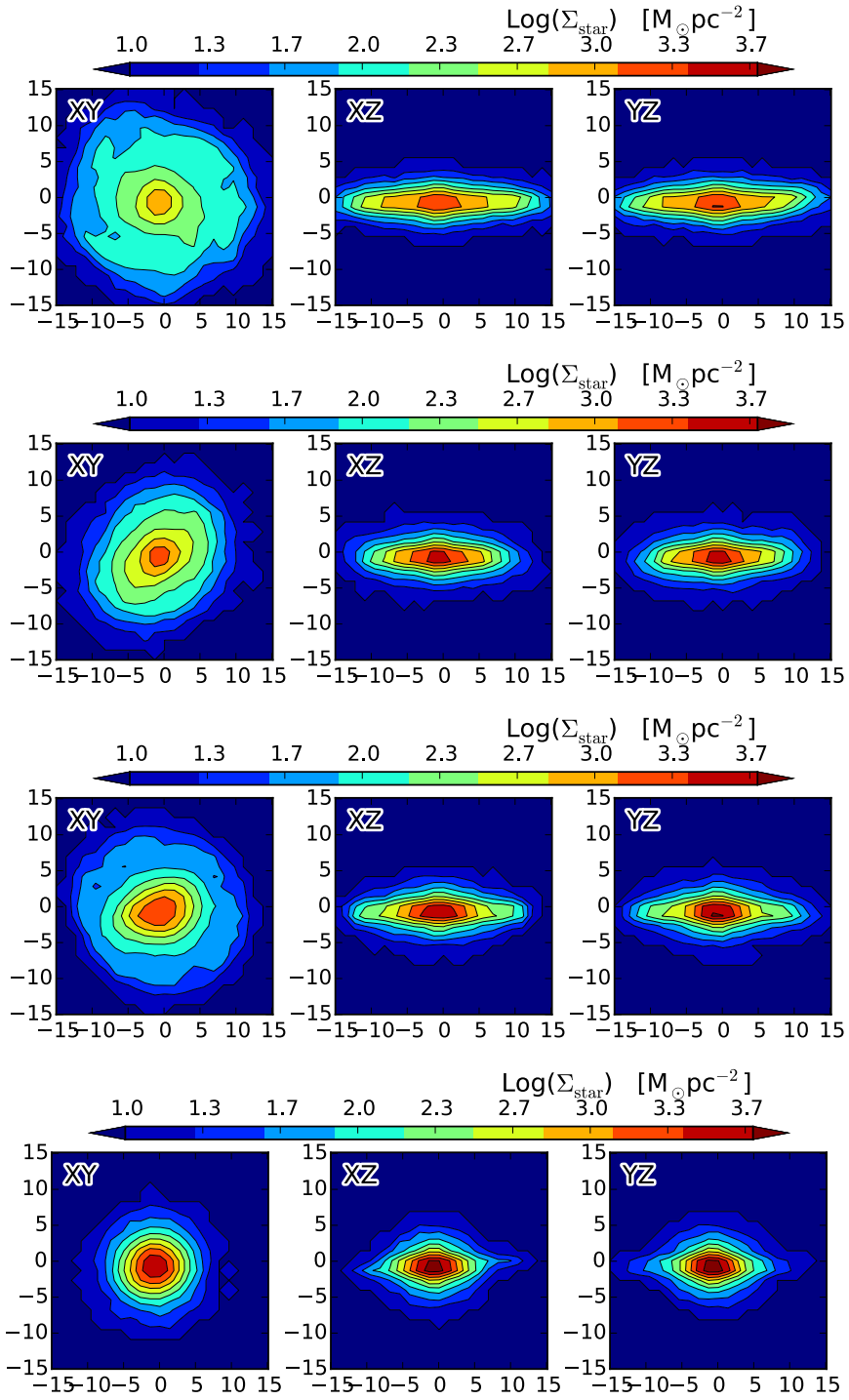

Figure 5.6: Projected stellar maps of the AqC6 galaxies at $z = 0$ in boxes centred on the galaxy that extend 30 kpc across. Colour coding follows the Log of stellar mass surface density as indicated by the colour bar. The three columns show projections in the face-on XY-plane (left), edge-on XZ-plane (middle) and edge-on YZ-plane (right). First row shows the AqC6, second row shows AqC6$_{j1}$, third row shows AqC6$_{j3}$ and fourth row shows AqC6$_{j10}$.

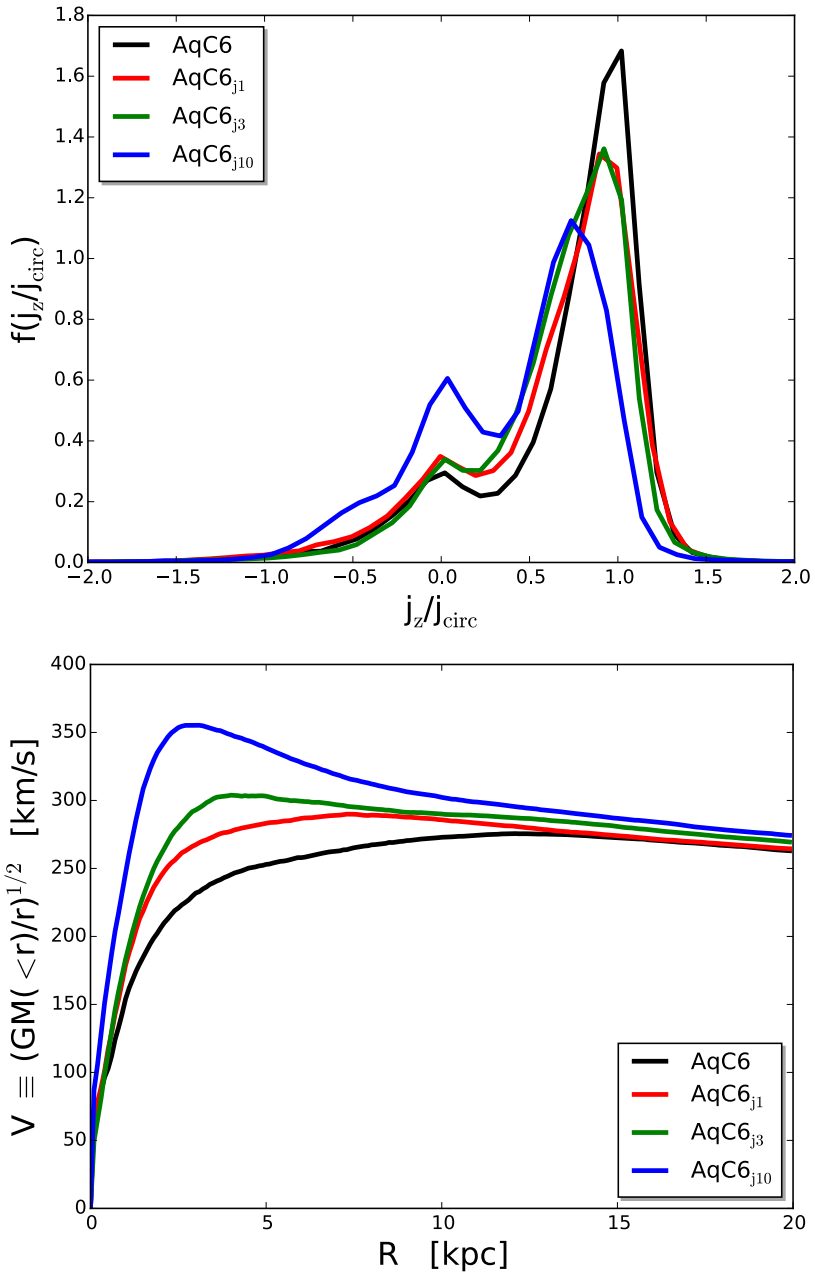

Figure 5.7: Top panel: distribution $f(\epsilon)/d\epsilon$ of the circularity parameter for the AqC6 simulations at $z = 0$, for the stellar component, as a function of the circularity $\epsilon = J_z/J_{\rm circ}$. Black line for AqC6, red line for AqC6$_{\rm j1}$, green line for AqC6$_{\rm j3}$ and blue line for AqC6$_{\rm j10}$. Distributions are normalized so that $\int f(\epsilon)d\epsilon = 1$. Bottom panel: total rotation curves for the AqC6 (black line), AqC6$_{\rm j1}$ (red line), AqC6$_{\rm j3}$ (green line) and AqC6$_{\rm j10}$ (blue line).

as $v = \sqrt{GM(<r)/r}$, where G is the gravitational constant and $M(<r)$ the total mass (DM + baryons) within the radius r. While AqC6 and AqC6$_{j1}$ have a flat rotation curves, reaching their maxima at 12.1 (AqC6) and 7.3 (AqC6$_{j1}$) kpc, after which they gently decline, other galaxies (AqC6$_{j3}$ and AqC6$_{j10}$) show a peaked rotation curve in the central region because they are centrally concentrated.

From the visual appearance, from the distribution of circularities and from the shape of the rotation curves, it is clear that AqC6 and AqC6$_{j1}$ galaxies are disk-like with a modest central mass concentration, while AqC6$_{j3}$ and AqC6$_{j10}$ are compact disk galaxies in which most gas has been converted into stars.

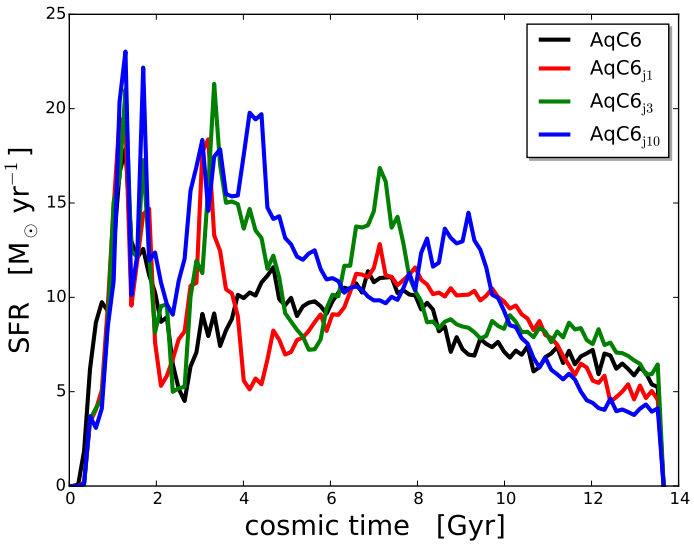

Figure 5.8: Star formation rate as a function of the cosmic time for AqC6 set. Black line for AqC6, red line for AqC6$_{j1}$, green line for AqC6$_{j3}$ and blue line for AqC6$_{j10}$.

Figure 5.8 shows the SFR relative to star particles which lie inside the galaxy radius R_{gal} at redshift $z = 0$. All runs have higher SFR at higher redshift. AqC6 (black line) shows a roughly bimodal distribution with a first, relatively narrow peak and a further broad component, while the others have more peaks and higher rates. Simulations produce very similar SFRs for the first 2 Gyrs; later SFR histories of AqC6$_{j1}$ (red line), AqC6$_{j3}$ (green line) and AqC6$_{j10}$ (blue line) have values of $\sim$20 M$_\odot$/yr at $\sim$3 Gyrs, but the star formation peaks are broader when the H_2-photodissociation rate grows. Then, SFR histories have other peaks at $\sim$7 Gyrs for AqC6$_{j1}$ and AqC6$_{j3}$, and later at $\sim$9 Gyrs for AqC6$_{j10}$.

From these findings it is clear that galaxy properties are modified when the molecular fraction used in the MUPPI model is computed by the (modified) chemical network. In the previous Section, star forming particles were found to have, at given pressure, lower molecular fraction, $f_{\rm mol}$, when the H_2-photodissociation rate grows (BR relation). In the MUPPI kinetic feedback prescription, the wind velocity is proportional to the square root of the molecular fraction, i.e. $v_{\rm wind} \propto \sqrt{f_{\rm mol}}$. As a consequence, the resulting feedback efficiency shows some dependence on H_2-photodissociation rate dependence. The result is that for high radiation field the feedback is less efficient and the conversion of gas into stars is enhanced. Results presented in this Section are a work in progress at the moment of writing. More analysis have to be performed to fully understand the complex interplay between the (modified) chemical network and the MUPPI model.

5.8 Concluding remarks

MUPPI algorithm uses an RK integration scheme, while the chemical network adopts a BDF method. The latter has been developed by Anninos et al. (1997) and it is designed for solving stiff set of equations with both accuracy and speed. The preliminary coupling between MUPPI and the chemical network, described in Section 5.5, has been designed as a test integration scheme within GADGET-3; as discussed, different integration schemes impose some assumptions and consequently some approximations. During my PhD, a version of the chemical network that adopts the RK integration scheme has been implemented, whose results are presented in Di Cerbo (2015). The GSL algorithm that performs the RK adaptive integration has been modified, because in the original form it was unable to deal with the very different time-scales involved in the chemical reactions. After resolving such a technical problem, species abundances have been found to change by less then $\sim$1% adopting RK integration scheme instead of BDF one. The main bottleneck is the speed of the calculation that makes unfeasible to adopt RK scheme in the chemical network in cosmological runs. An increase of speed is achieved when a minimal chemical model, that incorporates only the essential processes needed to accurately model the formation of H_2, is used. Following Abel et al. (1997), HD, D and D^+ can be neglected[3], since they are important in the formation of H_2 and in the modelling of the molecular cooling in a primordial context, but relatively negligible in the galaxy formation context. The species abundances have been found to

[3]Metals become the most-efficient coolants in metal-enriched ISM, as shown in Figure 5.1.

change less then ∼1% also between the original code that adopts BDF integration and the minimal chemical network that adopts RK integration (Di Cerbo, 2015). The gain in computational speed is remarkable compared to the full RK chemical network, but larger by a factor of ∼40 than the BDF network.

Maio et al. (2007) presented a chemical network devised to study the formation and evolution of structures at high redshift. During my PhD, the chemical network has been extended to take into account the H_2 formation onto dust grains and its UV-photodissociation. The latter has been implemented assuming that the UV radiation field within a multi-phase particle is constant and redshift-independent.

The main goal is to track self-consistently the non-equilibrium abundance and cooling processes of H_2 and H_2-based star formation in simulations of galaxy formation.

The modified chemical network has been widely tested for porting the code in GADGET-3, as described in Di Cerbo (2015). Then, the MUPPI algorithm and the modified chemical network has been coupled in preliminary form within GADGET-3.

A number of physical and technical points must be addressed in future:

i) as discussed above, MUPPI algorithm uses a RK integration scheme, while the chemical network adopts a BDF method. This point has been partially faced in the preliminary coupling, as stated above; the full coupling between MUPPI and the chemical network will be addressed devising a unique integration scheme in which MUPPI and chemical equations are solved, requesting both accuracy and speed during the calculation; for what discussed above, RK integration scheme might not be the choice;

ii) the full coupling could require to modify the MUPPI algorithm, since, for instance, the temperature of the cold phase is no longer constant during the evolution, but it should be evaluated on the fly by the chemical network;

iii) an approach must be devised to estimate the local time-dependent LW radiation field based on the SFR of each gas particle, instead of the over-simplified assumption of a constant and redshift-independent LW flux. This amounts to solving radiative transfer on the fly. However, this process is known to require a very large overhead of computing time, so the possibility of adopting some approximate and fast schemes will be investigated; an example could be OTVET with a model for self-shielding, as done by Gnedin et al. (2009); or even of inferring the properties of the radiation field from the local stellar population as in Christensen et al. (2012).

However, first results show that the BR relation is predicted by the model presented in this Chapter. Moreover, the properties of resulting disk galaxies are broadly in agreement with "realistic" ones obtained by the (original) MUPPI algorithm.

6

Conclusions

Modelling galaxy formation in a cosmological context is challenging due to many physical processes and a wide range of scales involved. It is then convenient to address the problem by means of numerical techniques. Observations across the electromagnetic spectrum reveal that processes such as star formation, stellar feedback, gas outflows, galactic fountains and galaxy interactions are shaping the characteristics of galaxies. Cosmological simulations are still orders of magnitude away from capturing directly the spatial scales where stars actually form. The treatment of the interstellar medium, with multiple gas phases co-existing at very different densities and temperatures, needs to be included in simulations in the form of sub-resolution effective models.

Nowadays, different authors (Stinson et al., 2013; Aumer et al., 2013; Vogelsberger et al., 2014; Marinacci et al., 2014; Hopkins et al., 2014; Cen, 2014; Schaye et al., 2015; Agertz & Kravtsov, 2015b) produced, in a cosmological context, late-type spiral galaxies with low bulge-over-total ratios and low baryon fractions. Even though the results are converging and broadly in agreement with observations, no consensus has been reached on the source and detailed behaviour of the required feedback energy.

In Murante et al. (2015), cosmological simulations of individual disk galaxies, carried out with GADGET-3 (Springel, 2005), are presented including the sub-resolution model MUlti-Phase Particle Integrator (MUPPI). Late-type galaxies are obtained with properties in broad agreement with observations (disk size, mass

surface density, rotation velocity, gas fraction) and also with results shown by other groups. The resulting spiral galaxies, named GA and AqC, host an extended bar. They are available at two resolution levels, allowing to consider these bars as due to physical and not to numerical processes and thus to study the trigger of this instability in a full cosmological context (i.e. within a non idealized dark matter halo). During my PhD project, the properties of the bars in simulated galaxies are quantified and presented in Goz et al. (2015). Morphology, kinematic and radial streaming motions are in agreement with observations of local Universe (Seidel et al., 2015). In the GA galaxy, Fourier analysis of the surface density of the disk reveals that bar length and strength are remarkably independent of resolution. In the GA simulations, the onset of bar instability is found to take place when the disk is Toomre-unstable due to accumulation of mass in the disk. However, in the AqC ones the onset of bar instability is different. In the higher resolution simulation the growth of bar strength is found in coincidence of nearby passages of a satellite, supporting the idea that the bar is triggered by tidal interactions. The lower AqC resolution behaves analogously to the GA simulations, so in that case the cause of the bar instability seems to be driven by the disk secular evolution.

Many of the fundamental properties of galaxies are encoded in their spectral energy distributions and they provide the basis for the modern understanding of galaxy formation and evolution. The complex task to calculate the emerging spectral energy distribution of a simulated galaxy, treating the reprocessing of light emitted by stars by means of dusty ISM, has been faced using the post-processing code GRASIL-3D (Domínguez-Tenreiro et al., 2014). During my PhD, GRASIL-3D has been interfaced with the outputs of the simulation and modified to better manage the quantities provided by the MUPPI algorithm.

Although simulations of isolated halos offer high spatial and mass resolution, they do not provide a statistical sample of objects to compare with observations in order to test, for example, if sub-grid models are able to reproduce the scaling relations of baryonic components of galaxies. In this Thesis, results of a sample of simulated galaxies at $z = 0$ are shown[1], extracted from one large volume simulation presented by Barai et al. (2015), in which feedback and star formation are modelled by MUPPI. In broad agreement with observations of the local Universe, simulated galaxies reproduce the gas mass scaling, the main sequence, the relation between the gas-phase metallicity and stellar mass. Infrared predicted spectra, binned by stellar mass, gas metallicity, SFR and morphology, are remarkably in

[1]These results will be presented in forthcoming paper Goz et al. (prep).

agreement with the available Herschel Reference Survey (Ciesla et al., 2014) templates calibrated with observations on nearby galaxies. The latest findings point to extend the analysis at high redshift in forthcoming works, investigating deeply the infrared emission of both molecular clouds and diffuse gas component. Using larger planned cosmological simulations, the study of the infrared luminosity function at high redshift will be also possible.

Most codes today are able to take into account cooling from metal lines emission, which dominates at $10^4 \lesssim T \lesssim 10^8$ Kelvin, and the photo-ionization of metals by the background radiation field (Haardt & Madau, 2012), tracking the interstellar medium chemical evolution (e.g. Tornatore et al., 2007; Oppenheimer & Davé, 2008; Wiersma et al., 2009). H_2 and HD are effective in cooling primordial gas below the temperature of $\sim 10^4$K, but usually the non-equilibrium radiative rates are only approximate, typically either assuming collisional ionization equilibrium or ignoring metal-line cooling altogether, rather than computing them explicitly. Maio et al. (2007) have extended a previous non-equilibrium calculations of Yoshida et al. (2003) in order to include in the numerical code GADGET a detailed chemical network and to follow the formation/destruction of a wide range of species (mainly H-derived molecules), both with primordial and metal-enriched gas.

During my PhD project, the chemical network, presented by Maio et al. (2007), has been extended to take into account the H_2 formation onto dust grains and its UV-photodissociation. Then, the modified chemical network has been coupled in two different preliminary forms with the MUPPI algorithm within GADGET-3. The main aim, motivated by the tight observed connection between molecular hydrogen and star formation (e.g. Kennicutt et al., 2007; Bigiel et al., 2008), is to devise a way to track self-consistently non-equilibrium abundance and cooling processes of H_2 and H_2-based star formation in smoothed particle hydrodynamic simulations. First findings show that the observed correlation provided by Blitz & Rosolowsky (2006) is predicted by the modified chemical network when it is coupled with MUPPI in a passive manner (i.e., using ISM characteristics provided by MUPPI to determine the molecular fraction, that is however not used by MUPPI itself). Simulated disk galaxies show properties in broad agreement with those obtained in "realistic" galaxies using MUPPI, when the molecular fraction for star formation is instead directly provided by the modified chemical network. Future improvements will aim to devise a simplified implementation for a radiative transfer scheme on the fly, in order to couple properly radiation with chemistry, and to figure out how to fully couple the MUPPI algorithm and the chemical network in a unique integration

scheme. The last part of this Thesis work is fundamental to obtain a scheme able to predict self-consistently the amount of H_2 and to use it as a source of star formation, and therefore feedback, in cosmological simulation of galaxy formation.

Bibliography

Abadi M. G., Navarro J. F., Fardal M., Babul A., Steinmetz M., 2010, MNRAS, 407, 435

Abadi M. G., Navarro J. F., Steinmetz M., Eke V. R., 2003, ApJ, 597, 21

Abel T., Anninos P., Zhang Y., Norman M. L., 1997, New Astronomy, 2, 181

Agertz O., Kravtsov A. V., 2015a, ApJ, 804, 18

Agertz O., Kravtsov A. V., 2015b, ArXiv e-prints

Agertz O., Moore B., Stadel J., Potter D., et al. 2007, MNRAS, 380, 963

Agertz O., Teyssier R., Moore B., 2011, MNRAS, 410, 1391

Aguerri J. A. L., 2012, Advances in Astronomy, 2012, 28

Aguerri J. A. L., Beckman J. E., Prieto M., 1998, AJ, 116, 2136

Aguerri J. A. L., Debattista V. P., Corsini E. M., 2003, MNRAS, 338, 465

Aguerri J. A. L., Méndez-Abreu J., Corsini E. M., 2009, A&A, 495, 491

Anninos P., Zhang Y., Abel T., Norman M. L., 1997, New Astronomy, 2, 209

Asplund M., Grevesse N., Sauval A. J., Scott P., 2009, ARAA, 47, 481

Athanassoula E., 2005, MNRAS, 358, 1477

Athanassoula E., Machado R. E. G., Rodionov S. A., 2013, MNRAS, 429, 1949

Athanassoula E., Misiriotis A., 2002, MNRAS, 330, 35

Athanassoula E., Sellwood J. A., 1986, MNRAS, 221, 213

Aumer M., White S. D. M., Naab T., Scannapieco C., 2013, MNRAS, 434, 3142

Baldry I. K., Glazebrook K., Brinkmann J., et al. 2004, ApJ, 600, 681

Barai P., Monaco P., Murante G., Ragagnin A., Viel M., 2015, MNRAS, 447, 266

Barazza F. D., Jogee S., Marinova I., 2008, ApJ, 675, 1194

Barnes J., Hut P., 1986, Nature, 324, 446

Barnes J. E., 1988, ApJ, 331, 699

Barnes J. E., 1992, ApJ, 393, 484

Barnes J. E., Hernquist L. E., 1991, ApJ, 370, L65

Barrera-Ballesteros J. K., Falcón-Barroso J., Califa Collaboration 2014, A&A, 568, A70

Beck A. M., Murante G., Arth A., Remus R.-S., et al. 2015, ArXiv e-prints

Berentzen I., Shlosman I., Jogee S., 2006, ApJ, 637, 582

Bernardi M., Meert A., Sheth R. K., Vikram V., Huertas-Company M., Mei S., Shankar F., 2013, MNRAS, 436, 697

Berta S., Magnelli B., Lutz D., Altieri B., et al. 2010, A&A, 518, L30

Bianchi S., 2008, A&A, 490, 461

Bigiel F., Leroy A., Walter F., Blitz L., Brinks E., de Blok W. J. G., Madore B., 2010, AJ, 140, 1194

Bigiel F., Leroy A., Walter F., Brinks E., de Blok W. J. G., Madore B., Thornley M. D., 2008, AJ, 136, 2846

Black J. H., 1981, MNRAS, 197, 553

Blanton M. R., Moustakas J., 2009, ARAA, 47, 159

Blitz L., Rosolowsky E., 2006, ApJ, 650, 933

Booth C. M., Schaye J., 2009, MNRAS, 398, 53

Boselli A., Eales S., Cortese L., Bendo G., et al. 2010, PASP, 122, 261

Bosma A., 1978, PhD thesis, PhD Thesis, Groningen Univ., (1978)

Boudet N., Mutschke H., Nayral C., Jäger C., Bernard J.-P., Henning T., Meny C., 2005, ApJ, 633, 272

Bournaud F., Chapon D., Teyssier R., Powell L. C., et al. 2011, ApJ, 730, 4

Bournaud F., Perret V., Renaud F., Dekel A., et al. 2014, ApJ, 780, 57

Boylan-Kolchin M., Springel V., White S. D. M., Jenkins A., Lemson G., 2009, MNRAS, 398, 1150

Bruzual G., Charlot S., 2003, MNRAS, 344, 1000

Bryan G. L., Norman M. L., O'Shea B. W., Abel T., et al. 2014, ApJS, 211, 19

Bryan S. E., Kay S. T., Duffy A. R., Schaye J., Dalla Vecchia C., Booth C. M., 2013, MNRAS, 429, 3316

Buta R., Laurikainen E., Salo H., Block D. L., Knapen J. H., 2006, AJ, 132, 1859

Calzetti D., 2013, Star Formation Rate Indicators. p. 419

Calzetti D., Kennicutt Jr. R. C., Bianchi L., et al. 2005, ApJ, 633, 871

Camps P., Baes M., 2015, Astronomy and Computing, 9, 20

Caon N., Capaccioli M., D'Onofrio M., 1993, MNRAS, 265, 1013

Cardelli J. A., Clayton G. C., Mathis J. S., 1989, ApJ, 345, 245

Carraro G., Lia C., Chiosi C., 1998, MNRAS, 297, 1021

Cazaux S., Tielens A. G. G. M., 2004, ApJ, 604, 222

Cen R., 2014, ApJ, 781, 38

Cen R., Ostriker J. P., 1993, ApJ, 417, 415

Ceverino D., Klypin A., 2009, ApJ, 695, 292

Chabrier G., 2003, PASP, 115, 763

Chakrabarti S., Whitney B. A., 2009, ApJ, 690, 1432

Chandrasekhar S., 1960, Radiative transfer

Chen H.-W., Perley D. A., Pollack L. K., Prochaska J. X., Bloom J. S., Dessauges-Zavadsky M., Pettini M., Lopez S., Dall'aglio A., Becker G. D., 2009, ApJ, 691, 152

Christensen C., Quinn T., Governato F., Stilp A., Shen S., Wadsley J., 2012, MNRAS, 425, 3058

Ciesla L., Boquien M., Boselli A., Buat V., et al. 2014, A&A, 565, A128

Combes F., Elmegreen B. G., 1993, A&A, 271, 391

Cook D. O., Dale D. A., Johnson B. D., Van Zee L., Lee J. C., Kennicutt R. C., Calzetti D., Staudaher S. M., Engelbracht C. W., 2014a, MNRAS, 445, 899

Cook D. O., Dale D. A., Johnson B. D., Van Zee L., Lee J. C., Kennicutt R. C., Calzetti D., Staudaher S. M., Engelbracht C. W., 2014b, MNRAS, 445, 881

Cooper M. C., Tremonti C. A., Newman J. A., Zabludoff A. I., 2008, MNRAS, 390, 245

Couchman H., Pearce F., Thomas P., , 2011, Hydra: A Parallel Adaptive Grid Code, Astrophysics Source Code Library

Coupeaud A., Demyk K., Meny C., Nayral C., Delpech F., Leroux H., Depecker C., Creff G., Brubach J.-B., Roy P., 2011, A&A, 535, A124

Courteau S., Dutton A. A., van den Bosch F. C., et al. 2007, ApJ, 671, 203

Curir A., Mazzei P., 1999, A&A, 352, 103

Curir A., Mazzei P., Murante G., 2006, A&A, 447, 453

Curir A., Mazzei P., Murante G., 2007, A&A, 467, 509

Curir A., Mazzei P., Murante G., 2008, A&A, 481, 651

da Cunha E., Charlot S., Elbaz D., 2008, MNRAS, 388, 1595

Dale J. E., 2015, ArXiv, 68, 1

Dalla Vecchia C., Schaye J., 2008, MNRAS, 387, 1431

Dalla Vecchia C., Schaye J., 2012, MNRAS, 426, 140

de Souza R. E., Gadotti D. A., dos Anjos S., 2004, ApJS, 153, 411

de Vaucouleurs G., 1959, Handbuch der Physik, 53, 275

Debattista V. P., Mayer L., Carollo C. M., Moore B., Wadsley J., Quinn T., 2006, ApJ, 645, 209

Debattista V. P., Moore B., Quinn T., Kazantzidis S., Maas R., Mayer L., Read J., Stadel J., 2008, ApJ, 681, 1076

Debattista V. P., Sellwood J. A., 1996, ArXiv Astrophysics e-prints

Debattista V. P., Sellwood J. A., 2000, ApJ, 543, 704

DeBuhr J., Ma C.-P., White S. D. M., 2012, MNRAS, 426, 983

Dekel A., Sari R., Ceverino D., 2009, ApJ, 703, 785

Di Cerbo P., 2015, Master Thesis

Di Matteo T., Croft R. A. C., Springel V., Hernquist L., 2003, ApJ, 593, 56

Domínguez-Tenreiro R., Obreja A., Granato G. L., Schurer A., Alpresa P., Silva L., Brook C. B., Serna A., 2014, MNRAS, 439, 3868

Draine B. T., 1978, ApJS, 36, 595

Draine B. T., 2003, ARAA, 41, 241

Draine B. T., Bertoldi F., 1996, ApJ, 468, 269

Draine B. T., Dale et al. 2007, ApJ, 663, 866

Draine B. T., Lee H. M., 1984, ApJ, 285, 89

Dubinski J., 1994, ApJ, 431, 617

Dubinski J., Gauthier J.-R., Widrow L., Nickerson S., 2008, in Funes J. G., Corsini E. M., eds, Formation and Evolution of Galaxy Disks Vol. 396 of Astronomical Society of the Pacific Conference Series, Spiral and Bar Instabilities Provoked by Dark Matter Satellites. p. 321

Duffy A. R., Kay S. T., Battye R. A., Booth C. M., et al. 2012, MNRAS, 420, 2799

Dutton A. A., Conroy C., van den Bosch F. C., et al. 2011, MNRAS, 416, 322

Efstathiou G., Lake G., Negroponte J., 1982, MNRAS, 199, 1069

Elbaz D., Daddi E., Le Borgne D., Dickinson M., et al. 2007, A&A, 468, 33

Elbaz D., Dickinson M., Hwang H. S., Díaz-Santos T., et al. 2011, A&A, 533, A119

Ellison S. L., Patton D. R., Simard L., McConnachie A. W., 2008, ApJ, 672, L107

Elmegreen B. G., Bournaud F., Elmegreen D. M., 2008, ApJ, 688, 67

Elmegreen B. G., Elmegreen D. M., 1985, ApJ, 288, 438

Eskridge P. B., Frogel J. A., Pogge R. W., et al. 2000, AJ, 119, 536

Evrard A. E., 1988, MNRAS, 235, 911

Fabjan D., Borgani S., Tornatore L., Saro A., Murante G., Dolag K., 2010, MNRAS, 401, 1670

Falcón-Barroso J., Bacon R., Bureau M., et al. 2006, MNRAS, 369, 529

Fathi K., Beckman J. E., Piñol-Ferrer N., et al. 2009, ApJ, 704, 1657

Ferland G. J., Porter R. L., van Hoof P. A. M., et al. 2013, RMXAA, 49, 137

Frenk C. S., White S. D. M., Bode P., Bond J. R., et al. 1999, ApJ, 525, 554

Fritz J., Gentile G., Smith M. W. L., Gear W. K., et al. 2012, A&A, 546, A34

Fryxell B., Olson K., Ricker P., Timmes F. X., et al. 2000, ApJS, 131, 273

Gadotti D. A., 2008, MNRAS, 384, 420

Gadotti D. A., 2011, MNRAS, 415, 3308

Gadotti D. A., de Souza R. E., 2006, ApJS, 163, 270

Galli D., Palla F., 1998, A&A, 335, 403

Genel S., Naab T., Genzel R., Förster Schreiber N. M., et al. 2012, ApJ, 745, 11

Giovanelli R., Haynes M. P., Kent B. R., Saintonge A., et al. 2007, AJ, 133, 2569

Glover S. C. O., Brand P. W. J. L., 2003, MNRAS, 340, 210

Gnedin N. Y., Abel T., 2001, New Astronomy, 6, 437

Gnedin N. Y., Hollon N., 2012, ApJS, 202, 13

Gnedin N. Y., Kravtsov A. V., 2011, ApJ, 728, 88

Gnedin N. Y., Tassis K., Kravtsov A. V., 2009, ApJ, 697, 55

Gordon K. D., Bailin J., Engelbracht C. W., et al. 2006, ApJ, 638, L87

Gordon K. D., Clayton G. C., Misselt K. A., et al. 2003, ApJ, 594, 279

Governato F., Mayer L., Wadsley J., Gardner J. P., Willman B., Hayashi E., Quinn T., Stadel J., Lake G., 2004, ApJ, 607, 688

Governato F., Zolotov A., Pontzen A., Christensen C., Oh S. H., Brooks A. M., Quinn T., Shen S., Wadsley J., 2012, MNRAS, 422, 1231

Goz D., Monaco P., Granato G., Murante G., Domínguez-Tenreiro R., Obreja A., Annunziatella M., Tescari E., in prep., MNRAS

Goz D., Monaco P., Murante G., Curir A., 2015, MNRAS, 447, 1774

Granato G. L., Danese L., 1994, MNRAS, 268, 235

Granato G. L., Lacey C. G., Silva L., Bressan A., Baugh C. M., Cole S., Frenk C. S., 2000, ApJ, 542, 710

Granato G. L., Ragone-Figueroa C., Domínguez-Tenreiro R., Obreja A., Borgani S., De Lucia G., Murante G., 2015, MNRAS, 450, 1320

Gruppioni C., Pozzi F., Rodighiero G., Delvecchio I., et al. 2013, MNRAS, 432, 23

Guedes J., Callegari S., Madau P., Mayer L., 2011, ApJ, 742, 76

Guedes J., Mayer L., Carollo M., Madau P., 2013, ApJ, 772, 36

Guo Q., White S., Li C., Boylan-Kolchin M., 2010, MNRAS, 404, 1111

Haardt F., Madau P., 1996, ApJ, 461, 20

Haardt F., Madau P., 2001, in Neumann D. M., Tran J. T. V., eds, Clusters of Galaxies and the High Redshift Universe Observed in X-rays Modelling the UV/X-ray cosmic background with CUBA. p. 64

Haardt F., Madau P., 2012, ApJ, 746, 125

Haiman Z., Abel T., Rees M. J., 2000, ApJ, 534, 11

Haynes M. P., Giovanelli R., Martin A. M., et al. 2011, AJ, 142, 170

Hernquist L., Katz N., 1989, ApJS, 70, 419

Hinz J. L., Rieke G. H., Caldwell N., 2003, AJ, 126, 2622

Hiotelis N., Voglis N., 1991, A&A, 243, 333

Hirschmann M., Dolag K., Saro A., Bachmann L., Borgani S., Burkert A., 2014, MNRAS, 442, 2304

Hockney R. W., Eastwood J. W., 1988, Computer simulation using particles

Hollenbach D., Salpeter E. E., 1971, ApJ, 163, 155

Hopkins P. F., 2013, MNRAS, 428, 2840

Hopkins P. F., , 2014, GIZMO: Multi-method magneto-hydrodynamics+gravity code, Astrophysics Source Code Library

Hopkins P. F., Keres D., Onorbe J., Faucher-Giguere C.-A., et al. 2013, ArXiv e-prints

Hopkins P. F., Kereš D., Murray N., Quataert E., Hernquist L., 2012, MNRAS, 427, 968

Hopkins P. F., Kereš D., Oñorbe J., Faucher-Giguère C.-A., Quataert E., Murray N., Bullock J. S., 2014, MNRAS, 445, 581

Hopkins P. F., Quataert E., Murray N., 2011, MNRAS, 417, 950

Hopkins P. F., Somerville R. S., Cox T. J., et al. 2009, MNRAS, 397, 802

Hui L., Gnedin N. Y., 1997, MNRAS, 292, 27

Jenkins E. B., 2009, ApJ, 700, 1299

Jenkins E. B., 2014, ArXiv e-prints

Jiang X.-J., Wang Z., Gu Q., Wang J., et al. 2015, ApJ, 799, 92

Jones A., 2014, ArXiv e-prints

Jonsson P., Groves B. A., Cox T. J., 2010, MNRAS, 403, 17

Jubelgas M., Springel V., Enßlin T., Pfrommer C., 2008, A&A, 481, 33

Julian W. H., Toomre A., 1966, ApJ, 146, 810

Karpas Z., 1979, Chemical Physics Letters, 67, 446

Katz N., 1992, ApJ, 391, 502

Katz N., Gunn J. E., 1991, ApJ, 377, 365

Katz N., Weinberg D. H., Hernquist L., 1996, ApJS, 105, 19

Kazantzidis S., Kravtsov A. V., Zentner A. R., Allgood B., Nagai D., Moore B., 2004, ApJ, 611, L73

Kennicutt Jr. R. C., 1998, ApJ, 498, 541

Kennicutt Jr. R. C., Calzetti D., Walter F., et al. 2007, ApJ, 671, 333

Kereš D., Katz N., Weinberg D. H., Davé R., 2005, MNRAS, 363, 2

Klypin A., Yepes G., Gottlober S., Prada F., Hess S., 2014, ArXiv e-prints

Kormendy J., 1982, ApJ, 257, 75

Kormendy J., Fisher D. B., Cornell M. E., Bender R., 2009, ApJS, 182, 216

Kormendy J., Kennicutt Jr. R. C., 2004, ARAA, 42, 603

Krajnović D., Emsellem E., Cappellari M., et al. 2011, MNRAS, 414, 2923

Kraljic K., Bournaud F., Martig M., 2012, ApJ, 757, 60

Kravtsov A. V., Klypin A. A., Khokhlov A. M., 1997, ApJS, 111, 73

Kroupa P., Tout C. A., Gilmore G., 1993, MNRAS, 262, 545

Krumholz M. R., McKee C. F., Tumlinson J., 2009, ApJ, 699, 850

Krumholz M. R., Tan J. C., 2007, ApJ, 654, 304

Kuhlen M., Krumholz M. R., Madau P., Smith B. D., Wise J., 2012, ApJ, 749, 36

Laurikainen E., Salo H., Buta R., 2004, ApJ, 607, 103

Laurikainen E., Salo H., Buta R., Knapen J. H., 2009, ApJ, 692, L34

Leroy A. K., Bolatto A., Gordon K., Sandstrom K., t al. 2011, ApJ, 737, 12

Leroy A. K., Walter F., Bigiel F., Usero A., et al. 2009, AJ, 137, 4670

Leroy A. K., Walter F., Brinks E., Bigiel F., de Blok W. J. G., Madore B., Thornley M. D., 2008, AJ, 136, 2782

Leroy A. K., Walter F., Sandstrom K., Schruba A., et al. 2013, AJ, 146, 19

Li Y., Hopkins P. F., Hernquist L., Finkbeiner D. P., Cox T. J., Springel V., Jiang L., Fan X., Yoshida N., 2008, ApJ, 678, 41

Lia C., Carraro G., 2000, MNRAS, 314, 145

Lipovka A., Núñez-López R., Avila-Reese V., 2005, MNRAS, 361, 850

Lisenfeld U., Espada D., Verdes-Montenegro L., et al. 2011, A&A, 534, A102

Liu G., Koda J., Calzetti D., Fukuhara M., Momose R., 2011, ApJ, 735, 63

Lutz D., Poglitsch A., Altieri B., Andreani P., et al. 2011, A&A, 532, A90

Mac Low M.-M., Glover S. C. O., 2012, ApJ, 746, 135

Machacek M. E., Bryan G. L., Abel T., 2001, ApJ, 548, 509

Maio U., Dolag K., Ciardi B., Tornatore L., 2007, MNRAS, 379, 963

Mandelker N., Dekel A., Ceverino D., Tweed D., Moody C. E., Primack J., 2014, MNRAS, 443, 3675

Marinacci F., Pakmor R., Springel V., 2013, MNRAS

Marinacci F., Pakmor R., Springel V., 2014, MNRAS, 437, 1750

Marri S., White S. D. M., 2003, MNRAS, 345, 561

Martin C. L., 2005, ApJ, 621, 227

Mathis J. S., Cardelli J. A., 1992, ApJ, 398, 610

Mathis J. S., Mezger P. G., Panagia N., 1983, A&A, 128, 212

Mathis J. S., Rumpl W., Nordsieck K. H., 1977, ApJ, 217, 425

McKee C. F., Ostriker E. C., 2007, ARAA, 45, 565

McKee C. F., Ostriker J. P., 1977, ApJ, 218, 148

Menon H., Wesolowski L., Zheng G., Jetley P., Kale L., Quinn T., Governato F., 2015, Computational Astrophysics and Cosmology, 2, 1

Michel-Dansac L., Wozniak H., 2006, A&A, 452, 97

Mihos J. C., Hernquist L., 1996, ApJ, 464, 641

Monaco P., 2004, MNRAS, 352, 181

Monaco P., Murante G., Borgani S., Dolag K., 2012, MNRAS, 421, 2485

Monaghan J. J., 1992, ARAA, 30, 543

Montero-Dorta A. D., Prada F., 2009, MNRAS, 399, 1106

Moorthy B. K., Holtzman J. A., 2006, MNRAS, 371, 583

Moster B. P., Macciò A. V., Somerville R. S., et al. 2010, MNRAS, 403, 1009

Mouhcine M., Baldry I. K., Bamford S. P., 2007, MNRAS, 382, 801

Murante G., Borgani S., Brunino R., Cha S.-H., 2011, MNRAS, 417, 136

Murante G., Calabrese M., De Lucia G., Monaco P., Borgani S., Dolag K., 2012, ApJ, 749, L34

Murante G., Monaco P., Borgani S., Tornatore L., Dolag K., Goz D., 2015, MNRAS, 447, 178

Murante G., Monaco P., Giovalli M., Borgani S., Diaferio A., 2010, MNRAS, 405, 1491

Nagai D., Vikhlinin A., Kravtsov A. V., 2007, ApJ, 655, 98

Nair P. B., Abraham R. G., 2010, ApJS, 186, 427

Navarro J. F., Benz W., 1991, ApJ, 380, 320

Navarro J. F., Frenk C. S., White S. D. M., 1996, ApJ, 462, 563

Navarro J. F., Steinmetz M., 1997, ApJ, 478, 13

Navarro J. F., White S. D. M., 1994, MNRAS, 267, 401

Noeske K. G., Weiner B. J., Faber S. M., Papovich C., et al. 2007, ApJ, 660, L43

Noguchi M., 1996, ApJ, 469, 605

Obreja A., Brook C. B., Stinson G., Domínguez-Tenreiro R., Gibson B. K., Silva L., Granato G. L., 2014, MNRAS, 442, 1794

Oh S., Oh K., Yi S. K., 2012, ApJS, 198, 4

Ohta K., 1996, in Buta R., Crocker D. A., Elmegreen B. G., eds, IAU Colloq. 157: Barred Galaxies Vol. 91 of Astronomical Society of the Pacific Conference Series, Global Photometric Properties of Barred Galaxies. p. 37

Ohta K., Hamabe M., Wakamatsu K.-I., 1990, ApJ, 357, 71

Okamoto T., 2013, MNRAS, 428, 718

Okamoto T., Isoe M., Habe A., 2015, PASJ, 67, 63

Oohama N., Okamura S., Fukugita M., Yasuda N., Nakamura O., 2009, ApJ, 705, 245

Oppenheimer B. D., Davé R., 2006, MNRAS, 373, 1265

Oppenheimer B. D., Davé R., 2008, MNRAS, 387, 577

Oran E. S., Boris J. P., 1987, NASA STI/Recon Technical Report A, 88, 44860

Ostriker J. P., Peebles P. J. E., 1973, ApJ, 186, 467

Padovani P., Matteucci F., 1993, ApJ, 416, 26

Peebles P. J., Ratra B., 2003, Reviews of Modern Physics, 75, 559

Peng C. Y., Ho L. C., Impey C. D., Rix H.-W., 2002, AJ, 124, 266

Peng Y.-j., Lilly S. J., Kovac K., Bolzonella M., Pozzetti L., Renzini A., Zamorani G., Ilbert O., et al. 2010, ApJ, 721, 193

Peterson J. R., Aberth W. H., et al. 1971, Phys. Rev, 3, 1651

Petrosian V., 1976, ApJ, 209, L1

Pizagno J., Prada F., Weinberg D. H., Rix H.-W., et al. 2007, AJ, 134, 945

Planck Collaboration Abergel A., Ade P. A. R., Aghanim N., Alves M. I. R., Aniano G., Armitage-Caplan C., Arnaud M., Ashdown M., Atrio-Barandela F., et al. 2014, A&A, 571, A11

Planck Collaboration et al. 2015, ArXiv e-prints

Price D. J., 2012, Journal of Computational Physics, 231, 759

Read J. I., Hayfield T., 2012, MNRAS, 422, 3037

Rémy-Ruyer A., Madden S. C., Galliano F., et al. 2014, A&A, 563, A31

Richings A. J., Schaye J., Oppenheimer B. D., 2014, MNRAS, 440, 3349

Roberge W., Dalgarno A., 1982, ApJ, 255, 489

Roberts M. S., Haynes M. P., 1994, ARAA, 32, 115

Robertson B., Yoshida N., Springel V., Hernquist L., 2004, ApJ, 606, 32

Romeo A. B., Wiegert J., 2011, MNRAS, 416, 1191

Rosati P., Borgani S., Norman C., 2002, ARAA, 40, 539

Rybicki G. B., Lightman A. P., 1979, Radiative processes in astrophysics

Saintonge A., Kauffmann G., Kramer C., Tacconi L. J., et al. 2011, MNRAS, 415, 32

Saitoh T. R., Makino J., 2013, ApJ, 768, 44

Savin D. W., 2002, ApJ, 566, 599

Savin D. W., Krstić P. S., Haiman Z., Stancil P. C., 2004, ApJ, 606, L167

Scannapieco C., Athanassoula E., 2012, MNRAS, 425, L10

Scannapieco C., Gadotti D. A., Jonsson P., White S. D. M., 2010, MNRAS, 407, L41

Scannapieco C., Tissera P. B., White S. D. M., Springel V., 2006, MNRAS, 371, 1125

Scannapieco C., Wadepuhl M., Parry O. H., et al. 2012, MNRAS, 423, 1726

Scannapieco C., White S. D. M., Springel V., Tissera P. B., 2009, MNRAS, 396, 696

Schaye J., Crain R. A., Bower R. G., Furlong M., et al. 2015, MNRAS, 446, 521

Schaye J., Dalla Vecchia C., 2008, MNRAS, 383, 1210

Schechter P., 1976, ApJ, 203, 297

Schmidt M., 1959, ApJ, 129, 243

Seidel M. K., Falcón-Barroso J., Martínez-Valpuesta I., et al. 2015, MNRAS, 451, 936

Sellwood J. A., Nelson R. W., Tremaine S., 1998, ApJ, 506, 590

Sembolini F., Yepes G., Pearce F. R., Knebe A., et al. 2015, ArXiv e-prints

Sersic J. L., 1968, Atlas de galaxias australes

Shapiro P. R., Kang H., 1987, ApJ, 318, 32

Shen S., Mo H. J., White S. D. M., Blanton M. R., et al. 2003, MNRAS, 343, 978

Shi Y., Armus L., Helou G., Stierwalt S., Gao Y., Wang J., Zhang Z.-Y., Gu Q., 2014, Nature, 514, 335

Shimasaku K., Fukugita M., Doi M., Hamabe M., Ichikawa T., Okamura S., Sekiguchi M., Yasuda N., Brinkmann J., Csabai I., Ichikawa S.-I., Ivezić Z., Kunszt P. Z., Schneider D. P., Szokoly G. P., Watanabe M., York D. G., 2001, AJ, 122, 1238

Silva L., 1999, PhD thesis, SISSA - Trieste, Italy

Silva L., Granato G. L., Bressan A., Danese L., 1998, ApJ, 509, 103

Skrutskie M. F., Cutri R. M., Stiening R., et al. 2006, AJ, 131, 1163

Snyder G. F., Torrey P., Lotz J. M., Genel S., et al. 2015, ArXiv e-prints

Sofue Y., Rubin V., 2001, ARAA, 39, 137

Sommer-Larsen J., Gelato S., Vedel H., 1999, ApJ, 519, 501

Springel V., 2005, MNRAS, 364, 1105

Springel V., 2010, MNRAS, 401, 791

Springel V., 2014, ArXiv e-prints

Springel V., Di Matteo T., Hernquist L., 2005, MNRAS, 361, 776

Springel V., et al. 2005, Nature, 435, 629

Springel V., Hernquist L., 2003, MNRAS, 339, 289

Springel V., Wang J., Vogelsberger M., Ludlow A., et al. 2008, MNRAS, 391, 1685

Springel V., Wang J., Vogelsberger M., Ludlow A., Jenkins A., Helmi A., Navarro J. F., Frenk C. S., White S. D. M., 2008, MNRAS, 391, 1685

Springel V., White S. D. M., Tormen G., Kauffmann G., 2001, MNRAS, 328, 726

Springob C. M., Haynes M. P., Giovanelli R., Kent B. R., 2005, ApJS, 160, 149

Stancil P. C., Lepp S., Dalgarno A., 1998, ApJ, 509, 1

Steinmetz M., Muller E., 1995, MNRAS, 276, 549

Steinmetz M., Navarro J. F., 1999, ApJ, 513, 555

Stibbe D. T., Tennyson J., 1999, ApJ, 513, L147

Stinson G., Seth A., Katz N., Wadsley J., Governato F., Quinn T., 2006, MNRAS, 373, 1074

Stinson G. S., Brook C., Macciò A. V., et al. 2013, MNRAS, 428, 129

Stoehr F., White S. D. M., Tormen G., Springel V., 2002, MNRAS, 335, L84

Sutherland R. S., Dopita M. A., 1993, ApJS, 88, 253

Teyssier R., , 2010, RAMSES: A new N-body and hydrodynamical code, Astrophysics Source Code Library

Theuns T., Chalk A., Schaller M., Gonnet P., 2015, ArXiv e-prints

Thielemann F.-K., Argast D., Brachwitz F., et al. 2003, Nuclear Physics A, 718, 139

Thomas P. A., Couchman H. M. P., 1992, MNRAS, 257, 11

Tissera P. B., White S. D. M., Pedrosa S., Scannapieco C., 2010, MNRAS, 406, 922

Toomre A., 1964, ApJ, 139, 1217

Toomre A., 1977, in Tinsley B. M., Larson D. Campbell R. B. G., eds, Evolution of Galaxies and Stellar Populations Mergers and Some Consequences. p. 401

Tornatore L., Borgani S., Dolag K., Matteucci F., 2007, MNRAS, 382, 1050

Torrey P., Snyder G. F., Vogelsberger M., et al. 2015, MNRAS, 447, 2753

Tremonti C. A., Heckman T. M., Kauffmann G., et al. 2004, ApJ, 613, 898

Trumpler R. J., 1930, PASP, 42, 267

Tully R. B., Fisher J. R., 1977, A&A, 54, 661

Uhlig M., Pfrommer C., Sharma M., Nath B. B., Enßlin T. A., Springel V., 2012, MNRAS, 423, 2374

Valencic L. A., Clayton G. C., Gordon K. D., 2004, ApJ, 616, 912

van den Hoek L. B., Groenewegen M. A. T., 1997, A&AS, 123, 305

Verheijen M. A. W., 2001, ApJ, 563, 694

Vladilo G., Abate C., Yin J., Cescutti G., Matteucci F., 2011, A&A, 530, A33

Vogelsberger M., Genel S., Sijacki D., Torrey P., Springel V., Hernquist L., 2014, MNRAS, 438, 3607

Vogelsberger M., Genel S., Springel V., Torrey P., et al. 2014, MNRAS, 444, 1518

Vogelsberger M., Zavala J., Simpson C., Jenkins A., 2014, MNRAS, 444, 3684

Wadepuhl M., Springel V., 2011, MNRAS, 410, 1975

Wadsley J. W., Stadel J., Quinn T., 2004, New Astronomy, 9, 137

Walker I. R., Mihos J. C., Hernquist L., 1996, ApJ, 460, 121

Walter F., Brinks E., de Blok W. J. G., Bigiel F., Kennicutt R. C., Thornley M. D., Leroy A., 2008, AJ, 136, 2563

Wang B., Silk J., 1994, ApJ, 427, 759

Wang J. G., Stancil P. C., 2002, Physica Scripta, 2002, 72

Weingartner J. C., Draine B. T., 2001a, ApJ, 548, 296

Weingartner J. C., Draine B. T., 2001b, ApJ, 548, 296

Wetzstein M., Nelson A. F., Naab T., Burkert A., 2009, ApJS, 184, 298

Wiersma R. P. C., Schaye J., Smith B. D., 2009, MNRAS, 393, 99

Wiersma R. P. C., Schaye J., Theuns T., Dalla Vecchia C., Tornatore L., 2009, ArXiv e-prints

Wolfire M. G., Tielens A. G. G. M., Hollenbach D., Kaufman M. J., 2008, ApJ, 680, 384

Wong T., Blitz L., 2002, ApJ, 569, 157

Woosley S. E., Weaver T. A., 1995, ApJS, 101, 181

York D. G., SDSS Collaboration 2000, AJ, 120, 1579

Yoshida N., Abel T., Hernquist L., Sugiyama N., 2003, ApJ, 592, 645

Yoshida N., Oh S. P., Kitayama T., Hernquist L., 2007, ApJ, 663, 687

Young C. K., Currie M. J., 1994, MNRAS, 268, L11

Young J. S., Scoville N. Z., 1991, ARAA, 29, 581

Zemp M., Gnedin O. Y., Gnedin N. Y., Kravtsov A. V., 2012, ApJ, 748, 54